RANDOM SUBSET FEATURE SELECTION

FOR ECOLOGICAL NICHE MODELING

OF WILDFIRE ACTIVITY

AND THE MONARCH BUTTERFLY

A Dissertation

by

JAMES L. TRACY

Submitted to the Office of Graduate and Professional Studies of
Texas A&M University
in partial fulfillment of the requirements for the degree of

DOCTOR OF PHILOSOPHY

Chair of Committee,	Robert N. Coulson
Co-Chair of Committee,	Allen E. Knutson
Committee Members,	Micky D. Eubanks
	A. Michelle Lawing
Head of Department,	David W. Ragsdale

December 2018

Major Subject: Entomology

ABSTRACT

Correlative ecological niche models (ENMs) are essential for investigating distributions of species and natural phenomena via environmental correlates across broad fields, including entomology and pyrogeography featured in this study. Feature (variable) selection is critical for producing more robust ENMs with greater transferability across space and time, but few studies evaluate formal feature selection algorithms (FSAs) for producing higher performance ENMs. Variability of ENMs arising from feature subsets is also seldom represented. A novel FSA is developed and evaluated, the random subset feature selection algorithm (RSFSA). The RSFSA generates an ensemble of higher accuracy ENMs from different feature subsets, producing a feature subset ensemble (FSE). The RSFSA-selected FSEs are novelly used to represent ENM variability.

Wildfire activity presence/absence databases for the western US prove ideal for evaluating RSFSA-selected MaxEnt ENMs. The RSFSA was effective in identifying FSEs of 15 of 90 variables with higher accuracy and information content than random FSEs. Selected FSEs were used to identify severe contemporary wildfire deficits and significant future increases in wildfire activity for many ecoregions.

Migratory roosting localities of declining eastern North American monarch butterflies (*Danaus plexippus*) were used to spatially model migratory pathways, comparing RSFSA-selected MaxEnt ENMs and kernel density estimate models (KDEMs). The higher information content ENMs best correlated migratory pathways with nectar resources in grasslands. Higher accuracy KDEMs best revealed migratory pathways through less suitable desert environments.

Monarch butterfly roadkill data was surveyed for Texas within the main Oklahoma to Mexico Central Funnel migratory pathway. A random FSE of MaxEnt roadkill ENMs was used to estimate a 2-3% loss of migrants to roadkill. Hotspots of roadkill in west Texas and Mexico were recommended for assessing roadkill mitigation to assist in monarch population recovery.

The RSFSA effectively produces higher performance ENM FSEs for estimating optimal feature subset sizes, and comparing ENM algorithms and parameters, and environmental scenarios. The RSFSA also performed comparably to expert variable selection, confirming its value in the absence of expert information. The RSFSA should be compared with other FSAs for developing ENMs and in data mining applications across other disciplines, such as image classification and molecular bioinformatics.

DEDICATION

This study is dedicated to my parents, Bill and Betsy, wife, Debbie, and son, Nathaniel, for their patience and support through my lengthy and rewarding period of PhD education and dissertation research at Texas A&M University.

ACKNOWLEDGEMENTS

CONTRIBUTORS AND FUNDING SOURCES

(Chapter II) and the Texas Comptroller of Public Accounts, Economic Growth and Endangered

Species Management Division, Interagency Contract No. 16-5979 (Chapters III and IV).

AUC_{bgp} — Area Under the Curve (AUC) background/presence accuracy statistic; default AUC calculation of MaxEnt software environment using background and presence data as absences

AUC_{diff} — Model overfitting statistics calculated as training AUC (AUC_{train}) minus testing AUC (AUC_{test})

AUC_{pa} — AUC presence/absence accuracy statistic; calculated outside of MaxEnt software environment using absence data as absences

AUC_{psa} — AUC presence only accuracy statistics; calculated outside of MaxEnt software environment using pseudoabsence data

$AUC_{pa\_wrappertrain}$ — AUC_{pa} wrapper train; derived from wrapper model training data; used in calculating wrapper data overfitting (see $AUC_{pa\_diff\_wrapper}$) and evaluating wrapper data underfitting in conjuction with $AUC_{pa\_wrappertest}$

$AUC_{pa\_wrappertest}$ — AUC_{pa} wrapper test; derived from wrapper model testing data; random subset feature selection algorithm (RSFSA) wrapper for ranking models

$AUC_{pa\_finaltrain}$ — AUC_{pa} final train; derived from final model testing data; used in calculating final data overfitting (see $AUC_{pa\_diff\_final}$) and in evaluating final data underfitting in conjunction with $AUC_{pa\_finaltest}$

$AUC_{pa\_finaltest}$ — AUC_{pa} final test; derived from final model testing data; used for evaluating RSFSA selected model performance

$AUC_{pa\_diff\_wrapper}$	AUC_{pa} difference wrapper; derived from wrapper model data; model overfitting statistic calculated as $AUC_{pa\_wrapperrtrain}$ minus $AUC_{pa\_wrappertest}$; smaller values optimal; RSFSA wrapper for ranking models
$AUC_{pa\_diff\_final}$	AUC_{pa} difference final; derived from final model training and testing data; calculated as $AUC_{pa\_finaltrain}$ minus $AUC_{pa\_finaltest}$; used for evaluating RSFSA selected model performance
AUC_{test}	AUC derived from model testing data
AUC_{train}	AUC derived from model training data; model underfitting is indicated when both AUC_{train} and AUC_{test} are low
AET	Actual Evapotranspiration
AICc	Corrected Akaike Information Criterion (AIC) calculated for GLM and Glmnet models using null deviance and model fit deviance
$AICc_{bg}$	Corrected Akaike Information Criterion (AIC) background statistic; niche model complexity and information statistic calculated from background point data (proposed in this study); smaller values optimal
$AICc_{bg\_reg}$	Corrected Akaike Information Criterion (AIC) background statistic-regression calculated; niche model complexity and information statistic calculated for a GLM or Glmnet model using a regression equation relating AICc to $AICc_{bg}$ for comparison with MaxEnt $AICc_{bg}$
$AICc_{bg\_wrapper}$	$AICc_{bg}$ from wrapper model data; RSFSA wrapper for ranking models

AICc$_{bg\_final}$	AICc$_{bg}$ from final model training data; used for evaluating RSFSA selected model performance
BEE	Background Evaluation Extent; area from which wildfire model training and testing data is derived; model projections less certain outside of this area
CSME	Climate Scenario Model Ensemble; assembly of niche models differing only in the climate scenario from which they were developed
ENM	Ecological Niche Model; a correlational ENM is the spatial projection of the distribution of a species or natural phenomenon on the basis of correlation between occurrence points and environmental features using a computer algorithm.
ETRT	Evapotranspiration Ratio; AET/PET
Filter	Search criterion in feature selection that does not require computation of the induction algorithm (e.g., classification algorithm) for which the features are being selected. An example filter is intervariable correlation.
FSA	Feature Selection Algorithm; an algorithm designed to search through a larger set of variables to find a smaller subset of more relevant and less redundant variables for improving performance of an induction algorithm, such as for classification or regression.
FSE	Feature Subset Ensemble; assembly of niche models differing only in the variable subsets from which they were developed
GCM	General circulation model for future climate scenarios

HE   Hadley Global Environmental Model 2 – Earth System GCM

KDE   Kernel Density Estimate; nonparametric spatial point pattern method for analyzing a point intensity surface; often used with animal telemetry data for assessing frequency of utilization of an area and defining animal home ranges

KDEM   Kernel Density Estimate Model; KDE normalized from zero to one and calibrated using TSS

MAE   Multi-Algorithm Ensemble; assembly of niche models differing only in the classification algorithm from which they were developed

MRSFS   Multiple Randomized Sequential Forward Selection; type of sequential search strategy in feature selection involving multiple iterations of random sequential forward selection (SFS)

MPE   Model Parameter Ensemble; assembly of niche models differing only in the model parameters for the classification algorithm from which they were developed

MTBS   Monitoring Trends in Burn Severity; historical burn severity records

PET   Potential Evapotranspiration

RCP   Representative Concentration Pathway for CO_2 future climate scenarios

RSFSA   Random Subset Feature Selection Algorithm; ensemble hybrid filter/wrapper feature selection algorithm using an unsupervised correlation filter and various subset wrappers (such as $AUC_{pa\_wrappertest}$ or

AICc$_{bg\_wrapper}$) for selecting and ranking models produced from variable subsets

RSS   Random Subset Selection; type of randomized search strategy in feature selection involving ranking the performance of randomly generated variable subsets

SBS   Sequential Backward Selection; type of sequential search strategy in feature selection that starts from many features and reduces to fewer features

SFS   Sequential Forward Selection; type of sequential search strategy in feature selection that starts from one to few features and builds to more features

SWD   Samples With Data format used for more rapid calculation of MaxEnt models using point presence and background data rather than raster data

TSE   Training Set Ensemble; assembly of niche models differing only in the training set data from which they were developed

TSS$_{pa}$ True Skill Statistic presence/absence; calculated using absence data as absences; used for calibrating binary presence absence niche models

TSS$_{psa}$ TSS calculated using pseudoabsence data as absences; used for calibrating binary presence only niche models

Wrapper   Search criterion in feature selection algorithm that is derived from executing the induction algorithm (e.g., for classification) for which the features are being selected. The feature selection algorithm is said to be

"wrapped" around the induction algorithm when wrappers are utilized.

An example wrapper is the accuracy of the induction model.

β   Beta regularization multiplier for determining restrictiveness of L1

regularization in MaxEnt models, "0" equals no L1 regularization (no

restrictions on model parameters), progressively higher numbers equals

greater L1 regularization (high restriction on model parameters)

TABLE OF CONTENTS

LIST OF TABLES

CHAPTER I

INTRODUCTION[*]

Overview

Correlational ecological niche models (ENMs) are an important landscape ecological tool

in spatially projecting species habitats from the relationship of occurrence points with

environmental conditions and resources (Elith and Leathwick, 2009a; Franklin, 2010). The

ENMs have wide applications in diverse fields of study, including invasive species (Elith, 2017),

conservation (Elith and Leathwick, 2009b, Franklin, 2013), endangered species (Fitzgerald et al.,

2018), epidemiology (Escobar and Craft, 2016), phylogeography (Alvarado-Serrano et al., 2014;

Gavin et al. 2014), biological control (Mukherjee et al., 2012), global change (Hijmans and

Graham, 2006; Ehrlén and Morris, 2015; Beaumont et al., 2015), agriculture (Beck, 2013;

Hannah et al., 2013), forestry (Meentemeyer et al., 2008), taxonomy (Raxworthy et al., 2007),

and restoration (Pollack et al., 2012). Although ENMs are most often employed in modeling the

distribution of species (species distribution models), they are also used to model the spatial

distribution of natural phenomena, such as wildfire activity (pyrogeography; Parisien et al.,

2012), migratory movement (Williams et al., 2017), and road mortality (Ha and Shilling, 2018),

all three of which are used as case studies in this investigation. Applications for ENMs cross

many taxa of biological disciplines, including (from most to least examples using the MaxEnt

ENM algorithm), botany, herpetology, mammalogy, ornithology, entomology, bryology,

arachnology, and ichthyology (Bradie and Leung, 2016). This investigation develops new

---

[*] Background section modified with permission from Appendix A, Introduction, of Tracy JL, Trabucco A, Lawing AM, Giermakowski T, Tchakerian M, Drus GM, Coulson RN (2018) Random subset feature selection of ecological niche models for wildfire activity in western North America. Ecological Modelling 383:52-68. Copyright 2018 Ecological Modelling.

presence/absence dataset of wildfire activity in western North America. The tools are then applied in entomological studies of fall migratory and roadkill phenomena for the declining monarch butterfly (*Danaus plexippus*).

The choice of variables in ENMs is critical in that it can strongly influence model outcomes, sometimes to a greater degree than various landscape scenarios under study, such as climate change scenarios (Synes and Osborne, 2011). Consequently, the development of more robust ENMs requires methods to (1) select more optimal variables (feature selection) and (2) account for the variability arising from selected features (Synes and Osborne, 2011; Porfirio et al., 2014). Formal feature selection algorithms (FSAs) are well developed in the disciplines of text mining, image classification, and bioinformatics (Jović et al., 2015), but less extensively investigated for ENMs (but see Gobeyn et al., 2017). Feature selection is a data mining tool for screening large sets of features to find a smaller set of features with higher relevancy and lower redundancy that can improve the performance of various types of analyses, such as classification, regression, and clustering (Jović et al., 2015). Feature selection stands in contrast to feature extraction, such as principal components analysis, which achieves similar objectives through ordination of variables along orthogonal axes and retaining only the first few axes that explain the most variation in the dataset. Feature selection preserves the original variables, which can facilitate clearer interpretation of variable influence in the model (Guyon and Elisseeff, 2003; Jović et al., 2015). Although many studies have employed some form of feature selection for ENMs (see Background below), few have evaluated a formal FSA on ENM performance, and developed methods to account for ENM variability resulting from feature selection. In this study, a novel ensemble random subset feature selection algorithm (RSFSA) tool is developed for ENMs that is similar to the random sets feature selection method developed for image

2

classification (Garcia et al., 2006). This new tool is formally tested with the popular MaxEnt algorithm ENM (Phillips et al., 2006; Bradie and Leung 2016) for its ability to both improve model performance and represent model variability resulting from different feature subsets.

Background

The basic terminology of variable selection criteria and variable search strategies used in feature selection is reviewed below in the context of niche modeling, particularly for MaxEnt, and the proposed novel ensemble random subset feature selection algorithm.

Selection Criteria

Feature selection algorithms are divided into four approaches based on the types of selection criteria: (1) filter methods, (2) wrapper methods, (3) embedded wrapper methods, and (4) hybrid filter-wrapper methods (John et al., 1994; Kohavi and John, 1997; Somol et al., 2010; Tang et al., 2015, Jović et al., 2015). A filter criterion is derived from the data prior to running a niche model, while a wrapper criterion is derived from the results of the niche model (the FSA is said to be "wrapped" around the model; John et al. 1994), requiring much more time for computation. Embedded wrappers are wrappers integrated within a model, such as occur in the algorithms of MaxEnt and random forests. Hybrid filter-wrapper methods combine filters and wrappers for feature selection (Jović et al., 2015; Tang et al., 2015).

Various types of filters are used to screen for the redundancy or relevancy of individual variables (univariate filters) or several variables (multivariate filters). An unsupervised filter is used to screen variables irrespective of the labeled class data (e.g., presence versus absence). An example is an unsupervised correlation filter that reduces variable redundancy by excluding any variables from a feature subset above a certain correlation threshold with the other variables. Such correlation filters have been used in conjunction with wrappers in several hybrid filter-

wrapper feature selection approaches using MaxEnt (e.g., Lahoz-Monfort et al., 2010; Bellamy and Altringham, 2015). Supervised filters screen for variable relevancy using criteria for distinguishing between labeled class data, such as species presence versus absence from a location. For example, a supervised filter can rank individual variables based on assessing the mutual information of variable values with respect to presence versus absence classes (Guyon and Elisseeff, 2003; Liu and Yu, 2005).

In contrast to filters, wrappers for ranking variable relevancy are derived from the computation of the niche model algorithm. Although they require increased computation time, wrappers are much more effective than filters in feature selection for optimizing model performance (Jović et al., 2015). A common example of a wrapper is a classification accuracy statistic used to rank the relevancy of an individual variable (univariate wrapper) or several variables (multivariate wrapper). Several variable selection strategies for MaxEnt have employed univariate wrappers derived from jackknife runs of the model with a single variable (singlet wrapper, this study), with all variables except for a single variable (leave one feature out, LOFO, wrapper; Liu et al., 2013b), or both (e.g., Parolo et al., 2008; Yost et al., 2008; Bradley et al., 2010; Lahoz-Monfort et al., 2010; Bellamy and Altringham, 2015; Jueterbock et al., 2016; Zeng et al., 2016). Specific univariate wrappers used for ranking environmental variables with MaxEnt include the area under the curve (AUC) accuracy statistic (Parolo et al., 2008; Lahoz-Monfort et al., 2010; Bellamy and Altringham, 2015), the corrected Akaike information criterion (AICc) complexity statistic (Zeng et al., 2016), variable percent contribution statistic for the model (Jueterbock et al., 2016), training gain (Yost et al., 2008), and restrictiveness of the model projection area, requiring additional computation for model projection (Bradley et al., 2010).

Only a few studies have employed multivariate wrappers in feature selection with MaxEnt (e.g., Halvorsen et al., 2015, 2016; Jueterbock et al., 2016). Halvorsen et al. (2015, 2016) utilized the R package MIAmaxent for performing both univariate and multivariate wrapper selections for MaxEnt models in two main stages. In the first stage, a univariate leave one feature out wrapper is used to evaluate each individual derived variable that MaxEnt generates from a given environmental variable (e.g., various linear, quadratic, threshold and hinge features; Wilson, 2009). In the second stage, a multivariate wrapper is used to evaluate entire sets of derived variables for a given environmental variable selected during the first stage. The wrappers used in both stages consists of an F-test statistic comparing the model made from leaving out single or multiple derived variables to models that include the left-out variables.

Embedded wrappers are wrapper search criteria which are built into the niche model algorithm. They facilitate more rapid assessment of the effect of a variable on model performance, accomplishing feature selection and model fitting simultaneously (Tang et al., 2015). The GARP niche model includes an embedded wrapper of the intrinsic correct classification rate (Anderson et al., 2003). Random forests and classification and regression trees (CART) also include embedded wrappers (Jović et al., 2015), and are commonly used in species distribution modeling (Elith and Leathwick, 2009a; Mi et al., 2017). The MaxEnt algorithm incorporates lasso L1 regularization of model variable coefficients for feature selection (Phillips and Dudík, 2008), which is a type of embedded wrapper (Tang et al., 2015). The embedded wrapper of MaxEnt is regarded as generally effective in feature selection for smaller sets of variables, but screening of larger sets is advised prior to using MaxEnt (Elith et al., 2011).

Search Strategies

Search strategies for optimal models in feature selection algorithms are generally categorized as (1) exponential (or complete), including exhaustive search; (2) sequential, and (3) randomized (Liu and Yiu, 2005; Jović et al., 2015). Verbruggen et al. (2013) used an exhaustive search algorithm (Maxent Model Surveyor) for calculating wrappers of AUC on all possible subsets of eight variables (i.e., all variable subsets ranging from one to eight in size; $2^8 - 1 = 255$ subsets). The latest version of the Maxent Model Surveyor (v.1.07) also calculates the AIC and Bayesian Information Criterion (BIC) (Verbruggen, 2017). Exhaustive exponential search strategies are generally not practical for large sets of variables. For example, there are 4.6 x 10^{16} possible combinations of unique 15-variable subsets that can be made from 90 variables. Other, more complex, exponential search algorithms can reduce the search effort, such as branch and bound (Liu and Yu, 2005), but they do not appear to have been used with niche modeling. In contrast to the exhaustive search strategy, the sequential and randomized search strategies discussed below cannot identify the uniquely most optimal features, but they represent a more rapid practical heuristic approach of identifying features that approach optimal from a large set of features (Jović et al., 2015).

Feature selection for larger variable sets with MaxEnt and other niche models have typically involved sequential search strategies of either (1) sequential forward selection (SFS) (e.g.; Halvorsen et al., 2015, 2016), (2) sequential backward selection (SBS) (e.g., Yost et al., 2008; Jueterbock et al., 2016; Zeng et al., 2016), or (3) a combination of the two (e.g.; Mouton et al., 2009; Bradley et al., 2010; Lahoz-Monfort et al., 2010; Bellamy and Altringham, 2015). In SFS, a variable or set of variables are added to a variable subset by trial and error to satisfy a wrapper criterion, such as increased model accuracy or reduced complexity. In SBS, the screening process proceeds in reverse, with an individual variable or set of variables removed

from a larger set of variables in accordance with a wrapper criterion. The R package MaxentVariableSelection utilizes an SBS search strategy with the multivariate wrapper criterion of relative variable contribution score and a wrapper for correlation with the highest contributing variable at each step (Jueterbock et al., 2016). These sequential search strategies are affected by the order in which variables are evaluated, and they are potentially subject to becoming trapped in local minima from choosing the best variable subset at the moment (Liu and Motoda, 1998; Jović et al., 2015). A variety of more sophisticated and time-consuming sequential search algorithms, such as sequential forward floating selection, can better avoid entrapment in local minima (Mayer et al., 2000; Liu and Yu, 2005; Somol et al., 2010), but they do not appear to have been implemented for niche modeling.

The randomized search strategy that is used in this study incorporates randomness into the search procedure and can avoid entrapment in local minima that can occur with a sequential search strategy (Jović et al., 2015). In addition, the randomized search strategy facilitates exploration of a wider selection of variable subset combinations more quickly than possible with exclusively sequential search strategies described above, especially when using parallel processing (Breiman, 2001; Garcia et al., 2006). There are a wide variety of random search algorithms, such as the genetic algorithm (Liu and Yu, 2005). The GARP model incorporates an embedded genetic algorithm for ensemble niche modeling and has been widely used (Stockwell and Peters, 1999; Anderson et al., 2003). Simple genetic algorithms have also been used for feature selection with a variety of types of niche models of aquatic organisms, including decision trees (e.g., D'heygere et al., 2003) and habitat suitability index models (e.g., Gobeyn et al., 2017). The random forests algorithm also uses a randomized search strategy for its embedded ensemble feature selection (Breiman, 2001). The proposed random subset feature selection

algorithm in this study incorporates a type of randomized search strategy, here referred to as *random subset selection* (RSS), that Garcia et al. (2006) proposed for the random sets feature selection method (for details, see Chapter II and Appendix A, Methods, RSFSA).

Types of Niche Modeling Ensembles

At least five types of ensembles are used to represent niche model variability (Araújo and New, 2007; revised nomenclature here): (1) multi-algorithm ensembles (MAEs; Schumann et al., 2009; Model Classes of Araújo and New, 2007), which only differ in the classification algorithm, such as MaxEnt versus random forests (e.g., Marmion et al., 2009); (2) training set ensembles (TSEs; Rokach 2005; Initial Conditions of Araújo and New, 2007), for which models differ only in the training data (e.g., bagging; Breiman 1996); (3) climate scenario model ensembles (CSMEs; part of Boundary Conditions of Araújo and New, 2007), a combination of models solely differing in climate scenarios, such as various General Circulation Models (GCMs), or variations of a given GCM, and CO_2 emission scenarios (e.g., Beaumont et al., 2007, 2008); (4) model parameter ensembles (MPEs; Model Parameters of Araújo and New, 2007), in which models differ only by the specified parameters of either the classification algorithm (e.g., beta regularization multiplier for MaxEnt) or component features (e.g., variable coefficients); and (5) feature subset ensembles (FSEs; Aly and Atiya, 2006; part of Boundary Conditions of Araújo and New, 2007), an assembly of models differing only in the feature subsets from which they were developed. Combinations of types of ensembles are often employed in niche modeling. The MAEs, TSEs, and CSMEs are probably most commonly used to represent niche model variability for deterministic niche models (same input features and training data always produces same results), such as MaxEnt (e.g., Zhang et al., 2015). Various stochastic niche models (same input features and training data produce different results) with built-in ensemble

8

feature selection (producing several models or model combinations) produce a combination MPE/TSE/FSE, such as Genetic Algorithm for Rule-set Production (GARP; Stockwell and Peters, 1999), GARP with Best Subsets (Anderson et al., 2003), and random forests (Breiman, 2001). This study appears to be the first to solely employ FSEs in niche modeling.

Objectives

The main objectives of the study are to (1) demonstrate the novel ensemble RSFSA as a tool for developing higher performance ENMs from wildfire activity presence/absence data and illustrate the innovative use of FSEs to represent ENM variability (Chapter II); (2) establish the usefulness of RSFSA with typical pseudoabsence data for ENMs, comparing them with a novel KDE model for identifying monarch fall migratory pathways (Chapter III); and (3) illustrate the use of random FSEs developed using the correlation filter portion of the RSFSA for representing variability in ENMs of monarch fall road mortality where there is insufficient data to utilize the entire RSFSA (Chapter IV).

In the first study (Chapter II) a large dataset of presence/absence data of wildfire activity in the western US serves ideally for demonstrating the ability of RSFSA to select wildfire activity ENMs with significantly improved performance (e.g., higher accuracy and information content) compared to random models using model training and testing data held out from the RSFSA. The RSFSA is also used in this study to identify a roughly optimal feature subset size (number of variables per model) beyond which little is gained in terms of model performance. Top ranked variables selected by RSFSA from an unusually large pool of 90 initial variables are compared to important variables identified in previous wildfire activity model studies. The utility of FSEs is demonstrated for characterizing variability in statistical comparisons of ENM performance among parameterizations of various regression-based ENM algorithms, including

MaxEnt, General Linear Models (GLM), and Glmnet algorithms. A combination of frequency of variable appearance in RSFSA selected FSEs and MaxEnt variable permutation importance is uniquely used to identify important influential variables for ENMs. In addition, FSEs are employed in statistically comparing wildfire activity ENMs from various current and future climate scenarios. Contemporary wildfire deficit maps derived from the wildfire activity FSEs are used to display widespread areas of high wildfire susceptibility across western North America. The FSEs of future climate wildfire activity ENMs reveal significant differences among current and future climate scenarios for specific ecoregions.

In the second study (CHAPTER III), the use of RSFSA is further demonstrated in developing MaxEnt ENMs using pseudoabsence (presence only) data for monarch overnight roosts to identify fall migratory pathways of eastern monarch butterflies. The RSFSA results are also used to identify potentially important variables influencing migratory pathways. The migratory MaxEnt FSE facilitates a unique detailed comparison with performance characteristics of a substantially different novel spatial migratory model, a spatial point pattern Kernel Density Estimate model (KDEM), derived from spatial patterns rather than environmental correlates. The FSE of the MaxEnt ENM is utilized to facilitate a statistical comparison with a KDEM TSE.

In the third study (CHAPTER IV), the stand-alone value of the multiple random sequential forward selection portion of the RSFSA is demonstrated for building random variable subsets of less than |0.7| correlation for developing an FSE to characterize variability in results of a MaxEnt monarch autumn roadkill ENM from Oklahoma to Mexico. In addition, the FSE is used in ranking average permutation importance of variables in the different roadkill ENMs. The results are used to recommend a roadkill mitigation assessment for monarch conservation.

CHAPTER II

RANDOM SUBSET FEATURE SELECTION FOR ECOLOGICAL NICHE MODELS OF

WILDFIRE ACTIVITY IN WESTERN NORTH AMERICA[*]

Synopsis

Variable selection in ecological niche modeling can influence model projections to a degree comparable to variations in future climate scenarios. Consequently, it is important to select feature (variable) subsets for optimizing model performance and characterizing variability. A novel random subset feature selection algorithm (RSFSA) for niche modeling is used to select an ensemble of optimally sized feature subsets of limited correlation ($|r| < 0.7$) from 90 climatic, topographic and anthropogenic indices, generating wildfire activity models for western North America with higher performance. Monitoring Trends in Burn Severity and LANDFIRE wildfire data were used to develop thousands of MaxEnt, GLM and Glmnet models. The RSFSA-selected models performed better than random models, having higher accuracy (Area Under the Curve statistic; AUC), lower complexity (corrected Akaike Information Criterion; AICc), and, in some cases, lower overfitting (AUC_{diff}). The RSFSA-selected MaxEnt quadratic/hinge (β-regularization 2) feature models generally had higher AUC and lower AICc outperforming other niche model parameterizations and methods. Feature subset ensembles of RSFSA-selected 15-variable MaxEnt quadratic/hinge models were used to characterize variability in projected areas of large wildfires for three burn severities under current, 2050, and 2070 climate scenarios. Expert screening of variables before RSFSA did not improve model performance. Widespread

contemporary wildfire deficits and projected regional changes in wildfires highlight the need to manage fuel loads and restore natural fire regimes. The RSFSA is valuable for optimizing niche model performance and generating feature subset ensembles to characterize model variability across niche models of various feature subset sizes, modeling methods, and climate scenarios.

Introduction

Projected climate changes over the next century may increase the likelihood of large wildfires in western North America (Stavros et al., 2014; Barbero et al., 2015; Liu and Wimberly, 2016; Parks et al., 2016), impacting a variety of ecosystems (Guyette et al., 2014) and associated anthropogenic landscapes (Schoennagel et al., 2017). In addition, a broad-scale trend of anthropogenically decreased global fire activity has recently been detected (Andela et al., 2017). Niche modeling techniques serve as important tools in spatial modeling of current wildfire activity, including binomial logistic regression (Kalabokidis et al., 2002; Barbero et al., 2014), MaxEnt (Parisien and Moritz, 2009; Parisien et al., 2012), boosted regression trees (Parks et al., 2015; Liu and Wimberly, 2015, 2016), random forests (Liu and Wimberly, 2016), and Gaussian linear regression (Robinne et al., 2016). Several of these niche models have been used in projecting future increased trends in wildfire activity in western North America (Barbero et al., 2015; Parks et al., 2016; Liu and Wimberly, 2016). Higher quality niche models of wildfire activity at finer resolution are needed to better identify areas of decreased fire activity where action can be taken to restore more natural fire regimes and reduce wildfire risks to human assets. Both the selection of appropriate predictor variables and taking into account the effects of different sets of predictors are critical in developing better niche models of wildfire activity for both current and future climate scenarios.

The choice of predictor variables can produce great variability in niche model outcomes (Beaumont et al., 2005; Synes and Osborne, 2011; Braunisch et al., 2013; Harris et al., 2013; Porfirio et al., 2014). Synes and Osborne (2011) found that dissimilarities in outcomes due to different variable sets can be greater than dissimilarities resulting from niche model projections of different future climate scenarios. They concluded that dissimilar outcomes resulted in an unmanageable level of uncertainty in projections of both current and future climate niche models. In order to address this issue, they stressed the importance of developing better methods of selecting predictor variables and better representation of niche model variability related to variable selection. However, there is no standard for researchers to determine appropriate variable sets. For example, the size of variable sets of future wildfire activity models developed for the western US range in number from five variables (selected on the basis of previous studies) (Parks et al., 2016), to 28 variables, screened using a boosted regression trees model (Liu and Wimberly, 2016).

This study investigates a novel formal feature selection algorithm for screening and selection of variables to improve ecological niche modeling performance. A variety of strategies have been previously employed in feature (variable) selection (also known as Input Variable Selection, IVS; Galelli et al., 2014) for niche modeling, especially using MaxEnt (e.g., Bradley et al., 2010; Halvorsen et al., 2015, 2016; Jueterbock et al., 2016; Zeng et al., 2016), which additionally includes a built-in feature selection strategy (Phillips et al., 2006). However, there are few examples of feature selection for niche modeling being characterized in the context of a formal feature selection algorithm (FSA; e.g., Jović et al., 2015; but see Gobeyn et al., 2017). An FSA is a data-mining tool for selecting a subset of variables with high relevancy and low redundancy for improving performance and efficiency of a variety of analyses, such as

13

classification, regression, and clustering (Jović et al., 2015). The smaller variable sets identified through feature selection can produce niche models with reduced complexity and overfitting, which can increase model generalization and transferability across space and time (Jiménez-Valverde, et al. 2008; Warren and Seifert, 2011; Verbruggen et al., 2013; Moreno-Amat et al., 2015). In addition, lower redundancy among variables can also facilitate model transferability (Dormann et al., 2013). Lower numbers of variables also reduce model computation time and facilitate interpretation (Jović et al., 2015).

Several authors have drawn attention to the need for characterizing the variability of current and future climate niche models arising from the choice of predictor variables in order to produce more robust forecasts (e.g., Synes and Osborne, 2011; Porfirio et al., 2014). However, characterization of feature-related niche model variability is seldom done, and this is made another focus of the study. Combinations of models that differ only in the feature subsets from which they were developed are known as feature subset ensembles (FSEs; Aly and Atiya, 2006; part of Boundary Conditions of Araújo and New, 2007). This study is the first to formally employ stand-alone FSEs in niche modeling. The feature subset ensembles are utilized to represent niche model variability arising from different predictor sets and facilitate comparisons across (1) different niche modeling methods for a given current climate scenario, and (2) climate scenarios for a given niche modeling method (see Chapter I, Background, for a more detailed review of feature selection and ensemble types in the context of niche modeling).

The large set of fire presence and absence data for western North America is ideally suited for demonstrating new techniques involving both the application of a novel formal feature selection algorithm for niche modeling, and the representation of niche model variability arising from predictors through the use of feature subset ensembles. The available 31-year historical fire

data includes large fires of three burn severities (low, moderate, and high) that are not mutually exclusive within an area over such a long period, making them suitable for development of separate niche models. Separate niche models for each of the three burn severities also illustrate uncertainty in the type of burn severity projected for a given area. In addition, individual niche models for each burn severity, rather than a single multinomial model for all three burn severities, facilitates the development and evaluation of new ensemble feature selection techniques for commonly employed two-class regression-based niche modeling methods. These methods include presence-only MaxEnt niche models and presence/absence binomial logistic regression GLM and Glmnet niche models. Both MaxEnt and GLM have been previously utilized in spatial modeling of wildfire activity. MaxEnt is one of the most commonly used presence-only niche modeling methods (Elith et al., 2006; Merow et al., 2013), and it is particularly suitable for projecting the likelihood of fires in areas that may not have burned during a study period (e.g., Parisien and Moritz, 2009; Parisien et al., 2012). The lasso L1 regularization of model variable coefficients built into MaxEnt (Phillips and Dudik, 2008) is generally effective in feature selection for smaller sets of variables. However, additional screening of larger variable sets is advised (Elith et al., 2011). To this end, the ability of a novel feature selection algorithm to identify smaller subsets of potentially important variables from a larger and more varied initial set of features than used for previous wildfire activity models is demonstrated, including 90 variables from the categories of climatic, topographic and anthropogenic indices. Many of these indices have been previously identified as important in wildfire activity models (e.g., Kalabokidis et al., 2002; Parisien and Moritz, 2009; Dillon et al., 2011; Liu and Wimberly, 2016). The proposed novel FSA utilizes a randomized search strategy involving screening a large number of niche models developed from random feature subsets of

limited correlation and of a given size (e.g., Garcia et al, 2006). The algorithm identifies a feature subset ensemble of high performance niche models. The selected feature subset ensembles are employed to represent niche model variability in statistical comparisons of wildfire activity niche modeling results across various modeling methods and climate scenarios.

This study has three main objectives: (1) demonstrate the ability of a novel random subset feature selection algorithm (RSFSA) (e.g., Garcia et al., 2006) to improve performance of wildfire activity models for western North America; (2) employ an innovative use of RSFSA-selected feature subset ensembles in niche modeling to characterize wildfire activity model variability and provide a basis for comparing both niche modeling methods and model projections across climate scenarios; and (3) analyze ecoregion level projections of wildfire activity for three different burn severity classes (low, moderate, and high) under current and future 2050 and 2070 climate scenarios for both low and high estimates for CO_2 emissions over western North America.

Methods

Study Area

The study site consisted of the region in the western coterminous United States from which fire occurrence data (see below) was available for fires larger than 405 ha (generally west of ca. -93.5ºW longitude) (Figure II.1). This region was used as the background evaluation extent (BEE) for model training and evaluation. In order to incorporate portions of ecoregions extending across the US border into Mexico and Canada into the wildfire activity models, the projection area was extended beyond the background evaluation extent to include northern Mexico (generally north of ca. 16ºN latitude) and a portion of southwestern Canada (generally

16

Figure II.1. Selected western US Level I and Level III Ecoregions (numbered; CEC 2005) over MaxEnt wildfire activity model projection area, including background evaluation extent within continental US for model training and evaluation (dark outline) (Tracy et al., 2018b).

17

south of ca. 58ºN latitude). In the interest of analyzing results across a commonly accepted

ecoregion classification scheme for North America, projected burned areas were calculated for

53 Commission for Environmental Cooperation (CEC, 2005) Level III ecoregions (46 within the

background evaluation extent) that are encompassed by nine CEC Level I ecoregions (Figure

II.1).

Fire Occurrence Data

Monitoring Trends in Burn Severity (MTBS, 2016) and LANDFIRE (2016) data was

combined to obtain spatial occurrences of large wildland fires generally greater than or equal to

405 ha in extent for each of the 31 years from 1984 to 2014. The MTBS data were derived from

correlations of Landsat satellite derived spectral indices with ground-based burn severity indices

(Key and Benson, 2006; Eidenshink et al., 2007; Finco et al., 2012). Data on prescribed fires was

excluded from both databases in order to analyze only wildland fires. Raster wildfire

presence/absence data for three burn severities of low, moderate and high at 30 m resolution

were spatially aggregated to point data at 1 km resolution. All point data were spatially filtered to

produce a minimum 10 km distance between points (e.g., Boria et al., 2014) in order to reduce

spatial autocorrelation and the associated inflation of model performance (Veloz, 2009;

Radosavljevic and Anderson, 2014) (Figure II.2) (for further details on burn severity classes and

resampling burn data, see Appendix A, Methods, Fire Occurrence Data).

Wildfire Activity Models

Environmental Variables

A total of 90 environmental predictor variables at one km resolution were assembled for

model input, including 57 climatic indices, 16 topographic indices, and 17 anthropogenic indices
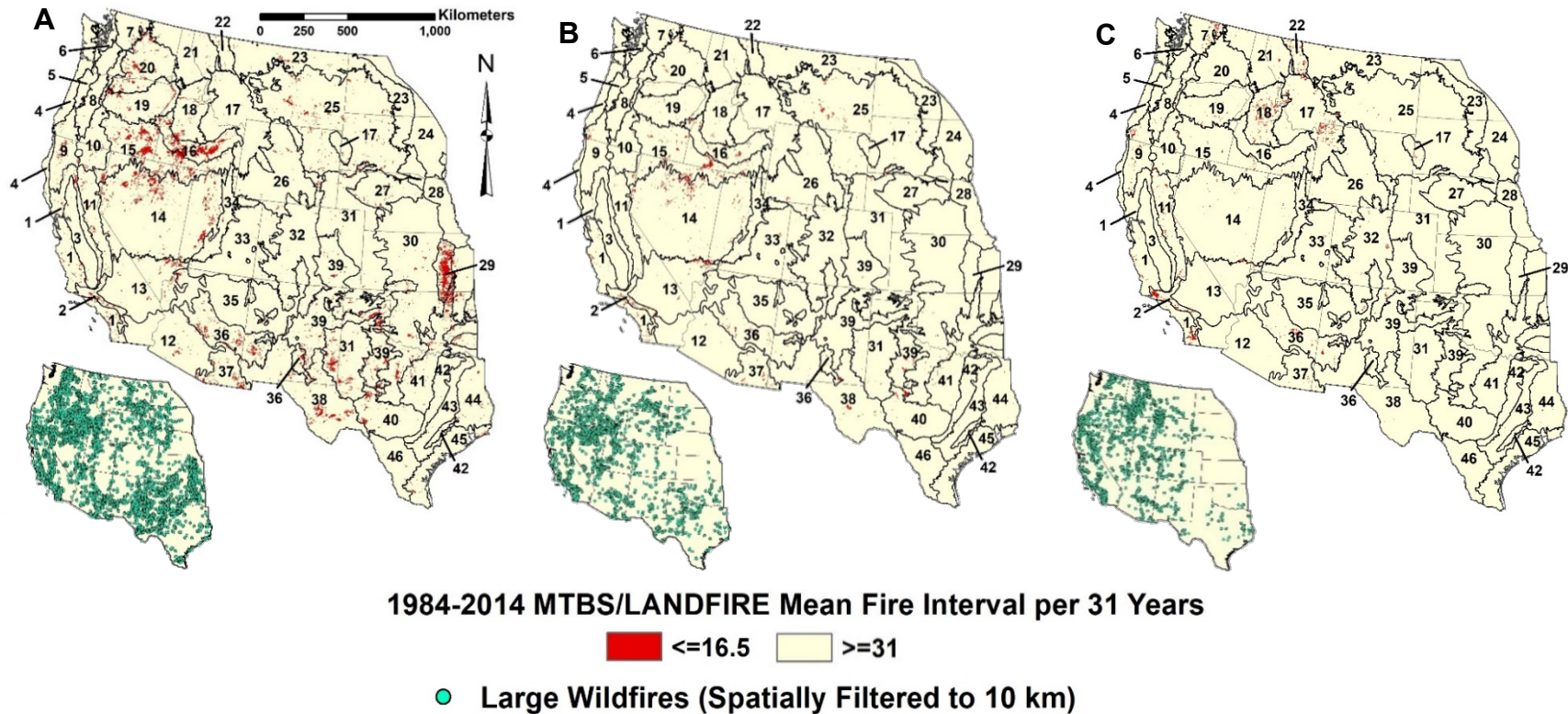
Figure II.2. Western continental US Level I and Level III Ecoregions (see Figure II.1 for number key; CEC 2005) and one km resolution rasters of low (A), moderate (B), and high (C) burn severity large wildfires from 1984 to 2014 that were aggregated from 30 m resolution Monitoring Trends in Burn Severity (MTBS) and LANDFIRE data rasters. Inset of raster data converted to fire presence points for wildfire activity niche model training and evaluation over the background evaluation area (Tracy et al., 2018b).

Table II.1. Ninety environmental predictor indices (30 arc second, one km resolution) used in developing MaxEnt wildfire activity models with 15 of 90 variables for three burn severities (Tracy et al., 2018b).

Variable Index (Source)	Grid Name Abbreviation[a]	Variable Frequency in Four Selected Models for Each Burn Severity			
		Low	Moderate	High	Total (% of 180)[b]
57 Climatic Indices (for 1960–1990 derived from WorldClim [2017] of Hijmans et al. [2005])					
19 Bioclim Indices (WorldClim, 2017)					
Annual mean temperature	bio_1*	0	2	0	2 (1.1)
Mean diurnal range (mean of monthly TMAX – TMIN)	bio_2	1	1	1	3 (1.7)
Isothermality (bio_2/bio_7) (× 100)	bio_3	1	1	1	3 (1.7)
Temperature seasonality (standard deviation × 100)	bio_4	0	0	1	1 (0.6)
Maximum temperature of warmest month	bio_5*	0	0	0	0 (0.0)
Minimum temperature of coldest month	bio_6	0	0	0	0 (0.0)
Temperature annual range (bio_5 – bio_6)	bio_7	0	2	1	3 (1.7)
Mean temperature of wettest quarter	bio_8	1	1	3	4 (2.2)
Mean temperature of driest quarter	bio_9	3	2	1	6 (3.3)
Mean temperature of warmest quarter	bio_10*	0	0	0	0 (0.0)
Mean temperature of coldest quarter	bio_11	0	0	0	0 (0.0)
Annual precipitation	bio_12	0	0	0	0 (0.0)
Precipitation of wettest month	bio_13	0	0	0	0 (0.0)
Precipitation of driest month	bio_14*	1	0	1	3 (1.7)
Precipitation seasonality (coefficient of variation)	bio_15	0	0	3	3 (1.7)
Precipitation of wettest quarter	bio_16	0	0	0	0 (0.0)
Precipitation of driest quarter	bio_17	0	2	0	2 (1.1)
Precipitation of warmest quarter	bio_18	0	0	0	0 (0.0)
Precipitation of coldest quarter	bio_19*	1	0	0	1 (0.6)
Subtotal		8	11	12	31 (17.2)

19 Supplementary Climatic (suppclim) Indices[c,d]

Table II.1. Continued.

Variable Index (Source)	Grid Name Abbreviation[a]	Variable Frequency in Four Selected Models for Each Burn Severity			
Annual mean minimum temp. of coldest month (TMIN)	tmin_ann*	0	0	0	0 (0.0)
	tmin_winq,	0	0	0	0 (0.0)
	tmin_sprq*,	0	0	0	0 (0.0)
Quarterly mean monthly minimum	tmin_sumq*,	0	0	0	0 (0.0)
temperature (4)	tmin_autq*	0	0	1	1 (0.6)
Annual mean maximum temp. of warmest month (TMAX)	tmax_ann*	0	0	0	0 (0.0)
	tmax_winq*,	0	0	0	0 (0.0)
	tmax_sprq*,	0	0	0	0 (0.0)
Quarterly mean monthly maximum	tmax_sumq*,	0	0	0	0 (0.0)
temperature (4)	tmax_autq*	1	0	0	1 (0.6)
Annual mean monthly rainfall (P) (mm)	prec_ann*	0	0	0	0 (0.0)
	prec_winq*,	1	0	1	2 (1.1)
	prec_sprq*,	1	0	0	1 (0.6)
Quarterly mean monthly rainfall	prec_sumq*,	3	3	2	8 (4.4)
(50%) (4)	prec_autq*	0	0	1	1 (0.6)
Effective Warmth Index (from mean monthly temperatures × 10 above 5ºC)	ew_indx	2	0	0	2 (1.1)
Rivas-Martinez (RM) ombrothermic index (from monthly MTMP and P)	ombro_index	0	0	0	0 (0.0)
RM continentality index (TMAX – TMIN) × 10 (CONT)	cont_index	2	0	1	3 (1.7)
RM thermicity index (MTMP + TMX_COLD + TMN_COLD) × 10	therm_index	0	0	0	0 (0.0)
Subtotal		10	3	6	19 (10.6)

19 Actual and Potential Evapotranspiration (AET-PET) Indices (PET; Zomer et al., 2007; 2008; AET; Trabucco and Zomer, 2010)[d]

Total annual reference evapotranspiration from Hargreaves model (PETH) (mm)	tpeth_ann	0	2	0	2 (1.1)
	peth_winq,	0	0	1	1 (0.6)
	peth_sprq*,	0	0	0	0 (0.0)
	peth_sumq*,	0	0	1	1 (0.6)
Quarterly mean monthly PETH (4)	peth_autq	1	0	1	2 (1.1)

Table II.1. Continued.

Variable Index (Source)	Grid Name Abbreviation[a]	Variable Frequency in Four Selected Models for Each Burn Severity			
Thornwaite summer concentration thermal efficiency (summer PETH/annual PETH) × 1000	tpeths_tpetha	0	0	1	1 (0.6)
Willmott and Feddema climate moisture index (from total annual PETH and PREC) × 1000	im_index	0	0	0	0 (0.0)
Total annual actual evapotranspiration from Thornwaite-Mather water balance model (TMWBM) (AETT) (mm)	taett_tann*	2	0	0	2 (1.1)
	aett_winq,	0	1	1	2 (1.1)
	aett_sprq*,	0	3	1	4 (1.7)
	aett_sumq*,	0	0	0	0 (0.0)
Quarterly mean monthly AETT (4)	aett_autq	1	0	1	2 (1.1)
Total annual evapotranspiration ratio (AETT/PETH) × 10	etrt_ann	1	0	0	1 (0.6)
	etrt_winq,	0	0	0	0 (0.0)
	etrt_sprq,	1	1	1	3 (1.7)
Quarterly mean monthly AETT/PETH (4) × 1000	etrt_sumq,	0	0	1	1 (0.6)
	etrt_autq	0	0	0	0 (0.0)
Modified Continentality index of Driscoll-Yee Fong[e]	cont_dfmo	1	2	0	3 (1.7)
Climate water deficit (tpeth_ann – taett_tann)	cwd_ann*	1	0	0	1 (0.6)
Subtotal		8	9	9	26 (14.4)

16 Topographic Indices

12 Geomorphologic Indices (derived from 15 arc second resolution HydroSHEDs grids of Lehner et al. [2008]; last 10 indices calculated using Geomorphometry and Gradient Metrics Toolbox for ArcGIS [Evans et al., 2014])[d]

Elevation	elev*	3	1	3	7 (3.9)
Slope	slope*	3	4	4	11 (6.1)
Martonne's Modified Dissection Coefficient (Dissection, DISS), 3 km circular radius	diss3kr*	2	1	1	4 (2.2)

Table II.1. Continued.

Variable Index (Source)	Grid Name Abbreviation[a]	Variable Frequency in Four Selected Models for Each Burn Severity			
Topographic Position Index (TPI; = Slope Position Index, SPI), 3 km circular radius	*tpi3kr**	0	1	1	2 (1.1)
TPI, 9 km circular radius	*tpi9kr*	0	2	0	2 (1.1)
TPI, 19 km circular radius	*tpi19kr*	2	1	0	3 (1.7)
Elevation Relief Ratio (ERR, = Surface Relief Ratio, SRR), 3 km circular radius	*err3kr**	1	0	0	1 (0.6)
Compound Topographic Index (CTI, = Topographic Wetness Index, TWI)	*cti**	1	0	0	1 (0.6)
Heat Load Index (HLI)	*hli**	0	1	2	3 (1.7)
Integrated Moisture Index (IMI)	*imi*	1	0	1	2 (1.1)
Site Exposure Index (SEI)	*sei**	0	3	1	4 (2.2)
Slope Cosine Aspect Index (SCAI)	*scai**	2	0	1	3 (1.7)

Four Hydrogeomorphologic Indices (derived from 15 arc second resolution HydroSHEDs polyline river network shapefile of Lehner et al. [2008])

Distance to Streams (STRMDIST)	*strmdist**	0	1	0	1 (0.6)
Distance to Low Flow Accumulation Areas (100–5,000 cells; STRMLOFLODIST)	*strmloflodist*	1	0	0	1 (0.6)
Distance to Medium Flow Accumulation Areas (5,000–60,000 cells; STRMMDFLODIST)	*strmmdflodist*	0	3	2	5 (2.8)
Distance to High Flow Accumulation Areas (>60,000 cells; STRMHIFLODIST)	*strmhiflodist*	11	2	3	6 (3.3)
Subtotal		17	20	19	56 (31.1)

17 Anthropogenic Indices

11 Human Population Indices (popden; CIESIN [2016]; derived from popden, this study)

Human Population Density per 1 km, Year 2000 (POPDEN)	*popden*	0	1	1	2 (1.1)

Table II.1. Continued.

Variable Index (Source)	Grid Name Abbreviation[a]	Variable Frequency in Four Selected Models for Each Burn Severity			
Mean POPDEN in 3 cell radius	*mnpopden3r*	1	1	1	3 (1.7)
Mean POPDEN in 9 cell radius	*mnpopden9r*	0	1	0	1 (0.6)
Mean POPDEN in 19 cell radius	*mnpopden19r*	0	0	0	0 (0.0)
Distance to POPDEN < 10, None/Sparse Rural Distance (SPRURDIS)	*sprurdist*	2	1	1	4 (2.2)
Distance to POPDEN 10 to <100, Low Rural Distance (LORURDIS)	*lorurdist*	2	1	2	5 (2.8)
Distance to POPDEN 100 to <200, Medium Rural Distance (MEDRURDIS)	*medrurdist*	1	1	0	2 (1.1)
Distance to POPDEN 200 to <300, High Rural Distance (HIRURDIS)	*hirurdist*	1	0	0	1 (0.6)
Distance to POPDEN 300 to <900, Low Urban Distance (LOURBDIS)	*lourbdist*	0	2	0	2 (1.1)
Distance to POPDEN 900 to <1,500, Medium Urban Distance (MEDURBDIS)	*medurbdist**	1	1	0	2 (1.1)
Distance to POPDEN >= 1,500, High Urban Distance (HIURBDIS)	*hiurbdist*	0	1	0	1 (0.6)

Four Road Indices (roads of 1980 to 2010 from CIESIN and ITOS [2013])

Variable Index (Source)	Grid Name Abbreviation				
Distance to Road (ROADDIST)	*roaddist**	0	1	0	1 (0.6)
Road Density, km road per 3 km circular radius (ROADDEN3KR)	*roadden3kr*	1	2	1	4 (2.2)
Road Density, km road per 9 km circular radius (ROADDEN9KR)	*roadden9kr*	2	0	2	4 (2.2)
Road Density, km road per 19 km circular radius (ROADDEN19KR)	*roadden19kr*	1	0	1	2 (1.1)

Two Anthropogenic Land Cover Indices (for 2001 to 2005 from Tuanmu and Jetz [2014] and EarthEnv [2016])

Variable Index (Source)	Grid Name Abbreviation				
Cultivated and Managed Vegetation Percent Cover per 1 km^2	*agric_lc**	4	4	4	12 (6.7)

Table II.1. Continued.

Variable Index (Source)	Grid Name Abbreviation[a]	Variable Frequency in Four Selected Models for Each Burn Severity			
Urban/Built-up Percent Cover per 1 km²	*urban_lc*	1	0	1	2 (1.1)
Subtotal		17	17	14	48 (26.7)

[a]Asterisks indicate 38 expert selected variables from previous studies (Table A.2).
[b]Total frequency of 15 variables times four models times three burn severities = 180 instances.
[c]Quarters: winter- Jan, Feb, Mar; spring – Apr, May, Jun; summer – Jul, Aug, Sep; autumn – Oct, Nov, Dec. PREC = precipitation; TMAX = mean temperature of warmest month; TMIN = mean temperature of coldest month; TMAX_COLD = mean maximum temperature of coldest month; TMN_COLD = mean minimum temperature of coldest month.
[d]For additional sources of indices, see Table A.1.
[e]Incorporates moisture correction factor of AET/PET × 10 (for details, see Appendix A, Methods, Wildfire Activity Models, Environmental Variables; Figure A.1)

(Table II.1). To evaluate importance of different types of indices in wildfire activity models, indices were further divided into the eight subgroups (Table II.1). Parks et al. (2016) was followed in regarding climatic indices as proxies for potential vegetation, which simplified projection of vegetation under future climates. Parisien et al. (2012) found that omitting vegetation fuel percent cover from their MaxEnt wildfire activity models for the western US had negligible effect on model accuracy. Liu and Wimberly (2016), Dillon et al. (2011), and Parisien et al. (2012) were followed in including topographic and anthropogenic indices in addition to climatic indices in the wildfire activity models. The maximum absolute value of Spearman rank correlation among variables used in any given wildfire activity niche model was limited to 0.7 in order to reduce variable collinearity and improve model transferability (Dormann et al., 2013) (Figure A.2) (for additional information regarding the sources and calculations for indices, see Appendix A, Methods, Wildfire Activity Models, Environmental Variables).

Climate Scenarios

The Hadley Global Environmental Model 2 – Earth System (HadGEM2-ES, or HE) General Circulation Model (GCM) (Jones et al., 2011) was chosen to simulate future climate scenarios for 2050 (average 2041–2060) and 2070 (average 2061–2080). Two CO_2 Representative Concentration Pathway (RCP) scenarios were chosen: RCP2.6 and RCP8.5, which represent the extremes of low and high concentrations in greenhouse gases, respectively. The 19 supplementary climate indices (suppclim) were calculated using one km resolution monthly gridded climate data for these scenarios available from WorldClim (2016). The monthly AET and PET climate indices layers needed to calculate the 19 AET-PET Indices were derived from future WorldClim (2017) layers according to methods of Zomer et al. (2007, 2008) and Trabucco and Zomer (2010). Topographic and anthropogenic indices were assumed constant over all climate scenarios (for additional details on climate scenarios, see Appendix A, Methods, Wildfire Activity Models, Climate Scenarios).

Niche Models

Wildfire activity niche models were developed for each of the three burn severity classes (i.e., low, moderate and high). Using top-selected niche models of each burn severity class, the current and future distributions of binary fire frequency classes were projected for the 1984–2014 period: (1) $\leq$ 16.5 year mean fire interval (MFI, average number of years between fires), representing fire presence data; and (2) $\geq$ 31 years MFI, representing fire absence. The fire absence data represents "quasi-absence" data that is subject to stochasticity related to fire ignition events and some error of fire detection over the 31-year study period (e.g., Parisien and Moritz, 2009). The fire absence points were buffered to occur at least 20 km from fire presence

points in order to increase model sensitivity and minimize the percentage of true presences predicted as absences (e.g., Barbet-Massin et al., 2012).

Niche models of several regression-based methods and parameterization complexities were developed for performance comparison using the feature subset ensembles developed from random subset feature selection (see Methods, Random Subset Feature Selection Algorithm). MaxEnt version 3.3.3 (Phillips et al., 2006) in R (R Core Team, 2018) dismo package (Hijmans et al., 2011) was used to develop presence-only niche models with various feature complexities: (1) linear features only, (2) linear and quadratic features with no interactions, (3) quadratic and forward and reverse hinge features (quadratic/hinge features), in which linear features were only used if hinge features were not used (models generally employed only hinge features), and (4) various levels of L1 regularization (various β regularization multiplication parameters from $\beta1$ to $\beta40$) with quadratic/hinge features (for details on analyses of β regularization parameter values, see Appendix A, Methods, Wildfire Activity Models, Niche Models, Model Parameters). In order to restrain potentially unnecessary MaxEnt model complexity, additional product and threshold features were not used. Presence/absence binomial logistic regression niche models were developed for GLM from the R dismo package and for Glmnet using the Glmnet R package (Friedman et al., 2010) with (1) linear and (2) orthogonalized linear/quadratic features. In order to simplify computations, only raw (non-orthogonalized) linear/quadratic feature Glmnet models were used when projecting to raster (performance did not differ between raw and orthogonalized Glmnet linear/quadratic models; Figure A.3). Model parameters and coefficients for final selected MaxEnt models were presented (Appendix B, Tables B.1-3), which is seldom done (Halvorsen 2013).

Model evaluation statistics, such as the True Skill Statistic (TSS) and Area under the Curve (AUC) (Fielding and Bell, 1997), were calculated with the R PresenceAbsence package (Freeman and Moisen, 2008) using fire presence/absence data (AUC_{pa}). This approach to calculating AUC utilizes only the true fire absence data as absence data. In contrast, the default calculation of AUC carried out within the MaxEnt implementation of the R dismo package utilizes both random background data (AUC_{bg}; Smith, 2013) and presence points (AUC_{bgp}) as absence data. The corrected Akaike Information Criterion (AICc) for MaxEnt (Warren and Seifert, 2011) was calculated as a measure of model complexity and information content (Bozdogan, 1987). The typical calculation of AICc for MaxEnt, using the ENMeval R package (Muscarella et al., 2014), requires the time-consuming generation of a MaxEnt prediction raster. Consequently, an R script was developed to more rapidly calculate AICc for thousands of models using MaxEnt samples with data (SWD) mode predictions for background and training presence point data, representing background AICc, or $AICc_{bg}$ (for more details on calculation of $AICc_{bg}$, see Appendix A, Methods, Wildfire Activity Models, Background Corrected Akaike Information Criterion). Values of AICc calculated using available methods for GLM and Glmnet models have different scales than either AICc or $AICc_{bg}$ calculated for MaxEnt models, making comparisons problematic. In order to facilitate an approximate comparison of AICc for these models, a linear calibration equation was derived under the assumption that $AICc_{bg}$ for MaxEnt β2 linear feature models was equivalent to AICc of GLM linear feature models using the same training data and numbers and types of variables (for further details see Appendix A, Methods, Wildfire Activity Models, Calibration of AICc Values between GLM, Glmnet and MaxEnt Models). All comparisons between niche modeling methods were made using the same training data and the same initial set of randomly generated variable subsets.

Top-selected models by RSFSA AUC ranking were calibrated using a random 2/3 of all data for training and 1/3 data for testing, selecting a threshold of maximum TSS_{pa} (Liu et al., 2013a) to yield a binary burned/unburned classification for the two mean fire intervals (fire presence or absence in 31 years). This same threshold was applied to wildfire activity models parameterized with variables of future climate scenarios. The top four selected binary wildfire activity models for each burn severity were combined by frequency consensus (cf., Porfirio et al., 2014) to form feature subset ensembles. Different highly ranked variables in the selected niche models were compared across different climate scenarios in terms of their linear relationships with latitude across the study area (for additional details on model selection and variable rankings, see Appendix A, Methods, Wildfire Activity Models, Model and Variable Rankings)

Contemporary Wildfire Deficit

In contrast to the practice of Parks et al. (2015) for assessing wildfire surplus or deficit using wildfire activity modeling, areas with high human influence are included in training the models, which utilize additional anthropogenic and topographic variables. This allowed a *contemporary* wildfire surplus or deficit to be distinguished, which takes into account current anthropogenic influences. Relative differences between actual and projected burned areas are compared in order to estimate contemporary wildfire deficit and surplus for the ecoregions as defined by the Commission for Environmental Cooperation (CEC 2005). For each burn severity, a contemporary wildfire deficit/surplus rating map is developed through comparing the raster of historical fire presence with the model projected wildfire activity (for further details, see Appendix A, Methods, Wildfire Activity Models, Contemporary Wildfire Deficit Rating Maps).

Random Subset Feature Selection Algorithm

The RSFSA was carried out in two stages: (1) the optimal feature subset size estimation stage, and (2) the variable subset selection stage, which includes statistical evaluation of the effectiveness of feature-selected versus random feature niche models (Figure II.3). Within each of these two stages were two phases employing differing feature selection criteria and search strategies: (1) the univariate filter phase, involving a sequential forward search strategy to build hundreds or thousands of random variable subsets of various sizes with the filter of an absolute value of Spearman's rank correlation coefficient ($|r_s|$) less than 0.7 (Dormann et al., 2013) between any variables of a subset, and (2) the subset wrapper phase, in which a random subset search strategy is utilized with wrappers of AUC or AICc to rank the performance of niche models developed from the randomly generated variable subsets with wrapper training and testing data. For evaluation of any feature selection algorithm, it is critical to use randomly partitioned final training and testing data (data used to evaluate performance of random versus feature selected niche models) which is held out from the wrapper training and testing data (data used for training, testing and ranking niche models with a test wrapper) in order to avoid selecting features performing better only for the model wrapper training and testing data (Kohavi and John, 1997). The final product of RSFSA is a feature subset ensemble niche model developed from top-ranked variable subsets of the selected size that perform better than random subsets (Figure II.3). Final RSFSA evaluation was replicated with 3 randomizations of wrapper training and testing and final training and testing data (Stracuzzi, 2007) to test the stability of the RSFSA to different sets of training data (Kalousis et al., 2007).

90 environmental rasters at 1 km resolution

Use multiple randomized sequential forward feature selection (MRSFS) in parallel to create 250 random feature subsets with maximum correlations below 0.7 for varying variable subset sizes: 3, 6, 8, 10, 12, 15, 20, and 25

Univariate Filter Phase

Filter 2/3 training and 1/3 testing point presence/absence data (half of all data)

Wrapper Data

Calculate in parallel 250 wrapper models for each subset size and use random subset selection (RSS) to find top 10 ranked models by wrapper AUC or $AICc_{bg}$

Subset Wrapper Phase

Final 2/3 training and 1/3 testing point presence/absence data (half of all data)

Final Data

Calculate in parallel 250 final models and compare AICc, AUC, and AUC_{diff} for 10 top ranked and 10 random of 250 random

Evaluation

For further investigation, select at least 2-3 smaller subset sizes for optimizing AUC, AICc, and AUC_{diff}

I. Optimal Feature Subset Size Estimation

Use MRSFS to create 3 replicates of 3,000 (N = 9,000 total) random feature subsets with maximum correlations below 0.7 for above selected variable subset sizes, and prepare 3-fold randomized partitions of ½ wrapper and ½ final data per rep

Univariate Filter Phase

Wrapper Data Randomized per Rep

For 3 reps, calculate in parallel 3,000 filter models of selected subset size and use RSS to select top 250 (n) models by wrapper AUC for each

Subset Wrapper Phase

Increase sample size (n) or repeat search with more random models (N) and/or different subset size or wrapper (e.g., $AICc_{bg}$)

Final Data Randomized Per Rep

For each rep, calculate in parallel 500 final models, including 250 selected models and 250 random models, and compare AICc, AUC, and AUC_{diff}

Evaluation

No

For all three reps, are 250 selected models significantly better in AICc, AUC, and AUC_{diff} than 250 random models?

II. Variable Subset Selection

Yes

All Data

Use random 2/3 data to train and 1/3 to test for calibrating top 10 models from each of three reps (30 total) for selected subset sizes. Optionally make visual and quantitative assessment for the effect of subset size on model restriction for calibrated projections

III. Assess Model Project-ions

Feature Subset Ensemble

Create feature subset ensemble (FSE) of 4 selected variable subset models combined by frequency consensus (sum) of binary calibrated projections

Figure II.3. Flowchart for random subset feature selection algorithm (RSFSA) to select environmental variable subsets for feature subset ensemble niche models (Tracy et al., 2018b).

The ensemble RSFSA is a hybrid filter-wrapper approach (c.f. Jović et al., 2015). The generation of random subsets of a given size and the ranking of these subsets by wrapper performance is incorporated in the modeling method as in Garcia et al. (2006). This RSFSA is novel in several ways, including (1) application of a correlation filter when building the random subsets, (2) estimating an optimal feature subset size, (3) using niche model AUC or AICc as wrappers for ranking subsets, and (4) selecting a feature subset ensemble model of top-selected subsets, rather than combining the variables from top-selected subsets. This RSFSA also differs from the random subset feature selection (RSFS) of Räsänen and Pohjalainen (2013), which ranks individual features (not feature subsets) by the wrapper performance of multiple random subsets in which they appear, pooling top ranked features into a single subset for subsequent modeling. The RSFSA was developed using R software that takes advantage of parallel processing in both the filter and wrapper phases to simultaneously generate and evaluate thousands of variable subsets for the different niche modeling algorithms (R code for RSFSA with MaxEnt, GLM and Glmnet, including Glmnet model raster prediction functions, available at https://github.com/jamesltracy/RSFSA_R). Alternative novel RSFSA variants were also developed and compared that use expert screened variables for MaxEnt quadratic/hinge ($\beta 2$) low burn severity wildfire activity niche models (for details on RSFSA phases, stages, and variants, see Appendix A, Methods, Wildfire Activity Models, Random Subset Feature Selection Algorithm).

The RSFSA-selected and random wildfire activity niche models were compared for three evaluation statistics: (1) higher accuracy as measured by testing AUC, $AUC_{pa\_finaltest}$; (2) relatively lower complexity and higher information content, as measured by lower $AICc_{bg\_final}$; and (3) lower overfitting of the training data, as measured by a lower difference between final

32

training data, $AUC_{pa\_finaltrain}$, and final testing data $AUC_{pa\_finaltest}$, which yields $AUC_{pa\_diff\_final}$ (AUC_{train} minus AUC_{test}; Warren and Seifert, 2011). Training AUC ($AUC_{pa\_finaltrain}$) was compared with testing AUC ($AUC_{pa\_finaltest}$) to evaluate underfitting among modeling methods. Relatively poor model accuracy for both the training data ($AUC_{pa\_finalrain}$) and testing data ($AUC_{pa\_finaltest}$) indicates a poorly fitted model (c.f. Harrell et al., 1996). The RSFSA allows the researcher flexibility in both stages to subjectively balance niche model underfitting, overfitting, and information content with the desired level of model complexity in terms of the selected numbers of environmental variables and derived parameters.

Additional Model Assessment

The post-RSFSA stage III involved final calibration of RSFSA-selected models from Stage II using all of the presence data divided into 2/3 training and 1/3 testing (described above in Methods, Niche Models) (Figure II.3). The potential influence of the number of variables in low burn severity wildfire activity models on projected burned area was evaluated within and beyond the background evaluation extent (e.g., Beaumont et al., 2005). From the RSFSA-selected models, more conservative models were additionally selected in terms of projected burned area and map accuracy according to regional indices (described in Appendix A, Methods, Wildfire Activity Models, Calibration of AICc Values between GLM, Glmnet and MaxEnt Models) in order to better inform conservation management decisions (e.g., Schwartz, 2012).

Statistical Tests

In order to allow for observed cases of unequal variance among wildfire activity model results, the Welch ANOVA was used to test whether (1) model evaluation statistics did not differ among RSFSA-selected models and random models, and (2) projected burned areas within ecoregions or larger areas did not differ between models for current and future climate scenarios.

Following a significant Welch ANOVA test, separate secondary paired tests were performed using a Welch t-test with the Holm correction to control for Type I error related to the number of paired comparisons for each set of tests. Following a significant Welch's one-way ANVOVA test, pairwise multiple comparisons were conducted using the Games Howell (1976) pairwise multiple comparison test which also allows for unequal variance and sample sizes.

Results

Niche Modeling Methods and Feature Selection

In estimating the optimal variable subset size (RSFSA Stage I), there were apparent trends of increased accuracy (high $AUC_{pa\_finaltest}$), lower complexity (low $AICc_{bg\_final}$), and higher overfitting ($AUC_{pa\_diff\_final}$) as the number of variables per subset increased from three to 25 for wildfire activity models. These trends hold for all three burn severity models as well as for all types of niche modeling methods, including various parameterizations of MaxEnt, GLM, and Glmnet models (Figures II.4-5, A.5-8). For all burn severities, MaxEnt quadratic/hinge models using β regularization multipliers of one, two or three (β1, β2, β3) and GLM and Glmnet linear/quadratic models tended to exhibit higher training and testing AUC, which indicated lower underfitting, and lower $AICc_{bg}$ (i.e., greater information content). However, these models also displayed greater overfitting than simpler models as revealed by higher AUC_{diff} (Figures II.4, A.6-8). GLM and Glmnet models of the same feature parameterization generally performed similarly for all evaluation statistics (Figures II.4, A.5-7). An exception was the poor performance of some RSFSA-selected linear/quadratic GLM models for moderate and high burn severities with larger-sized variable subsets (Figures A.6-7).
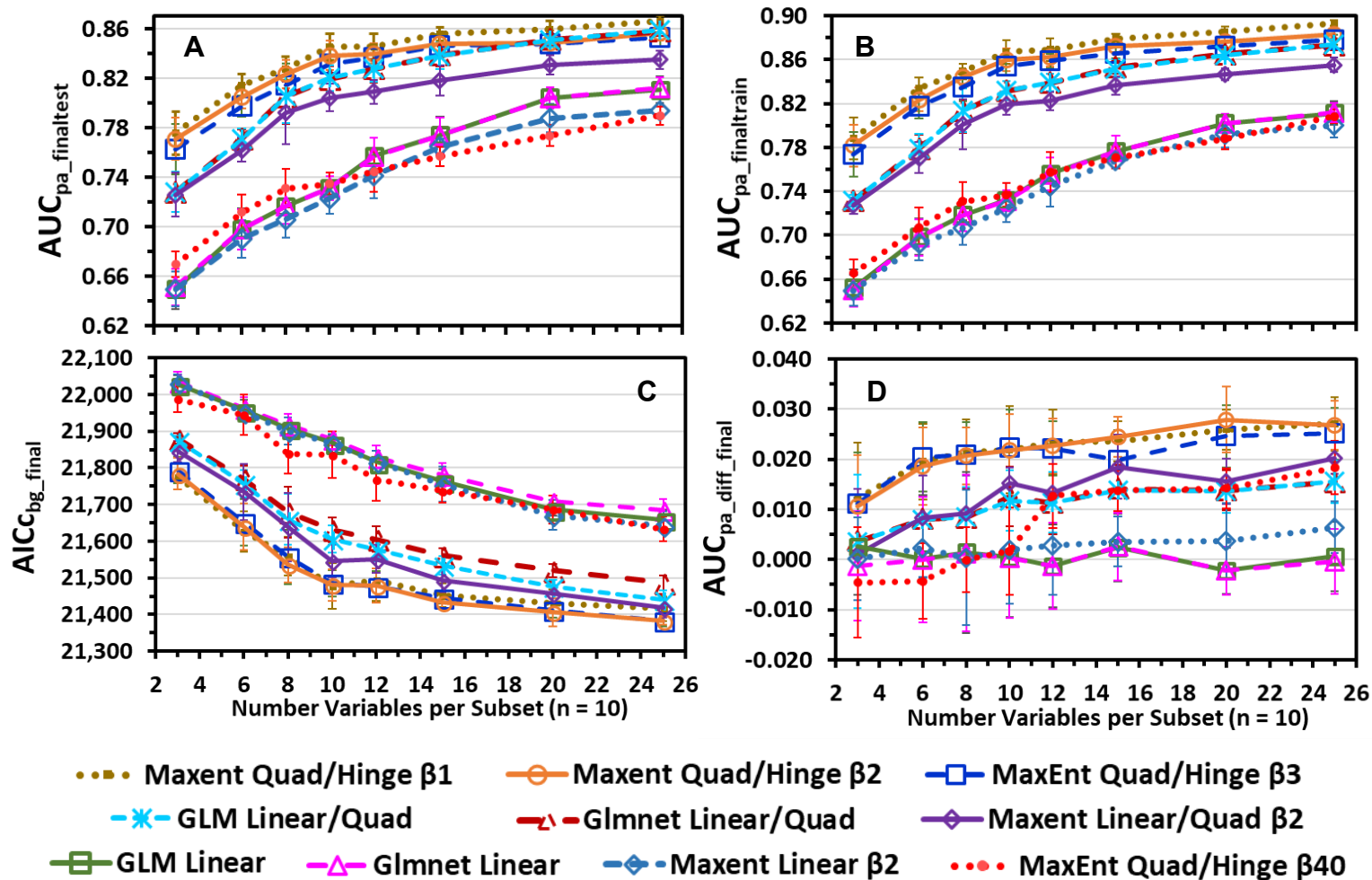
Figure II.4. Low burn severity wildfire activity model evaluation statistics (mean ± SD) for MaxEnt, Glmnet, and GLM niche models: (A) $AUC_{pa\_finaltest}$, (B) $AUC_{pa\_finaltrain}$, (C) $AICc_{bg\_final}/AICc_{bg\_final\_reg}$ (approximated for GLM and Glmnet), and (D) $AUC_{pa\_diff\_final}$ (overfitting). Models developed from top ten random subset feature selection algorithm-selected variable subsets ranked by AUC. Variable subsets were selected from 250 randomly generated variable subsets of various sizes derived from 90 variables (Tracy et al., 2018b).
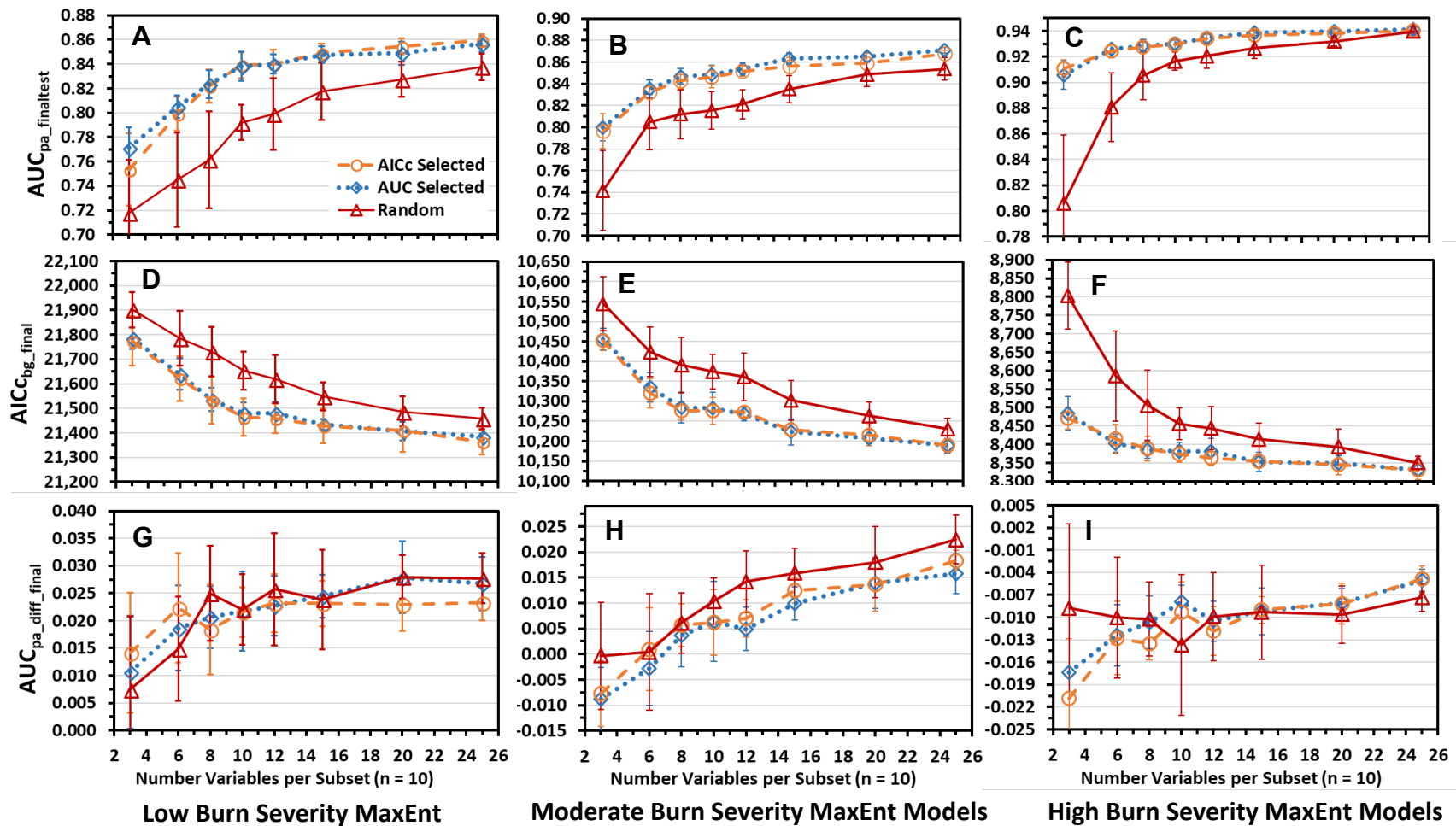
Figure II.5. MaxEnt quadratic/hinge β2 wildfire activity model evaluation statistics (mean ± SD): (A-C) $AUC_{pa\_finaltest}$, (D-F) $AICc_{bg\_final}$, and (G-I) $AUC_{pa\_diff\_final}$ (overfitting). Models developed from top ten random subset feature selection algorithm-selected variable subsets ranked by AUC or AICc and models developed from ten random subsets. Variable subsets were selected from 250 randomly generated variable subsets of various sizes derived from 90 variables for three large wildfire burn severities: low (A, D, G); moderate (B, E, H); and high (C, F, I) (Tracy et al., 2018b).

An increase in MaxEnt quadratic/hinge model β regularization values from zero (no regularization) to 40 (high regularization) (Figure A.8) produced a range in model performance similar to the various feature parameterization complexities of MaxEnt, GLM, and Glmnet models (Figures II.4, A.6-7). Increasing L1 regularization for MaxEnt quadratic/hinge models lowered testing and training AUC, raised $AICc_{bg}$, and, below 12 variable subsets, lowered overfitting (AUC_{diff}). Only low burn severity MaxEnt quadratic/hinge models with β regularization values around five or less ($\beta \lesssim 5$) achieved lower $AICc_{bg}$ than MaxEnt models with no L1 regularization (β0) (Figure A.8C). The RSFSA-selected variable subset models ranked by either $AUC_{pa\_wrappertest}$ or $AICc_{bg\_wrapper}$ show improvement over random models for all of the niche modeling methods (Figures II.5, A.5). Generally, the sharpest visual changes in model evaluation statistics occurred over an increase in subset size from six to 15 variables. Consequently, six and 15-variable subsets were chosen for further evaluation in RSFSA Stage II.

For RSFSA Stage II, replications were increased for 15-variable models with the best performance in AUC and $AICc_{bg}$, the MaxEnt quadratic/hinge (β1, β2, β3) and GLM and Glmnet linear/quadratic models. Low burn severity MaxEnt quadratic/hinge models exhibited significantly lower underfitting as indicated by higher training and testing AUC, and lower AICc than the three training replicate sets of GLM and Glmnet linear/quadratic models ($P < 0.05$, Games Howell Pairwise Multiple Comparison Test, preceded by significant Welch's one-way ANOVA test, $P < 0.05$; Figure A.9A-C). In contrast, the GLM and Glmnet linear/quadratic models performed significantly better in terms of lower overfitting (Figure A.9D). Among the low burn severity MaxEnt quadratic/hinge models, those of β1 and β2 performed significantly better in most training sets than β3 models in terms of lower underfitting (higher training and testing AUC) (Figure A.9A- B). In addition, the MaxEnt quadratic/hinge β2 models performed

37

better than β1 and β3 models in terms of lower $AICc_{bg}$ (Figure A.9C), and, for most training

replicates, they usually had significantly lower overfitting than β1 models (Figure A.9D).

Corresponding results for moderate and high burn severity models were generally similar, but

not as consistent due to unstable results for RSFSA with linear/quadratic GLM models in some

training replicates (Figures A.10-11; for details see Appendix A, Results, Niche Modeling

Methods and Feature Selection). Overall, MaxEnt quadratic/hinge β2 models performed best in

terms of lower underfitting and higher information content, and they were selected for further

evaluation for wildfire activity niche models of all three burn severities.

Comparison of six and 15-variables MaxEnt quadratic/hinge β2 models revealed

significant trends for both higher accuracy and lower complexity for 15-variable models across

all three training set replications when using the RSFSA $AUC_{pa\_wrappertest}$ wrapper ($P < 0.05$;

Welch t-test with Holm correction, preceded by significant Welch ANOVA test, $P < 0.05$; Figure

A.12A-F). However, a little over half of these RSFSA replications across all burn severities

showed a significant increasing trend for overfitting from six to 15 variable subsets (Figure

A.12G-I). The projected burned areas (in mHa) were compared for RSFSA-selected six, ten and

15-variable MaxEnt quadratic/hinge and 15-variable Glmnet linear quadratic wildfire activity

binary models for low burn severity. No apparent differences and no relationships were found in

the areas projected as burned either within or beyond the background evaluation extent (Figure

A.13A-B). The 15-variable subset size was selected for MaxEnt quadratic/hinge β2 models for

further evaluation with RSFSA in order to compare ranking using AUC versus $AICc_{bg}$.

In completing RSFSA Stage II evaluations, further comparisons were made of the efficiency of

the $AUC_{pa\_wrappertest}$ versus the $AICc_{bg\_wrapper}$ for improving performance of the chosen 15-

variable MaxEnt quadratic/hinge β2 models. Significantly higher accuracy ($AUC_{pa\_finaltest}$) was

found for models selected with RSFSA wrappers of either $AUC_{pa\_wrappertest}$ or $AICc_{bg\_wrapper}$ compared to random models for all three replications of all three burn severities ($P < 0.05$; Welch t-test with Holm correction, preceded by significant Welch ANOVA test, $P < 0.05$; Figure II.6A-C). Consistently improved (lower) model complexity ($AICc_{bg\_final}$) was found for all three burn severities using the $AUC_{pa\_wrappertest}$ wrapper but not the $AICc_{bg\_wrapper}$ wrapper (Figure II.6D-F). The RSFSA-selected models from $AICc_{bg\_wrapper}$ and $AUC_{pa\_wrappertest}$ wrappers achieved significantly reduced overfitting compared to random models across all three replications for the low burn severity (Figure II.6G) and high burn severity models (Figure II.6I), respectively. The RSFSA $AUC_{pa\_wrappertest}$ wrapper method was chosen for greater consistency in optimizing $AICc_{bg\_final}$ and used for selecting MaxEnt wildfire models for all three burn severities. Attempts to obtain significantly lower overfitting for all three replicates for moderate burn severity models using 10, 12 and 17 variable subset sizes or combinations of wrappers (e.g, $AUC_{pa\_wrappertest}$ and $AICc_{bg\_final}$) were also unsuccessful (results not shown). In consideration of the variability of burned areas projected for RSFSA selected 15-variable subset models (Figures A.13A, A.14), regional indices were employed to select the top four most conservative models in terms of burned area within the background evaluation extent (for details, see Appendix A, Methods, Wildfire Activity Models, Model and Variable Rankings). The RSFSA-selected 15-variable MaxEnt β2 quadratic/hinge models for all three burn severities actually employed 14 to 15 environmental variables from which 81–103 derived features were used in the model equation (see Appendix B, Tables B.1-3, for derived features for each selected model provided in embedded MaxEnt lambdas pdf files).

The use of an expert filter to narrow down the initial set of variables from 90 to 38 did not significantly improve performance of the RSFSA for MaxEnt quadratic/hinge β2 15-variable
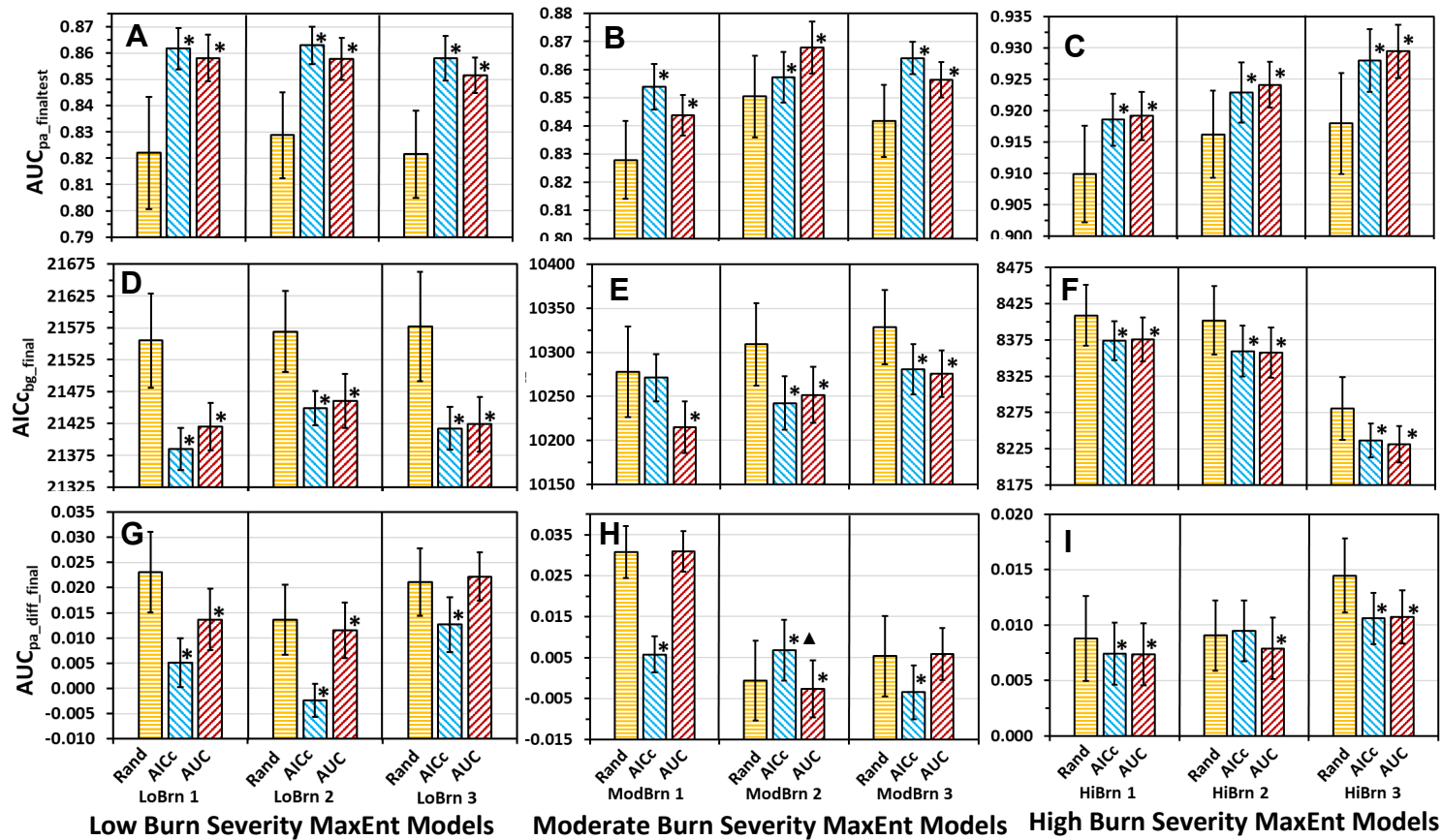
Figure II.6. MaxEnt quadratic/hinge β2 wildfire activity model evaluation statistics (mean ± SD) for three burn severities (low- A,D,F; moderate- B,E,H; and high-C,F,I): (A-C) $AUC_{pa\_finaltest}$, (D-F) $AICc_{bg\_final}$, and (G-I) $AUC_{pa\_diff\_final}$ (overfitting). Models developed from three replicates of 3,000 variable subsets of 15 of 90 variables (total 9,000 15-variable subsets) that were narrowed per replicate to: (1) 300 (n) subsets selected randomly (Rand), (2) 250 (n) subsets ranked by $AICc_{bg\_wrapper}$ with random subset feature selection algorithm (RSFSA) (AICc), and (3) 250 (n) subsets ranked by $AUC_{pa\_wrappertest}$ with RSFSA (AUC). Means for AUC or AICc RSFSA-selected model statistics within a replicate with an asterisk are significantly more optimal (higher for $AUC_{pa\_finaltest}$ and lower for $AICc_{bg\_final}$ and $AUC_{pa\_diff\_final}$) from that of random selected models (P < 0.05; Welch t-test with Holm correction, preceded by significant Welch ANOVA test, P < 0.05; models with asterisk and "▲" are significantly less optimal than random models) (Tracy et al., 2018b).

low burn severity wildfire activity models. Only models developed from random sets of 38 of 90 variables and ranked with $AUC_{pa\_wrappertest}$ (AUC38of90) consistently produced significant improvement over models developed from unranked random sets (Rand38of90) in all three evaluation statistics, including overfitting ($AUC_{pa\_diff\_final}$) (Figure A.15). Improvements over random models for evaluation statistics of RSFSA selected models derived from 38 expert selected variables were generally similar to that seen in RSFSA-selected models from 38 random variables or the entire 90 variable set (Figure A.15).

Selected Features for Wildfire Activity Models

The top four RSFSA $AUC_{pa\_wrappertest}$ wrapper-selected 15-variable MaxEnt quadratic/hinge β2 wildfire activity models for each of the three burn severities (12 models total) were quite varied in their composition of variables. Sixty of the 90 total variables were used at least once in the four RSFSA-selected models of each burn severity (Table II.1). Variables correlated above the r_s threshold of 0.7 which were not allowed in the same model could sometimes appear in different RSFSA-selected models in the selected feature subset ensemble. For example, winter and spring quarter evapotranspiration are correlated at 0.96 (r_s) over the background/presence points, and these two variables each appeared in two of the selected four low burn severity wildfire activity models.

For top-selected models of all burn severities, three variables were shared among the top ten ranked variables by mean permutation importance and frequency of appearance (Table A.3): (1) slope (*slope*), with higher values more associated with more wildfire (Figures A.16F, A.17A, A.18A); (2) percent agricultural land cover (*agric_lc*), with higher values associated with less wildfire (Figures A.16D, A.17D, A.18D); and (3) precipitation in the summer quarter (*prec_sumq*), with higher values generally associated with more fire (Figure A.17F). In addition,

41

five of the top ten variables were shared among models of at least two burn severities: (1) mean temperature of the driest quarter (*bio_9*), (2) elevation (*elev*), (3) evapotranspiration ratio of the spring quarter (*etrt_sprq*), (4) actual evapotranspiration for the spring quarter (*aett_spr*), and (5) mean temperature of the wettest quarter (*bio_8*). Among these eight commonly high ranked variables, five are climatic indices, two are topographic indices, and one is an anthropogenic index.

There were some clear differences among the three burn severities in the top-ranked variables in the four RSFSA-selected models (Table A.3). For example, the three top ranked variables in low burn severity models were precipitation in the spring quarter (3/4 models), percent agricultural land cover (all four models), and mean temperature of the driest quarter (*bio_9*; 3/4 models). The three top-ranked variables in moderate burn severity models were *slope* (all four models), actual evapotranspiration for the spring quarter (3/4 models), and percent agricultural land cover (all four models). For high burn severity models, the three top ranked variables were slope (all four models), mean temperature of the wettest quarter (*bio_8*; 3/4 models), and elevation (3/4 models) (for permutation importance and response curves for variables of the single top models, see Appendix A, Results, Selected Features for Wildfire Activity Models; Table A.4, Figures A.16-19).

Projections for Wildfire Activity Models

Current Climate

The mean $AUC_{pa\_finaltest}$ values ranged from 0.84 to 0.93 for RSFSA-selected current climate MaxEnt quadratic/hinge β2 wildfire activity models for the three MTBS burn severity classes (Figure II.6A-C). For at least 60% of the 46 Level III ecoregions within the background evaluation extent, the projected burned areas for all three burn severities were 5% greater than
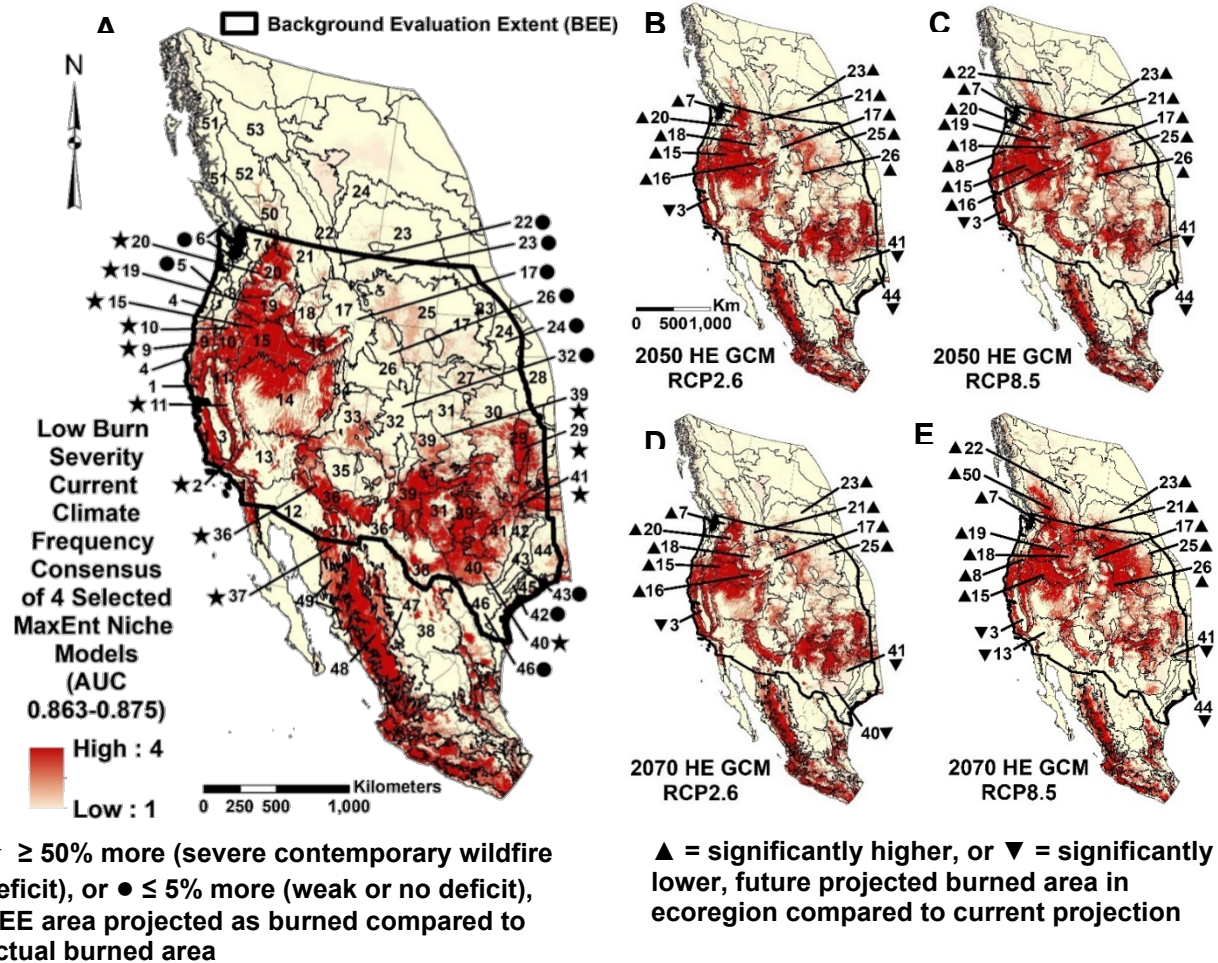
Figure II.7. Low burn severity MaxEnt quadratic/hinge β2 wildfire activity feature subset ensemble models for large wildfires with mean fire interval of ≤ 16.5 yrs per 31 yrs. Models represent frequency consensus of four selected variable subset models of 15 of 90 variables (arrows of significant differences according to Welch t-test with Holm correction, $P < 0.05$, preceded by significant Welch ANOVA test, $P < 0.05$; Table A.5) (Tracy et al., 2018b).
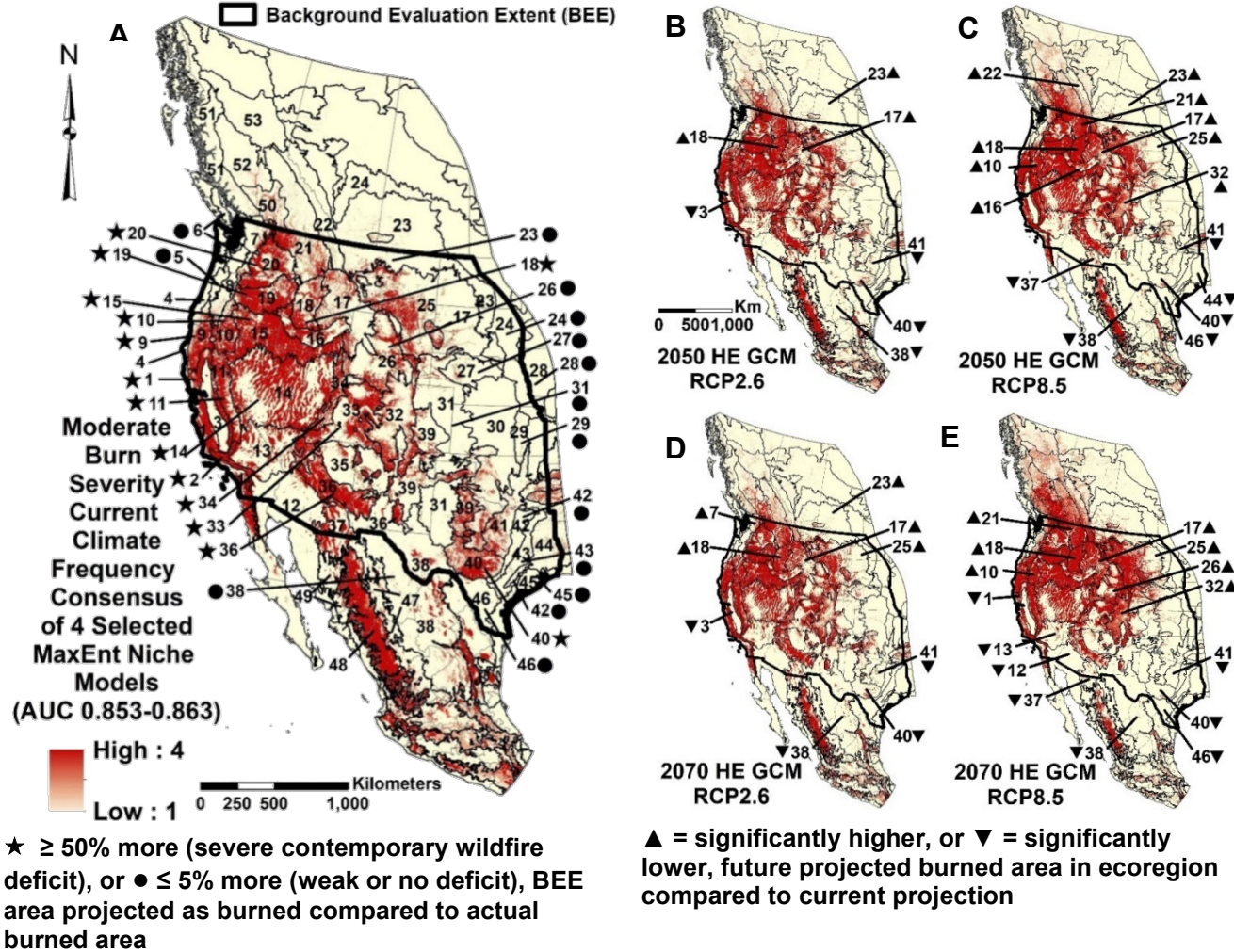
Figure II.8. Moderate burn severity MaxEnt quadratic/hinge β2 wildfire activity feature subset ensemble models for large wildfires with mean fire interval of ≤ 16.5 yrs per 31 yrs. Models represent frequency consensus of four selected variable subset models of 15 of 90 variables (arrows of significant differences according to Welch t-test with Holm correction, $P < 0.05$, preceded by significant Welch ANOVA test, $P < 0.05$; Table A.6) (Tracy et al., 2018b).
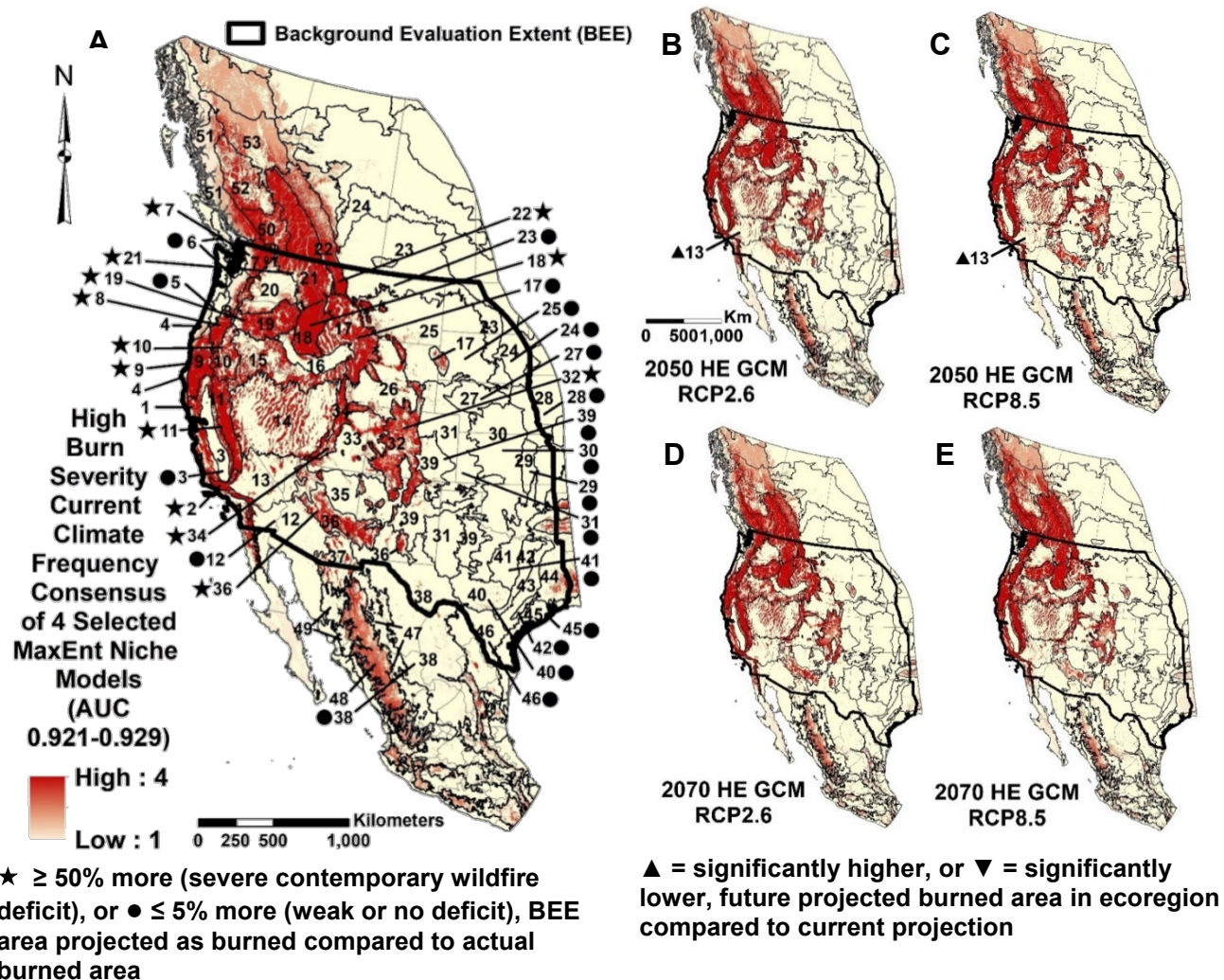
Figure II.9. High burn severity MaxEnt quadratic/hinge β2 wildfire activity feature subset ensemble models for large wildfires with mean fire interval of ≤ 16.5 yrs per 31 yrs. Models represent frequency consensus of four selected variable subset models of 15 of 90 variables (arrows of significant differences according to Welch t-test with Holm correction, P < 0.05, preceded by significant Welch ANOVA test, P < 0.05; Table A.7) (Tracy et al., 2018b).

the area actually burned (Figures II.7-9, Tables A.5-7). At least 25% of the Level III ecoregions

for all three burn severities exhibited severe contemporary wildfire deficits, with projected

burned areas greater than or equal to 50 percentage points higher than the actual area burned. In

addition, these ecoregions also had at least 50% (usually much more) of their total area projected

as burned. Very high contemporary wildfire deficit ratings were widespread in various

ecoregions throughout the western US for all three burn severities (Figures A.20-22) (for further

details, including zipped shapefiles for wildfire deficit rating maps for each burn severity, see

Appendix A, Results, Current Climate).

Future Climate

There were generally more significant differences between current and future projected

burned areas for low burn severity wildfire activity models in the 56 Level III ecoregions in

comparison to models for moderate and high burn severities (Welch t-test with Holm correction,

$P < 0.05$, preceded by significant Welch ANOVA test, $P < 0.05$; Figures II.7B–E, II.8B–E,

II.9B–E; Tables A.5-7). Most of the projected future significant changes involved increases in

burned area of ecoregions. These projected increases were in ecoregions that were generally

above 35ºN, which is around the border between the Central Basin and Range (14) and Mojave

Desert (13). In contrast, the fewer ecoregions with future projected significant decreases in large

wildfires were generally below 35ºN (for further details, including relationships between

important climate indices and latitude across the study area for climate scenarios of different

burn severities, see Appendix A, Results, Future Climate Model Projections, and Figure A.23).

Discussion

Niche Modeling Methods and Feature Selection

Feature selection with RSFSA facilitates optimizing the performance of a variety of niche modeling methods in terms of both the number of variables employed and the features included in the variable subsets. No improvement in RSFSA-selected model performance was found when using an expert-based filter for the initial set of 90 variables. The feature selection ensembles generated through RSFSA facilitate comparison of niche modeling methods and niche models across different species, phenomena, or scenarios (e.g., climates). For example, feature subset ensembles based on RSFSA-selected models were utilized to identify statistical differences in projected burned areas across climate scenarios. In addition, feature subset ensembles allowed the use of highly correlated variables in different wildfire activity models, improving representation of model uncertainty, which is especially important for climate scenario models (Braunisch et al., 2013).

The RSFSA-generated feature subset ensembles which facilitated comparison of niche modeling methods across a variety of subset sizes for different feature types (e.g., linear versus quadratic) and levels of L1 regularization ($\beta 1$-$\beta 40$; e.g., Warren and Seifert, 2011; Anderson and Gonzalez, 2011; Morales et al., 2017). Simpler linear or linear/quadratic MaxEnt, GLM and Glmnet models had lower overfitting (AUC_{diff}) than more complex quadratic/hinge MaxEnt models. However, these simpler models also had comparably higher underfitting (lower training and testing AUC) and lower information content (higher $AICc_{bg}$). Model underfitting has been observed to more negatively affect performance of MaxEnt models than overfitting using simulation data with a variety of metrics (Warren and Seifert, 2011). Consequently, the reduction of model underfitting and increased information content was emphasized by choosing the

MaxEnt quadratic/hinge models over simpler Glmnet or GLM models for projecting wildfire activity. Other studies have found that MaxEnt models using all features and or just linear/quadratic features outperform linear/quadratic probit GLM (Thibaud et al., 2014) and logistic Glmnet (Dicko et al., 2014) models, respectively. However, Guillera-Arroita et al. (2014) found that logistic Glmnet linear/quadratic models outperformed MaxEnt quadratic/hinge models in terms of root-mean-squared error with simulated data. For moderate and high burn severities models developed from larger variable subsets, feature selection results were more stable for MaxEnt and Glmnet linear/quadratic models than for GLM linear/quadratic models.

In agreement with Radosavljevic and Anderson (2014), a MaxEnt beta regularization multiplier value slightly above the default value of $\beta1$, namely $\beta2$, could reduce overfitting for MaxEnt models. In addition, the MaxEnt quadratic/hinge $\beta2$ models generally had lower $AICc_{bg}$ compared to both $\beta1$ and $\beta3$ models. A MaxEnt beta regularization value of around five or less ($\lesssim \beta5$) was necessary to see improvement in lower $AICc_{bg}$ than MaxEnt wildfire activity models without regularization ($\beta0$). As MaxEnt quadratic/hinge model L1 regularization is increased (from $\beta1$ to $\beta40$) over a broad range of variable subset sizes, model overfitting decreases (lower AUC_{diff}), but there is an increase in model underfitting (lower training and testing AUC) and decrease in model information content (higher $AICc_{bg}$). Although the MaxEnt quadratic/hinge $\beta2$ wildfire activity models had high numbers of derived features, MaxEnt software outputs of variable permutation importance and variable response curves allowed interpretation of the more important variables. The potential use of RSFSA to directly select derived MaxEnt variables, as Halvorsen et al. (2015, 2016) did using sequential feature selection, may facilitate further model optimization with lower numbers of parameters. MaxEnt quadratic/hinge $\beta2$ niche models are

potentially widely suitable for use in RSFSA with large sets of occurrence data and many environmental variables.

The RSFSA-selected MaxEnt quadratic/hinge β2 models exhibited significantly lower underfitting (higher training and testing AUC), higher information content (lower AICc), and, sometimes, lower overfitting (AUC_{diff}) in comparison to models generated from random variable subsets. In contrast, increasing levels of embedded feature selection using L1 regularization (higher values of β) for RSFSA-selected MaxEnt quadratic/hinge models resulted in lower overfitting (lower AUC_{diff}), but greater underfitting (lower training and testing AUC) and lower information content ($AICc_{bg}$). The combined use of RSFSA and L1 regularization can work together for improving the balance of overfitting, underfitting, and information content in niche models. The success of the RSFSA in reducing model underfitting and improving information content probably stems from an ability to identify variable combinations that are synergistic in terms of model relevancy among the thousands of screened models (Guyon and Elisseeff, 2003).

The employed randomized search strategy has several advantages over the sequential search strategy (evaluation of individual variables in sequence), that has most often been employed in feature selection for niche modeling, especially with MaxEnt (e.g., Mouton et al., 2009; Bradley et al., 2010; Lahoz-Monfort et al., 2010; Bellamy and Altringham, 2015; Halvorsen et al., 2015, 2016; Yost et al., 2008; Jueterbock et al., 2016; Zeng et al., 2016). The random subset selection search strategy can (1) better avoid entrapment in local minima (selecting the best feature subset at the moment) (Liu and Motoda, 1998; Jović et al., 2015), (2) better identify synergistic combinations of variables (Guyon and Elisseeff, 2003), and (3) take better advantage of parallel processing in evaluating several random variable subsets simultaneously (Garcia et al., 2006).

The tendency of niche models utilizing larger sets of variables to exhibit a higher AUC_{test} has been demonstrated previously (e.g., Synes and Osborne, 2011). Thus, a convergence in AUC_{test} values between random and RSFSA-selected models is expected as AUC_{test} values increase with growing variable subset size. Over a broad range of niche modeling methods of increasing variable subset sizes, there was a strong correlation between improved increasing values of AUC_{test} and improved decreasing values $AICc_{bg}$. Zeng et al. (2016; their Figure 1) also observed a general decrease in AICc as the number of MaxEnt environmental variables increased.

Similar to Beaumont (2005), there was no effect of variable subset sizes from six to 15 variables on the projected area burned in MaxEnt models. There was also no correlation among projected burned areas within the background evaluation extent with the projected area burned in beyond the background evaluation extent. Therefore, the projected area burned within the background evaluation extent for current climate probably also has little to no relationship to the projected area burned across future climate scenarios either within or beyond the background evaluation extent. Accordingly, the choice of more conservative MaxEnt models in terms of current projected area burned within the background evaluation extent probably did not produce more conservative estimates for burned areas when extrapolating the models across space or time.

Selected Features for Wildfire Activity Models

Only about half of the top ranked variables across RSFSA-selected MaxEnt quadratic/hinge β2 models for all three burn severities were expert selected variables from previous studies (Table A.2). Consequently, screening a wider initial set of 90 variables allowed us to identify additional important variables for modeling wildfire activity, such as mean

temperature of the driest quarter (*bio_9*), mean temperature of the wettest quarter (*bio_8*), spring actual evapotranspiration (*aett_sprq*), and spring evapotranspiration ratio (*etrt_sprq*). For the top four RSFA-selected wildfire activity models for each burn severity, a generally higher proportion of climatic indices (42%) were utilized compared to topographic (31%) and anthropogenic (27%) indices (Table II.1). In contrast, Dillon et al. (2011) found that topographic variables, especially elevation and topographic position index with a 2 km radius, were generally more important than climate and weather variables for non-spatial high burn severity models developed with the random forests algorithm. Similar to this study, they found models performed better when including several categories of topographic, climate and weather variables together in contrast to using a single category of topographic variables.

Within the climatic indices for the MaxEnt quadratic/hinge β2 wildfire activity models, there was a tendency for top RSFSA-selected models to include about equal percentages of Bioclim and AET-PET indices, indicating the importance of including both of these groups of indices in wildfire activity models. Although lower percentages of suppclim indices were used in the wildfire activity models compared to other climatic indices (Table II.1), some were among the top ranked indices, such as precipitation in the summer quarter (*prec_sumq*). Within the topographic indices, the geomorphologic indices ranked higher than the hydrogeomorphologic indices (Table A.3). Three of the five variables used in the wildfire activity models of Parks et al. (2015) were included in this study: (1) annual actual evapotranspiration, (2) annual precipitation, and (3) annual climate water deficit (snow water equivalent and soil moisture were excluded). Two of these variables, total annual evapotranspiration and annual climate water deficit, appeared in some of the RSFSA-selected 15-variable MaxEnt quadratic/hinge β2 models

for low burn severity wildfires (Table II.1). In addition, precipitation in the summer quarter, closely related to annual precipitation, occurred in models for all three burn severities.

Of the 17 anthropogenic indices, only agricultural land cover was among the top ten ranked variables for RSFSA-selected MaxEnt quadratic/hinge β2 wildfire activity models of all three burn severities, appearing in every model. Higher amounts of agricultural land cover were associated with lower probability of wildfire for all three burn severities. Reduced wildfire probability with higher agricultural land cover is probably related to reduced availability of woody vegetation as fuel. Several other studies have also found that anthropogenic indices, especially agricultural land cover, are of critical importance to modeling large scale wildfire activity (Kalabokidis et al., 2002, Liu and Wimberly, 2016; Robinne et al., 2016; Mann et al., 2016).

Projections for Wildfire Activity Models

Current Climate

Wildfire activity was projected at one km resolution over a larger area of western North America than has been done previously, employing a novel combination of different niche model types with the MTBS data used by Liu and Wimberly (2016) and Parks et al. (2016), and additional data from the MTBS and LANDFIRE databases. The AUC_{test} values of the wildfire models for the three burn severity classes were fairly high (above 0.84), even though severe contemporary wildfire deficits were projected for many ecoregions. Similar to Parks et al. (2015), there was a general trend of greater contemporary wildfire deficits projected among forested ecoregions. In addition, the proportion of ecoregions projected with severe contemporary wildfire deficits increased with increasing burn severity for the Northwestern Forested Mountains. The current climate multiclass burn severity category models of Parks et al.

(2016) also project greater high burn severity fires in these northwestern forested ecoregions. In contrast to projections for forested ecoregions, only a small proportion of *non-forested* Level I ecoregions with severe contemporary wildfire deficits was projected for the low and moderate burn severity categories. The severity of projected contemporary wildfire deficits in forested ecoregions for all burn severity categories were generally much greater than found for wildfire deficits in similarly defined forested ecoregions by Parks et al. (2015). The generally higher projected contemporary wildfire deficits in this study could be related to finer scale detection of variation in wildfire activity due to use of a higher spatial resolution (one km^2) and additional variables, particularly agricultural land cover. The 1 km resolution contemporary wildfire deficit ratings map shapefiles were made available for all three burn severities for the western US that may assist land managers in identifying areas with greater long-term potential hazard for large wildfires (see shapefiles in Appendix A, Results, Current Climate). Many areas with little or no data on contemporary wildfire deficits (e.g., much of the East Texas Central Plains and Arizona/New Mexico Plateau ecoregions) may have had pre-Columbian mean fire return intervals greater than or equal to those seen in the recent historical 31-year 1984–2014 period used in this study, but land use/land cover change to cultivation, urbanization and heavy grazing has probably led to long term anthropogenic fire suppression.

Future climate

Future projections of increased low burn severity wildfires in several northern ecoregions may be associated with projected changes in three important bioclimatic indices: (1) higher mean temperatures of the driest quarter (*bio_9*), (2) decreases in mean precipitation during the summer quarter (*prec_sumq*) in the north (but not in the south), and (3) increases in mean precipitation during the spring quarter (*prec_sprq*) in the north (but not in the south). Potentially increased

primary productivity for northern ecoregions associated with projected increases in spring precipitation may favor larger areas of low burn severity wildfires. Projected increases in temperature for the driest quarter (*bio_9*) and decreases in summer precipitation (*prec_sumq*) in the north may favor wildfire ignition and propagation of low burn severity wildfires. Rogers et al. (2011) similarly projected future increased wildfire activity in the Pacific Northwest from increased summer droughts related to decreased summer precipitation and higher summer temperatures, and increased fuel loads related to higher winter precipitation. Projections of smaller areas of large low burn severity wildfires in some southern ecoregions may be related to projected reductions in rainfall (e.g., *prec_sprq*) at southern latitudes which could be associated with lower primary productivity (for further discussion of variable influence on climate projections, see Appendix A, Discussion, Projections for Wildfire Activity Models).

These wildfire activity models do not attempt to incorporate projections of the complex long-term interactions between vegetation population dynamics and changes in extreme weather events, such as prolonged drought, that could greatly impact future landscape wildfire activity (McKenzie and Littell, 2017). In addition, there is considerable uncertainty in the accuracy of both the original MTBS burn severity classifications used in training models for this study (Kolden et al., 2015) and in the GCMs used for projecting future climate in western North America. For example, several GCMs project generally drier and warmer conditions in southwestern North America over this century (Swain and Hayhoe, 2015), such as was observed in projected reduced spring precipitation (*prec_sprq*) with the HadGEM2-ES GCM for 2070 (Figure A.23B). However, Chylek et al. (2014) report that the historically cyclic influences of the Atlantic multi-decadal oscillation (AMO) and Pacific decadal oscillation (PDO) indices are poorly incorporated into GCMs. Furthermore, they maintain that projected AMO/PDO cycles

may lead to stable temperatures and increased precipitation over the next several decades in the southwestern US, which is in contrast to projections from GCMs. Caution should be used in the interpretation of the wildfire activity model projections in areas, such as central Mexico, that are far beyond the background evaluation extent of continental US training data. In spite of uncertainties, models from this study are in general agreement with several other recent studies projecting future increases in burned areas in western North America, especially for low and moderate burn severity wildfires (Parks et al., 2016; Liu and Wimberly, 2016).

Conclusions

Feature Selection for Niche Modeling

A novel random subset feature selection algorithm was used to effectively screen a large number of variables to develop a feature subset ensemble of optimally-sized feature subsets that can increase performance for a variety of niche modeling methods. The feature selection algorithm does not improve niche model performance over expert-selected models, but it facilitates identification of new relevant variables or variable combinations that can be useful in developing and interpreting the models. The algorithm is especially useful for identifying variables for modeling tasks about which little expert information is available. In addition, identification of alternative high performing models of different variable subsets by the feature selection algorithm is important in accounting for model uncertainty in comparisons across modeling methods or scenarios. The utilization of highly collinear variables in separate models of selected feature subset ensembles is especially valuable for reflecting model uncertainty. This feature selection algorithm affords the researcher flexibility in balancing the levels of niche model underfitting, overfitting, and information content and the number and complexity of model parameters. The combination of random subset feature selection with L1 regularization

via MaxEnt quadratic/hinge β2 models appears to be especially suitable for developing feature subset ensembles representing higher performance niche models when large sets of occurrence data and environmental variables are available, as is the case with wildfire activity.

Further studies are needed to assess the performance of the random subset feature selection algorithm for improving niche models for species, and of other phenomena, and using differing niche modeling methods, such as BIOCLIM and random forests (c.f. Jović et al., 2015). The degree of spatial variability in feature-selected models versus random models for current and future climate scenarios should also be examined. Comparisons of the spatial variability of feature subset ensemble models from random subset feature selection should also be made with other types of model ensembles, such as training set ensembles and multi-algorithm ensembles (e.g., Zhang et al., 2015). Additional niche model evaluation statistics could also be investigated for use in feature selection, such as the Hosmer-Lemeshow goodness of fit statistic for logistic regression. Potential improvements in model transferability across space and time using various feature selection strategies can also be explored.

Implications for Conservation

Comparisons of historical and projected wildfire activity indicate that unnaturally low fire return intervals, amounting to severe contemporary wildfire deficits, are widespread in the western US, including in areas of conservation concern such as the Madrean Archilpelago ecoregion of southern Arizona and New Mexico (for zipped shapefiles of contemporary wildfire deficits, see Appendix A, Results, Current Climate). Where feasible, reduction of anthropogenic fire suppression, such as by limiting grazing and increasing prescribed or wildland fires, may be critical for maintaining the integrity of fire dependent western montane ecosystems (e.g., Noss et al., 2006). The projected reductions in fire frequency through climate change in southwestern

North America could further degrade natural fire regimes of fire dependent ecosystems, making long-term reduction of anthropogenic fire suppression even more imperative. In contrast, models in this study projected future increases in wildfire activity in forested ecoregions of northwestern North America. In these northwestern forests, it will be critical to remove excess fuel build-up, such as through prescribed burns, to prevent increased wildfire damage to human lives and property in and around these ecosystems.

CHAPTER III

MODELING MONARCH FALL MIGRATION PATHWAYS AND

SPATIALLY IDENTIFYING POTENTIAL MIGRATORY HAZARDS

FOR THE EASTERN MONARCH BUTTERFLY

Synopsis

Identifying migratory pathways is important for developing conservation priorities for declining migratory species. However, few studies have compared modeling approaches to evaluate their different contributions for understanding migration patterns. The contributions of MaxEnt ecological niche models and interpolative kernel density estimation models (KDEMs) are compared for identifying core migratory pathways for the eastern monarch butterfly (*Danaus plexippus*). These pathways are used to spatially delineate potential anthropogenic hazards within these pathways. The objectives include: (1) compare monarch fall migration pathways using KDEMs and MaxEnt, (2) characterize annual migration pathway variability, (3) identify core migratory pathways, and (4) spatially identify potential anthropogenic hazards along the core migratory pathways. Citizen scientist reports from Journey North of overnight roosts for eastern migratory monarchs from 2002–2016 were used to model the fall migration at 10 km spatial resolution with MaxEnt and KDEMs. Potential anthropogenic threats to the fall migration were spatially identified along the core migration routes. The KDEM migration pathways best represented directed movement patterns of monarchs towards overwintering locations. The MaxEnt models better coincided with nectar resource habitats of the Great Plains grasslands. The KDEMs varied annually in both width and location within the Central Flyway. Potential hazards spatially identified along the migration routes included monarch roadkill, areas of intensive agriculture, neonicotinoid contamination of nectar and honeydew food resources, and mosquito

spraying. MaxEnt and KDEM were complementary in modeling monarch migratory pathways. The spatially identified potential hazards can form the basis for future risk assessments.

Introduction

Many migratory species of conservation concern are declining worldwide (Hardesty-Moore, 2018). Conservation strategies for these migratory species must take into account breeding, migratory stopover, and overwintering sites. Annual mortality for migrant species, such as birds, can be highest across migratory routes, especially in narrower portions of migratory pathways. Spatial models of migratory pathways are an important tool for identifying conservation priorities (Runge et al., 2014). Common approaches for defining migratory pathways include kernel density estimation (KDE), and correlative ecological niche models, such as MaxEnt. These methods have not been thoroughly compared to evaluate their contributions to migratory pathway analyses.

Kernel density estimation is a nonparametric spatial point pattern method for analyzing point intensity that is often used with telemetry data for assessing the frequency of utilization of an area in defining animal home ranges (Worton, 1989; Kie et al., 2010). The KDE intensity surface has also been used to delineate migratory movement, particularly for birds, based on telemetry data of stopover locations for certain seasons (Rayner et al., 2017), months (Muzaffar et al., 2017), or over the entire migratory pathway (Gearin et al., 2017; Pierce et al., 2017; Wytinski and Bonter, 2018). Moore and Krementz (2017) used non-telemetry bird band return data with KDE to analyze migration origin and destination locations. The KDE does not appear to have been previously used in defining the entire migratory pathway with non-telemetry data as is done in this study. Correlative ecological niche models, particularly MaxEnt, have been used to model migratory pathways using the same types of telemetry data in conjunction with

environmental layers (e.g., Huff et al., 2012; Quillfeldt et al., 2013; Williams et al., 2017). Migratory niche models have also been incorporated into a larger framework for delineating migration routes, either as resistance layers in connectivity models for ungulates (Poor et al., 2012; Bond et al., 2017), or as a refueling resource layer in individual-based models for birds (Smith and Deppe, 2008).

The KDE intensity surface has also been used in developing interpolative KDE models (KDEMs) of species distributions (Pennay et al., 2011). For more detailed analyses of migration pathways with KDE that facilitate comparisons across years and with MaxEnt models, novel training set ensembles of migratory KDEMs were developed from normalized KDE surfaces, performing calibration and testing in the same manner as niche models. Interpolative KDEMs are restricted to projecting occurrence over an area limited by the radius of the selected KDE bandwidth around the training data points. In contrast, correlative niche models incorporate environmental data to create a predictive surface that can be extrapolated beyond the boundaries of the training data. While migratory KDEMs cannot directly incorporate environmental layers, they should be more sensitive to clustered point patterns related to organismal movement (endogenous autocorrelation) that have little or no relationship to the spatial distribution of environmental conditions (exogenous correlation) (c.f., Bahn and McGill, 2007). The KDEMs and MaxEnt are compared for analyzing migratory pathways for the eastern monarch butterfly (*Danaus plexippus* Linnaeus) (Nymphalidae: Danainae).

The migratory phenomenon of eastern monarchs is in danger of disappearing (Brower et al., 2012). The migrant overwintering population has potentially declined as much as 80% over the past two decades (Vidal and Rendón-Salinas, 2014). Many studies have focused on habitat loss on the breeding grounds (Brower et al., 2012; Pleasants, 2017; Malcom, 2018) and at

overwintering sites (Brower et al., 2012; Vidal et al., 2014; Malcolm, 2018). Thogmartin et al., (2017) modeled the impact of these factors on the population decline of monarchs, including climatic factors, disease, and agricultural insecticide use, and observed strong negative effects from all of these threats, particularly by glyphosate herbicide use. Mortality during the fall migration has also been suggested as a significant factor contributing to the decline in monarchs (e.g., Badgett and Davis, 2015; Ries et al., 2015; Inamine et al., 2016; Agrawal and Inamine, 2018). However, few studies have focused on potential anthropogenic threats to the fall migration (but see McKenna et al., 2001 and below).

The majority of the eastern monarch population migrates to Central Mexico for overwintering. Monarchs originating from summer breeding sites as far north as southern Canada migrate south to oyamel fir (*Abies religiosa* Kunth) forests in Central Mexico from August to November. These same individuals that successfully overwinter will migrate north the next spring to the southern United States. Subsequent generations reach the northern USA and southern Canada in June (Brower, 1995; Calvert and Wagner, 1999; Brower et al., 2006).

Two main flyway routes have been described for the fall migration of the eastern monarch based on overnight roost sites: (1) the Central Flyway proceeding from Canada and the Midwest southwards, and bounded to the east by the Appalachian Mountains and to the west by the Rocky Mountains, excluding the coastal areas; and (2) the Eastern or Coastal Flyway proceeding from the northeastern US southwards, following the Atlantic and Gulf coasts (Calvert and Wagner, 1999; Howard and Davis, 2009). Roosts consist of a few to several thousand monarchs aggregated within trees and shrubs. Overnight roosting behavior is almost exclusively associated with the monarch fall migration (Davis and Garland, 2004; Brower et al., 2006; Howard and Davis, 2009). Journey North (2017) maintains an extensive citizen science database of monarch

sightings, including fall migratory overnight roost locations since 2002. Models of the migratory pathways developed from these data will provide important information on yearly variation in migration routes, with important implications for spatially assessing conservation priorities and threats.

A variety of potential anthropogenic hazards to adult fall migrating monarchs occur along the migratory routes. Potential threats include: (1) mortality due to collision with vehicles (McKenna et al., 2001) or other moving structures; (2) reduced nectar resources due to land cover/land use change, including increased herbicide use on agricultural lands (Brower et al., 2006), (3) exposure to systemic neonicotinoid insecticides through feeding on flower nectar or other sugar sources near agriculture (Krischik et al., 2015); and (4) exposure to insecticides (e.g., resmethrin and permethrin) from mosquito control (Oberhauser et al., 2006; 2009). Further study is needed to spatially identify these potential anthropogenic hazards along the migration pathways, especially as the migration pathway narrows as it approaches the overwintering sites (Brower et al., 2006; Badgett and Davis, 2015). Climate change has also been proposed to threaten the eastern North American monarch population, including the fall migration (Malcolm, 2018). For example, the migration route could be lengthened if the breeding range shifts farther north in warmer climates, and habitat suitability for fall nectar plant resources could be reduced by lower precipitation and higher temperatures. Spatially identifying the potential hazards along the migratory pathway is prerequisite to assessing exposure to hazards as part of any migratory risk assessment (e.g., Liechti et al., 2013).

The goals of this study are to utilize KDEM and MaxEnt for defining the core fall migration pathways of the eastern monarch, and to identify potential migratory hazards along these pathways. The specific objectives are to (1) project and compare the eastern monarch fall

migratory pathways with the two approaches of MaxEnt and KDEM; (2) analyze annual variability in the migration pathways; (3) delineate core migratory pathways of the Central and Eastern/Coastal flyway divisions; and (4) spatially identify potential hazards to the fall migration as a foundation for planning future migratory risk assessments.

Methods

Study Site

The Rocky Mountains and Sierra Madre Oriental was used to define the western boundary for the eastern monarch (Brower 1995; Figure III.1). The southern boundary in Florida follows the boundary of the spring breeding range as delimited by Oberhauser et al., (2017). The background evaluation extent for training and evaluation of monarch migration models is derived from a 500 km buffer around a convex hull polygon formed using the 2002 to 2016 overnight roost records from Journey North (2017) (Figure III.1). This background evaluation extent encompasses most of the range of the eastern monarch migratory population.

Overnight Roosting Records

Journey North citizen scientist volunteers have been reporting their spring monarch observations to the program since 1997, and records of overnight roosts since 2002 (Journey North, 2017). Comparison of geocoordinates with the location descriptions in the comments of roosting records revealed that the spatial accuracy of the data was approximately ±5 km. Consequently, roosting locations were aggregated across a raster with spatial resolution of 10 km^2. This aggregation of roost locations also serves as a 10 km spatial filter for reducing sample bias and spatial autocorrelation among the data (Boria et al., 2014). A total of 2,803 roosting records from the 15 years of 2002–2016 were used in the study, ranging from 25 (2002) to 422 (2015) records per year (Table C3.1). The 12 consecutive years from 2005 to 2016 were used
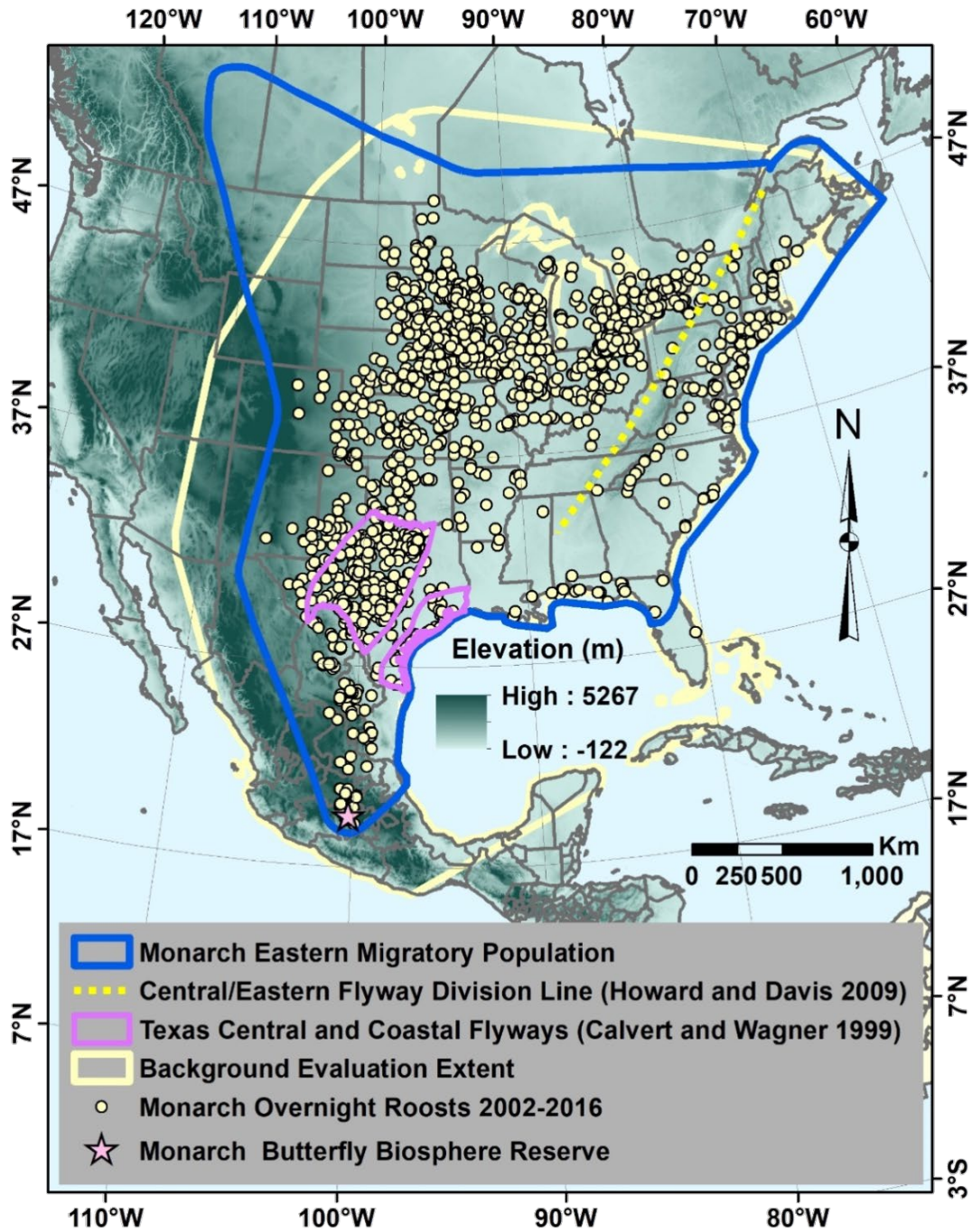
Figure III.1. Monarch overnight roosts from 2002 to 2016 (Journey North 2017), range of the monarch eastern migratory population, previous monarch flyway divisions, and background evaluation extent for model training and testing.

for annual models of migration, based on a minimum requirement of 100 records per year. Data were spatially thinned separately by year for annual models. For the purpose of developing presence-only migration pathway models, all Journey North roost records within the 10 km spatial filter were regarded as indicative of the presence of migratory roosting individuals within a given year, regardless of butterfly count data per roost.

MaxEnt Migration Pathway Models

An initial set of 80 environmental variables generalized to 10 km resolution were used in developing the MaxEnt niche models, including 57 climatic indices, 12 topographic indices, and 11 land cover indices (Table C3.2). MaxEnt version 3.3.3 models (Phillips et al., 2006) were developed from monarch roost locations using the R-software (R Core Team, 2018) dismo package (Hijmans et al., 2011). About 10,000 pseudoabsence points were generated for model evaluation within the background evaluation extent. The pseudoabsences were buffered at 20 km from the presence points (e.g., Barbet-Massin et al., 2012). The R PresenceAbsence package (Freeman and Moisen, 2008) was used with presence and pseudoabsence points for calculating the pseudoabsence (psa) versions of the true skill statistic (TSS_{psa}) and area under the curve statistic (AUC_{psa}). In order to reduce MaxEnt model complexity and overfitting for improved model generalization (Jiménez-Valverde et al., 2008; Warren and Seifert, 2011), the MaxEnt beta regularization was adjusted from the default of one to two and only quadratic and hinge features were used (Tracy et al., 2018b). A random subset feature selection algorithm (RSFSA) was used to select 12 of 9,000 MaxEnt models using smaller subsets of the 80 variables that exhibited higher accuracy (AUC_{psa}), lower complexity, as measured by lower corrected Akaike information criterion (AICc), and lower overfitting, as measured by AUC_{psa_diff} (training AUC_{psa} minus test AUC_{psa}; Warren and Seifert, 2011) than other random subsets (Tracy et al., 2018b).

This study represents the first instance of applying RSFSA with pseudoabsence data as opposed to true absence data. The absolute value of the Spearman's rank correlation coefficient (r_s) among variables in variable subsets was limited to 0.7 (Dormann et al., 2013) and AUC_{psa} was used in selecting variable subset models. MaxEnt models using six of the 80 variables were considered as optimal (for additional details, see Supplementary material, Methods). The 12 final MaxEnt models were calibrated to binary presence/absence format using a threshold of maximum TSS_{psa} (Liu et al., 2013a), and they were combined using frequency consensus to form a feature subset ensemble (FSE). The AICc was calculated for the 12 models from the MaxEnt model raw version rasters and training presence point data using the ENMeval R package (Muscarella et al., 2014). The variables were jointly ranked for the top 12 MaxEnt models using a higher weighting of 0.6 for the model mean variable permutation importance (e.g., Halvorsen, 2013) and a lower weighting of 0.4 for the frequency of variable appearance in the top 12 models (for details, see Appendix C, Methods).

Kernel Density Estimation Model Migration Pathways

The KDEs were developed at 10 km resolution using presence-only monarch roost locations with the ArcGIS (ESRI Inc., Redlands, California) Kernel Density tool (Geodesic method, points as values), which employs a quartic (biweight) kernel function. The North America Albers Equal Area Conic Projection (North American 1983 datum) was used as the required equal area projection for KDE. The optimal KDE bandwidth (smoothing parameter) was automatically calculated in ArcGIS by a spatial variant of Silverman's Rule-of-Thumb that is robust to outliers. In order to compensate for higher numbers of observers in densely populated areas, monarch overnight roost locations at 10 km resolution were weighted by a grid of mean human population density per 1 km for the year 2000 (Center for International Earth Science

Information Network, CIESIN, 2005) (for details, see Supplementary material, Methods). The weighting process yielded index values from one (high human population, representing most points) to ten (low human population, representing few points) for each roosting record, constraining the influence of human population density. The KDE raster was then calculated and normalized from zero to one to create a raw KDEM surface of probability of occurrence. The final KDEM was created by restricting the boundaries of the raw KDEM to that of a calibrated binary presence/absence version using a threshold of maximum TSS_{psa} as was done for MaxEnt models. A KDEM without any adjustment for human population was also calculated for comparison. For calculation of AICc using the ENMeval R package, the raw KDEM was utilized (e.g., Graham et al., 2013), with values of zero changed to 0.000001 and all values recalculated to add to one within the background evaluation area (analogous to the MaxEnt raw values used with ENMeval R). This recalculated raw KDEM raster and associated model values for training presence points were then used in calculating AICc. Accuracy statistics of TSS_{psa} and AUC_{psa} were calculated for raw KDEMs in the same way as described above for MaxEnt. A total of three different KDEMs were derived from standard three-fold partitions of two-thirds training and one-third testing data using the 2002–2016 roost data. From the three training KDEMs, a training subset ensemble (TSE) was developed. From the TSE, a minimum consensus TSE model was derived representing the area encompassing at least one of the three training KDEMs. The minimum consensus TSE was used as a boundary for display of the average consensus of the continuous raster training KDEMs. The 100% consensus KDEM TSE boundary was also calculated for display (see Table C.4 for shapefile; R code and Arc python code for generating and analyzing KDEMs is available at https://github.com/jamesltracy/KDEMs).

67

Comparison of MaxEnt and Kernel Density Estimation Model Migration Pathways

Statistical comparisons of AUC_{psa}, AICc and AUC_{psa_diff} (overfitting) between the 12

MaxEnt model feature subset ensemble and the three KDEM training set ensemble were performed

using an R core implementation of the Welch t-test, which allowed for the case of unequal

variance. Models were also evaluated for ability to identify different regions of the migration

pathways as a basis for further analyses described below.

Annual Kernel Density Estimation Model Migration Pathways

The same procedure described above to create three binary calibrated minimum

frequency consensus TSEs of KDEMs was followed for modelling the annual fall migration

routes for individual years from 2005 to 2016 and for all years combined from 2002 to 2016 for

comparison. The means and standard deviations for the width and relative centroid shifts of

annual KDEM migratory pathways were calculated for the northern (37-50°N latitude) and

southern (27-37°N latitude) portions of the Central Flyway. The 37°N north-south boundary was

based upon the approximate latitude where the migration pathway starts to narrow as it proceeds

south along the Central Flyway. Low numbers of observations of annual roosts were not

conducive to similar analyses for either the Eastern Flyway or areas south of 27°N latitude.

Migration pathway width and centroid shift calculations were performed for the annual models

and for the combined 2002-2016 model. Migratory pathway dimensional characteristics included

(1) average pathway widths of the annual KDEMs (directly proportional to area), (2) the north to

south shift of the centroid for the annual KDEMs from the 2002-2016 KDEM centroid, and (3)

the east to west shift of the centroid for the annual KDEMs from the 2002-2016 KDEM centroid.

Spearman correlation coefficients were calculated between annual average KDEM widths and

centroid shifts, and the area of overwintering colonies in Mexico (Vidal and Rendón-Salinas, 2014; Monarch Watch, 2017).

Flyways and Core Migratory Pathways

Flyway division boundaries within the larger monarch eastern migratory population from Canada to Mexico were updated using the migration pathways identified by a minimum consensus ensemble of the combined 2002 to 2016 KDEM TSEs and individual roost records. Core fall migration routes, including core pathways through the narrower southern funnel portions, were also identified by generally following the boundaries of flyways and the 100% consensus boundary of the annual KDEM ensemble (see Table C.4 for shapefiles).

Anthropogenic Fall Migration Hazards

The literature was reviewed on non-climate change related anthropogenic lethal and sublethal hazards to monarchs and other beneficial insects, such as pollinators, and identified potential hazards for adult fall migrating monarchs (see Introduction). Hazards were then spatially identified, especially focusing on the important southern core migration pathways, by combining and analyzing a variety of spatial data obtained from citizen science databases, online GIS layers, publications, and other sources. Analyses included temporal matching of hazards with the monarch fall migration period (typically October to November in the South) (e.g., mosquito control) and identification of areas with potentially greater hazards (e.g., areas of high cultivated land cover or neonicotinoid use) (for sources, see Supplementary material, Methods; see Table C.4 for shapefiles).

Results

MaxEnt Migration Pathways

The random subset feature selection algorithm was effective in selecting 12 six-variable MaxEnt models with higher AUC_{psa} values than random models, ranging from 0.968 to 0.982 (Figure C.1). A total of 42 out of 80 variables were used at least once in the 12 selected models (Tables C.2-3). The ten variables jointly ranked highest by MaxEnt model permutation importance and frequency of appearance in the 12 models were all climatic indices (Table C.3). Four of these top ten climate variables were Supplementary Climatic indices, four were Actual and Potential Evapotranspiration (AET-PET) indices, and two were Bioclim indices. The top three ranked variables were the Supplementary Climatic index of spring monthly minimum temperature, and two AET-PET indices of autumn mean monthly actual evapotranspiration, and total annual actual evapotranspiration. The eleven land cover indices generally had the lowest MaxEnt permutation importance and frequency of appearance in the twelve selected models (Tables C.2-3).

The 100% consensus of the 12 calibrated MaxEnt models is mostly concentrated within the Central Flyway (Figure III.2A). A large portion of the MaxEnt 100% consensus boundary for the Central Flyway coincides with the grasslands of the Great Plains Level I ecoregion (Commission for Environmental Cooperation, CEC, 2005) (Figure III.2A). The MaxEnt 100% consensus boundary includes only northern portions of the Eastern Flyway.

Kernel Density Estimation Model Migration Pathways

The AUC_{psa} values for the three training KDEMs for the entire 15-year data set (2002–2016) ranged from 0.995 to 0.998 (default KDE bandwidths ranged from 226 to 231 km). The KDEM 100% consensus boundary is mostly associated with the Central Flyway, but it includes

Portions of CEC Level I Ecoregions
- Great Plains
- Eastern Temperate Forests
- North American Deserts

Monarch Fall Migration Flyway Divisions
- Central
- Eastern

A

MaxEnt Feature Subset Ensemble (12)
High : 0.72
Low : 0.02

B

KDEM Training Set Ensemble (3)
High : 0.94
Low : 0

Km
0 250 500 1,000

100% Consensus

⭐ Monarch Butterfly Biosphere Reserve

CEC Levels II and III Ecoregions

1 Temperate Plains
2 South Central Semiarid Prairies
3 Tamaulipas-Texas Semiarid Plain
4 Texas-Louisiana Coastal Plain
5 Mississippi Alluvial and Southeast USA Coastal Plains

6 Mixed Wood Plains
7 Central USA Plains
8 Ozark/Ouachita-Appalachian Forests
9 Southeastern USA Plains
10 Chihuahuan Desert (Level III)

Figure III.2. Monarch fall migration pathway minimum calibration consensus of average consensus models for 2002–2016, including CEC (2005) ecoregions (including 100% consensus boundaries): (A) MaxEnt feature subset ensemble of 12 models developed from subsets of six of 80 variables by random subset feature selection for high AUC_{psa}; and (B) kernel density estimation model (KDEM) training set ensemble of three models developed by three-fold training data partition (see Table C.4 for shapefiles; see Figures III.5A and III.6 for binary minimum consensus KDEM).

the northern portion of the Eastern Flyway as well as the coastal Eastern Flyway in Alabama and the Florida panhandle (Figure III.2B). The same Great Plains ecoregion coinciding with the MaxEnt 100% consensus boundary also overlaps much of the KDEM 100% consensus boundary in the Central Flyway (Figure III.2B). However, the eastern portion of the Chihuahuan Desert Level III ecoregion is also included in the KDEM 100% consensus boundary. In addition, the KDEM 100% consensus overlays with several Level I ecoregions that approach or encompass the overwintering sites in central Mexico. Much of the KDEM 100% consensus boundary for the Eastern Flyway is occupied by Level II coastal plains ecoregions (Figure III.2B). A lower projected density of roosting is apparent in forested Level II ecoregions of the Eastern Flyway. In comparison to KDEMs that did not account for human population density related observer bias (Figure III.3A), the KDEMs accounting for human population density appeared to project much reduced, but not eliminated, bias towards higher roost densities around metropolitan areas, such as Minneapolis/St Paul, Dallas/Fort Worth, and Austin/San Antonio (Figure III.3B). However, differences in the KDEM 100% consensus boundaries for the two models appear to be less pronounced (Figure III.3A-B).

Comparison of MaxEnt and Kernel Density Estimation Model Migration Pathways

The accuracy (AUC_{psa}) of the KDEM training set ensemble was significantly higher than that of the 12-model MaxEnt feature subset ensemble in projecting the monarch migration pathways (Figure III.4A). However, the model complexity (AICc) was significantly lower in the MaxEnt ensemble (Figure III.4B). No significant difference in model overfitting between MaxEnt and KDEM ensembles was found (Figure III.4C). The 100% consensus KDEM boundary better distinguished the migratory pathway through the western Chihuahuan Desert and Mexico where the MaxEnt 100% consensus boundary was mostly absent (Figure III.2). In addition, the
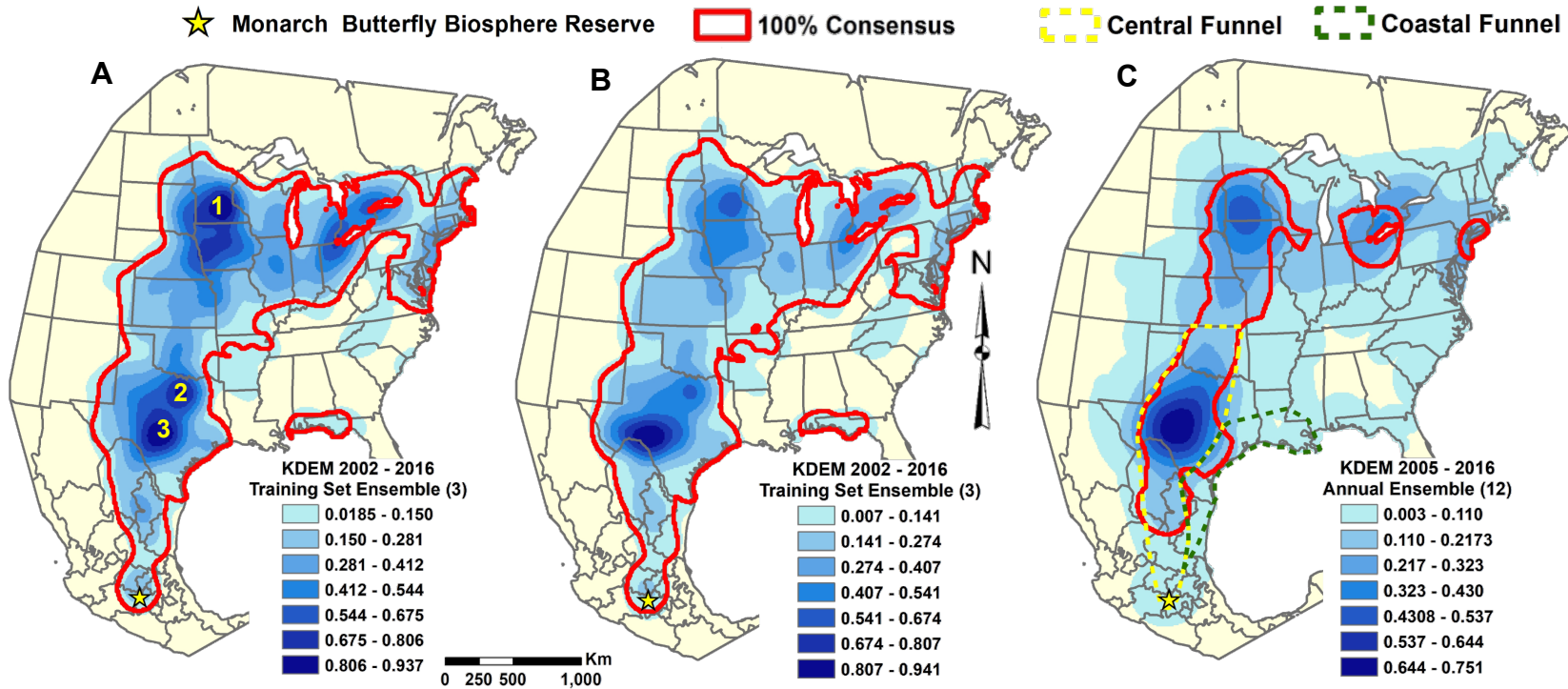
Figure III.3. Monarch fall migration pathway minimum calibration of average consensus kernel density estimation model (KDEM) ensembles with 100% consensus boundaries of training set models (n = 3) for 2002-2016 without (A) and with (B) reduction of human observer bias using the monarch roost human population density index (Figure III.2B), and (C) annual models (n = 12) from 2005–2016, including the Central Funnel and Coastal Funnel core migration pathways (see Figure III.5 for individual annual minimum consensus models). Metropolitan areas of Minneapolis/St Paul (1), Dallas/Fort Worth (2), and Austin/San Antonio (3) are identified in (A) (see Table C.4 for shapefiles).
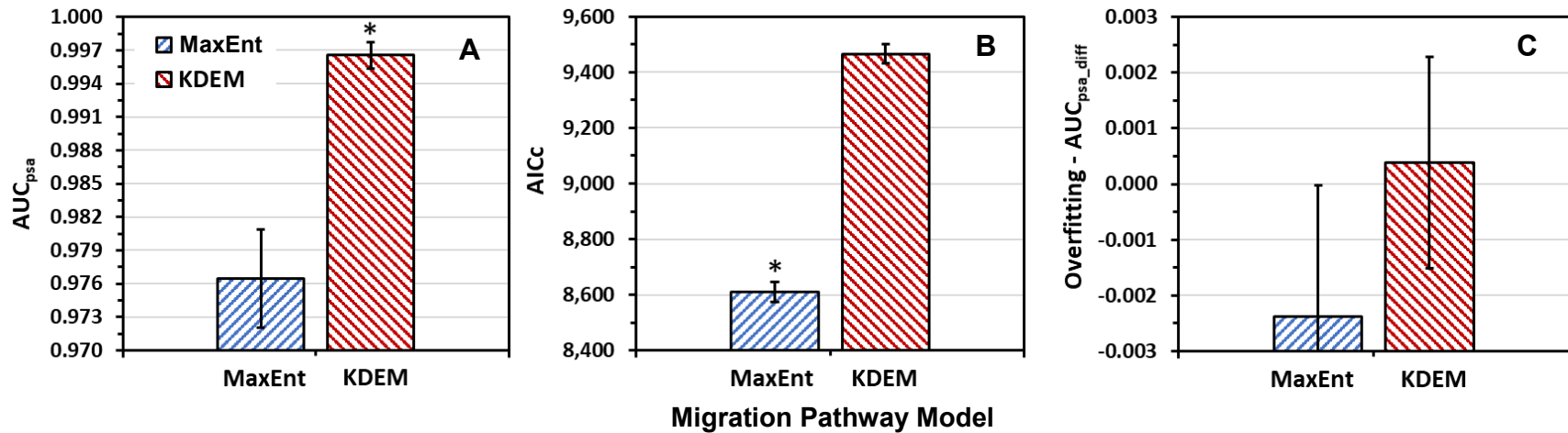
Figure III.4. Evaluation statistics of MaxEnt niche model versus kernel density estimation model (KDEM) of monarch fall migration pathways (mean ± SD): (A) AUC_{psa}, (B) AICc, and (C) AUC_{psa_diff} (overfitting) (see Figure III.2 for models). Means with an asterisk for a statistic are significantly more optimal (higher for AUC_{psa} and lower for AICc and AUC_{psa_diff}) (P < 0.05; Welch t test).

100% consensus KDEM boundary incorporated larger portions of the Eastern Flyway. The KDEM approach was selected for further delineation of the Central and Eastern Flyway divisions and their core pathways, and for investigation of the annual variation in the migratory pathway of the Central Flyway.

Annual Kernel Density Estimation Model Migration Pathways

The migration pathways of annual KDEM training set consensus models varied considerably from year to year between 2005 to 2016 in the Central Flyway division (Figure III.5B-M). The annual average width of the modeled migration pathways varied as much as 662 km in the northern portion and 392 km in the southern portion of the Central Flyway (Figure C.2A, D). The annual north to south shift of the centroids, compared to the 2002-2016 KDEM centroid (Figure III.4), varied as much as 143 km (between north and south extremes) in the northern area and 113 km in the southern area (Figure C.2B, E). The annual east to west centroid shift varied as much as 353 km in the northern area and 306 km in the southern area. The greatest observed annual centroid shift measured from the 2002-2016 KDEM centroid was an approximately 200 km westwards shift in the southern migratory pathway for 2015 (Figures III.5L, C.2F). With a single exception, no significant relationships were found between dimensional characteristics of the annual KDEMs and the areas of overwintering monarchs in Mexico for the same year (Figure C.3). The exception was a significant, but weak, correlation (r_s = 0.48, R^2 = 0.21; p = 0.0031) indicating the association of a western shift in the north centroid of the Central Flyway KDEM (Figure III.4) and a lower area of overwintering monarchs in Mexico (Figure C.3C).
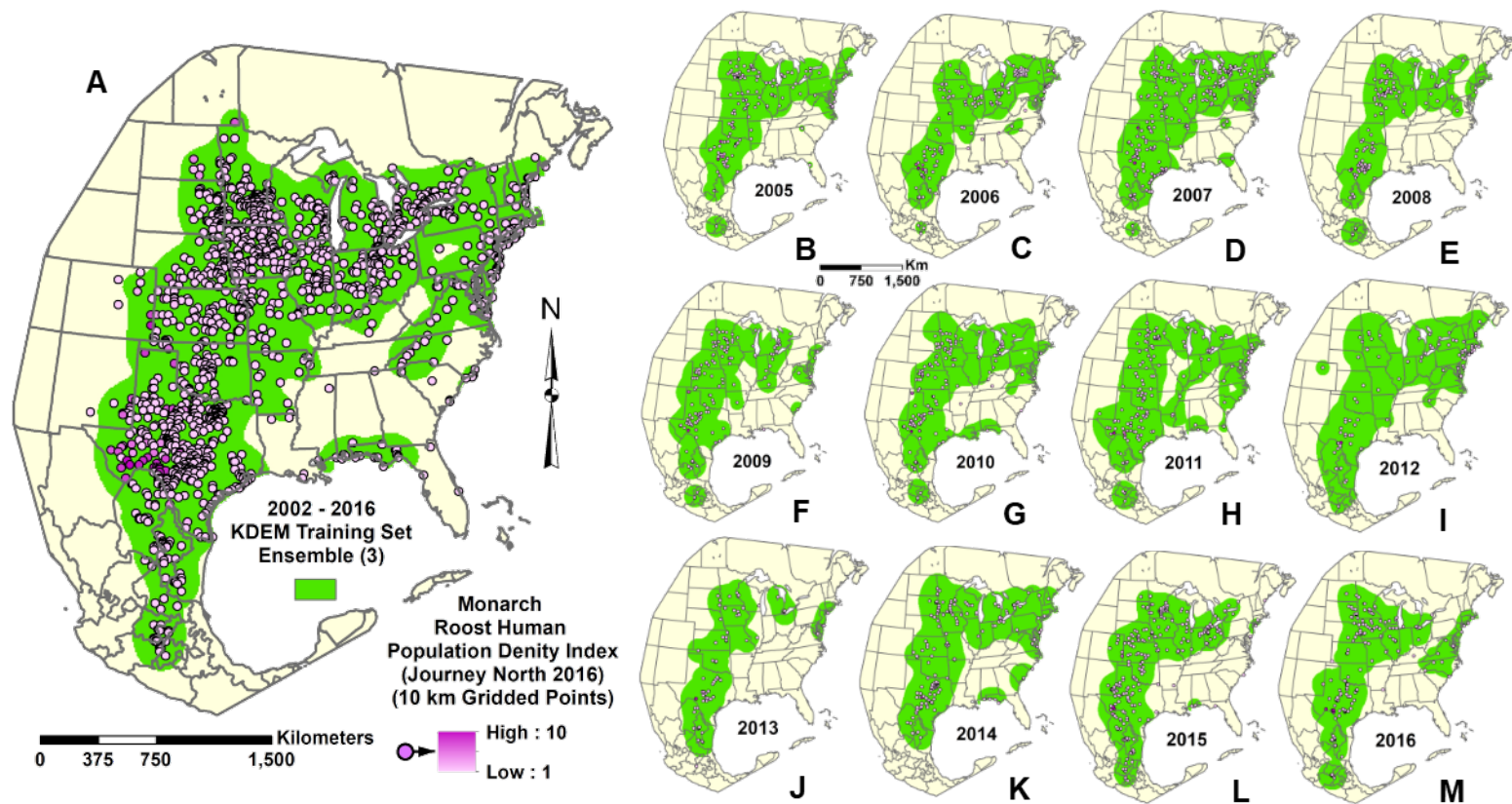
Figure III.5. Monarch fall migration pathway kernel density estimation models (KDEMs) from (A) 2002–2016 combined data, and (B–M) for each year from 2005 to 2016. Models represent minimum frequency consensus training set ensemble of three binary calibrated models developed from a three-fold training data partition.
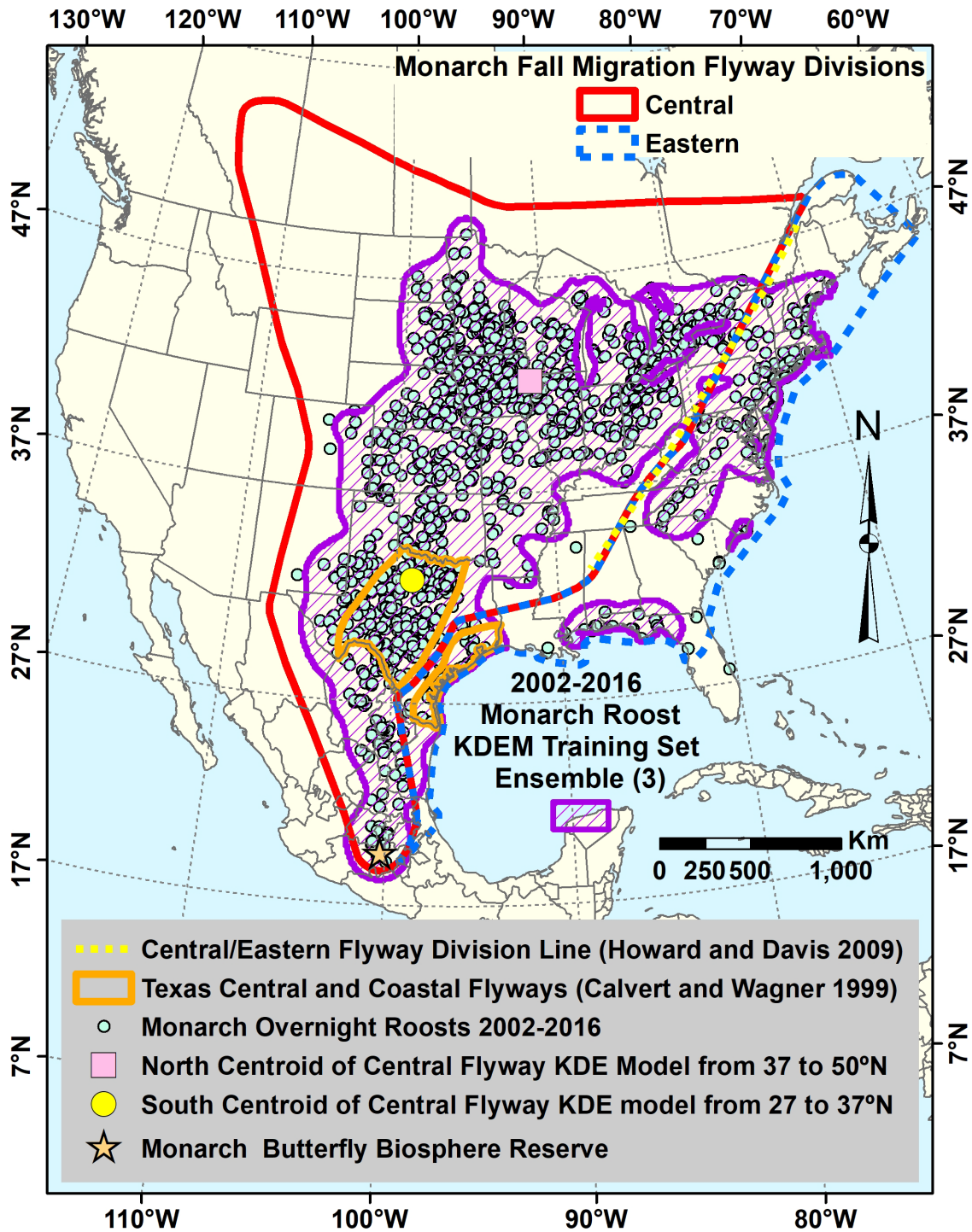
Figure III.6. Central and Eastern flyway division boundaries for fall migration of the eastern monarch population, including migration pathway of minimum consensus kernel density estimation model (KDEM) (from Figure III.5A), and north (37-50ºN) and south (27-37ºN) centroids for the KDEM in the Central Flyway (see Table C.4 for shapefiles).

Flyways and Core Migratory Pathways

Guided by the 100% consensus 2002-2016 KDEM, the boundary division between the Central Flyway and Eastern Flyway of Howard and Davis (2009) was extended to proceed southwest from Alabama to the border of eastern Texas (Figure III.6). Through Texas, the division boundary was continued by following a line bisecting the Central and Eastern (Coastal) Flyways, as identified by Calvert and Wagner (1999). The division boundary from the Texas border was extended towards the Monarch Butterfly Biosphere Reserve in Central Mexico by generally following the eastern boundary of roost records.

The 100% consensus 2002-2016 KDEM outlines a fairly broad migration pathway extending from the Great Lakes region to northeastern Mexico, and it includes portions of the Eastern Flyway (Figure III.3B). In contrast, the 100% consensus annual KDEM encompasses a narrower pathway that is primarily restricted to the Central Flyway division, with the exception of the Texas-Louisiana Coastal Plain (Figure III.3C). The narrower 100% consensus annual KDEM was used to define the core migratory pathway and guide the delineation of southern core migratory pathway funnels for each of the two flyway divisions (Figure III.3C). The Central Funnel was defined along the 100% consensus annual KDEM in the Central Flyway from Oklahoma to the Mexican overwintering sites. The Coastal Funnel was defined within the Eastern Flyway from southern Louisiana along the coastal region of Texas to Northeast Mexico where it was merged with the Central Funnel (Figure III.3C).

Anthropogenic Fall Migration Hazards

Several potential anthropogenic hazards to fall migrating monarchs were spatially identified along the core migration pathways. Five monarch roadkill hotspots were identified along the Central Funnel in Texas (Journey North, 2017) and Mexico (Correo Real, 2015; Rogelio
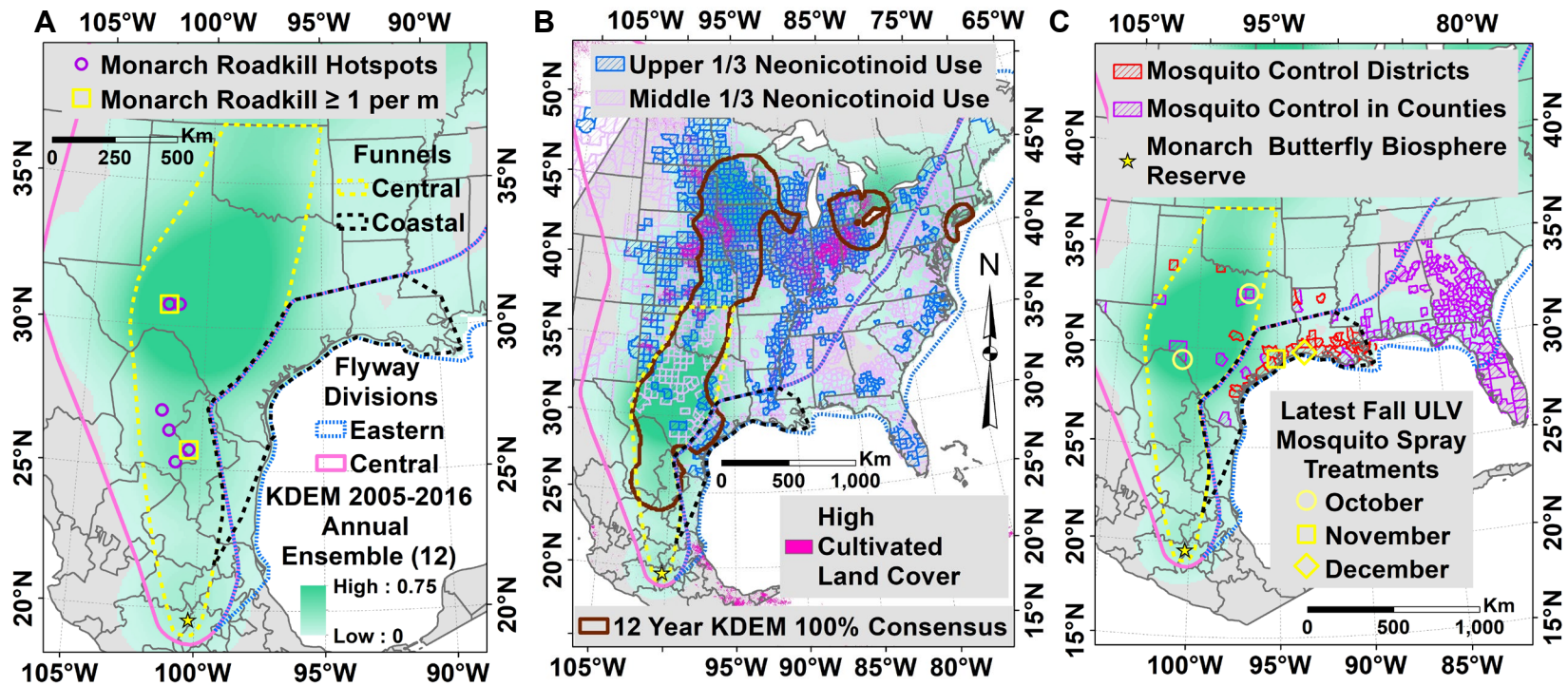
Figure III.7. Potential anthropogenic hazards spatially identified along the monarch fall migratory pathways: (A) monarch roadkill hotspots; (B) high cultivation land cover per 1 square kilometer, and upper and middle 1/3 level uses of neonicotinoids (imidacloprid, clothianidin, and thiamethoxam) in 2014 by US county; (C) counties in US with potential mosquito adulticide ultra-low volume (ULV) spray treatments in October-November (see Table C.4 for shapefiles).

79

Carrerra, Universidad Autonoma de Nuevo Leon, Nuevo Leon, Mexico, personal communication), including two sites with ≥ 1 roadkill monarchs per meter (Figure III.7A). Large areas of high cultivated land cover with potentially reduced nectar resources were mainly located within the northern portion of the Central Flyway, particularly in the Midwest (Figure III.7B). Smaller areas of concentrated agricultural lands occur along the northern and northwestern portions of the Central Funnel. The areas of highest neonicotinoid use that could contaminate nectar resources generally corresponded with the areas of high cultivation (Figure III.7B). Southeastern US counties with potential mosquito adulticide ultra-low volume (ULV) treatments that can extend into October and November are mostly concentrated along the coastal areas of the lower Eastern Flyway, including the Coastal Funnel, with scattered occurrence in the Central Funnel (Figure III.7C).

Discussion

Comparison of MaxEnt and Kernel Density Estimation Models

The combined analysis of spatially interpolative models, such as KDEMs, and niche models, such as MaxEnt, can be complementary in studying different aspects of migratory pathways. Similar to Bahn and McGill (2007), spatially interpolative models were found to perform with higher accuracy than niche models. Both the higher accuracy (AUC_{psa}) and complexity (AICc) of the KDEMs compared to MaxEnt models appears to be related to the sensitivity of the KDEMs to endogenous spatial patterns of migratory movement towards the overwintering sites (Figures III.2, 4). The KDEMs are probably also more sensitive to spatial patterns of observer bias from local human population densities, the effects of which were not completely removed. However, the boundaries of the KDEM migration pathways appears to be less influenced by this observer bias (Figure III.3A, B). Although the spatially interpolative

KDEMs might be expected to overfit the training data more than MaxEnt, there were no significant differences in model overfitting between KDEM and MaxEnt.

The KDEMs best identified the migration pathway through southern portions of the Eastern Flyway around the Florida panhandle and the southern portion of the Central Flyway in Mexico (Figure III.2). The 100% consensus KDEM projection of the monarch fall migration pathway in Mexico includes several ecoregions either mostly or entirely absent from the 100% consensus MaxEnt models, such as eastern portions of the Chihuahuan Desert and the Temperate Sierras near the overwintering sites (Figure III.2B). These ecoregions in the southern portion of the Central Flyway do not necessarily reflect the favorable environmental conditions present over most of the flyway, contributing to their poor representation in the MaxEnt projections. The ability of KDEMs to detect the endogenous directed movement pattern of monarchs approaching the Mexican overwintering locations leads to better projection of the migration pathway over most of Mexico compared to modeling of environmental suitability by MaxEnt. The isolated portions of the Eastern Flyway identified by KDEM (but not MaxEnt) probably also represent environmental conditions very different from the more strongly represented Central Flyway. Reduced availability of roosting data from Mexico and the Eastern Flyway may have also hampered the MaxEnt model performance in these regions. Consequently, the 100% consensus KDEMs were utilized for representing the general (Figures III.2B, 3B) and core (Figure III.3C) fall migration pathways for the eastern migratory population of the monarch butterfly. In contrast, the MaxEnt migration models best emphasize the correlation of large portions of the Central Flyway with grassland ecoregions that may provide a more stable source of nectar for migrating monarchs than more forested ecoregions to the east. The migratory pathways appear to

follow suitable habitat only in certain areas, only partly supporting the suggestion by Dingle and Drake (2007) that migratory pathways should correlate with suitable habitat.

Annual Kernel Density Estimation Model Migration Pathways

No significant inter-annual variation was found in the location and width of the migration pathway within the Central Flyway division as defined by the annual KDEMs (Figure III.5). Calvert and Wagner (1999) also observed variation in width and location of the migration pathway of the Central Flyway in Texas from 1993-1995. Although the data were too sparse for a similar analysis of the Eastern Flyway, there is likely some inter-annual variation in this flyway as well. Inter-annual variation in migratory pathways has been observed in a variety of species (Griffioen and Clarke, 2002; Cheke and Tratalos, 2007; Dingle and Drake, 2007). Despite year-to-year variation, a solid trend in species migratory pathways can usually be identified (Dingle and Drake, 2007). The 100% consensus annual KDEM (Figure III.3C) was the best representation of the narrower core migration pathway for most years through the Central Flyway division. The core pathway also includes a small portion of the Eastern Flyway division along the coastal prairie in Texas.

A west to east shift in the centroid of the annual migration pathway in the northern Central Flyway (Figure III.6), from central Iowa towards northwestern Illinois, was weakly but significantly associated with a larger area of overwintering roosts in Mexico (Figure C.3C). Recent studies have indicated that the Upper Midwest from eastern Colorado to Indiana that encompasses the region of this shift represents the source for a large proportion of the overwintering population (Flockhart et al., 2017). A west to east shift in the densities of roosts for the northern migration pathway may indicate an increased source population of migrating monarchs to the east. Further investigation is needed to confirm the significance of the observed weak correlation between larger

overwintering areas and an eastern shift in the northern migration pathway through the Central Flyway.

Flyways and Core Migratory Pathways

The KDEMs indicate the Central Flyway as the primary route of the fall monarch migration (Figures III.2B, III.3B-C, III.6). Few sites with regular fall accumulations and roosting currently exist in the Eastern Flyway (Garland and Davis, 2002). Howard and Davis (2009) hypothesized that smaller roost sizes in the southern portion of the Eastern Flyway may result in roosts being less noticed, leading to fewer reports from this area. Further studies of regional variations in roost densities across the two flyways are needed, especially for the Coastal Funnel in Mexico where data are totally lacking. The southern narrower Central Funnel and Coastal Funnel pathways (Figure III.3C) can serve to focus further research into conservation planning for the fall monarch migration.

Anthropogenic Fall Migration Hazards

Of the potential anthropogenic hazards spatially identified along the fall migration pathways, roadkill is the best-known for its potential impact on monarchs. McKenna et al. (2001) estimated that as many as 500,000 monarchs were killed statewide in Illinois within the first week of September 1999. However, they did not report hotspots of high monarch roadkill, such as has been observed in the Central Funnel. Monarch roadkill during the fall migration through the Central Funnel region could be greater than in Illinois. Collisions with other structures, such as wind turbines, could also contribute to fall monarch mortality, but has not been studied (Journey North 2018a). Residue from dead insects is common on wind turbine blades and known to lower turbine performance (Corten and Veldcamp, 2001; Dalili et al., 2009). The presence of wind turbines in the core migration pathways (USFWS, 2018; USGS, 2018) requires confirmation as a

potential hazard for fall migrating monarchs.

Potential habitat loss for nectar resources may be most severe where the highest concentrations of cultivated land cover are found in the Midwest and certain regions of the Central and Coastal funnels. These same areas have greater potential for nectar contamination with agricultural neonicotinoids. Risk of systemic pesticide contamination of monarch food resources may be greater during droughts and in arid areas, including much of the southern Central Funnel, where agricultural irrigation may provide attractive food resources, such as the nectar of field-bordering wildflowers or pecan aphid honeydew (Journey North, 2018b; Charles Allen, Texas A&M AgriLife Extension Service, San Angelo, Texas, personal communication). Although Krischik et al. (2015) identified no acute lethal effects of neonicotinoid contamination of nectar resources on adult monarchs, further research is needed to evaluate chronic and sublethal effects, including from potentially synergistically toxic combinations of systemic fungicides and neonicotinoids (e.g., Tsvetkov et al., 2017).

Adult mosquito control programs with ULV insecticide spraying are potentially active from October to November when monarchs migrate through much of the lower Eastern Flyway and Coastal Funnel, including some localized areas in the Central Funnel during the height of migration in October. Oberhauser et al. (2006) found high mortality among adult monarchs exposed to permethrin residues on plants treated with barrier hand sprayer treatments one day earlier. Mosquito truck ULV sprayer applications of resmethrin can also produce high mortality among adult monarchs caged within eight to 15 m downwind of the application (Oberhauser et al., 2009). Typical evening and night ULV treatments to reduce non-target impacts (Ginsberg et al., 2017) could still expose roosting monarchs, but vegetation cover can provide protection from direct contact with spray droplets (Peterson et al., 2016).

Implications for Conservation

Conservation efforts are needed to support monarch fall migrations. It is critical to focus habitat conservation and restoration in areas with the largest impact (Oberhauser et al., 2017). The MaxEnt model supports the importance of conserving nectar resources found in grassland habitats of the Great Plains, including throughout the Central Funnel of Oklahoma, and Texas. Brower et al. (2015) suggested that nectar sources of Texas and North Mexico are likely crucial for the fall migration (also see Inamine et al., 2016). The potential for changes in land cover and land use across the Central Funnel to impact nectar resources needs further investigation. Spatial risk assessment is needed to determine the degree of exposure to the identified potential anthropogenic hazards along the monarch core fall migration pathways. The current tendency of the Central Funnel to shift as much as 200 km in some years, especially towards the West, should also be considered in assessing annual variations in exposure of monarchs to certain hazards. The identified core migration pathways and potential hazards can provide a focus for both monarch habitat enhancement and hazard reduction in continued efforts to preserve the unique phenomenon of the eastern monarch fall migration.

Conclusion

The fundamentally different approaches of interpolative spatial point pattern KDEMs and correlative ecological niche models, such as MaxEnt, can provide valuable complementary our perspectives on animal migration pathways. Several novel applications of spatially interpolative KDEMs were made for identifying broad spatial patterns of migratory movement, revealing their value for modeling movement through areas that may be of low environmental suitability. Minimum consensus annual training subset ensemble KDEMs are useful for investigating yearly variability in migratory movement patterns, which can then be correlated with population

indices. Total (100%) consensus annual KDEM ensembles are effective in delineating narrower core migration pathways over several years. Correlative niche models can reveal the most environmentally suitable habitats along the migratory pathway. The combination of these approaches can facilitate spatially identifying migratory hazards, migratory risk assessments, and conservation planning for declining migratory species.

The benefits of utilizing the two migration modeling approaches were demonstrated in developing fall migration models for the eastern population of monarch butterflies. The KDEM was best suited in defining the entire fall migration pathway, including through arid scrubland habitat of probably low nectar plant suitability. The MaxEnt model best revealed the alignment of the migration pathway of the Central Flyway with nectar resources in the Great Plains grasslands. The overlap of the identified core monarch migration pathways with various potential anthropogenic hazards can help focus future conservation activities and risk assessments for the fall migration of the eastern North American population of monarchs (available shapefiles of core migration pathways and potential hazards are listed in Table C.4). The results of this study additionally affirm the high value of citizen science efforts, such as Journey North, in understanding the eastern monarch migration. Complementary approaches such as KDEMs and correlative niche modeling should be further explored for migration modeling of monarchs and other migratory animals of conservation concern.

CHAPTER IV

SPATIAL RISK ASSESSMENT OF EASTERN MONARCH BUTTERFLY ROAD

MORTALITY DURING AUTUMN MIGRATION WITHIN THE SOUTHERN CORRIDOR

Synopsis

Road mortality may contribute to the population decline of eastern monarch butterflies (*Danaus plexippus* L.). We estimated autumn monarch roadkill rates within the primary Oklahoma to Mexico southern migration corridor (i.e., Central Funnel). Dead monarchs were surveyed along Texas roadsides during four weeks of autumn migration in 2016 and 2017. Roadkill averaged 3.4 monarchs per 100 m transect, reaching 66 per 100 m in a roadkill hotspot in southwestern Texas. Extrapolations of Central Funnel roadkill based on survey data and road types ranged from 1.6 to 1.0 million in 2016 and 2017, respectively. Spatial distribution of roadkill across the Central Funnel was projected from Texas survey data using 30 m resolution MaxEnt niche models. Highest roadkill probability was linked to arid climate and low human population density. The latter variables may not be directly related to roadkill, but instead represent indirect correlates of increased densities of monarchs where the migration corridor narrows southwards. The higher roadkill projected in southwest Texas and Mexico by MaxEnt models agrees with previously reported monarch roadkill hotspots. MaxEnt-based 2016-2017 projections for annual roadkill rates throughout the Central Funnel averaged 1.4 million. This figure compares closely to 1.3 million by simple extrapolation, and represents about 2% of the overwintering monarch population for these years. Combining hotspot data with other data across the Central Funnel increases annual roadkill estimates to about 5-8 million. Mitigation at roadkill hotspots in the Central Funnel could reduce monarch roadkill mortality during migration and contribute towards conservation efforts for the monarch butterfly.

Introduction

Wildlife-vehicle collision is the most widely acknowledged impact of roads on wildlife, and can contribute to the decline of species of conservation concern (Tok et al., 2011; Visintin et al., 2016; Bennet, 2017), including globally declining pollinator insect species (Baxter-Gilbert et al., 2015). Roadkill can result in high mortality and lower abundance for species with large area requirements, pronounced migratory movements, small population sizes, and slow reproduction rates (Seiler and Helldin, 2006; Fahrig and Rytwinski, 2009). Wildlife-vehicle collisions are often spatially and temporally aggregated and substantial annual and inter-annual variation have been associated with environmental factors and traffic volume (Seiler and Helldin, 2006; Shilling and Waetjen, 2015). This tendency for high spatio-temporal variability in roadkill can be difficult to interpret based solely on the mapping of field survey data. Accordingly, there is a trend to use predictive spatial models to account for the variability in investigating the impacts of roads on wildlife mortality (Bennet, 2017). Typical roadkill niche models use a combination of environmental and anthropogenic variables, and are often restricted to small areas (Visintin et al., 2016). Species distribution modeling has previously been used to project roadkill risk of mammals (Grilo et al., 2009; Roger and Ramp, 2009; Visintin et al., 2016, 2017) and owls (Gomes et al., 2009). Spatial models for insect roadkill have not yet been developed.

Only five out of 215 roadkill studies (2%) between 2011 and 2015 were specifically focused on invertebrates (Bennet, 2017). Despite this taxonomic bias in the literature, insect roadkill may be a substantial threat to certain populations. Baxter-Gilbert et al. (2015) projected that hundreds of billions of pollinating insects are lost annually to roadkill across North America. Relatively few studies exist on butterfly road mortality, although researchers have suggested that butterflies are one of the most common insect orders killed by vehicles (McKenna et al., 2001;

Rao and Girish, 2007). Despite the high numbers of road-killed butterflies, the risk of Lepidopteran roadkill has been estimated as low to moderate (Baxter-Gilbert et al., 2015; Muñoz et al. 2015). Several studies have estimated butterfly roadkill numbers and examined contributing factors (Munguira and Thomas, 1992; McKenna et al., 2001; Ries et al., 2001; Rao and Girish, 2007; Skórka et al., 2013), but most of these studies concentrate on local, relatively sedentary butterfly populations and their utilization of roadside habitats rather than migratory butterflies. Migratory danaine butterflies (Nymphalidae: Danainae) appear to be especially susceptible to roadkill during migration, including the double-branded crow, *Euploea sylvester* (Fab.), in Taiwan (Her, 2008; Taiwan Environmental Protection Administration [EPA], 2010) and southern India (Santhosh and Basavarajappa, 2014), the common crow, *Euploea core* (Cramer), and the dark blue tiger, *Tirumala septentrionis* (Butler), in southern India (Santhosh and Basavarajappa, 2014), and the monarch butterfly, *Danaus plexippus* L., in the United States (McKenna et al., 2001) and Mexico (Correo Real, 2015).

Significant population decline of the eastern migratory monarch butterfly has been observed at the overwintering sites in Central Mexico during the past two decades (Vidal and Rendón-Salinas, 2014; Thogmartin et al., 2017). Consequently, the persistence of the migratory phenomenon of the eastern population may be endangered (Brower et al., 2012). The long-distance migration of monarchs is unique among butterflies. Mortality during the autumn migration (often referred to as fall migration) has been suggested as a contributing factor to the decline (Badgett and Davis, 2015; Ries et al., 2015; Inamine et al., 2016; Agrawal and Inamine, 2018). Road mortality may significantly affect monarch survival during migration, especially where monarchs become highly concentrated as the migration narrows in Texas and northern Mexico (Badgett and Davis, 2015). Only McKenna et al. (2001) have previously evaluated

monarch butterfly roadkill. They reported monarchs as the second-most killed butterfly species during six weeks of autumn in Illinois (McKenna et al., 2001). They estimated that more than 500,000 monarchs were killed statewide along interstate highways during one week in early September 1999. There are several unpublished citizen-science reports of locally high monarch roadkill occurrence in West Texas and northern Mexico during the autumn migration, with observed roadkill reaching 5.7 monarchs per meter near Monterrey, Mexico (Correo Real, 2015; Journey North, 2017). Incidences of high monarch road mortality in northern Mexico have led to the placement of road signs along portions of highways in Mexico to reduce speed in the presence of monarchs (Vanguardia, 2016).

Monarch roadkill has yet to be quantified in relation to an overall population estimate. Seiler and Helldin (2006) point out that any sustained mortality factor, such as roadkill, can be especially damaging for species that are either approaching or are in an annual population decline, such as the monarch. The extent of monarch roadkill needs to be assessed to estimate its potential contribution to the species population decline and support conservation planning. Our main goal was to develop MaxEnt niche models for monarch road mortality during the autumn migration within the main migration pathway in Texas. The MaxEnt algorithm has been employed before to spatially investigate vehicle-animal collisions of birds and mammals (Ha and Shilling, 2017). The roadkill models are also projected throughout the Central Funnel, which is the identified main southern autumn migratory pathway within the Central Flyway for monarchs from Oklahoma to Mexico (Tracy et al., 2018a). This study includes the first analysis of monarch roadkill data outside of Illinois, and the first development of a spatial roadkill model for an insect. Our specific objectives were to (1) conduct monarch roadkill field surveys within the Central Funnel in Texas, (2) develop MaxEnt niche models for roadkill within the Texas survey

area, and project these models throughout the Central Funnel, (3) estimate monarch roadkill numbers within the survey area and the Central Funnel using both simple field survey-based and model-based extrapolation techniques, and (4) discuss the results in the context of monarch conservation and potential applications to other species of conservation concern.

Methods

Study Species

The monarch autumn migration is uniquely accomplished by one generation. Adults begin migrating in late August to September from the summer breeding grounds, traveling to overwintering grounds in Central Mexico (Brower, 1995; Calvert and Wagner, 1999). Most migrants usually reach Oklahoma and North Texas in late September or early October (Calvert and Wagner, 1999; Monarch Watch, 2018a) and arrive at the overwintering grounds in November (Brower et al., 2006). There are two main migration routes, the Central Flyway and the Eastern or Coastal Flyway (Calvert and Wagner, 1999; Howard and Davis, 2009). The Central Flyway through the Great Plains is the most heavily traveled route (Howard and Davis, 2009), which narrows into the Central Funnel from Oklahoma southwards (Tracy et al., 2018a).

Autumn migrants fly during the day and stop at night and during inclement weather to nectar and colonially roost in trees and shrubs (Brower, 1996). These roosts may comprise a few to several thousand individuals and may last one to several days (Davis and Garland, 2004; Howard and Davis, 2009). In the morning, roosting monarchs either resume migration or search for nectar. These behaviors are influenced by wind patterns or lipid levels (Brower, 1996; Davis and Garland, 2004). During unfavorable northerly winds, monarchs may roost for several days (Schmidt-Koenig, 1985). Migrating monarchs are observed to nectar in a variety of locations, including in right-of-ways (Brower et al., 2006) where they may be vulnerable to vehicle

collisions. Brower et al. (2006) suggested that monarchs shift their behavior upon reaching Texas and spend more time nectaring to accumulate lipids for the winter and re-migration. Migrating monarchs regularly fly at high altitudes, around 300-500 m (Gibo and Pallett, 1979; Gibo, 1981; 1986), but may fly close to the ground, especially when facing headwinds or during overcast weather (Gibo, 1986; Brower, 1996), exposing them to road mortality. Citizen science observations also include reports of low flying fall migrating monarchs over roadways (Correo Real, 2015).

Monarch Roadkill Surveys and Simple Roadkill Extrapolation

Monarch roadkill field surveys were conducted within the region of the main autumn migration through the Central Funnel in Texas (Figure IV.1). Four four-day surveys were conducted in each of the autumns of 2016 and 2017, between 10th October to 4th November and 3-27 October, respectively. The survey area was divided into four north to south sections, with surveys timed to generally occur after the average peak migration (Journey, North 2017; Monarch Watch, 2018a) along each survey route to allow time for the accumulation of road-killed monarchs. Surveyed road types included (1) highways, (2) primary roads, and (3) secondary roads. Each survey location comprised at least a single 100 m by one m transect along the grassy edge of one side of the roadway. To assess if the side of the road surveyed influenced the number of dead monarchs, additional transects were surveyed across multiple edges of single and divided-lane highways at some sites. Transects were located using a handheld GPS device (accuracy up to ± 3m). Roadkill transects were spaced according to travel and survey time constraints at about 30 to 100 km intervals along the primarily east to west pre-planned survey routes, with additional surveys in 2016 in the southwestern portion of the study area where high monarch roadkill was found (Figure IV.1). All dead monarchs or parts of monarchs were
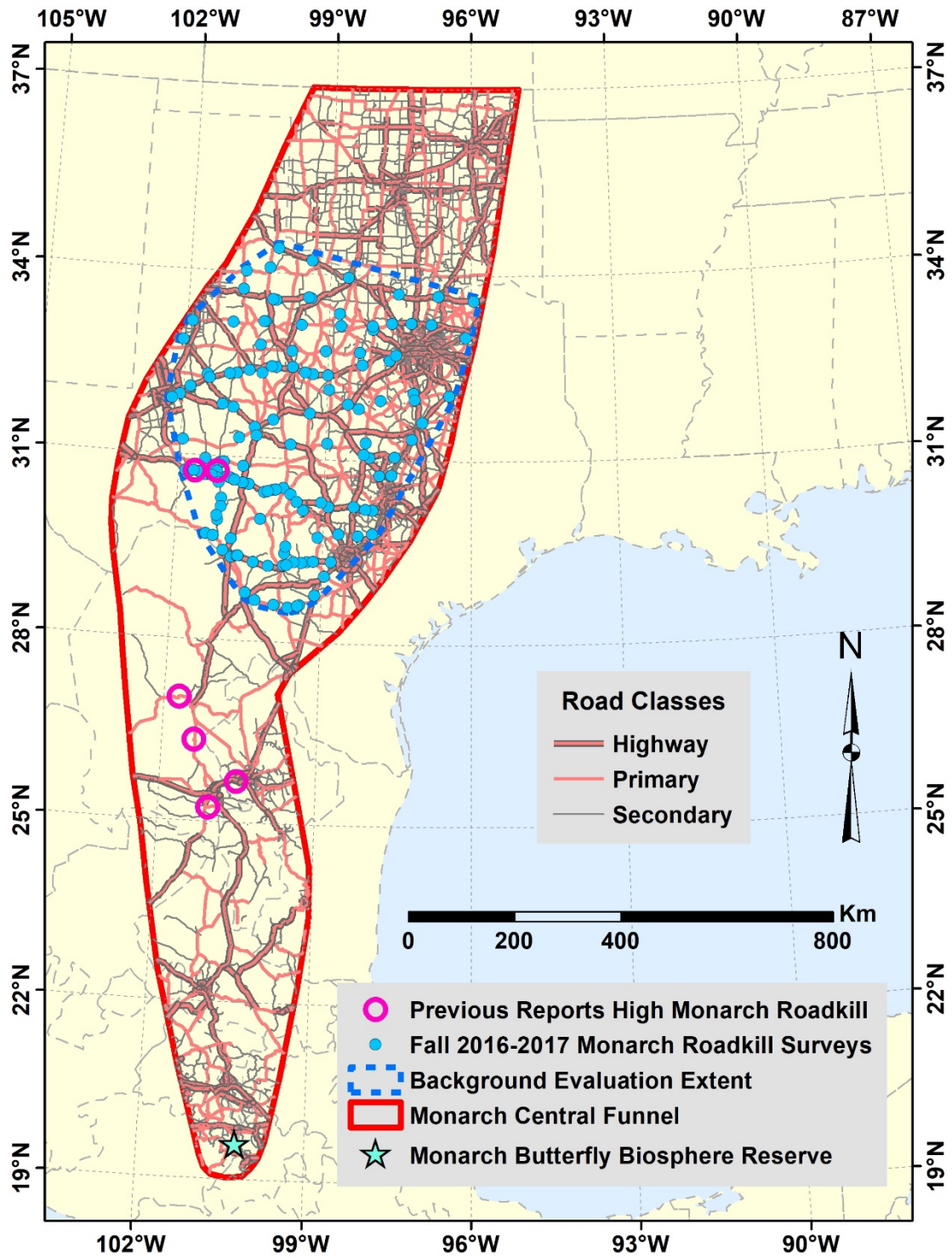
Figure IV.1. Monarch roadkill survey 100 m transects for autumn 2016 and 2017 along three major road classes within the monarch Central Funnel in Texas.

collected to estimate the total number and sex of dead monarchs along the transects. A similar spring monarch roadkill survey was conducted in Texas during April to May of 2017 (Figure D.1; for details, see Appendix D, Spring 2017 Texas Monarch Roadkill Survey). The boundary of the background evaluation extent for the roadkill study was defined by a 10 km buffer around a convex hull polygon formed using un-thinned 2016 to 2017 monarch roadkill survey locations within the Central Funnel (Figure IV.1). Mean roadkill counts for the three road types were extrapolated over the background evaluation extent and Central Funnel in a manner similar to that of McKenna et al. (2001). We estimated roadkill separately within the Sonora-Sheffield roadkill hotspot area, which was defined as the 95 km section of Interstate Highway (IH) 10 from Sonora to 24 km east of the Pecos River, including a portion of Texas state highway (SH) 163 extending from 7.6 km south of Ozona to 5 km north of Ozona and a 2 km section of SH-137 extending west from the junction with SH-163.

Environmental Variables

Thirty environmental variables were initially screened for use in the roadkill modeling (Table D.1, Figure D.2). These variables were selected for their value in previous roadkill niche models and for their use in characterizing the environment of the study area. The variables consisted of nine topographic indices (including four stream indices), eight land cover indices, six road indices, three human population indices, and four climatic indices. All indices were either calculated at 30.8 m spatial resolution or resampled with bilinear interpolation to the 30.8 m resolution, to match the resolution of the base layer of one arc second Shuttle Radar Topography Mission (SRTM) digital elevation model (DEM) data obtained from USGS Earth Explorer (https://earthexplorer.usgs.gov/). The high spatial resolution of 30.8 m facilitated

modeling of roadkill along individual surveyed roadways over a broad area (see more details in Appendix D, Environmental Variables).

Monarch Roadkill Models

Preliminary MaxEnt model runs indicated that there was not enough data from 2017 to obtain good accuracy statistics with single year models. Consequently, 2016 and 2017 roadkill presence data were combined and spatially thinned to 2 km to reduce spatial autocorrelation. Ten thousand background points were randomly generated within the road mask evaluation area. Background/presence versions of the area under the curve statistic (AUC_{bgp}) and true skill statistic (TSS_{bgp}) were calculated using R software (R Core Team, 2018) and the PresenceAbsence package (Freeman and Moisen, 2008). In the same manner, the presence/absence version of AUC (AUC_{pa}) and TSS (TSS_{pa}) was calculated using transects with no observed monarch roadkill as absence data, although roadkill may have occurred in these absence locations as well. The MaxEnt beta regularization value was adjusted to two and only quadratic and hinge features were used to reduce model complexity and overfitting for improving model generalization (Jiménez-Valverde et al., 2008; Warren and Seifert, 2011; Tracy et al., 2018b).

Roadway rasters served as a mask for analysis of environmental variables. The original set of 30 environmental variables was decreased to 20 variables. Nine variables were dropped which exhibited zero or negative testing gain of AUC_{bgp} from a MaxEnt threefold jackknife run (Table D.1, Figure D.3). Traffic volume was also dropped because data were not readily available for Mexico. Traffic volume was utilized in preliminary niche models for the background evaluation extent. Preliminary runs indicated that no substantial gain in model performance was achieved with more than 10 of the 20 variables, and that employing fewer

variables (three) substantially increased undesired high spatial variability in roadkill among models. Consequently, final MaxEnt roadkill models were developed from ten random sets of ten of the 20 variables to represent model variability due to variable selection. The absolute Spearman rank correlation of variables within random variable sets was limited to less than 0.7 using the multiple randomized sequential forward selection procedure within the random subset feature selection algorithm (RSFSA) of Tracy et al. (2018b; data were lacking to obtain improved model performance from us of the entire RSFSA). The final MaxEnt models were calibrated to binary presence/absence format using a threshold of maximum TSS_{pa} (Liu et al., 2013a), and combined using frequency consensus to form a feature subset ensemble. Presence/absence niche models were developed for monarch roadkill using linear and quadratic binomial logistic regression with the R Glmnet package (Friedman et al., 2010) for the same ten random sets of ten of 20 variables. These presence/absence models produced lower AUC_{bgp} values and similar AUC_{pa} values compared to MaxEnt models, and these models were not investigated further (results not shown).

Results

Monarch Roadkill Survey and Simple Roadkill Extrapolation

A total 16.1 km of roadsides (161 100 m transects), 8.8 km in 2016 and 7.3 km was surveyed in 2017. Surveys revealed 581 dead monarchs in 59 locations (102 absence locations), for an average of 3.4 monarchs per transect. A total of 546 dead monarchs in 2016 and 35 in 2017 were recorded. Of the 546 monarchs in 2016, 501 (92%) were located along or near Interstate 10 between Sonora and Sheffield (24 transects) (Figure IV.2). In addition, 466 (93%) of the dead monarchs occurred in 14 transects ranging from ten to 66 per 100 m (Figure D.4). Most of the transects with high numbers occurred along IH-10, but one high count (21/100 m)

96
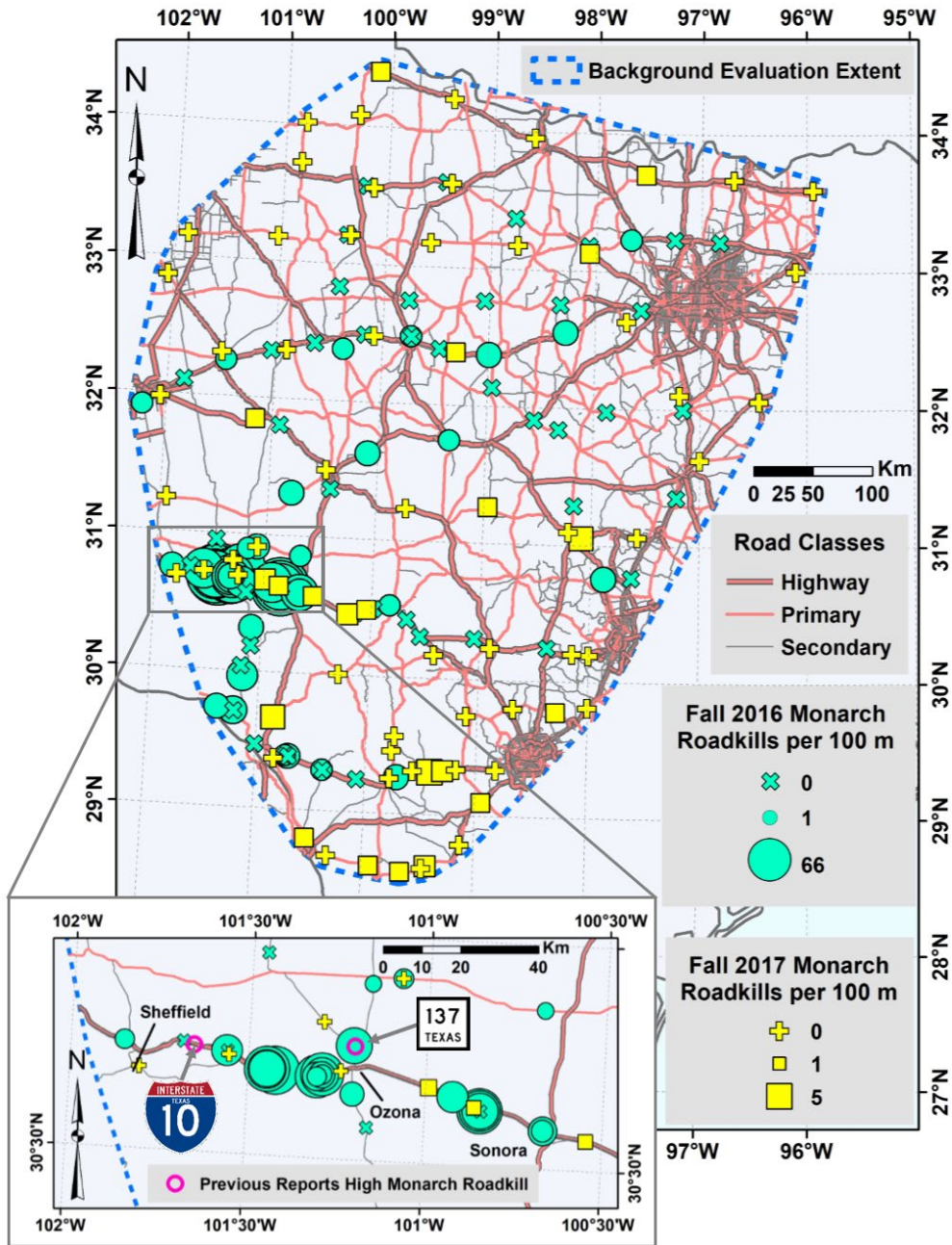
Figure IV.2. Monarch roadkill autumn 2016 and 2017 survey results for 100 m transects along major road classes within the background evaluation extent in the monarch Central Funnel in Texas, including previously reported locations of high monarch roadkill.

occurred along Texas Highway 37, around four km north of IH-10 at Ozona (for survey count data, see Appendix D, Texas Monarch Roadkill Survey Data). A total of 257 monarchs were sexed in 2016-2017, of which ca. 38% were female (n=98). The portion of females was 41% in 2016 (132 males, 91 females) and 21% in 2017 (27 males, 7 females). After the 2 km spatial thinning, the field survey data consisted of 151 transects (53 presence and 98 absence) and 249 individual dead monarchs. These thinned data were used in all further analyses. Only two road-killed male monarchs were found among 54 transects in the spring 2017 roadkill survey (Figure D.1).

Southern edges of roadsides contained 43.8% (± 36%, n = 13) of the roadkill found in the northernmost edge for both single and divided-lane roads. This relationship was used to estimate roadkill across all two or four edges per roadway when extrapolating roadkill per km (for details, see Appendix D, Texas Monarch Roadkill Survey Data and MaxEnt Roadkill Extrapolations). Estimated roadkill ranged from 6.15 to 645 monarchs per km depending on year, road type and location in relation to the hotspot area (Table IV.1). Estimated roadkill rates based on densities along different road types and separately analyzing the area defined as a hotspot, ranged from about 1.6 million to 1 million monarchs in 2016 and 2017, respectively. When hotspot data was merged with other data in calculating roadkill rates throughout the study area, the estimated roadkill in 2016 rose to over 8 million (Table IV.1). In 2016, about 49% of the roadkill within the Central Funnel was projected to occur within the Texas background evaluation extent, of which 5% was projected to occur in the Sonora-Sheffield hotspot area. In 2017, only about 0.3% of the roadkill within the Central Funnel was projected within the hotspot area, and the percent roadkill in the background area ranged from 31% when hotspot data was analyzed separately to 48% when hotspot data was merged with other data (Table IV.1).

Table IV.1. Monarch butterfly roadkill estimates for 2016 to 2017 over the Sonora-Sheffield roadkill hotspot, background evaluation extent (BEE) and the Central Funnel (Fig. IV.1) extrapolated from the field data per road type.

| | Length (km) | | | Roadkill per km[a] | | | Monarch Road Mortality[b] | | | | |
| | | | | | BEE/Central Funnel | | Hotspot Data Separated | | | Hotspot Data Merged | |
Road Type	Sonora-Sheffield Hotspot	BEE	Central Funnel	Sonora-Sheffield Hotspot	Hotspot Data Separated	Hotspot Data Merged	Sonora-Sheffield Hotspot	BEE	Central Funnel	BEE	Central Funnel
2016											
Highway	95	8,907	18,617	645.38	12.64	269.15	61,272	172,630	295,345	2,397,310	5,010,969
Primary	0	11,878	25,918	-	10.75	10.75	-	127,636	278,498	127,636	278,498
Secondary	28	17,705	38,169	442.56	25.79	85.32	12,312	468,135	995,804	1,510,687	3,256,740
Total (% Over-wintering Pop.)[c]							73,584 (0.09%)	768,401 (0.90%)	1,569,647 (1.82%)	4,035,633 (4.55%)	8,546,208 (9.17%)
% Funnel Mortality							4.69%	48.95%		47.22%	
2017											
Highway	95	8,907	18,617	52.78	31.67	36.54	5,011	284,077	591,606	325,469	680,310
Primary	0	11,878	25,918	-	8.32	8.32	-	98,857	215,702	98,857	215,702
Secondary	28	17,705	38,169	-	6.15	6.15	-	108,936	234,845	108,936	234,845
Total (% Over-wintering Pop.)[c]							5,011 (0.01%)	491,871 (0.79%)	1,042,154 (1.67%)	533,262 (0.86%)	1,130,858 (1.81%)
% Funnel Mortality							0.32%	31.34%		47.16%	
2016-2017											
Highway	95	8,907	18,617	584.96	18.58	208.67	55,536	219,3.2	396,772	1,858,631	3,884,998
Primary	0	11,878	25,918	-	9.42	9.42	-	111,828	244,005	111,828	244,005
Secondary	28	17,705	38,169	71.26	12.88	37.11	1,231	229,097	493,752	657,088	1,416,550
Total (% Over-wintering Pop.)[c]							53,518 (0.09%)	561,227 (0.91%)	1,137,529 (1.82%)	2,627,547 (4.10%)	5,545,553 (8.28%)
% Funnel Mortality							3.66%	35.75%		30.75%	

[a]The mean roadkill rates are calculated from data in the Central Funnel and incorporate estimates for all road edges (see Appendix D, Texas Monarch Roadkill Survey Data and MaxEnt Roadkill Extrapolations).

[b]Based on multiplying length of road type by roadkill density per km for road type.

[c]Based on 84.61 and 61.4 million monarchs overwintering in 2016 and 2017, respectively (Monarch Watch 2018b). Estimated from 21 million monarchs per hectares overwintering (Thogmartin et al. 2017).

Monarch Roadkill Model

The feature subset ensemble of ten MaxEnt roadkill niche models provided excellent discrimination of roadkill presence locations from background locations within the background evaluation extent, with AUC_{bgp} values ranging from 0.82 to 0.88 (0.86 ± 0.02, mean ± SD). The models provided marginally poor discrimination of roadkill presences from absences observed in the field, with AUC_{pa} values ranging from 0.60 to 0.67 (0.64 ± 0.02, mean ± SD). Among the top eight variables with the highest permutation importance in the MaxEnt models (Table IV.2), were three human population density indices and two climatic indices. Other top ranked variables included elevation, road density over a three km radius, and percent cover of artificial surfaces within a 500 m radius. Traffic volume ranked third in permutation importance in preliminary models, but it was not available for Mexico, precluding its use in the final models.

The MaxEnt response curves for population density indices all indicated that lower human population densities had higher association with monarch roadkill (Figure IV.3 A, E). The climatic indices indicated that roadkill was associated with more arid climates (Figure IV.3 B, C). Lower road densities and lower percent cover of artificial surface were also associated with higher monarch roadkill (Figure IV.3 F, G). The response curve for traffic volume, which was not used in the final models, indicated that the highest roadkill was associated with lower traffic volume. The traffic volume response curve was very similar to that of percent cover of artificial surface (Figure IV.3 G, H), with which it was moderately correlated ($r_s = 0.58$).

The proportion of MaxEnt models projecting monarch roadkill generally increased from northeast to southwest within both the background evaluation extent and Central Funnel (Figure IV.4; see Appendix D, MaxEnt Roadkill Consensus Model for shapefile of MaxEnt

Table IV.2. MaxEnt model variable permutation importance for 19 variables used in ten random sets of ten of the 20 variables in monarch roadkill models.

Variable[a]	Abbreviation	Permutation Importance[b], Mean ± SD
Human population density per km in 9 km radius	*popden9kr*	44.2 ± 3.8 (3)
Autumn quarterly mean monthly AETT/PETH × 1000	*etrt_autq*	41.7 ± 23.3 (2)
Annual mean monthly rainfall (P) (mm)	*prec_ann*	36.4 ± 15.6 (4)
Human population density per km in 3 km radius	*popden3kr*	30.1 ± 0.0 (1)
Elevation	*elev*	27.9 ± 5.5 (4)
Distance to urban areas ≥ 300 humans per km	*urbdist*	27.1 ± 10.8 (4)
Road density, km road per 3 km radius	*roadden3kr*	19.6 ± 2.4 (2)
Artificial surfaces	*artsur_500mr*	13.4 ± 3.2 (3)
Autumn quarterly mean monthly maximum temperature	*tmax_autq*	10.5 ± 9.8 (3)
Distance to highways	*hwydist*	10.4 ± 2.5 (7)
Latitude	*latitude*	6.4 ± 4.3 (3)
Grasslands	*grslnd_500mr*	5.6 ± 3.4 (9)
Autumn mean quarterly wind speed (m/second)	*wndsp_autq*	5.6 ± 5.4 (4)
Distance to secondary roads	*secrddist*	5.1 ± 2.9 (8)
Shrublands	*shrub_500mr*	4.5 ± 3.4 (9)
Distance to primary roads	*primrddist*	2.3 ± 3.0 (4)
Road density, km road per 500 m radius	*roadden500mr*	2.2 ± 3.8 (5)
Distance to High Flow Accumulation Areas (>60,000)	*strmhiflodist*	1.2 ± 1.0 (5)
Topographic Position Index (TPI), 3 km radius	*tpi3kr*	1.0 ± 0.2 (5)
Cultivated land	*cult_500mr*	0.0 ± 0.0 (0)[c]

[a] See Table D.1 for sources of variables. Variables ordered from highest to lowest mean permutation importance.
[b] Permutation importance of the variable in the MaxEnt models, number of models in which the variable was used out of the 10 random models in parentheses.
[c] Cultivated land layer was initially included in all 10 random models, but it was not included by MaxEnt in calculating any of the models.
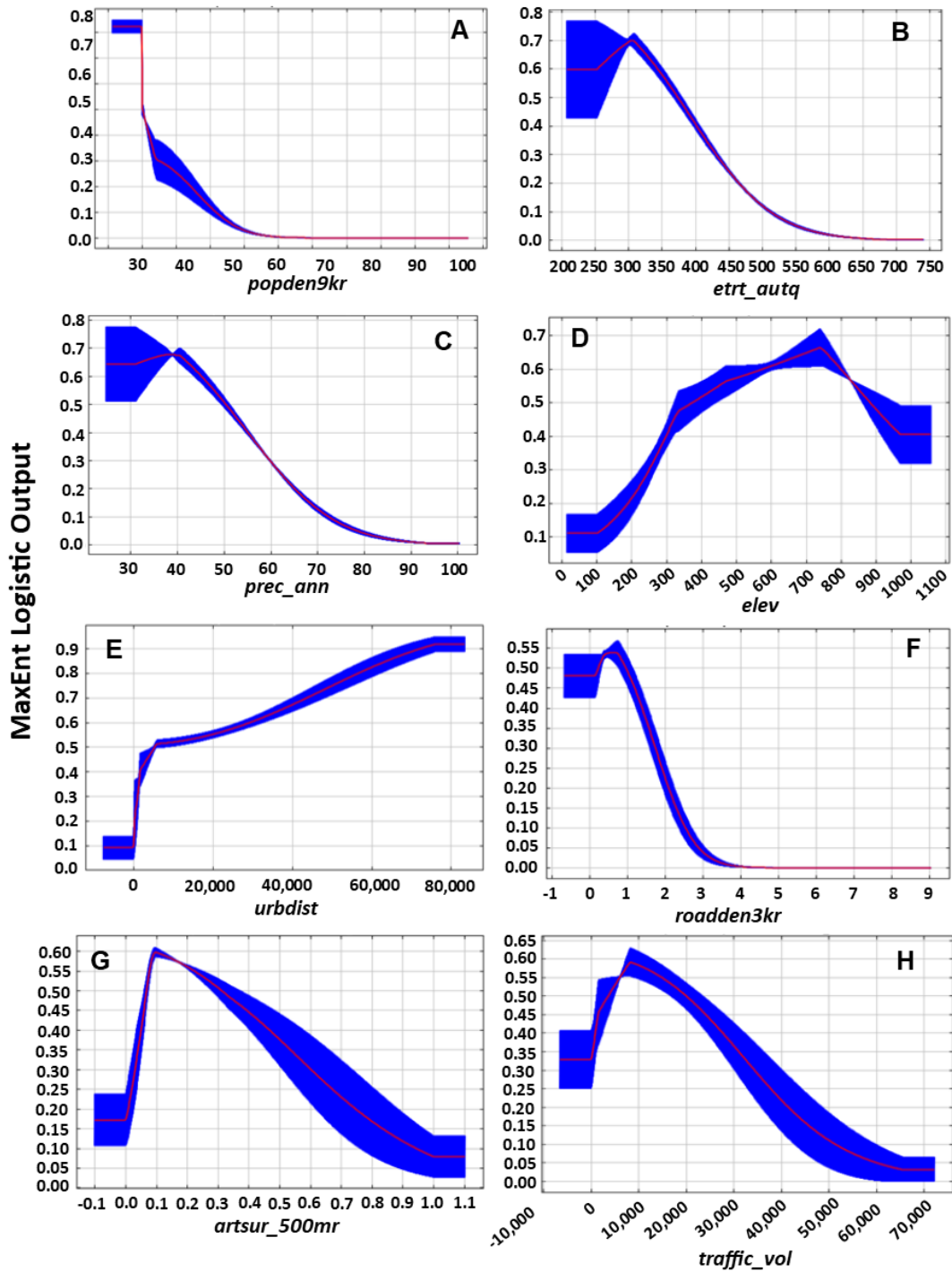
Figure IV.3. MaxEnt variable response curves (logistic output probability of presence vs. variable) representative of the final ten models (A–G) and for a 30-variable model (H): (A) popden9kr, (B) etrt_autq, (C) prec_ann, (D) elev, (E) urbdist, (F) roadden3kr, (G) artsur_500mr, (H) traffic_vol (traffic volume for 2015) (see Table IV.2 for abbreviations and permutation importance).
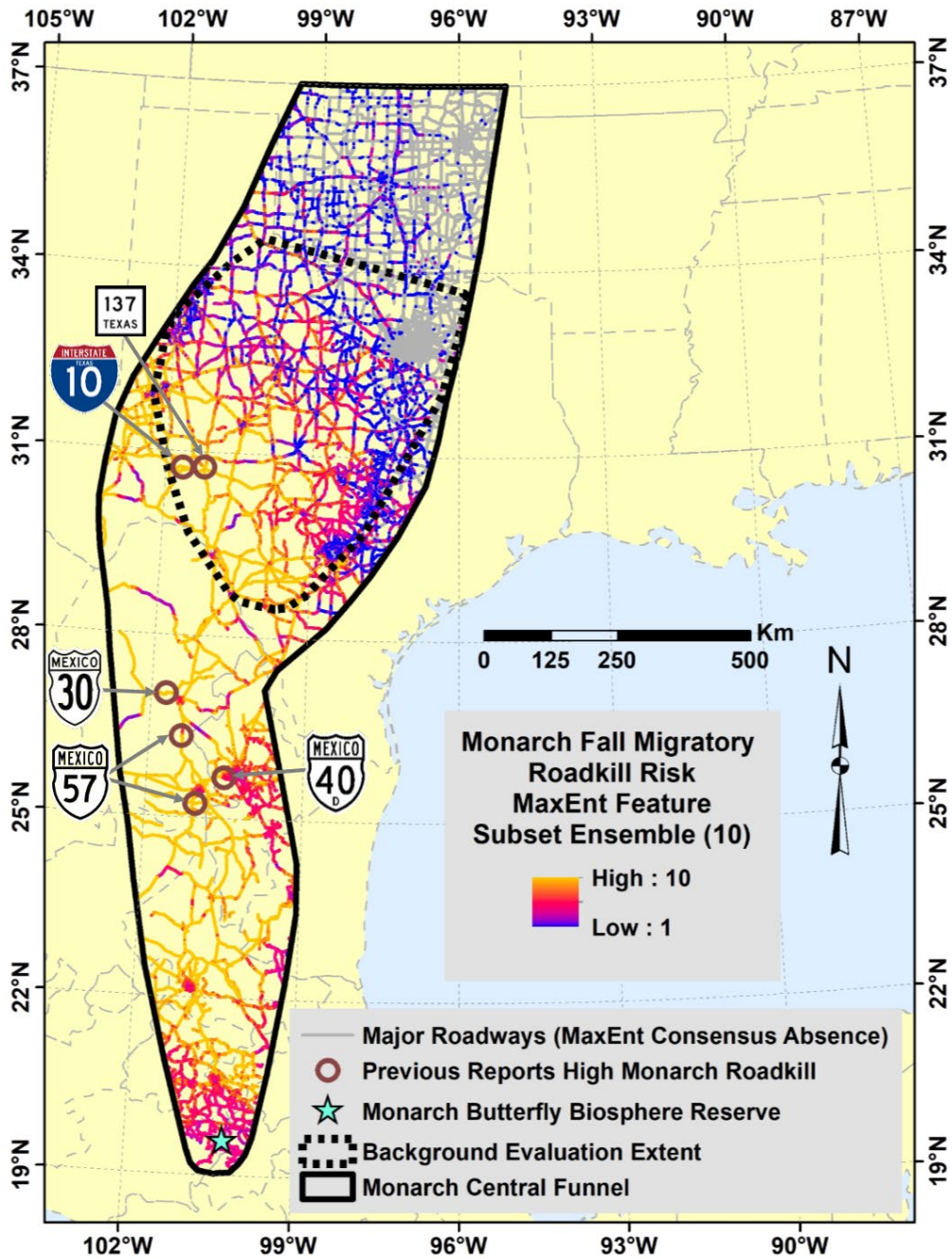
Figure IV.4. MaxEnt frequency consensus for feature subset ensemble of ten models developed from random subsets of ten of 20 variables correlated less than 0.7 (see Appendix D, MaxEnt Roadkill Consensus Model for zipped shapefile of MaxEnt consensus model).

consensus model). The highest number of models projected roadkill within much of southwest Texas and Mexico in the Central Funnel. None of the MaxEnt models projected monarch roadkill over most of the northeastern Central Funnel, including the Dallas/Fort Worth metroplex and most of eastern Oklahoma.

The average annual roadkill rates per km across each year and both years combined for each of the ten MaxEnt models were calculated based on lengths of each road type with predicted presence and location in relation to the hotspot (for details, see Appendix D, Texas Monarch Roadkill Survey Data and MaxEnt Roadkill Extrapolations). Extrapolating roadkill rates across the Central Funnel, an average of 1.3 ± 0.3 and 1.6 ± 0.4 million (mean $\pm$ SD) road-killed monarchs were estimated for 2016 and 2017, respectively (Table D.2). Combining roadkill data across both years for the Central Funnel yielded annual roadkill rates of 1.2 ± 0.5 million with hotspot data considered separately, and 4.8 ± 1.0 million with hotspot data merged with other data (Table D.3). The mean projected percentage of road-killed monarchs in the Central Funnel that occurred within the background evaluation extent ranged from 54% to 50% in 2016 and 2017, respectively (Table D.2).

Discussion

Monarch Roadkill Survey and Simple Roadkill Extrapolation

In the 2016 autumn roadkill survey (but not 2017), high monarch roadkill was found along an area corresponding to the only two previous citizen-science (Figure IV.2). It is unclear why hotspots have occurred in this area. The high roadkill may be partly related to higher densities of migrating monarchs in more southern areas of the Central Funnel. In addition, local stochastic weather events probably influence the occurrence of roadkill hotspots, such as

unfavorable winds that may induce lower monarch flight patterns or extended roosting and nectaring behavior close to the ground in the vicinity of roadways.

Observed monarch roadkill densities most likely represent accumulations of dead migrating monarchs over a period of one or two days to a few weeks during the main migration pulse through an area (Munguira and Thomas, 1992). Overall roadkill rates varied from 11 to 646 dead monarchs per km depending on year, road type, and location within the Sonora-Sheffield hotspot (Table IV.1). Previously reported general butterfly roadkill rates range from 0.45 to 80 per km per day in North America, Asia, and Europe (Rao and Girish, 2007; De la Puente et al., 2008; Yamada et al., 2010; Skórka et al., 2013; Baxter-Gilbert et al., 2015), and those for monarchs range from 1.3 to 11.9 butterflies per km per week in Illinois (McKenna et al., 2001) to 115 butterflies per 20 m (575/100 m) along toll highway 40D southwest of Monterrey, Mexico in October 2015 (Correo Real, 2015). Several other independent October 2015 surveys along a 27 km stretch of this same road yielded an average of 10 roadkill per 4 m (2.5 roadkill per m) which could extend to 2,500 roadkill per km (Correo Real, 2015; for data, see Appendix D, Correo Real Roadkill Report). Roadkill at this Monterrey hotspot could quickly add to over 67,500 dead monarchs per 27 km over one side of the road, and more detailed surveys are urgently needed along this and other hotspots in Mexico. The observed variation in monarch roadkill rates between the two years of this survey is common for roadkill studies (Seiler and Helldin, 2006). It is not clear how frequently roadkill hotspots occur in this region, and it is possible that one or both years represent an outlier.

About 38% of the dead monarchs in the autumn field surveys were females, ranging from 21% in 2017 to 41% in 2016. These figures generally match two separate citizen science observations on the percentage of female monarch roadkill in Mexico of 27% and 36% in

October 2015 (Correo Real, 2015) and are within the range reported from other roadkill studies (
(McKenna et al. 2001), as well as studies of sex ratios during migration (Borland et al., 2004) or
on the overwintering grounds (Steffy 2015). Davis and Rendón-Salinas (2010) found a
decreasing trend (~10%) in percent female monarchs at the Mexican overwintering sites from
1976–2008 (but see Beall, 1946), which they suggested could reflect female biased mortality
produced by the protozoan parasite *Ophryocystis elektroscirrha*.

Estimates of monarch roadkill in this study are likely conservative given the narrow
width of transects (1 m) and difficulty of observing dead monarchs or parts of monarchs in
roadside vegetation. Roadkill estimates are expected to be conservative for a variety of reasons,
such as other species modifying the distribution and abundance of dead butterflies (McKenna et
al., 2001; Seiler and Helldin, 2006) or weather conditions influencing carcass persistence.
Munguira and Thomas (1992) placed butterfly specimens on roadsides and found that only one
of their 50 specimens disappeared during two weeks (daily loss rate of 0.15%), suggesting
persistence may not be an issue, at least under some circumstances.

Monarch Roadkill Models

Roadkill Projections

Most of the MaxEnt models projected monarch roadkill from the southwestern portion of
the Central Funnel from West Texas to Mexico (Figure IV.4). The MaxEnt consensus projection
agrees with all seven of the previously known citizen science reports of monarch roadkill
hotspots in North America (Figure IV.4), including two hotspots in West Texas (Journey North,
2017) and five hotspots in northern Mexico (Correo Real, 2015; Rogelio Carrerra, Universidad
Autonoma de Nuevo Leon, Nuevo Leon, Mexico, personal communication).

MaxEnt-based roadkill estimates for monarch mortality ranged from 1.3 to 1.6 million throughout the Central Funnel for 2016 and 2017, respectively. These MaxEnt roadkill estimates were similar to the estimates based on simple roadkill extrapolation by road type when hotspot data was analyzed separately for the two years of field surveys (1.6 and 1 million). Most of the roadkill projected by MaxEnt models outside of the study area occurred in Mexico, indicating that more MaxEnt models are projecting roadkill along the sparser road network within the Central Funnel over northern and central Mexico, which is evident in the MaxEnt consensus model (Figure IV.4). As the autumn migration pathway narrows in the South, the migrating monarchs become more concentrated in the Central Funnel. This higher concentration may contribute to higher roadkill densities in the southern parts of the Central Funnel in Mexico, where most previous reports of monarch roadkill hotspots have originated (Figure IV.4). Although the models project some increased southward mortality risk, the extent of this risk in Mexico could be underestimated based on previous reports of roadkill hotspots. The extrapolations combining hotspot data with other roadkill data and projecting higher annual roadkill of around 5-8 million in the Central Funnel may be more realistic considering the probability of multiple roadkill hotspots in Mexico of higher density than seen in Texas. The MaxEnt models project little to no roadkill in the Northeastern part of the funnel area, including the Dallas/Fort Worth area and eastern Oklahoma. However, some roadkill likely does occur in this area, but possibly at a lower rate than in the more southern areas of the Central Funnel. Further research and field surveys are needed to verify roadkill rates outside of the survey area in the southern and northern parts of the Central Funnel. Additional data may allow effective use of roadkill density models, rather than presence only MaxEnt models used in this study. Roadkill

density models can better reveal regional roadkill patterns useful in refining projections, especially for northern Mexico where roadkill could be much higher than in Texas.

Factors Affecting Roadkill

MaxEnt projections of monarch roadkill within the Central Funnel were generally associated with more arid climate and less densely populated areas (Figure IV.3). These conditions generally describe those for the seven previous monarch roadkill hotspots reported from Texas and Mexico, with the possible exception of the roadkill hotspot in the vicinity of Monterrey, Mexico (Figure IV.4). This could be related to a variety of factors. For example, autumn migrating monarchs have been observed to spend additional time flying lower to the ground during the afternoon in desert areas, perhaps to seek shelter from the heat or find nectar (Journey North, 2018c). Monarchs may need to spend more time searching for nectar in arid environments, although this has not been evaluated. Finally, the increased roadkill rates may simply reflect the increased number of monarchs in more southern areas of the Central Funnel. This locality factor cannot be associated with most of the predictors, except latitude, but may be the most important explanation. Local climate, weather patterns, and geography affect monarch movement and behavior and are likely important contributors to road mortality. Wind patterns (direction, duration, and speed) may be more important than anthropogenic factors, but short-term weather events could not incorporated in the models.

Traffic volume has been noted as one of the most important variables in previous roadkill studies (Bennet, 2017). Traffic volume ranked high in importance in preliminary roadkill models, but model accuracy (AUC) was not significantly affected by its removal. Other variables that were correlated with traffic volume likely compensated for its absence, including human population density, artificial surface cover, distance to urban areas, and road density. In models

including traffic volume, the highest roadkill was associated with fairly low average annual daily traffic (AADT) values, similar to the study by McKenna et al. (2001). In general, higher roadkill has been associated with higher traffic volume due to increased probability of vehicle collisions (Seiler and Helldin, 2006; Skórka et al., 2013). Samways (1994) suggested that roads with high traffic volume serve as corridors for high butterfly mortality. In this study, low traffic volume, along with related anthropogenic variables, is correlated with locations of monarch roadkill hotspots, but may not be directly related to the road mortality. As the human population grows, traffic volume should increase in the lower traffic volume monarch roadkill hotspot areas, likely leading to higher roadkill rates (Bennet, 2017).

Spatial and Temporal Variation

The timing of our field surveys relative to peak migration may have varied among transect locations and years, which could have influenced our results. If peak migration occurred after our field surveys in one or both years, we may have underestimated roadkill numbers. For example, in 2017, the autumn migration was later than usual due to unusually hot summer (Agrawal and Inamine, 2018). Few other studies have identified roadkill hotspots for butterflies (but see Samways, 1994; Her, 2008). Monarch roadkill hotspots may vary from year to year and may be difficult to locate or may not occur in some years. These roadkill hotspots most likely result from unpredictable stochastic weather patterns, such as heavy winds occurring where clusters of migrating monarchs are crossing roadways.

Much higher monarch road mortality was observed during the autumn migration than in the spring (Figure D.1), indicating that seasonality is a factor contributing to monarch roadkill rates. However, the monarch spring migration is more spatio-temporally dispersed making comparisons difficult. Temporal variability can occur between years, within the migration phase,

or even within a day. For example, monarch behavior, such as flying low in the mornings (McKenna et al., 2001), probably affects the risk of roadkill at different times of day. Temporal patterns affecting monarch roadkill should be investigated further. Other sampling methods may be effective in detecting additional roadkill hotspots, such as adaptive cluster sampling (ACS), which was developed for inventorying scattered and clustered phenomena (Thompson, 1990). More frequent samples in a given location can also be critical for detecting roadkill hotspots (Santos et al., 2015).

Implications and Impacts in Relation to Monarch Conservation

Autumn Migration Mortality

Butterfly roadkill is a density independent mortality factor (Rodewald and Gehrt, 2014) with the incidence of roadkill being subject to high variability. Consequently, roadkill percentage of the migrating population is very unpredictable in any given year. The annual percentage of migrating monarchs subject to road mortality in the Central Funnel was conservatively estimated by dividing a roadkill estimate by the combined overwintering populations and roadkill estimate (overwintering cohort). The size of the overwintering populations is calculated by multiplying the hectares of roosting monarchs at the Mexican overwintering sites from Rendón-Salinas et al. (2018) by the value of 21.1 million monarchs per ha suggested by Thogmartin et al. (2017). Based on these amounts, the estimated annual roadkill rates from our MaxEnt models in the Central Funnel represent from 2.1 to 2.5% (1.3 to 1.6 million) of the overwintering cohort for 2016 and 2017, respectively. Using the corresponding roadkill rates based on simple extrapolation separately for the two years, the monarch roadkill rates in the Central Funnel represent mortality of 1.8 and 1.7% (1.6 to 1.0 million) for 2016 and 2017, respectively. Merging hotspot data for simple extrapolation in 2016 yields a 9% roadkill rate (8.5 million) for the

overwintering cohort, which may better reflect missing roadkill hotspot data from Mexico. In contrast, the projection of 500,000 road-killed monarchs by McKenna et al. (2001) in Illinois during one week in 1999 represents only 0.26% of the overwintering cohort that year (191 million, 9.05 ha), indicating potentially lower roadkill rates for areas north of the Central Funnel in some years.

The actual monarch population decline within a given year can be much higher than the differences in overwintering cohort sizes from year to year, since it includes the unknown quantities of butterflies recruited, or not recruited due to habitat loss, during spring and summer breeding. Mortality at the Mexican overwintering sites due to occasional winter storms can produce very high mortality, estimated at around 75% in 2002 (Brower et al., 2004) and greater than 40% in 2016 (Brower et al., 2017). Average monarch overwintering mortality is around 36% ± 21% (n = 7; range 4-55%) based on data from Ries et al. (2015; their Figure 24.7). Lowered recruitment due to loss of milkweed habitat has been identified as the primary factor in monarch population declines (Pleasants, 2017; Thogmartin et al., 2017), with losses of milkweed resources in Iowa estimated at 76% from 1999-2014 (Pleasants et al., 2017). Other studies place more importance on mortality during the fall migration in the decline of monarchs (Badgett and Davis, 2015; Inamine et al., 2016; Agrawal and Inamine, 2018). Consequently, it is complex to evaluate the relative importance of roadkill to other factors in the monarch population decline, but it is probably lower compared to the factors of milkweed habitat loss and overwintering mortality. Northward expansion of the monarch summer breeding range is anticipated with climate change (Batalden et al., 2007; Lemoine, 2015), making the southward autumn migration route even longer, increasing both exposure to traffic and associated road mortality (Badgett and

111

Davis, 2015). Monarch roadkill during autumn migration should be further evaluated in the context of other mortality factors along the migration path (Baxter-Gilbert, 2015).

Brower et al. (2012) fitted an exponential decline curve to the estimated monarch overwintering populations in Mexico from 1994 to 2010 ($P = 0.015$, $R^2 = 0.336$). Inclusion of six additional years of data through 2017 (Vidal and Rendón-Salinas, et al. 2014; Monarch Watch, 2018b) increases the significance of fit for a standard geometric power curve ($y = ax^{bx}$; Figure IV.5) ($P = 0.0009$; adjusted $R^2 = 0.486$; ZunZun.com, 2018). A concave exponential curve
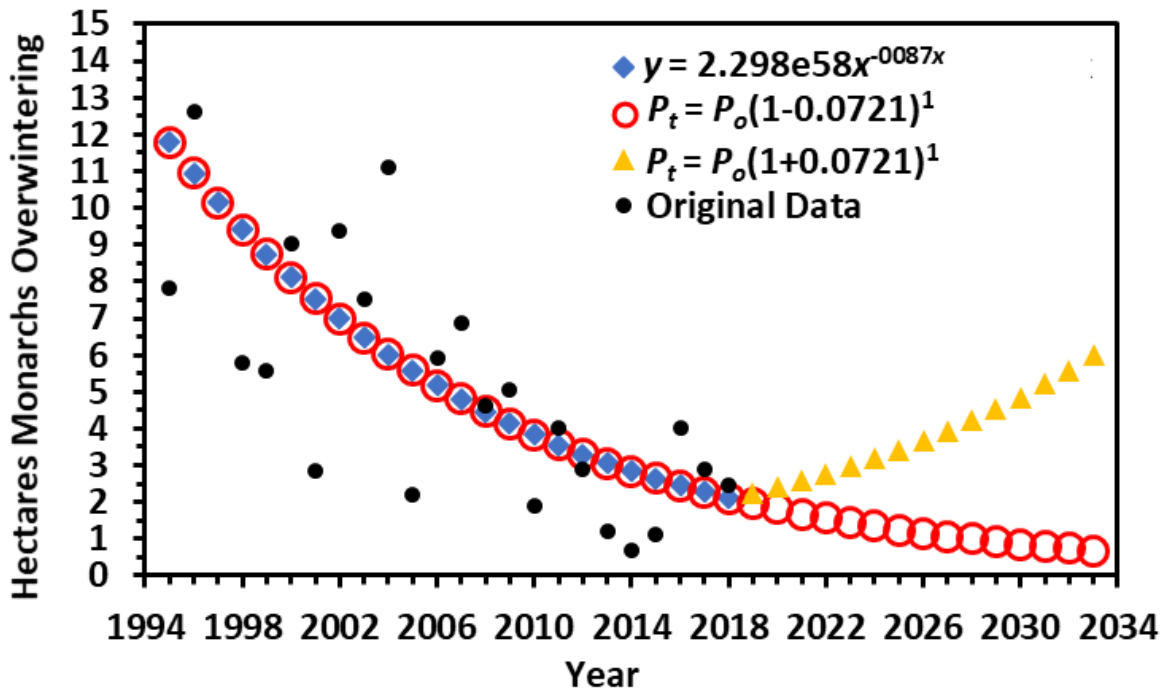
Figure IV.5. Annual monarch population in hectares in Mexican overwintering sites from 1995 to 2018 (original data, black circles; Vidal and Rendón-Salinas et al., 2014; Monarch Watch, 2018b) with fitted geometric power curve, $y = ax^{bx}$ (adjusted $R^2 = 0.49$; $P = 0.00009$; blue diamonds), and corresponding geometric population growth equation curve, $P_t = P_o(1 + r/n)^{nt}$, where P_t is the final hectares (2.11), P_o is the initial hectares (11.79), t is the number of years (23), n is the number of sub-periods (1), and r is the population growth (or declination) rate (derived population declination of 7.21% per year; open red circles). Fourteen years to restore 6 ha of overwintering monarchs based on totally reversing the current decline to 7.21% growth per year (gold triangles).

represents the most serious form of species population decline, indicating constant proportional negative pressure on the population (Di Fonzo et al., 2013). A standard geometric population growth curve, fit to the modeled power curve, reveals a -7.21% annual population decline over the last 23 years of an overall 82% population reduction (for details, see Appendix D, Monarch Population Decline Curve). Continuance of this rate of decline would result in an average of 0.7 ha of overwintering monarchs within the next 14 years (by 2033) (Fig. IV.5), greatly increasing the chance of extirpation of eastern migrating monarchs by an extreme winter storm mortality event. A total reversal of the 7.21% annual monarch decline over the next 14 years, coupled with an annual 7.21% population increase (net change 14.4%), is needed to restore the size of the overwintering population to current conservations goal of six hectares (Thogmartin et al., 2017). A 0.5% annual reduction in migrating monarch mortality through roadkill mitigation could significantly contribute to a reversal in the long-term 7.2% annual exponential decline in monarch populations (Figure IV.5).

Roadkill Mitigation

While some major factors in the monarch decline are difficult to reduce, such as overwintering mortality, the opportunity for reducing road mortality is possible through roadkill mitigation (see Rytwinski et al. [2016] for a recent review on mammal roadkill mitigation). A variety of roadkill mitigation measures have been implemented for danaine migratory butterflies. In Taiwan, a four-meter high net was placed along a 400 m section of bridge on National Freeway 3 to successfully induce spring migrating double-banded crow butterflies to fly over and above the traffic, reducing on site roadkill from around 2.5% to 0.5%. In addition, an outer traffic lane was closed when more than 500 butterflies per minute were crossing (Her, 2008; Taiwan EPA, 2010). In response to heavy autumn migratory monarch roadkill observed in

Coahuila state of Mexico, traffic signs were posted in 2015 limiting the maximum speed to 60 km per hour (37 mph) in the presence of monarchs (Miranda, 2015). Police have been observed slowing traffic in Nuevo Leon state in Mexico to reduce monarch mortality along a highway south of Monterrey (Dr. Orley R. Taylor, personal communication). In view of the potential harm of roadkill to the recovery of monarch populations, additional research is needed to test and assess the effectiveness of these types of butterfly roadkill mitigation strategies for monarch roadkill hotspots in west Texas and Mexico.

Conclusions

This study represents a novel approach for projecting roadkill of a migratory insect through ecological niche modeling. Annual monarch roadkill rates during autumn migration varied substantially. There was close agreement between two methods of estimating monarch roadkill rates, simple extrapolation by road type and MaxEnt roadkill model projections. About 1.25 million roadkill monarchs per year were projected during the autumn migration over the Central Funnel, which could represent 2% of the Mexican monarch overwintering population. MaxEnt model roadkill projections also aligned with several previously known monarch roadkill hotspots, which suggests MaxEnt models could be used to identify additional monarch roadkill within the Central Funnel. Roadkill rates may be higher for the Central Funnel in northern Mexico than in the Texas survey area, and should be further investigated. The spatial and temporal variability in monarch road mortality in the Central Funnel should be further investigated, including how local and short-term weather events, especially related to wind, influence monarch roadkill hotspots. With the new information on Central Funnel roadkill hotspots, conservation efforts could be implemented to mitigate monarch mortality at roadkill hotspots. Examples of mitigation efforts include reducing traffic speeds when large numbers of

monarchs are present (Miranda, 2015) or using netting over short sections of roadway to encourage flight above the level of traffic (Her, 2008). Reducing the 2% roadkill rate over the Central Funnel for the eastern monarch population is as an important step towards reversing the continuing decades long decline of this iconic butterfly.

CHAPTER V

CONCLUSIONS

A novel randomized ensemble hybrid feature selection algorithm, the RSFSA, was developed and demonstrated for applications in ecological niche modeling. The algorithm generated novel high performance ENM FSEs, facilitating data mining of important variables and providing a statistical basis for evaluating niche model performance across feature subset sizes, model parameters and algorithms, and environmental scenarios. The strict training and testing data randomization protocol developed for comparing RSFSA-selected and random ENMs provided a statistical basis for validation of the RSFSA. The RSFSA also selected ENMs developed from small subsets of a large pool of variables that performed comparable to ENMs developed using expert selected variables.

The two basic components of the RSFSA are (1) the generation of thousands of random subsets of environmental variables of a given size that meet a maximum correlation threshold, typically $|r| < 0.7$ (correlation filter), using multiple random sequential forward selection, and (2) ranking these random feature subsets according to accuracy (AUC) or information content (AICc) (subset wrappers) derived from running the niche model algorithm (e.g., MaxEnt) for each of the thousands of random feature subsets from (1). The top ranked feature subsets represent an RSFSA-selected FSE. The selected FSE is then evaluated against an FSE of random subsets for improvement of AUC or AICc to verify the effectiveness of RSFSA using held out model training and testing data. The calculation of thousands of MaxEnt models for ranking by AUC and AICc with RSFSA is basically a brute-force approach to finding higher performance niche models that requires much computation time, but which is reduced by parallel processing. An advantage of the random subset search strategy of RSFSA is that subsets of variables are

116

evaluated as a group in niche models, allowing identification of potentially synergistic combinations of variables that can be missed using sequential selection algorithms that are typically used for niche models, which evaluate single variables at a time.

The application of RSFSA or RSFSA components in improving ENM analyses was demonstrated for a variety of natural phenomena related to the landscape ecology of wildfires and monarch butterfly migration. The RSFSA-selected wildfire activity MaxEnt ENMs using 15 of 90 variables had significantly improved model accuracy (AUC), information content (AICc), and, in some cases, lower overfitting (AUC$_{diff}$) compared to random models. The RSFSA results identified several important variables for modeling wildfire activity that had not been identified in previous studies. For example, of the 20 top ranked variables used in RSFSA selected low burn severity wildfire activity models, only nine were found important in previous studies modeling wildfire activity in the western US and Greece. Newly identified important variables included mean temperature of the driest quarter (*bio_9*), annual evapotranspiration ratio (*etrt_ann*), and spring quarter evapotranspiration ratio (*etrt_sprq*). Utilizing the MaxEnt FSEs produced by RSFA, ecoregions were identified with relatively high or low projected areas of burn compared to historical burned areas and maps of contemporary wildfire deficit were developed. Projected high wildfire deficits were widespread throughout western North America, emphasizing the need to carefully manage associated fuel load build up that could endanger anthropogenic assets and sensitive areas of high biodiversity, such as sky island habitats. The RSFSA-selected MaxEnt wildfire activity FSEs also revealed significant differences between projected burned areas in current and future climate scenarios for some ecoregions. For example, many northern ecoregions had significant future projected increases in burned areas for low burn severity wildfires. Projected future increases in burned areas in western North America are in

117

general agreement with recent previous studies (Parks et al., 2016; Liu and Wimberly, 2016), further highlighting the critical importance of managing already excessive fuel loads in many managed ecosystems.

In spatial modeling of the monarch fall migration, a six of 80 variable FSE of RSFSA-selected MaxEnt ENMs formed the basis of a novel detailed comparison with a TSE of spatial point pattern KDEMs. The KDEMs were found to have significantly higher accuracy than ENMs, but ENMs had higher information content (lower complexity). The ENMs best revealed the suitability of Great Plains grassland ecoregions for the monarch fall migration, which was probably associated with increased nectar resource availability. The KDEMs best reveal migratory pathways through less environmentally suitable areas of the Chihuahuan Desert in West Texas and northern Mexico. The ten most important variables identified for monarch migratory ENMs through RSFSA were all climatic indices, including spring monthly minimum temperature (*tmn_sprq*), autumn mean monthly evapotranspiration (*aett_sprq*), and total annual evapotranspiration (*taett_tann*). The RSFSA again proved useful in revealing the importance of less utilized or studied environmental variables for ENMs. For example, eight of the top ten ranked indices included four Supplementary Climatic indices and four AET-PET indices. These Supplementary and AET-PET indices are not nearly as often employed in ENMs as the 19 BioClim indices (Bradie and Lueng, 2016). The KDEM migratory pathways were used to identify strong annual variability in the monarch fall migratory pathways and delineate the core Central and Coastal funnels of the southern Central and Eastern flyways, respectively. A number of important potential hazards along the fall migratory pathways were spatially identified, including road mortality, loss of nectar resources to land cover/land use change, exposure to

118

neonicotinoid contamination of nectar and honeydew food sources, and exposure to mosquito adulticides.

Monarch road mortality MaxEnt ENMs were developed in the Central Funnel for 2016 to 2017 using the MRSFS portion of the RSFSA to produce a random FSE of ten ENMs using ten of 20 variables. The eight top ranked variables by permutation importance in the ENMs included three human population indices, two climatic indices, elevation, road density over a 3 km radius, and percent cover of artificial surfaces over a 500 m radius. The importance of climate variables in roadkill niche models had not previously been identified. Arid, less populated areas from west Texas to northern Mexico were projected to have the highest roadkill probability by the MaxEnt ENM FSE. These same areas correspond with the locations of previously known monarch roadkill hotspots. The ENM FSE was used to estimate roadkill of about 1.25 ± 0.3 million monarchs per year across the Central Funnel, which agreed with simple extrapolation of roadkill according to road types. This Central Funnel roadkill estimate represents about 2-3% of the monarch overwintering population in Mexico for the study periods. Low rates of mortality can be very detrimental to species in decades long exponential population decline, such as the monarch. Results from this study are used to recommend assessing roadkill mitigation strategies in West Texas roadkill hotspots for their potential to reduce road mortality in support of monarch population recovery efforts.

In addition to the above discussed applications for conservation related phenomenological ENMs in pyrogeography and entomology, a wide variety of biological fields can benefit from the data mining capabilities of RSFSA for ENMs, including species distribution ENMs important for studies in invasive species, global change, agriculture, forestry, biological control, conservation, and restoration. The RSFSA can also be can also be used to study how the

inclusion or omission of certain classes of indices, such as AET-PET indices, impacts performance of RSFSA-selected ENMs. The RSFSA should be tested for the ability to filter out meaningless dummy variables, such as artist paintings (e.g., Fourcade et al., 2017), and improve spatial or temporal transferability of ENMs. The relative transferability of ENMs ranked using AUC calculated from randomly partitioned data versus AUC from spatially partitioned blocked data (Roberts et al., 2017) should be evaluated using RSFSA. Application of RSFSA with binomial (two-class) ENM algorithms other than MaxEnt, such as random forests and environmental envelope algorithms, should also be explored and compared with other feature selection strategies, such as sequential forward selection. In addition, RSFSA can be evaluated for improving performance of multinomial (multi-class) classifiers, such as the random forests or support vector machine algorithms used in image classification for remote sensing applications (e.g., Zhou et al., 2018). The hybrid RSFSA also has potential applications alongside other hybrid FSAs utilized in data mining for molecular bioinformatics with high dimensional omics data (e.g., Perez-Riverol et al., 2017). Potential applications of RSFSA extend beyond ENMs to other burgeoning fields utilizing hybrid FSAs for data mining, such as remote sensing image classification and molecular bioinformatics. The RSFSA should be compared with other hybrid FSAs for potential broad scope applications in data mining.

REFERENCES

Agrawal AA, Inamine H (2018) Mechanisms behind the monarch's decline. Science 360:1294-1296.

Alvarado-Serrano DF, Knowles LL (2014) Ecological niche models in phylogeographic studies: applications, advances and precautions. Molecular Ecology Resources 14:233-248.

Aly MA, Atiya AF (2006) Novel methods for the feature subset ensembles approach. International Journal of Artificial Intelligence and Machine Learning 6:1-7.

Andela N, Morton DC, Giglio L, Chen Y, van der Werf GR, Kasibhatla PS, DeFries RS, Collatz GJ, Hantson S, Kloster S, Bachelet D (2017) A human-driven decline in global burned area. Science 356:1356-1362.

Anderson RP, Gonzalez Jr I (2011) Species-specific tuning increases robustness to sampling bias in models of species distributions: an implementation with Maxent. Ecological Modelling 222:2796-2811.

Anderson RP, Lew D, Peterson AT (2003) Evaluating predictive models of species' distributions: criteria for selecting optimal models. Ecological Modelling 162:211-232.

Araújo MB, New M (2007) Ensemble forecasting of species distributions. Trends in Ecology and Evolution 22:42-47.

Badgett G, Davis AK (2015) Population trends of monarchs at a northern monitoring site: Analyses of 19 years of fall migration counts at Peninsula Point, MI. Annals of the Entomological Society of America 108:700-706.

Bahn V, McGill BJ (2007) Can niche-based distribution models outperform spatial interpolation?. Global Ecology and Biogeography 16:733-742

Barbero R, Abatzoglou JT, Larkin NK, Kolden CA, Stocks B (2015) Climate change presents

increased potential for very large fires in the contiguous United States. International

Journal of Wildland Fire 24:892-899

Barbero R, Abatzoglou JT, Steel EA, Larkin NK (2014) Modeling very large-fire occurrences

over the continental United States from weather and climate forcing. Environmental

Research Letters 9:124009 (11 pp).

Barbet-Massin M, Jiguet F, Albert CH, Thuiller W (2012) Selecting pseudo-absences for species

distribution models: how, where and how many? Methods in Ecology and Evolution

3:327–338.

Batalden RV, Oberhauser K, Peterson AT (2007) Ecological niches in sequential generations of

eastern North American monarch butterflies (Lepidoptera: Danaidae): the ecology of

migration and likely climate change implications. Environmental Entomology 36:1365-

73.

Baxter-Gilbert JH, Riley JL, Neufeld CJ, Litzgus JD, Lesbarrères D (2015) Road mortality

potentially responsible for billions of pollinating insect deaths annually. Journal of Insect

Conservation 19:1029-1035.

Beall G (1946) Seasonal variation in sex proportion and wing length in the migrant butterfly,

Danaus plexippus L. (lep. Danaidae). Ecological Entomology 97:337-353.

Beaumont LJ, Hughes L, Poulsen M (2005) Predicting species distributions: use of climatic

parameters in BIOCLIM and its impact on predictions of species' current and future

distributions. Ecological Modelling 186:251-270.

Beaumont LJ, Pitman AJ, Poulsen M, Hughes L (2007) Where will species go? Incorporating

new advances in climate modeling into projections of species distributions. Global

Change Biology 13:1368-1385.

Beaumont LJ, Hughes L, Pitman AJ (2008) Why is the choice of future climate scenarios for

species distribution modeling important?. Ecology Letters 11:1135-1146.

Beaumont LJ, Graham E, Duursma DE, Wilson PD, Cabrelli A, Baumgartner JB, Hallgren W,

Esperón-Rodríguez M, Nipperess DA, Warren DL, Laffan SW (2015) Which species

distribution models are more (or less) likely to project broad-scale, climate-induced shifts

in species ranges?. Ecological Modelling 342:135-146.

Beck J (2013) Predicting climate change effects on agriculture from ecological niche modeling:

who profits, who loses?. Climatic Change 116:177-189.

Bellamy C, Altringham J (2015) Predicting species distributions using record centre data: multi-

scale modeling of habitat suitability for bat roosts. PloS One 10:e0128440.

Bennett VJ (2017) Effects of road density and pattern on the conservation of species and

biodiversity. Current Landscape Ecology Reports 2:1-11.

Bond ML, Bradley CM, Kiffner C, Morrison TA, Lee DE (2017) A multi-method approach to

delineate and validate migratory corridors. Landscape Ecology 32:1705-1721.

Boria RA, Olson LE, Goodman SM, Anderson RP (2014) Spatial filtering to reduce sampling

bias can improve the performance of ecological niche models. Ecological

Modelling 275:73-77.

Borland J, Johnson CC, Crumpton III TW, Thomas M, Altizer SM, Oberhauser KS (2004)

Characteristics of fall migratory monarch butterflies, *Danaus plexippus*, in Minnesota and

Texas. In: Oberhauser KS, Solensky MJ (eds), The Monarch Butterfly: Biology and Conservation, Cornell University Press, Ithaca, NY, pp. 97-104.

Bozdogan H (1987) Model selection and Akaike's information criterion (AIC): The general theory and its analytical extensions. Psychometrika 52:345-370.

Bradie J, Leung B (2016) A quantitative synthesis of the importance of variables used in MaxEnt species distribution models. Journal of Biogeography 44:1344-1361.

Bradley BA, Wilcove DS, Oppenheimer M (2010) Climate change increases risk of plant invasion in the Eastern United States. Biological Invasions 12:1855-1872.

Braunisch V, Coppes J, Arlettaz R, Suchant R, Schmid H, Bollmann K (2013) Selecting from correlated climate variables: a major source of uncertainty for predicting species distributions under climate change. Ecography 36:971-983.

Breiman L (1996) Bagging predictors. Machine Learning 24:123-140.

Breiman L (2001) Random forests. Machine Learning 45:5-32.

Brindza L, Brower LP, Davis AK, Van Hook T (2008) Comparative success of monarch butterfly migration to overwintering sites in Mexico from inland and coastal sites in Virginia. Journal of the Lepidopterists' Society 62:189-200.

Brower LP (1995) Understanding and misunderstanding the migration of the monarch butterfly (Nymphalidae) in North America: 1857–1995. Journal of the Lepidopterists' Society 49:304-385.

Brower LP (1996) Monarch butterfly orientation: Missing pieces of a magnificent puzzle. Journal of Experimental Biology 199:93-103.

Brower LP, Fink LS, Kiphart RJ, Pocius V, Zubieta RR, Ramírez MI (2015) Effect of the 2010–2011 drought on the lipid content of monarchs migrating through Texas to overwintering

sites in Mexico. In: Oberhauser KS, Nail KR, Altizer S (eds), Monarchs in a Changing World: Biology and Conservation of an Iconic Butterfly, Cornell University Press, Ithaca, New York, pp 117-129.

Brower LP, Fink LS, Walford P (2006) Fueling the fall migration of the monarch butterfly. Integrative and Comparative Biology 46:1123-1142.

Brower LP, Kust DR, Rendón Salinas E, García-Serrano E, Kust KR, Miller J, Fernandez del Rey C, Pape K (2004) Catastrophic winter storm mortality of monarch butterflies in Mexico during January 2002. In: Oberhauser KS, Solensky MJ (eds), The Monarch Butterfly: Biology and Conservation, Cornell University Press, Ithaca, NY, pp. 151-166.

Brower LP, Taylor OR, Williams EH, Slayback DA, Zubieta RR, Ramirez MI (2012) Decline of monarch butterflies overwintering in Mexico: is the migratory phenomenon at risk? Insect Conservation and Diversity 5:95-100.

Brower LP, Williams EH, Jaramillo-López P, Kust DR, Slayback DA, Ramírez MI (2017) Butterfly Mortality and Salvage Logging from the March 2016 Storm in the Monarch Butterfly Biosphere Reserve in Mexico. American Entomologist 63:151-164.

Calvert WH, Wagner M (1999) Patterns in the monarch butterfly migration through Texas—1993 to 1995. In: Hoth J, Merino L, Oberhauser K, Pisanty I, Price S, Wilkinson T (eds) 1997 North American Conference on the Monarch Butterfly. Commission for Environmental Cooperation, Montreal, Canada, pp 119-125.

Center for International Earth Science Information Network (CIESIN) (2005) Gridded Population of the World, Version 3 (GPWv3): Population Density (Year 2000). National Aeronautics and Space Administration Socioeconomic Data and Applications Center,

Palisades, New York. http://sedac.ciesin.columbia.edu/data/set/gpw-v3-population-density/data-download (11 December 2017)

Center for International Earth Science Information Network (CIESIN) - Columbia University (2016) Gridded Population of the World, Version 4 (GPWv4): Population Density. NASA Socioeconomic Data and Applications Center (SEDAC), Palisades, New York, Available from: http://sedac.ciesin.columbia.edu/data/set/gpw-v4-population-density/data-download (13 December, 2016)

Center for International Earth Science Information Network - CIESIN - Columbia University, and Information Technology Outreach Services - ITOS - University of Georgia (CIESIN and ITOS) (2013) Global Roads Open Access Data Set, Version 1 (gROADSv1). NASA Socioeconomic Data and Applications Center (SEDAC), Palisades, New York, Available from: http://sedac.ciesin.columbia.edu/data/set/groads-global-roads-open-access-v1/data-download (13 December 2016)

Cheke RA, Tratalos JA (2007) Migration, patchiness, and population processes illustrated by two migrant pests. AIBS Bulletin 57:145-154.

Chen J, Chen J, Liao A, Cao X, Chen L, Chen X, He C, Han G, Peng S, Lu M, Zhang W (2015) Global land cover mapping at 30 m resolution: A POK-based operational approach. ISPRS Journal of Photogrammetry and Remote Sensing 103:7-27.

Chylek P, Dubey MK, Lesins G, Li J, Hengartner N (2014) Imprint of the Atlantic multi-decadal oscillation and Pacific decadal oscillation on southwestern US climate: past, present, and future. Climate Dynamics 43:119-129.

Commission for Environmental Cooperation (CEC) (2005) Ecological Regions of North America, Level 3, Scale 1:4,000,000, second edition, CEC, Montreal, Quebec, Canada.

Shapefiles available at: http://www.cec.org/tools-and-resources/map-files/terrestrial-ecoregions-level-iii (12 January 2017)

Correo Real (2015) Correo Real Bulletin 15, 8 November.

Corten GP, Veldkamp HF (2001) Aerodynamics: Insects can halve wind-turbine power. Nature 412:41-42.

D'heygere T, Goethals PL, De Pauw N (2003) Use of genetic algorithms to select input variables in decision tree models for the prediction of benthic macroinvertebrates. Ecological Modelling 160:291-300.

Dalili N, Edrisy A, Carriveau R (2009) A review of surface engineering issues critical to wind turbine performance. Renewable and Sustainable Energy Reviews 13:428-438.

Davis AK, Garland MS (2004) Stopover ecology of monarchs in coastal Virginia: using ornithological techniques to study monarch migration. In: Oberhauser KS, Solensky MJ (eds) The Monarch Butterfly: Biology and Conservation. Cornell University Press, Ithaca, NY, pp 89-96.

Davis AK, Rendón-Salinas, E (2010) Are female monarch butterflies declining in eastern North America? Evidence of a 30-year change in sex ratios at Mexican overwintering sites. Biology Letters 6:45-47.

De la Puente D, Ochoa C, Viejo JL (2008) Butterflies killed on roads (Lepidoptera, Papilionoidea) in "El Regajal-Mar de Ontigola" Nature Reserve (Aranjuez, Spain). XVII Bienal de la Real Sociedad Española de Historia Natural 17:137-152.

Dicko AH, Lancelot R, Seck MT, Guerrini L, Sall B, Lo M, Vreysen MJ, Lefrançois T, Fonta WM, Peck SL, Bouyer J (2014) Using species distribution models to optimize vector

control in the framework of the tsetse eradication campaign in Senegal. Proceedings of the National Academy of Sciences 111:10149-10154.

Di Fonzo M, Collen B, Mace GM (2013) A new method for identifying rapid decline dynamics in wild vertebrate populations. Ecology and Evolution, 3:2378-2391.

Dillon GK, Holden ZA, Morgan P, Crimmins MA, Heyerdahl EK, Luce CH (2011) Both topography and climate affected forest and woodland burn severity in two regions of the western US, 1984 to 2006. Ecosphere 2:1-33.

Dingle H, Drake, VA (2007) What is migration? Bioscience 57:113-121.

Dormann CF, Elith J, Bacher S, Buchmann C, Carl G, Carré G, Marquéz JR, Gruber B, Lafourcade B, Leitão PJ, Münkemüller T (2013) Collinearity: a review of methods to deal with it and a simulation study evaluating their performance. Ecography 36:27-46.

Driscoll DM, Yee Fong, JM (1992) Continentality: A basic climatic parameter re-examined. International Journal of Climatology 12:185-192.

EarthEnv (2016) EarthEnv: Global, Remote-sensing Supported Environmental Layers for Assessing Status and Trends in Biodiversity, Ecosystems, and Climate; Global 1-km Consensus Land Cover. Available at http://www.earthenv.org/landcover (16 January 2017)

Eidenshink JC, Schwind B, Brewer K, Zhu ZL, Quayle B, Howard SM (2007) A project for monitoring trends in burn severity. Fire Ecology 3:3-21.

Elith J (2017) Predicting distributions of invasive species. In: Robinson AP, Walshe T, Burgman MA, Nunn M (eds), Invasive species: Risk assessment and management. Cambridge University Press, Cambridge, United Kingdom, pp. 93-129.

Elith J, Leathwick JR (2009a) Species distribution models: ecological explanation and prediction across space and time. Annual Review of Ecology, Evolution, and Systematics 40:677-697.

Elith J, Leathwick J (2009b) The contribution of species distribution modelling to conservation prioritization. In: Moilanen A, Wilson, KA, Possingham, H (eds), Spatial Conservation Prioritization: Quantitative Methods and Computational Tools, Oxford University Press, Oxford, United Kingdom, pp. 70-93.

Elith, J, Phillips, SJ, Hastie, T, Dudík, M, Chee, YE, Yates, CJ (2011) A statistical explanation of MaxEnt for ecologists. Diversity and Distributions 17:43-57.

Elith J, Graham CH, Anderson RP, Dudík M, Ferrier S, Guisan A, Hijmans RJ, Huettmann F, Leathwick JR, Lehmann A, Li J (2006) Novel methods improve prediction of species' distributions from occurrence data. Ecography 1:129-251.

Ehrlén J, Morris WF (2015) Predicting changes in the distribution and abundance of species under environmental change. Ecology Letters 18:303-314.

Escobar LE, Craft ME (2016) Advances and limitations of disease biogeography using ecological niche modeling. Frontiers in Microbiology 7:1174.

Evans JS, Oakleaf J, Cushman SA, Theobald D (2014) An ArcGIS Toolbox for Surface Gradient and Geomorphometric Modeling, version 2.0-0. Available from: https://www.arcgis.com/home/item.html?id=63ffcecf3b2a45bf99a84cdaedefaccf (13 December 2016)

Fahrig L, Rytwinski T (2009) Effects of roads on animal abundance: an empirical review and synthesis. Ecology and Society 14:21.

Fielding AH, Bell JF (1997) A review of methods for the assessment of prediction errors in conservation presence/absence models. Environmental Conservation 24:38-49.

Finco M, Quale B, Zhang Y, Lecker J, Megown KA, Brewer KC (2012) Monitoring trends in burn severity (MTBS): Monitoring wildfire activity for the past quarter century using Landsat data. In: Morin RS, Liknes GC (eds), Moving from Status to Trends: Forest Inventory and Analysis (FIA) Symposium 2012, 4-6 December, 2012, Baltimore, Maryland, USDA Forest Service Technical Report NRS-P-105, USDA Forest Service, Northern Research Station, Newton Square, Pennsylvania, pp. 222-228. Available at http://www.nrs.fs.fed.us/pubs/gtr/gtr-nrs-p-105papers/35finco-p-105.pdf (21 December 2016)

Fitzgerald M, Coulson R, Lawing AM, Matsuzawa T, Koops K (2018) Modeling habitat suitability for chimpanzees (*Pan troglodytes verus*) in the Greater Nimba Landscape, Guinea, West Africa. Primates 9:1-5.

Flockhart DT, Brower LP, Ramirez MI, Hobson KA, Wassenaar LI, Altizer S, Norris DR (2017) Regional climate on the breeding grounds predicts variation in the natal origin of monarch butterflies overwintering in Mexico over 38 years. Global Change Biology doi: 10.1111/gcb.13589.

Franklin J (2010) Mapping species distributions: spatial inference and prediction. Cambridge University Press, Cambridge, United Kingdom, 320 pp.

Franklin J (2013) Species distribution models in conservation biogeography: developments and challenges. Diversity and Distributions 19:1217-1223.

Freeman EA, Moisen G (2008) PresenceAbsence: An R package for presence absence analysis.
Journal of Statistical Software 23:1–31. Available from
http://www.jstatsoft.org/v23/i11/paper (2 August 2014)

Friedman J, Hastie T, Tibshirani R (2010) Regularization paths for generalized linear models via
coordinate descent. Journal Statistical Software 33:1–22.

Forman RT, Sperling D, Bissonette JA, Clevenger AP, Cutshall CD, Dale VH, Fahrig L, France
RL, Heanue K, Goldman CR, Jones J (2003) Road Ecology: Science and Solutions,
Island Press, Washington, DC, USA, 481 pp.

Fourcade Y, Besnard AG, Secondi J (2018) Paintings predict the distribution of species, or the
challenge of selecting environmental predictors and evaluation statistics. Global Ecology
and Biogeography 27:245-256.

Galelli S, Humphrey GB, Maier HR, Castelletti A, Dandy GC, Gibbs MS (2014) An evaluation
framework for input variable selection algorithms for environmental data-driven models.
Environmental Modeling & Software 62:33-51.

Garland MS, Davis AK (2002) An examination of monarch butterfly (*Danaus plexippus*) autumn
migration in coastal Virginia. American Midland Naturalist 147:170-174.

Games, PA, Howell, JF (1976) Pairwise multiple comparison procedures with unequal n's and/or
variances: A Monte Carlo study. Journal of Educational and Behavioral Statistics 1:113-
125.

Garcia DJ, Hall LO, Goldgof DB, Kramer K (2006) A parallel feature selection algorithm from
random subsets. In: Di Fatta, G, Berthold, MR, Parthasarathy, S (eds), Proceedings of the
International Workshop on Parallel Data Mining, 18 September, 2006, Berlin, Germany,
pp. 64-75. Available from

https://pdfs.semanticscholar.org/dcb5/94f8f5aa553a682e8a0c8fce1f01f6ca23ff.pdf (29 December 2017)

Gavin DG, Fitzpatrick MC, Gugger PF, Heath KD, Rodríguez-Sánchez F, Dobrowski SZ, Hampe A, Hu FS, Ashcroft MB, Bartlein PJ, Blois JL (2014) Climate refugia: joint inference from fossil records, species distribution models and phylogeography. New Phytologist 204:37-54.

Gearin PJ, Melin SR, DeLong RL, Gosho ME, Jeffries S (2017) Migration patterns of adult male California sea lions (*Zalophus californianus*). NOAA Technical Memo NMFS-AFSC-346, US Department of Commerce, National Oceanic and Atmospheric Administration, National Marine Fisheries Service, Alaska Fisheries Science Center, Seattle, Washington. Available at https://www.afsc.noaa.gov/Publications/AFSC-TM/NOAA-TM-AFSC-346.pdf (11 June 2018)

Gibo DL (1981) Altitudes attained by migrating monarch butterflies, *Danaus p. plexippus* (Lepidoptera: Danaidae), as reported by glider pilots. Canadian Journal of Zoology 59:571-572.

Gibo DL (1986) Flight strategies of migrating monarch butterflies (*Danaus plexippus* L.) in southern Ontario. In: Danthanarayana W (ed), Insect Flight, Dispersal and Migration, Springer, Berlin, Heidelberg, Germany, pp. 172-184.

Gibo DL, Pallett MJ (1979) Soaring flight of monarch butterflies, *Danaus plexippus* (Lepidoptera: Danaidae), during the late summer migration in southern Ontario. Canadian Journal of Zoology 57:1393-1401.

Ginsberg HS, Bargar TA, Hladik ML, Lubelczyk C (2017) Management of arthropod pathogen

    vectors in North America: Minimizing adverse effects on pollinators. Journal of Medical

    Entomology 54:1463-1475.

Gobeyn S, Volk M, Dominguez-Granda L, Goethals PL (2017) Input variable selection with a

    simple genetic algorithm for conceptual species distribution models: A case study of river

    pollution in Ecuador. Environmental Modeling and Software 92:269-316.

Gomes L, Grilo C, Silva C, Mira A (2009) Identification methods and deterministic factors of

    owl roadkill hotspot locations in Mediterranean landscapes. Ecological Research 24:355-

    370.

Graham J, Young N, Jarnevich CS, Newman G, Evangelista P, Stohlgren TJ (2013) The Hyper-

    Envelope Modeling Interface (HEMI): A novel approach illustrated through predicting

    tamarisk (*Tamarix* spp.) habitat in the western USA. Environmental Management 52:929-

    938.

Griffioen PA, Clarke MF (2002) Large-scale bird-movement patterns in eastern Australian atlas

    data. Emu 102:97-125.

Grilo C, Bissonette JA, Santos-Reis M (2009) Spatial–temporal patterns in Mediterranean

    carnivore road casualties: consequences for mitigation. Biological Conservation 142:301-

    313.

Guillera-Arroita G, Lahoz-Monfort JJ, Elith J (2014) Maxent is not a presence–absence method:

    a comment on Thibaud et al. Methods in Ecology and Evolution. 5:1192-1197.

Guyette RP, Thompson FR, Whittier J, Stambaugh MC, Dey DC (2014) Future fire probability

    modeling with climate change data and physical chemistry. Forest Science 60:862-870.

Guyon I, Elisseeff A (2003) An introduction to variable and feature selection. Journal of
Machine Learning Research 3:1157-1182.

Ha H, Shilling F (2018) Modelling potential wildlife-vehicle collisions (WVC) locations using
environmental factors and human population density: A case-study from 3 state highways
in Central California. Ecological Informatics 43:212-221.

Halvorsen R (2013) A strict maximum likelihood explanation of MaxEnt, and some implications
for distribution modeling. Sommerfeltia 36:1-32.

Halvorsen R, Mazzoni S, Bryn A, Bakkestuen V (2015) Opportunities for improved distribution
modeling practice via a strict maximum likelihood interpretation of
MaxEnt. Ecography 38:172-183.

Halvorsen R, Mazzoni S, Dirksen JW, Næsset E, Gobakken T, Ohlson M (2016) How important
are choice of model selection method and spatial autocorrelation of presence data for
distribution modeling by MaxEnt?. Ecological Modelling 328:108-118.

Hannah L, Roehrdanz PR, Ikegami M, Shepard AV, Shaw MR, Tabor G, Zhi L, Marquet PA,
Hijmans RJ (2013) Climate change, wine, and conservation. Proceedings of the National
Academy of Sciences 110:6907-6912.

Hardesty-Moore M, Deinet S, Freeman R, Titcomb GC, Dillon EM, Stears K, Klope M, Bui A,
Orr D, Young HS, Kuile AM, Hughey LF, McCauley DJ (2018) Migration in the
Anthropocene: How collective navigation, environmental system and taxonomy shape the
vulnerability of migratory species. Philosophical Transactions of the Royal Society B
373:20170017.

Harrell FE, Lee KL, Mark DB (1996) Multivariable prognostic models: issues in developing models, evaluating assumptions and adequacy, and measuring and reducing errors. Statistics in Medicine 15:361-387.

Harris R, Porfirio LL, Hugh S, Lee G, Bindoff NL, Mackey B, Beeton NJ (2013) To Be Or Not to Be? Variable selection can change the projected fate of a threatened species under future climate. Ecological Management and Restoration 14:230-234.

Her K (2008) Ensuring a Safe Journey. Taiwan Today, Taiwan Review, 1 August, 2008, Available at: http://taiwantoday.tw/news.php?post=23836&unit=14,29,34,45 (28 February 2018)

Hijmans RJ, Graham CH (2006) The ability of climate envelope models to predict the effect of climate change on species distributions. Global Change Biology 12:2272-2281.

Hijmans RJ, Phillips S, Leathwick J, Elith J (2011) Package 'dismo'. Available at: http://cran.r-project.org/web/packages/dismo/index.html (7 January 2016)

Hijmans RJ, Cameron SE, Parra JL, Jones PG, Jarvis A (2005) A very high resolution interpolated climate surfaces for global land areas. International Journal Climatology 25:1965–1978.

Howard E, Davis AK (2009) The fall migration flyways of monarch butterflies in eastern North America revealed by citizen scientists. Journal of Insect Conservation 13:279-286.

Huff DD, Lindley ST, Wells BK, Chai F (2012) Green sturgeon distribution in the Pacific Ocean estimated from modeled oceanographic features and migration behavior. PloS One 7:e45852.

Inamine H, Ellner SP, Springer JP, Agrawal AA (2016) Linking the continental migratory cycle of the monarch butterfly to understand its population decline. Oikos 125:1081-1091.

Jiménez-Valverde A, Lobo JM, Hortal J (2008) Not as good as they seem: the importance of concepts in species distribution modeling. Diversity and Distributions 14:885-890.

John GH, Kohavi R, Pfleger K (1994) Irrelevant features and the subset selection problem. In: Cohen, WW, Hirsh, H (eds), Machine Learning: Proceedings of the Eleventh International Conference, 10-13 July, 1994, New Brunswick, New Jersey, Morgan Kaufmann Publishers, San Francisco, California, pp. 121-129.

Jones CD, Hughes JK, Bellouin N, Hardiman SC, Jones GS, Knight J, Liddicoat S, O'Connor FM, Andres RJ, Bell C, Boo KO (2011) The HadGEM2-ES implementation of CMIP5 centennial simulations. Geoscientific Model Development 4:543-570.

Journey North (2017) Journey North - A Global Study of Wildlife Migration and Seasonal Change. https://www.learner.org/jnorth/ (23 June 2017)

Journey North (2018a) Answers from the monarch butterfly expert. https://www.learner.org/jnorth/tm/monarch/ExpertAnswer07.html (6 June 2018)

Journey North (2018b) Monarch migration update: October 13, 1999. http://www.learner.org/jnorth/fall1999/monarch/Update101399.html (19 June 2018)

Journey North (2018c) Fall Migration Cold Fronts and Winds. http://www.learner.org/jnorth/tm/monarch/FallMigrationColdFronts.html (6 March 2018)

Jović A, Brkić K, Bogunović N (2015) A review of feature selection methods with applications. In: Biljanovic P, Butkovic Z, Skala K, Mikac B, Cicin-Sain M, Sruk V, Ribaric S, Gros S, Vrdoljak B, Mauher M, Sokolic A (eds) 2015 38th International Convention on Information and Communication Technology, Electronics and Microelectronics (MIPRO), 25-29 May, 2015, Opatija, Croatia, Institute of Electrical and Electronics Engineers International, pp. 1200-1212.

Jueterbock A, Smolina I, Coyer JA, Hoarau G (2016) The fate of the Arctic seaweed *Fucus distichus* under climate change: an ecological niche modeling approach. Ecology and Evolution 6:1712-1724.

Kalabokidis KD, Konstantinidis P, Vasilakos C (2002) GIS analysis of physical and human impact on wildfire patterns. In: Viegas DX (ed), Proceedings of the IV International Conference on Forest Fire Research & Wildland Fire Safety, 18-23 November, 2002, Coimbra, Portugal, Millpress, Rotterdam, Netherlands, 11 pp.

Kalousis A, Prados J, Hilario M (2007) Stability of feature selection algorithms: A study on high-dimensional spaces. Knowledge and Information Systems 12:95-116.

Key CH, Benson NC (2006) Landscape assessment: sampling and analysis methods. USDA Forest Service, Rocky Mountain Research Station General Technical Report RMRS-GTR-164-CD. Available at https://www.fs.fed.us/postfirevegcondition/documents/publications/FIREMON_LandscapeAssessment.pdf (9 January 2017)

Kie JG, Matthiopoulos J, Fieberg J, Powell RA, Cagnacci F, Mitchell MS, Gaillard JM, Moorcroft PR (2010) The home-range concept: are traditional estimators still relevant with modern telemetry technology? Philosophical Transactions of the Royal Society B 365:2221-2231.

Kohavi R, John GH (1997) Wrappers for feature subset selection. Artificial Intelligence 97:273-324.

Kolden CA, Smith AM, Abatzoglou JT (2015) Limitations and utilisation of Monitoring Trends in Burn Severity products for assessing wildfire severity in the USA. International Journal of Wildland Fire 24:1023-1028.

Krischik V, Rogers M, Gupta G, Varshney A (2015) Soil-applied imidacloprid translocates to ornamental flowers and reduces survival of adult *Coleomegilla maculata*, *Harmonia axyridis*, and *Hippodamia convergens* lady beetles, and larval *Danaus plexippus* and *Vanessa cardui* butterflies. PloS One 10:e0119133.

Lahoz-Monfort JJ, Guillera-Arroita G, Milner-Gulland EJ, Young RP, Nicholson E (2010) Satellite imagery as a single source of predictor variables for habitat suitability modeling: how Landsat can inform the conservation of a critically endangered lemur. Journal of Applied Ecology 47:1094-1102.

LANDFIRE (2016) United States Disturbance 2014, LANDFIRE 2014, U.S. Department of the Interior, Geological Survey. Available at http://www.landfire.gov/disturbance_grids.php (20 December 2016)

Lehner B, Verdin K, Jarvis A (2008) New global hydrography derived from spaceborne elevation data. Eos 89:93-94.

Lemoine NP (2015) Climate change may alter breeding ground distributions of eastern migratory monarchs (*Danaus plexippus*) via range expansion of *Asclepias* host plants. PloS One 10:e0118614.

Liechti F, Guélat J, Komenda-Zehnder S (2013) Modelling the spatial concentrations of bird migration to assess conflicts with wind turbines. Biological Conservation 162:24-32.

Liu C, White M, Newell G (2013a) Selecting thresholds for the prediction of species occurrence with presence-only data. Journal Biogeography 40:778–789.

Liu H, Motoda H (1998) Feature Selection for Knowledge Discovery and Data Mining. Vol. 453, Kluwer Academic Publishers, Norwell, Massachusetts, 214 pp.

Liu J, Danait N, Hu S, Sengupta S (2013b) A leave-one-feature-out wrapper method for feature selection in data classification. In: 2013 6th International Conference on Biomedical Engineering and Informatics (BMEI), 16-18 December, 2013, Hangzhou, China, Institute of Electrical and Electronics Engineers, pp. 656-660.

Liu Z, Wimberly MC (2015) Climatic and landscape influences on fire regimes from 1984 to 2010 in the western United States. PLoS One 10:e0140839.

Liu Z, Wimberly MC (2016) Direct and indirect effects of climate change on projected future fire regimes in the western United States. Science of the Total Environment 542:65-75.

Liu H, Yu L (2005) Toward integrating feature selection algorithms for classification and clustering. IEEE Transactions on Knowledge and Data Engineering 17:491-502.

Malcolm SB (2018) Anthropogenic impacts on mortality and population viability of the monarch butterfly. Annual Review of Entomology 63:277-302.

Malo JE, Suárez F, Diez A (2004) Can we mitigate animal–vehicle accidents using predictive models?. Journal of Applied Ecology. 41:701-710.

McKenna DD, Malcolm SB, Berenbaum MR (2001) Mortality of Lepidoptera along roadways in Central Illinois. Journal of the Lepidopterist's Society 55:63-68.

Mann ML, Batllori E, Moritz MA, Waller EK, Berck P, Flint AL, Flint LE, Dolfi E (2016) Incorporating anthropogenic influences into fire probability models: effects of human activity and climate change on fire activity in California. PLoS One 11:e0153589.

Marmion M, Parviainen M, Luoto M, Heikkinen RK, Thuiller W (2009) Evaluation of consensus methods in predictive species distribution modeling. Diversity and Distributions 15:59-69.

Mayer H, Somol P, Huber R, Pudil P (2000) Improving statistical measures of feature subsets by conventional and evolutionary approaches. In: Ferri, FJ, Iñesta, JM, Amin, A, Pudil, P (eds), Advances in Pattern Recognition, Springer-Verlag, Berlin, Germany, pp. 77-86.

McKenzie D, Littell JS (2017) Climate change and the eco-hydrology of fire: Will area burned increase in a warming western USA?. Ecological Applications 27:26-36.

Meentemeyer RK, Anacker BL, Mark W, Rizzo DM (2008) Early detection of emerging forest disease using dispersal estimation and ecological niche modeling. Ecological Applications 18:377-390.

Merow C, Smith MJ, Silander JA (2013) A practical guide to MaxEnt for modeling species' distributions: what it does, and why inputs and settings matter. Ecography 36:1058-1069.

Mi C, Huettmann F, Guo Y, Han X, Wen L (2017) Why choose Random Forest to predict rare species distribution with few samples in large undersampled areas? Three Asian crane species models provide supporting evidence. PeerJ, 5:e2849.

Miranda F (2015) Roads Where the Monarch Passes Will Have a Limit of 60 km/h. Milenio.com, Culture, 28 October 2016, Available at: http://www.milenio.com/cultura/Caminos-mariposa_monarca-limite_de_velocidad-ruta_de_la_monarca_0_614938524.html (28 February 2018)

Monarch Watch (2017) Monarch population status. Blog of 11 February, 2017. http://monarchwatch.org/blog/2017/02/11/monarch-population-status-30/ (11 October 2017)

Monarch Watch (2018a) Peak Migration Dates: When will the migration peak in my area? https://www.monarchwatch.org/tagmig/peak.html (19 June 2018)

Monarch Watch (2018b) Monarch population status. Monarch Watch Blog, 7 March 2018.

>https://monarchwatch.org/blog/2018/03/07/monarch-population-status-32/ (16 October

>2018)

Monitoring Trends in Burn Severity (MTBS) (2016) National MTBS Burn Severity Mosaics;

>Continental US, 1984–2014. Available at http://mtbs.gov/nationalregional/download.html

>(21 December 2016)

Moore JD, Krementz DG (2017) Migratory connectivity of American Woodcock using band

>return data. Journal of Wildlife Management 81:1063-1072.

Morales NS, Fernández IC, Baca-González V (2017) MaxEnt's parameter configuration and

>small samples: are we paying attention to recommendations? A systematic review. PeerJ

>5:e3093.

Moreno-Amat E, Mateo RG, Nieto-Lugilde D, Morueta-Holme N, Svenning JC, García-

>Amorena I (2015) Impact of model complexity on cross-temporal transferability in

>Maxent species distribution models: An assessment using paleobotanical data. Ecological

>Modelling 312:308-317.

Mouton AM, De Baets B, Goethals PL (2009) Knowledge-based versus data-driven fuzzy habitat

>suitability models for river management. Environmental Modeling and Software 24:982-

>993.

Mukherjee A, Diaz R, Thom M, Overholt WA, Cuda JP (2012) Niche-based prediction of

>establishment of biocontrol agents: an example with *Gratiana boliviana* and tropical soda

>apple. Biocontrol Science and Technology 22:447-461.

Munguira ML, Thomas JA (1992) Use of road verges by butterfly and burnet populations, and
the effect of roads on adult dispersal and mortality. Journal of Applied Ecology 1:316-
329.

Muñoz PT, Torres FP, Megías AG (2015) Effects of roads on insects: a review. Biodiversity and
Conservation 24:659-682.

Muscarella R, Galante PJ, Soley-Guardia M, Boria RA, Kass J, Uriarte M, Anderson RP (2014)
ENMeval: An R package for conducting spatially independent evaluations and estimating
optimal model complexity for ecological niche models. Methods in Ecology and
Evolution 5:1198-1205.

Muzaffar SB, Clarke C, Whelan R, Gubiani R, Cook TR (2017) Short distance directional
migration in the threatened Socotra cormorant: link to primary productivity and
implications for conservation. Marine Ecology Progress Series 575:181-194.

Noss RF, Franklin J F, Baker WL, Schoennagel T, Moyle PB (2006) Managing fire-prone forests
in the western United States. Frontiers in Ecology and the Environment 4:481-487.

Oberhauser KS, Brinda SJ, Weaver S, Moon RD, Manweiler SA, Read N (2006) Growth and
survival of monarch butterflies (Lepidoptera: Danaidae) after exposure to permethrin
barrier treatments. Environmental Entomology 35:1626-1634.

Oberhauser KS, Manweiler SA, Lelich R, Blank M, Batalden RV, De Anda A (2009) Impacts of
ultra-low volume resmethrin applications on non-target insects. Journal of the American
Mosquito Control Association 25:83-93.

Oberhauser K, Wiederholt R, Diffendorfer JE, Semmens D, Ries L, Thogmartin WE, Lopez-
Hoffman L, Semmens B (2017) A trans-national monarch butterfly population model and
implications for regional conservation priorities. Ecological Entomology 42:51-60.

Parisien MA, Moritz MA (2009) Environmental controls on the distribution of wildfire at multiple spatial scales. Ecological Monographs 79:127-154.

Parisien MA, Snetsinger S, Greenberg JA, Nelson CR, Schoennagel T, Dobrowski SZ, Moritz MA (2012) Spatial variability in wildfire probability across the western United States. International Journal of Wildland Fire 21:313-327.

Parks SA, Miller C, Abatzoglou JT, Holsinger LM, Parisien MA, Dobrowski SZ (2016) How will climate change affect wildland fire severity in the western US? Environmental Research Letters 11:035002, 11 pp.

Parks SA, Miller C, Parisien MA, Holsinger LM, Dobrowski SZ, Abatzoglou J (2015) Wildland fire deficit and surplus in the western United States, 1984–2012. Ecosphere 6:1-13.

Parolo G, Rossi G, Ferrarini A (2008) Toward improved species niche modeling: *Arnica montana* in the Alps as a case study. Journal of Applied Ecology 45:1410–1418.

Pennay M, Law B, Lunney D (2011) Review of the distribution and status of the bat fauna of New South Wales and the Australian Capital Territory. In: Law B, Eby P, Lunney D, Lumsden L (eds), The Biology and Conservation of Australasian Bats, Royal Zoological Society of New South Wales, Mosman, Australia, pp. 226-256.

Perez-Riverol Y, Kuhn M, Vizcaíno JA, Hitz MP, Audain E (2017) Accurate and fast feature selection workflow for high-dimensional omics data. PloS One 12:e0189875.

Peterson RK, Preftakes CJ, Bodin JL, Brown CR, Piccolomini AM, Schleier JJ (2016) Determinants of acute mortality of *Hippodamia convergens* (Coleoptera: Coccinellidae) to ultra-low volume permethrin used for mosquito management. PeerJ 4:e2167.

Phillips SJ, Dudík M (2008) Modeling of species distributions with Maxent: new extensions and a comprehensive evaluation. Ecography 31:161-175.

Phillips SJ, Anderson RP, Schapire RE (2006) Maximum entropy modeling of species
geographic distributions. Ecological Modelling 190:231-259.

Pierce AK, Dinsmore SJ, Jorgensen D, Wunder MB (2017) Migration routes and timing of
Mountain Plovers revealed by geolocators. Journal of Field Ornithology 88:30-38.

Pleasants J (2017) Milkweed restoration in the Midwest for monarch butterfly recovery: estimates
of milkweeds lost, milkweeds remaining and milkweeds that must be added to increase the
monarch population. Insect Conservation and Diversity 10:42-53.

Pleasants JM, Zalucki MP, Oberhauser KS, Brower LP, Taylor OR, Thogmartin WE (2017)
Interpreting surveys to estimate the size of the monarch butterfly population: Pitfalls and
prospects. PloS One 12:e0181245.

Pollack JB, Cleveland A, Palmer TA, Reisinger AS, Montagna PA (2012) A restoration
suitability index model for the Eastern oyster (*Crassostrea virginica*) in the Mission-
Aransas Estuary, TX, USA. PLoS One 7:e40839.

Poor EE, Loucks C, Jakes A, Urban DL (2012) Comparing habitat suitability and connectivity
modeling methods for conserving pronghorn migrations. PLoS One 7:e49390.

Porfirio LL, Harris RM, Lefroy EC, Hugh S, Gould SF, Lee G, Bindoff NL, Mackey B (2014)
Improving the use of species distribution models in conservation planning and
management under climate change. PLoS One 9:e113749.

Quillfeldt P, Masello JF, Navarro J, Phillips RA (2013) Year-round distribution suggests spatial
segregation of two small petrel species in the South Atlantic. Journal of Biogeography
40:430-441.

R Core Team (2018) R: A language and environment for statistical computing. R Foundation for
Statistical Computing, Vienna, Austria. Avalaible at https://www.R-project.org/ (18 April
2018)

Radosavljevic A, Anderson RP (2014) Making better Maxent models of species distributions:
complexity, overfitting and evaluation. Journal of Biogeography 41:629-643.

Rao RS, Girish MS (2007) Road kills: Assessing insect casualties using flagship taxon. Current
Science 25:830-837.

Räsänen O, Pohjalainen J (2013) Random subset feature selection in automatic recognition of
developmental disorders, affective states, and level of conflict from speech. In:
INTERSPEECH 2013, 25-29 August, 2013, Lyons, France, pp. 210-214. Available at
https://pdfs.semanticscholar.org/5748/ed370ce60684c34e2caae4f860244998ca84.pdf (19
April 2018)

Raxworthy CJ, Ingram CM, Rabibisoa N, Pearson RG (2007) Applications of ecological niche
modeling for species delimitation: a review and empirical evaluation using day geckos
(*Phelsuma*) from Madagascar. Systematic Biology 56:907-923.

Rayner MJ, Taylor GA, Gaskin CP, Dunphy BJ (2017) Seasonal activity and unpredicted polar
front migration of northern New Zealand Common Diving Petrels (*Pelecanoides
urinatrix*). Emu-Austral Ornithology 117:290-298.

Rendón-Salinas E, Martínez-Meza F, Martínez-Pacheco A, Cruz-Piña M (2018) Superficie
forestal ocupada por las colonias de hibernación de la mariposa monarca en México
durante diciembre de 2017. WWF-Mexico, DF. 4 pp. Available at:
http://awsassets.panda.org/downloads/2017_Monitoreo_Mariposa_Monarca_en_Mexico_
2017-2018.pdf (5 September 2018)

145

Ries L, Debinski DM, Wieland ML (2001) Conservation value of roadside prairie restoration to butterfly communities. Conservation Biology 15:401-411.

Ries L, Taron DJ, Rendón-Salinas E (2015) The disconnect between summer and winter monarch trends for the eastern migratory population: Possible links to differing drivers. Annals Entomological Society of America 108:691-699.

Ries L, Taron DJ, Rendón-Salinas E, Oberhauser KS (2015) Connecting eastern monarch population dynamics across their migratory cycle. In: Oberhauser KS, Nail KR, Altizer S (eds), Monarchs in a Changing World: Biology and Conservation of an Iconic Butterfly, Cornell University Press, Ithaca, New York, pp. 268-281.

Roberts DR, Bahn V, Ciuti S, Boyce MS, Elith J, Guillera-Arroita G, Hauenstein S, Lahoz-Monfort JJ, Schröder B, Thuiller W, Warton DI, Wintle BA, Hartig F, Dormann CF (2017) Cross-validation strategies for data with temporal, spatial, hierarchical, or phylogenetic structure. Ecography 40:913-929.

Rodewald, AD, Gehrt SD (2014) Wildlife population dynamics in urban landscapes. In: McCleery RA, Moorman CE, Peterson MN (eds), Urban Wildlife Conservation: Theory and Practice, Springer, Boston, Massachusetts, pp. 117-147.

Roger E, Ramp D (2009) Incorporating habitat use in models of fauna fatalities on roads. Diversity and Distributions 15:222-231.

Robinne, FN, Parisien, MA, Flannigan, M (2016) Anthropogenic influence on wildfire activity in Alberta, Canada. International Journal of Wildland Fire 25:1131-1143.

Rogers BM, Neilson RP, Drapek R, Lenihan JM, Wells JR, Bachelet D, Law BE (2013) Impacts of climate change on fire regimes and carbon stocks of the US Pacific Northwest. Journal of Geophysical Research: Biogeosciences 116:G03037.

Rokach L (2005) Ensemble methods for classifiers. In: Maimon, O., Rokach, L (eds), Data

    Mining and Knowledge Discovery Handbook, Springer-Verlag, New York, New York,

    pp. 957-980.

Runge CA, Martin TG, Possingham HP, Willis SG, Fuller RA (2014) Conserving mobile

    species. Frontiers in Ecology and the Environment 12:395-402.

Rytwinski T, Soanes K, Jaeger JA, Fahrig L, Findlay CS, Houlahan J, Van Der Ree R, van der

    Grift EA (2016) How effective is road mitigation at reducing road-kill? A meta-analysis.

    PLoS One 11:e0166941.

Samways MJ (1994) Insect Conservation Biology, Chapman & Hall, London, 358 pp.

Santhosh S, Basavarajappa S (2014) Road mortality of migrant butterflies [Nymphalidae:

    Danaiane] at national highway-209 in Chamarajanagar District of Karnataka,

    India. Indian Journal of Applied Research 4:553-557. Available at:

    https://www.worldwidejournals.com/indian-journal-of-applied-research-

    (IJAR)/fileview.php?val=September_2014_1492849834__166.pdf (18 October 2018)

Santos SM, Marques JT, Lourenço A, Medinas D, Barbosa AM, Beja P, Mira A (2015)

    Sampling effects on the identification of roadkill hotspots: implications for survey design.

    Journal of Environmental Management 162:87-95.

Schmidt-Koenig K (1985) Migration strategies of monarch butterflies (*Danaus plexippus* (L.);

    Danaidae; Lepidoptera). In: Rankin MA (ed) Migration: Mechanisms and Adaptive

    Significance, University of Texas Contributions Marine Science 27 (Supplement),

    Austin, Texas, pp. 786-798.

Schoennagel T, Balch JK, Brenkert-Smith H, Dennison PE, Harvey BJ, Krawchuk MA,

    Mietkiewicz N, Morgan P, Moritz MA, Rasker R, Turner MG (2017) Adapt to more

wildfire in western North American forests as climate changes. Proceedings of the National Academy of Sciences 114:4582-4590.

Schumann G, Di Baldassarre G, Bates D (2009) The utility of spaceborne radar to render flood inundation maps based on multialgorithm ensembles. IEEE Transactions on Geoscience and Remote Sensing 47:2801-2807.

Schwartz MW (2012) Using niche models with climate projections to inform conservation management decisions. Biological Conservation 155:149-156.

Seiler A, Helldin JO (2006) Mortality in wildlife due to transportation. In: Davenport J, Davenport JL (eds), The Ecology of Transportation: Managing Mobility for the Environment, Springer, Dordrecht, pp. 165-189.

Seshadri KS, Ganesh T (2011) Faunal mortality on roads due to religious tourism across time and space in protected areas: A case study from south India. Forest Ecology and Management 262:1713-1721.

Shilling FM, Waetjen DP (2015) Wildlife-vehicle collision hotspots at US highway extents: scale and data source effects. Nature Conservation 11:41-60.

Skórka P, Lenda M, Moroń D, Kalarus K, Tryjanowski P (2013) Factors affecting road mortality and the suitability of road verges for butterflies. Biological Conservation 159:148-157.

Smith AB (2013) On evaluating species distribution models with random background sites in place of absences when test presences disproportionately sample suitable habitat. Diversity and Distributions 19:867-872.

Smith JA, Deppe JL (2008) Space-based ornithology: Studying bird migration and environmental change in North America. In: Neale CMU, Owe M, D'Urso G (eds) Remote Sensing for Agriculture, Ecosystems, and Hydrology X, 15-19 September, 2008,

Cardiff, Wales, United Kingdom. Society of Photographic Instrumentation Engineers

Press, Cardiff, Wales, 7104:710402. Available at

https://ntrs.nasa.gov/archive/nasa/casi.ntrs.nasa.gov/20090006863.pdf   (26 June 2018)

Soluk DA, Zercher DS, Worthington AM (2011) Influence of roadways on patterns of mortality

and flight behavior of adult dragonflies near wetland areas. Biological Conservation

144:1638-1643.

Somol P, Novovicová J, Pudil P (2010) Efficient feature subset selection and subset size

optimization. In: Herout A (ed), Pattern Recognition Recent Advances, InTech, Rijeka,

Croatia, pp. 75-97. Available at: https://www.intechopen.com/books/pattern-recognition-

recent-advances/efficient-feature-subset-selection-and-subset-size-optimization   (6

January 2018)

Stavros EN, Abatzoglou JT, McKenzie D, Larkin NK (2014) Regional projections of the

likelihood of very large wildland fires under a changing climate in the contiguous

Western United States. Climatic Change 126:455-468.

Steffy G (2015) Trends observed in fall migrant monarch butterflies (Lepidoptera: Nymphalidae)

east of the Appalachian Mountains at an inland stopover in southern Pennsylvania over

an eighteen year period. Annals of the Entomological Society of America 108:718-728.

Stockwell D, Peters D (1999) The GARP modeling system: problems and solutions to automated

spatial prediction. International Journal of Geographical Information Science 13:143-58.

Stracuzzi DJ (2007) Randomized feature selection. In: Liu H, Motoda H (eds), Computational

Methods of Feature Selection, CRC Press, Boca Raton, Florida, pp. 41-62.

Swain S, Hayhoe K (2015) CMIP5 projected changes in spring and summer drought and wet

conditions over North America. Climate Dynamics 44:2737-2750.

Synes NW, Osborne PE (2011) Choice of predictor variables as a source of uncertainty in continental-scale species distribution modeling under climate change. Global Ecology and Biogeography 20:904-914.

Taiwan Environmental Protection Administration (2010) Environmental Inspection: Highways yield to flyways– EPA takes up butterfly conservation. Environmental Policy Monthly (Environmental Protection Administration, R.O.C. [Taiwan]) 13:9-10. Available at: https://www.epa.gov.tw/cpDownloadCtl.asp?id=61993 (18 October 2018)

Tang J, Alelyani S, Liu H (2015) Feature selection for classification: A review. In: Aggarwal, CC (ed), Data Classification: Algorithms and Applications, CRC Press, Boca Raton, Florida, pp. 37-58.

Thibaud E, Petitpierre B, Broennimann O, Davison AC, Guisan A (2014) Measuring the relative effect of factors affecting species distribution model predictions. Methods in Ecology and Evolution, 5:947-955.

Thogmartin WE, Wiederholt R, Oberhauser K, Drum RG, Diffendorfer JE, Altizer S, Taylor OR, Pleasants J, Semmens D, Semmens B, Erickson R, Libby K, Lopez-Hoffman L (2017) Monarch butterfly population decline in North America: identifying the threatening processes. Royal Society Open Science 4:170760.

Thompson SK (1990) Adaptive cluster sampling. Journal of the American Statistical Association 85:1050-1059.

Tok CV, Ayaz D, Cicek K (2011) Road mortality of amphibians and reptiles in the Anatolian part of Turkey. Turkish Journal of Zoology 35:851-857.

Trabucco A, Zomer RJ (2010) Global Soil Water Balance Geospatial Database. Consultive Group on International Agricultural Research (CGIAR)- Consortium for Spatial

Information, Washington, DC. Available at: http://www.cgiar-csi.org/data/global-high-resolution-soil-water-balance (11 January 2017)

Tracy JL, Kantola T, Baum KA, Coulson RN (2018a) Modelling fall migration pathways and spatially identifying potential migratory hazards for the eastern monarch butterfly. Manuscript submitted for publication.

Tracy JL, Trabucco A, Lawing AM, Giermakowski T, Tchakerian M, Drus GM, Coulson RN (2018b) Random subset feature selection of ecological niche models for wildfire activity in western North America. Ecological Modelling 383:52-68.

Tsvetkov N, Samson-Robert O, Sood K, Patel HS, Malena DA, Gajiwala PH, Maciukiewicz P, Fournier V, Zayed A (2017) Chronic exposure to neonicotinoids reduces honey bee health near corn crops. Science 356:1395-1397.

Tuanmu MN, Jetz W (2014) A global 1-km consensus land-cover product for biodiversity and ecosystem modeling. Global Ecology and Biogeography 23:1031-1045.

US Fish and Wildlife Service (USFWS) (2018) Federal Aviation Administration (FAA) wind turbine location data. May 2018 data for built turbines (Determined with built date). Ecological Services, Southwest Region, Albuquerque, New Mexico. Available at https://www.fws.gov/southwest/es/Energy_Wind_FAA.html (9 June 2018)

US Geological Survey (USGS) (2018) U.S. wind turbine database. Available at https://eerscmap.usgs.gov/uswtdb/viewer/#3/37.25/-96.25 (8 June 2018)

Vangaurdia (2016) They build in Saltillo sanctuary for the monarch butterfly. 21 September 2016. Available at: https://www.vanguardia.com.mx/articulo/construyen-en-saltillo-santuario-para-la-mariposa-monarca (25 April 2018)

Veloz SD (2009) Spatially autocorrelated sampling falsely inflates measures of accuracy for
presence-only niche models. Journal of Biogeography 36:2290-2299.

Verbruggen H (2017) MMS: Maxent Model Surveyor, v.1.0.7. Available from
http://phycoweb.net/software/MMS/ (11 October 2017)

Verbruggen H, Tyberghein L, Belton GS, Mineur F, Jueterbock A, Hoarau G, Gurgel FD, De
Clerck O (2013) Improving transferability of introduced species' distribution models:
new tools to forecast the spread of a highly invasive seaweed. PLoS One 8:e68337.

Vidal O, Rendón-Salinas E (2014) Dynamics and trends of overwintering colonies of the
monarch butterfly in Mexico. Biological Conservation 180:165-175.

Vidal O, López-García J, Rendón-Salinas E (2014) Trends in deforestation and forest
degradation after a decade of monitoring in the Monarch Butterfly Biosphere Reserve in
Mexico. Conservation Biology 28:177-186.

Visintin C, Van Der Ree R, McCarthy MA (2016) A simple framework for a complex problem?
Predicting wildlife–vehicle collisions. Ecology and Evolution 6:6409-6421.

Visintin C, Van Der Ree R, McCarthy MA (2017) Consistent patterns of vehicle collision risk
for six mammal species. Journal of Environmental Management 201:397-406.

Warren DL, Seifert SN (2011) Ecological niche modeling in Maxent: the importance of model
complexity and the performance of model selection criteria. Ecological Applications
21:335-342.

Williams HM, Willemoes M, Thorup K (2017) A temporally explicit species distribution model
for a long distance avian migrant, the common cuckoo. Journal of Avian Biology
48:1624-1636.

Wilson D (2009) Guidelines for computing MaxEnt model output values from a lambdas file. Notes, Macquarie University, Department of Biological Sciences, New South Wales, Australia, 6 pp. Available from http://gsp.humboldt.edu/olm_2016/Courses/GSP_570/Learning%20Modules/10%20Blue Spray_MaxEnt_Uncertinaty/MaxEnt%20lambda%20files.pdf (8 February 2017)

Witynski ML, Bonter DN (2018) Crosswise migration by Yellow Warblers, Nearctic-Neotropical passerine migrants. Journal of Field Ornithology 89:37-46.

WorldClim (2017) WorldClim Version 1. Available from http://www.worldclim.org/version1 (6 March 2018)

Worton BJ (1989) Kernel methods for estimating the utilization distribution in home-range studies. Ecology 70:164-168.

Yamada Y, Sasaki H, Harauchi Y (2010) Composition of road-killed insects on coastal roads around Lake Shikotsu in Hokkaido, Japan. Journal of Rakuno Gakuen University 34:177-184.

Yost AC, Petersen SL, Gregg M, Miller R (2008) Predictive modeling and mapping sage grouse (*Centrocercus urophasianus*) nesting habitat using Maximum Entropy and a long-term dataset from Southern Oregon. Ecological Informatics 3:375-386.

Zeng Y, Low BW, Yeo DC (2016) Novel methods to select environmental variables in MaxEnt: A case study using invasive crayfish. Ecological Modelling 341:5-13.

Zhang L, Liu S, Sun P, Wang T, Wang G, Zhang X, Wang L (2015) Consensus forecasting of species distributions: the effects of Niche model performance and Niche properties. PloS One 10:e0120056.

Zhou Y, Zhang R, Wang S, Wang F (2018) Feature selection method based on high-resolution remote sensing images and the effect of sensitive features on classification accuracy. Sensors 18 doi:10.3390/s18072013.

Zomer RJ, Trabucco A, Bossio DA, van Straaten O, Verchot LV (2008) Climate change mitigation: A spatial analysis of global land suitability for clean development Mechanism Afforestation and Reforestation. Agric Ecosyst Environ 126: 67-80. Publication and data available from CGIAR Consortium for Spatial Information- Global aridity and PET database: http://www.cgiar-csi.org/data/global-aridity-and-pet-database (11 January 2017)

Zomer RJ, Bossio DA, Trabucco A, Yuanjie L, Gupta DC, Singh VP (2007) Trees and water: smallholder agroforestry on irrigated lands in northern India. Colombo, Sri Lanka: International Water Management Institute. pp 45. (IWMI Research Report 122). Publication and data available from CGIAR Consortium for Spatial Information- Global aridity and PET database: http://www.cgiar-csi.org/data/global-aridity-and-pet-database (11 January 2017)

ZunZun.com (2018) ZunZunSite3 online curve fitting and surface fitting website. http://zunzun.com (16 October 2018)

APPENDIX A

(CHAPTER II)*

Methods

Fire Occurrence Data

Fire occurrence data were in the form of separate 30 m resolution categorical rasters of wildland fire burn severity classes. Burn severity classification data from the LANDFIRE Disturbance database for 1999–2014 included some MTBS data and additional local agency derived data (LANDFIRE, 2016; Rollins, 2009). The combined MTBS and LANDFIRE data included four classes (Schwind, 2008) of large wildland fire burn severities: unburned, low, moderate, and high (e.g., Hamilton and Hann, 2015). Aggregation and resampling tools in ArcGIS ver. 10.3 (ESRI Inc., Redlands, California) were used to generalize the 30 m resolution MTBS and LANDFIRE rasters to ca. one km resolution before conversion to presence points. All burn severity presence, absence, and background point data were randomly thinned using R software to a maximum of 20,000 points per category to improve computational efficiency.

In order to allow a more simplified and accurate binary fire frequency classification for each of the three burn severity classes, all fire frequency data were pooled into two classes: zero fires in 31 years, and one or more fires over 31 years. The Mean Fire Interval (MFI; NWCG, 2016) was calculated for these two fire frequency classes over the western North America background evaluation extent as the 31-year period divided by the number of fire presences per one km cell plus one. This yields an MFI greater than 16.5 years for the no fire frequency absence class,

---

and an MFI less than or equal to 16.5 years for the presence class of one or more fires in 31 years (maximum MFI = 31/(1+1), or 16.5 years).

The MTBS burn severity classes were originally derived from interpretations of the spectral index of the difference Normalized Burn Ratio (dNBR) from multitemporal Landsat satellite imagery in order to correlate with the ground based Composite Burn Index (CBI) rating system of Key and Benson (2006) (Eidenshink et al., 2007; Finco et al., 2012). Schwind (2008) provides summary descriptions of field characteristics for the main MTBS burn severity classes that were modeled. The Monitoring Trends in Burn Severity (MTBS) low burn severity class represents a large fire with slight alterations to most of the ecosystems, although some components may have severe damage. Most litter would be consumed with some change in duff and woody debris, and low vegetation may be significantly scorched, but recovery is generally fairly quick within a year or two. Saplings of western conifers can suffer up to 50% mortality and up to 25% mortality can occur in intermediate and large overstory trees. Fires of the MTBS high burn severity class encompass large areas with fairly consistent loss of all litter and a loss of almost all herbaceous cover and duff, exposing 50% of newly exposed mineral or rock. Recovery of herbaceous vegetation and shrubs is usually evident within a few years. In forests, there is deep charring and partial consumption of woody debris, and 75% mortality of overstory trees. Overstory tree damage is long lasting, and forest development may begin within one to three years but take several decades to complete. Fires of the MTBS moderate burn severity class have intermediate characteristics between the above described low and high severity classes (Schwind 2008).

The original 30 m resolution MTBS and LANDFIRE burn severity category rasters for each year over the coterminous United States were clipped using ArcGIS software to include

156

only the states of western North America in which MTBS considers 405 ha as a minimum fire size. Separate binary (1/0) rasters of low, moderate, and high wildland burn severity were derived from the clipped rasters, and aggregated by sum to 990 × 990 m cells (or 33 × 33 cells of 30 m resolution to approach one km size) in the original Albers Equal Area Conic Projection of NAD83 datum. The resulting 990 × 990 m burn severity cells for each category were then categorized so that only cells having a value of greater than or equal to 544, representing at least 50% of the original 1,089 component 30 × 30 m cells, were considered as burn "presence" cells for large wildland fires and assigned a value of "one". Consequently, large wildland fire burn presence categories represent burn extents of about 49 to 98% (or 49 to 98 ha.) per year for each 1km resolution raster cell, which approximates at least the area of a National Wildfire Coordinating Group (NWCG, 2016) Class D fire (100 to 299.9 acres, or 40 to 121 ha.). The resulting yearly burn category presence rasters were resampled to 1000 × 1000 m using nearest neighbor interpolation for categorical data. These yearly one km resolution burn severity category rasters were then projected to a Geographic Coordinate System of WGS84 datum, and resampled and aligned to match the one km resolution environmental data.

For each year of overlap between MTBS and LANDIFIRE data (1999–2012), the occurrences for each burn severity category were combined in order to include MTBS data that was not included in the LANDFIRE data set. The aligned burn severity rasters for each class and year were then summed to yield a raster of fire presence frequency per 31 years at one km resolution. Preliminary investigations using 84 variables with a random forest multiclass classifier (Brieman, 2001; R caret package, Kuhn, 2008) provided poor discrimination among the spatial distributions of multiple fire frequency classes, such as one fire versus two fires per 31

years (results not shown). Consequently, single frequency classes of burn severity rasters were converted to point shapefiles for developing MaxEnt wildfire activity models.

Wildfire Activity Models

Environmental Variables

Seasonal climatic indices are important variables in wildfire activity models (e.g., Kalabokidis et al., 2002; Dillon et al., 2011; Parisien and Mortiz, 2009; Littell and Gwozdz, 2011; Liu and Wimberly, 2016). Consequently, novel hemispherically adjusted global quarterly seasonal climatic indices were calculated, such as mean monthly rainfall for the summer quarter (*prec_sumq*). Driscoll and Yee Fong (1992) suggested a moisture correction factor was needed for their continentality index. Therefore, a novel modified Driscoll and Yee Fong continentality index (*cont_dfmo*; Driscoll and Yee Fong, 1992) was calculated, which incorporates a moisture correction factor based on actual evapotranspiration divided by potential evapotranspiration (AET/PET) (Figure A.1).

The 57 climatic indices are all based upon the one km resolution WorldClim global grids of monthly precipitation and the monthly mean, minimum and maximum temperatures of Hijmans et al. (2005). The climatic indices were divided into three subsets of 19 indices (Tables II.1, A.1). The first is the Bioclim indices provided by WorldClim (2017). The second is supplementary climatic (suppclim) indices that include 12 seasonal quarterly and three annual indices of precipitation (*prec*) and minimum (*tmin*) and maximum (*tmax*) monthly temperatures, and four other bioclimatic indices (the first three of which are from Rivas-Martinez et al. 1999): (1) Rivas-Martinez (RM) ombrothermic index (*ombro_index*), (2) RM continentality index (*cont_index*), (3) RM thermicity index (*therm_index*), and (4) the Effective Warmth Index (*ew_indx*) of Chiu et al. (2012). The third group of climatic indices is the actual and potential

158
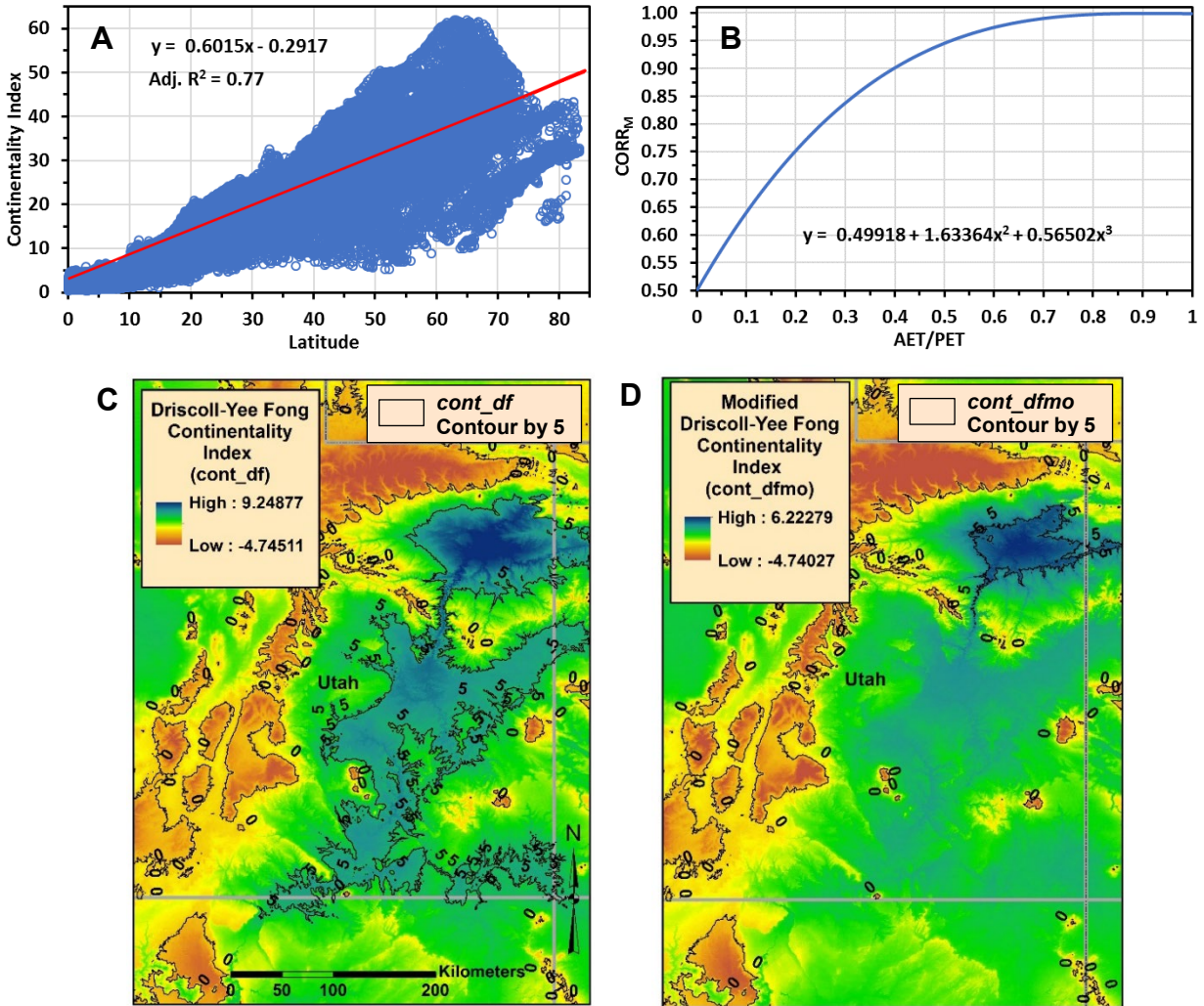
Figure A.1. (A) Global continentality versus absolute value of latitude (n = 56,606) with linear regression line (red); distance from a given point to the line is the Driscoll Yee Fong continentality index, *cont_df*, for that point (corresponds to Figure 2 of Driscoll and Yee Fong, 1992); (B) Novel moisture correction factor (CORR$_M$) based on third order cubic function of AET/PET ratio; when multiplied with *cont_df* yields modified *cont_df* (*cont_dfmo*); (C) *cont_df* for southeastern Utah with spurious maxima above five; (D) *cont_dfmo* for southeastern Utah with spurious maxima of five eliminated by CORR$_M$ (Tracy et al., 2018b).

159

Table A.1. Sources for various climatic and geomorphologic indices (Table II.1) (Tracy et al., 2018b).

Index	Source
Climatic Indices	
Effective Warmth Index (from mean monthly temperatures × 10 above 5ºC)	Chiu et al., 2012
Rivas-Martinez (RM) ombrothermic index (from monthly MTMP and P; Rivas-Martinez et al., 1999)	Rivas-Martinez et al., 1999
RM continentality index (TMAX – TMIN) × 10 (CONT)	Rivas-Martinez et al., 1999
Total annual reference evapotranspiration from Hargreaves model (PETH) (mm)	Zomer et al.; 2007, 2008
Thornwaite summer concentration thermal efficiency (summer PETH/annual PETH) × 1000	Thornwaite, 1948
Willmott and Feddema climate moisture index (from total annual PETH and PREC) × 1000	Willmott and Feddema, 1992
Total annual actual evapotranspiration from Thornwaite-Mather water balance model (TMWBM) (AETT) (mm)	Trabucco and Zomer, 2010
Modified Continentality index of Driscoll-Yee Fong	Driscoll-Yee Fong, 1992; This Study
Climate water deficit (total annual PETH – TMAET)	Stephenson, 1998
Geomorphologic Indices	
Matonne's Modified Dissection Coefficient (Dissection, DISS)	Evans, 1972
Topographic Position Index (TPI; = Slope Position Index, SPI)	Guisan et al., 1999
Elevation Relief Ratio (ERR, = Surface Relief Ratio, SRR)	Pike and Wilson, 1971
Compound Topographic Index (CTI, = Topographic Wetness Index, TWI)	Moore et al., 1993
Heat Load Index (HLI)	McCune and Keon, 2002
Integrated Moisture Index (IMI)	Iverson et al., 1997
Site Exposure Index (SEI)[a]	Balice et al., 2000
Slope Cosine Aspect Index (SCAI)	Stage, 1976

[a]The *sei* is similar to the *Solar Radiation Aspect Index* of Roberts and Cooper (1989), which was used by Dillon et al. (2011).

evapotranspiration indices (AET-PET indices) which were derived from monthly Hargreaves potential evapotranspiration (PET, *peth*) and Thornwaite-Mather actual evapotranspiration (AET, *aett*) grids developed by Zomer et al. (2007, 2008) and Trabucco and Zomer (2010), respectively. The AET-PET indices include 12 quarterly (winter, spring, summer and autumn; staring with winter in northern hemisphere, January, February, and March) and three annual indices of AET, PET, and AET/PET (*etrt*), as well as four other indices: (1) the Thornwaite (1948) summer concentration of thermal efficiency (*tpeths_tpetha*), (2) the climate water deficit (*cwd_ann*, AET – PET; Stephenson 1998), (3) the Willmott Feddema climate moisture index (*im_index*, Willmott and Feddema 1992), and (4) a novel modified version of the Driscoll and Yee Fong (1992) continentality index (*cont_dfmo*), which includes a new moisture correction factor derived from the annual AET/PET ratio (*etrt_ann*) (Table II.1).

The Willmott Feddema climate moisture index (*im_index*; Willmott and Feddema, 1992), is calculated using total annual precipitation (*tprec_ann*) and total annual potential evapotranspiration (*tpeth_ann*) from the following conditional formulae: if *prec_ann* ≥ *tpeth_ann*, then *im_index* = 1 – (*tpeth_ann*/*tprec_ann*); if both *prec_ann* and *tpeth_ann* are zero, then *im_index* = 0; if *tprec_ann* < *tpeth_ann*, then *im_index* = (*tprec_ann*/*tpeth_ann*) – 1.

The continentality index of Driscoll and Yee Fong (1992), *cont_df*, is calculated as the residual (or difference) between the annual temperature range (Rivas-Martinez (RM) continentality index, not multiplied by 10; *cont_index*) and the predicted value of *cont_indx* based on a least squares linear regression relationship with the absolute value of latitude (Figure A.1A). Driscoll and Yee Fong (1992) suggested accounting for moisture effects in order to eliminate spurious maxima in *cont_df* around the value of five in the southwestern US near southeastern Utah (their Figure 3). A novel moisture correction factor ($CORR_M$) was created to

161

multiply with *cont_df* and yield modified *cont_df*, or *cont_dfmo*, such that *cont_dfmo* = *cont_df* ×

CORR$_M$. The value of *CORR$_M$* is calculated by the following third order cubic function of the

Actual Evapotranspiration/Potential Evapotranspiration ratio (*AET/PET*, *etrt_ann*, floating point,

ranging from zero to one) that reduces *cont_df* by a maximum of 50% at zero *AET/PET*, with the

reduction sharply reduced to 25% at 0.2 *AET/PET*, and gradually reducing to 1% at 0.7

AET/PET: *CORR$_M$* = 0.49918 + 1.56849(*AET/PET*) - 1.63364(*AET/PET*)^2 + 0.56502(*AET/PET*)^3

(Figure A.1B). This correction factor effectively eliminates in *cont_dfmo* the spurious maxima of

five seen for *cont_df* in southwestern Utah (Figure A.1C-D). Additional spurious maxima in the

Taklimakan Desert of northwestern China are also eliminated by *cont_dfmo* (not shown).

All 24 of the quarterly seasonal suppclim (12) and AET-PET (12) indices are

hemispherically adjusted, in that the quarterly indices for the southern hemisphere are calculated

from monthly indices that were phase shifted by six months with respect to those for the northern

hemisphere. This hemispheric adjustment especially facilitates representation of more temperate

seasonal climates across hemispheres. However, hemispherical adjustment produces artefactual

differences in quarterly seasonal climates on either side of the equator within the Equatorial Zone

between 10ºN and 10ºS latitudes, making these 24 seasonal indices unsuitable for modeling of

phenomena or species in this region.

The sixteen topographic indices are divided into two subsets derived from the 15 arc

second resolution HydroSHEDS elevation data (Lehner et al., 2008): (1) 12 geomorphologic

indices based on the HydroSHEDs Digital Elevation Model (DEM) raster, and (2) four

hydrogeomorphologic indices based upon distances to a HydroSHEDs river network line

shapefile including maximum flow accumulations per stream reach (Table II.1). The

Geomorphometry and Gradient Metrics Toolbox for ArcGIS was utilized in calculating the ten

geomorphologic indices other than elevation and slope (Evans et al., 2014). All calculations with topographic data were conducted in Albers equal-area conic projection (NAD 83 datum) and the results were converted to non-projected geographic WGS 84 datum to match the climate variables, and resampled to one km. The hydrogeomorphologic indices represent distances to all streams (*strmdist*), and distances to three generalized stream flow classes based on the relative maximum flow accumulation according to the number of 15 arc second cells per reach. These stream flow accumulation categories were designed to each contain about one third of 301 occurrence points for the riparian obligate federally endangered Southwestern Willow Flycatcher (*Empidonax traillii extimus*) in southwestern North America: (1) low, from 100 to 5,000 cells (*strmloflodist*); (2) medium, from 5,000 to 60,000 cells (*strmmdflodist*); and (3) high, greater than 60,000 cells (*strmhiflodist*) (Table II.1).

The 17 anthropogenic indices are divided into three subsets: (1) human population indices based upon 30 arc second resolution grid cells of population density per square kilometer (CIESIN 2016, water/no value set to zero); (2) road indices derived from a Global Roads Layer shapefile for 1980 to 2010 (CIESIN and ITOS, 2013); and (3) anthropogenic land cover indices obtained from the Global 1-km Consensus Land Cover data set (Tuanmu and Jetz, 2014). For human population indices, focal statistics of year 2000 mean population densities were calculated from the using specified circular window neighborhoods (Table II.1). For the purposes of this study, high urban population density values were defined as greater than or equal to 1,500 people per square kilometer, and the minimum low urban population density was set at 300 people per square kilometer (Dijkstra and Poelman, 2014). Starting with these values, seven classes of population density per one square kilometer were defined: (1) none to sparse rural, less than 10, (2) low rural, 10 to less than 100, (3) medium rural, 100 to less than 200, (4) high rural,

200 to less than 300, (5) low urban, 300 to less than 900, (6) medium urban, 900 to less than 1,500, and (7) high urban, greater than or equal to 1,500 (Table II.1). These seven classes were then used to calculate Euclidean distances to varying population densities. For road indices, global road data from 1980 to 2010 (CIESIN and ITOS, 2013) was used to calculate distance to road and road density (km road length per square km) for specified circular windows at 15 arc second resolution in Albers Equal Area Projection, which was then converted to non-projected WGS 84 datum and resampled to one km resolution to match the WorldClim data. Anthropogenic land cover indices for the 2001–2005 period were obtained directly from EarthEnv (2016) website in the form of Global one-km Consensus Land Cover percent cover for one km^2 for two classes: (1) cultivated and managed vegetation (their Class 7), agricultural land cover (*agric_lc*), and (2) urban/built-up (their Class 9), urban land cover (*urban_lc*). The Global 1-km Consensus Land Cover variables of various vegetation types were not included since individual changes in cover of these vegetation types were not projected over time for future climate models, but climate variables were used as a proxy for current and future potential vegetation. All gridded indices were resampled and/or shifted as necessary to match the 30 arc second (1 km) resolution and grid alignment of the unprojected WorldClim data of WGS84 datum. Climatic variables rasters, other than Bioclim indices (already integer), were rounded to the nearest significant digit and converted to integer, sometimes following multiplication by 10, 100, or 1,000 in order to preserve significant digits. All non-climatic indices were integer normalized from zero to 10,000 (10K normalization; normalization of climatic grids was not done since it would interfere with range comparability across temporal climate scenarios).

Climate Scenarios

Hind casts of the HE GCM model generally perform well compared to other GCMs for southwestern North America (Sheffield et al., 2013; Langford et al., 2014). For each of the four future climate scenarios (2050 HE-RCP2.6, 2050 HE-RCP8.5, 2070 HE-RCP2.6, and 2070 HE-RCP8.5), 19 Bioclim indices from WorldClim (2017) were downloaded. Worldclim makes available GCM projections from the CMIP5 collection downscaled at very high resolution (i.e., one km) using a Delta method statistical approach.

Niche Models

Model Parameters

Both MaxEnt and Glmnet models utilize built-in feature selection with lasso L1 regularization (ridge regression L2 regularization, also available in Glmnet, was not employed). MaxEnt models were compared that employed the default beta regularization value of one (β1; standard lasso L1 regularization for MaxEnt) with zero (β0; no regularization) and seven higher values from two to 40 (β2–β40) providing progressively more stringent L1 regularization to reduce the number of parameters. Higher beta regularization values can potentially reduce model complexity and overfitting for improved model generalization (Jiménez-Valverde et al., 2008; Warren and Seifert, 2011). For individual models, the number of used environmental variables and the numbers and parameters of derived variables was recorded for each environmental variable. For MaxEnt models, this required utilizing the MaxEnt output lambdas file (Wilson, 2009; Elith et al., 2011; Halvorsen, 2013). Halvorsen (2013) noted that details on MaxEnt model parameters are very rarely provided in publications, and the MaxEnt lambdas files with all parameters and derived variables for final selected MaxEnt wildfire activity models are here provided (see Appendix B, Tables B.1-3).

165

Background Corrected Akaike Information Criterion

An R script was developed to more rapidly calculate AICc for MaxEnt using the same formula for calculating AICc from raster data with the ENMeval R package (Muscarella et al., 2014). However, instead of requiring the time-consuming generation of a MaxEnt prediction raster required for ENMeval to calculate AICc, the background AICc, $AICc_{bg}$, was calculated much more rapidly using MaxEnt samples with data (SWD) mode point RAW predictions for background and training point data (which all sum to one). Values of $AICc_{bg}$ were compared to AICc values calculated for the same MaxEnt models using the ENMeval package, and $AICc_{bg}$ was closely proportional to AICc (adjusted $R^2 = 0.90$), making it suitable for relative model comparisons (Figure A.2). In order to facilitate model ranking and statistical analysis, all models with $AICc_{bg}$ valued at infinity were omitted, and 0.001 was added to MaxEnt SWD point predictions of zero to eliminate uncommon aberrant extreme negative values of $AICc_{bg}$.

Calibration of AICc Values between GLM, Glmnet and MaxEnt Models

In order to compare AICc values from GLM and Glmnet models to $AICc_{bg}$ values of MaxEnt models, a regression-based calibration to calculate $AICc_{bg\_reg}$ for GLM and Glmnet models was performed. The calibration was based on the assumption that AICc is equivalent for linear GLM and linear MaxEnt models using the same variable subsets and training data. This assumption was supported by the combined observations that (1) the $AUC_{pa\_finaltest}$ values for the linear MaxEnt and linear GLM models were nearly equivalent ($R^2 = 0.98$; Figure A.4B), (2) there was a high correlation between $AUC_{pa\_finaltest}$ and AICc (or $AICc_{bg}$) among these models ($R^2 = 0.86$ to 0.91; Figures A.4C-D), and (3) there was a high correlation between AICc of linear GLM and $AICc_{bg}$ of linear MaxEnt models ($R^2 = 0.96$; Figure A.4E) (n = 250 per model method). For a given burn severity model, a linear relationship between AICc of GLM linear

166

Table A.2. Thirty-eight environmental predictor indices (30 arc second, one km resolution) of the 90 indices (Table II.1) used in this study that are closely related to indices found important in other studies modelling broad scale fire susceptibility in the western US and Greece (Tracy et al., 2018b).

Variable Index[a]	Consensus Variable Importance (lower values more important)[b]	Reference
25 Climatic Indices		
bio_1	38	Kalabokidis et al., 2002
bio_5	19	Kalabokidis et al., 2002; Parisien and Mortiz, 2009; Littell and Gwozdz, 2011
bio_10	36	Kalabokidis et al., 2002
bio_14	28	Parisien and Mortiz, 2009
bio_19	30	Liu and Wimberly, 2016
tmin_ann	35	Kalabokidis et al., 2002
tmin_sprq	26	Parisien and Mortiz, 2009
tmin_sumq	23	Parisien and Mortiz, 2009; Dillon et al., 2011
tmin_autq	31	Dillon et al., 2011
tmax_ann	37	Kalabokidis et al., 2002
tmax_winq	20	Parisien and Mortiz, 2009; Littell and Gwozdz, 2011
tmax_sprq	25	Parisien and Mortiz, 2009
tmax_sumq	16	Kalabokidis et al., 2002; Dillon et al., 2011; Parisien and Mortiz, 2009; Littell and Gwozdz, 2011
tmax_autq	27	Parisien and Mortiz, 2009
prec_ann	17	Kalabokidis et al., 2002; Parks et al., 2015; 2016
prec_winq	22	Parisien and Mortiz, 2009; Dillon et al., 2011
prec_sprq	15	Parisien and Mortiz, 2009; Dillon et al., 2011; Liu and Wimberly, 2016
prec_sumq	14	Kalabokidis et al., 2002; Dillon et al., 2011; Littell and Gwozdz, 2011; Abatzoglou and Kolden, 2013
prec_autq	18	Parisien and Mortiz, 2009; Dillon et al., 2011; Littell and Gwozdz, 2011
peth_sprq	33	Abatzoglou and Kolden, 2013
peth_sumq	24	Littell and Gwozdz, 2011; Abatzoglou and Kolden, 2013
taett_tann	28	Parks et al., 2015
aett_sprq	34	Littell and Gwozdz, 2011

Table A.2. Continued.

Variable Index[a]	Consensus Variable Importance (lower values more important)[b]	Reference
aett_sumq	32	Littell and Gwozdz, 2011
cwd_ann	21	Parks et al. 2015, 2016
10 Topographic Indices		
elev	1	Kalabokidis et al., 2002; Parisien and Mortiz, 2009; Dillon et al., 2011; Liu and Wimberly, 2016
slope	2	Kalabokidis et al., 2002; Dillon et al., 2011; Liu and Wimberly, 2016
diss3kr	4	Dillon et al., 2011
tpi3kr	3	Dillon et al., 2011
err3kr	6	Dillon et al., 2011
cti	9	Dillon et al., 2011
hli	5	Dillon et al., 2011
sei	8	Dillon et al., 2011
scai	7	Dillon et al., 2011
strmdist	10	Kalabokidis et al., 2002
3 Anthropogenic Indices		
medurbdist	11	Kalabokidis et al., 2002; Liu and Wimberly, 2016
roaddist	12	Kalabokidis et al., 2002; Liu and Wimberly, 2016
agric_lc	13	Kalabokidis et al., 2002

[a]See Table II.1 for index abbreviations. Period of climate variables may be an approximate match such as nearest seasonal quarter to a single month or several months. Spatial and temporal resolutions of indices among study will vary.
[b]Approximate rankings are based upon variable importance in various cited references, giving higher weight to studies comparing more variables (e.g., Parisien and Moritz, 2009, Dillon et al., 2011).

Table A.3. Ranking of variables (high to low) used in top four 15-variable MaxEnt wildfire activity models selected by random subset feature selection algorithm using joint criteria of (1) variable mean permutation importance in models where variable is present (0.6 weight), and (2) number of appearances in top four models (0.4 weight) (Tracy et al., 2018b).[a]

Low Burn Severity Models (40 of 90 variables used in top 4 models)		Moderate Burn Severity Models (36 of 90 variables used in top 4 models)		High Burn Severity Models (41 of 90 variables used in top 4 models)	
Variable	Permutation Importance, Mean ± SD (number of top four models)	Variable	Permutation Importance, Mean ± SD (number of top four models)	Variable	Permutation Importance, Mean ± SD (number of top four models)
prec_sumq*	25.1 ± 3.8 (3)	slope*	30.5 ± 3.1 (4)	slope*	27.1 ± 6.6 (4)
agric_lc*	15.6 ± 3.5 (4)	aett_sprq*	18.3 ± 3.5 (3)	bio_8	18.7 ± 6.3 (3)
bio_9	16.5 ± 6.2 (3)	agric_lc*	11.0 ± 0.7 (4)	elev*	14.8 ± 0.5 (3)
elev*	9.4 ± 3 (3)	tpeth_ann	16.8 ± 3.1 (2)	agric_lc*	9.8 ± 2.6 (4)
taett_tann*	14.5 ± 3.1 (2)	bio_9	15.6 ± 4.7 (2)	prec_winq*	26.9 ± 0 (1)
slope*	7.0 ± 1.2 (3)	etrt_sprq	22.2 ± 0 (1)	aett_winq	23.7 ± 0 (1)
prec_sprq*	17.7 ± 0 (1)	prec_sumq*	5.3 ± 1.6 (3)	bio_15	3.6 ± 3.2 (3)
etrt_ann	17.1 ± 0 (1)	bio_1*	9.3 ± 4.8 (2)	prec_autq*	15.9 ± 0 (1)
bio_14*	13.3 ± 0 (1)	cont_dfmo	7.6 ± 0.1 (2)	aett_sprq*	14.0 ± 0 (1)
etrt_sprq	11.9 ± 0 (1)	bio_8	8.0 ± 0 (1)	prec_sumq*	2.3 ± 2.6 (2)
sprurdist	3.9 ± 1.7 (2)	bio_17	2.0 ± 1.4 (2)	strmhiflodist	0.4 ± 0.2 (3)
lorurdist	3.8 ± 3.2 (2)	strmmdflodist	0.6 ± 0 (3)	bio_7	8.0 ± 0 (1)
ew_indx	2.9 ± 1.5 (2)	strmhiflodist	0.9 ± 0.7 (2)	lorurdist	0.7 ± 0.8 (2)
aett_autq	7.7 ± 0 (1)	tpi9kr	0.8 ± 0.1 (2)	hli*	0.5 ± 0 (2)
diss3kr*	0.9 ± 0.2 (2)	lourbdist	0.8 ± 0.2 (2)	roadden9kr	0.3 ± 0.2 (2)
cont_index	0.5 ± 0 (2)	bio_7	0.4 ± 0.1 (2)	strmmdflodist	0.2 ± 0.1 (2)
cwd_ann*	6.2 ± 0 (1)	roadden3kr	0.3 ± 0.1 (2)	etrt_sprq	6.2 ± 0 (1)
roadden9kr	0.3 ± 0.3 (2)	sei*	0.0 ± 0.1 (3)	aett_autq	5.5 ± 0 (1)
tpi19kr	0.3 ± 0.1 (2)	sprurdist	3.9 ± 0 (1)	peth_winq	4.2 ± 0 (1)
scai*	0.2 ± 0 (2)	aett_winq	2.8 ± 0 (1)	tmin_autq*	3.8 ± 0 (1)
peth_autq	4.0 ± 0 (1)	elev	2.6 ± 0 (1)	tpeths_tpetha	3.0 ± 0 (1)
prec_winq*	3.9 ± 0 (1)	tpi19kr	2.1 ± 0 (1)	bio_4	3.0 ± 0 (1)
bio_2	3.8 ± 0 (1)	popden	1.9 ± 0 (1)	sprurdist	2.1 ± 0 (1)

Table A.3. Continued.[a]

Low Burn Severity Models (40 of 90 variables used in top 4 models)		Moderate Burn Severity Models (36 of 90 variables used in top 4 models)		High Burn Severity Models (41 of 90 variables used in top 4 models)	
Variable	Permutation Importance, Mean ± SD (number of top four models)	Variable	Permutation Importance, Mean ± SD (number of top four models)	Variable	Permutation Importance, Mean ± SD (number of top four models)
cti*	3.2 ± 0 (1)	lorurdist	1.6 ± 0 (1)	bio_2	1.8 ± 0 (1)
cont_dfmo	3.2 ± 0 (1)	medrurdist	1.5 ± 0 (1)	bio_9	1.8 ± 0 (1)
medurbdist	3.1 ± 0 (1)	mnpopden3r	1.3 ± 0 (1)	peth_autq	1.7 ± 0 (1)
tmax_autq*	2.8 ± 0 (1)	bio_2	1.3 ± 0 (1)	imi*	1.2 ± 0 (1)
mnpopden3r	2.7 ± 0 (1)	diss3kr*	1.0 ± 0 (1)	bio_3	1.2 ± 0 (1)
bio_19*	2.3 ± 0 (1)	medurbdist*	0.6 ± 0 (1)	cont_index	1.1 ± 0 (1)
bio_8	1.8 ± 0 (1)	hiurbdist	0.6 ± 0 (1)	popden	1.1 ± 0 (1)
roadden3kr	0.8 ± 0 (1)	roaddist*	0.5 ± 0 (1)	diss3kr*	1.0 ± 0 (1)
medrurdist	0.5 ± 0 (1)	strmdist*	0.3 ± 0 (1)	sei*	0.8 ± 0 (1)
hirurdist	0.5 ± 0 (1)	mnpopden9r	0.2 ± 0 (1)	etrt_sumq	0.8 ± 0 (1)
bio_3	0.5 ± 0 (1)	hli*	0.1 ± 0 (1)	roadden19kr	0.7 ± 0 (1)
urban_lc	0.5 ± 0 (1)	tpi3kr*	0.1 ± 0 (1)	mnpopden3r	0.5 ± 0 (1)
strmhiflodist	0.5 ± 0 (1)	bio_3	0.0 ± 0 (1)	roadden3kr	0.5 ± 0 (1)
err3kr*	0.5 ± 0 (1)			bio_14	0.5 ± 0 (1)
strmloflodist	0.2 ± 0 (1)			urban_lc	0.3 ± 0 (1)
imi*	0.1 ± 0 (1)			tpi3kr*	0.2 ± 0 (1)
roadden19kr	0.0 ± 0 (1)			scai*	0.1 ± 0 (1)
				peth_sumq*	0.0 ± 0 (1)

[a]See Table II.1 for variable abbreviations and sources of variables. Asterisks (*) indicate expert selected variables from previous studies (Table A.2). Variables ranked using multi multi-objective optimization ranking by weighted joint criteria with MCDM R package. See Figures A.16-19 for examples of response curves for top ranked variables by permutation importance in the single top selected MaxEnt wildfire activity model for each burn severity (Table A.4). Darker shading indicates variables among top 10 ranked variables for all three burn severities, and lighter shading indicates variables among top 10 ranked variables for two burn severities.

Table A.4. Permutation importance of 15 variables in top selected MaxEnt wildfire activity models for three burn severities using the random subset feature selection algorithm (Tracy et al., 2018b)[a].

Permutation Importance for MaxEnt Wildfire Activity Model Variables for Three Burn Severities (Variable – Permutation Importance)		
Low	Moderate	High
bio_9 - 21.2	*slope* - 33.1	*slope* - 29
prec_sprq - 17.8	*aett_sprq* - 18.4	*aett_winq* - 23.3
etrt_sprq - 14.2	*tpeth_ann* - 16.3	*elev* - 15.9
agric_lc - 12.6	*agric_lc* - 9.4	*agric_lc* - 9.2
bio_14 - 12.2	*cont_dfmo* - 7.4	*bio_8* - 7.1
slope - 6.8	*prec_sumq* - 5.7	*etrt_sprq* - 6.5
aett_autq - 5.3	*sprurdist* - 4	*tmin_autq* - 3.4
peth_autq - 3.6	*bio_2* - 1.4	*bio_4* - 2.7
sprurdist - 3.1	*strmhiflodist* - 1.3	*sprurdist* - 1
lorurdist - 1.6	*lourbdist* - 0.9	*roadden3kr* - 0.6
strmhiflodist - 0.6	*strmmdflodist* - 0.8	*strmmdflodist* - 0.4
scai - 0.4	*roadden3kr* - 0.7	*strmhiflodist* - 0.4
err3kr - 0.3	*tpi9kr* - 0.5	*tpi3kr* - 0.3
cont_index - 0.2	*bio_3* - 0.1	*peth_sumq* - 0.2
roadden9kr - 0.1	*sei* - 0	*lorurdist* - 0.1

[a]See Table II.1 for variable abbreviations and Figures A.16-19 for response curves of selected variables.
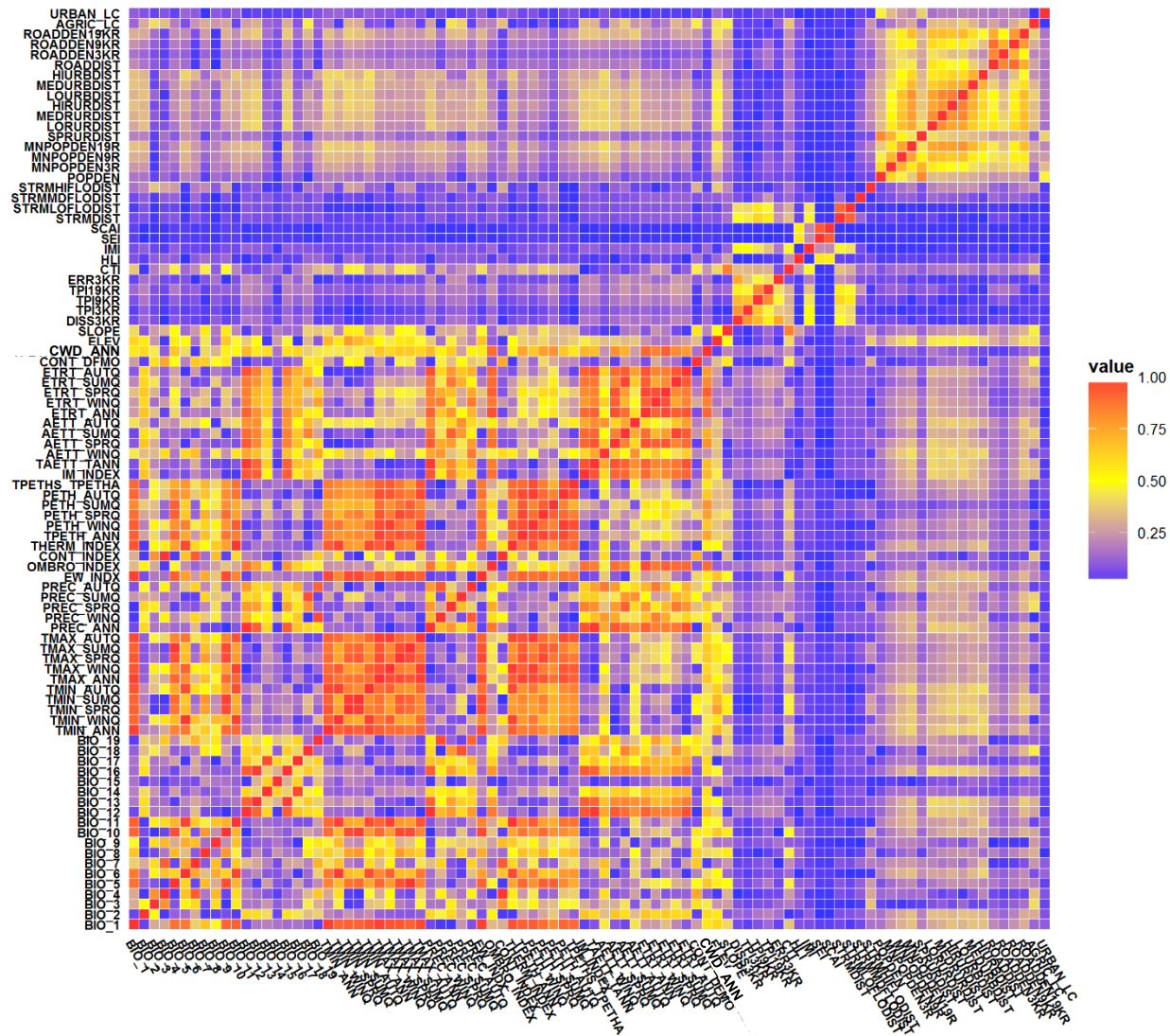
Figure A.2. Correlation heat map for 90 environmental variables (see Table II.1) using values derived from about 10,000 background points used for low burn severity wildfire activity niche models (Tracy et al., 2018b).
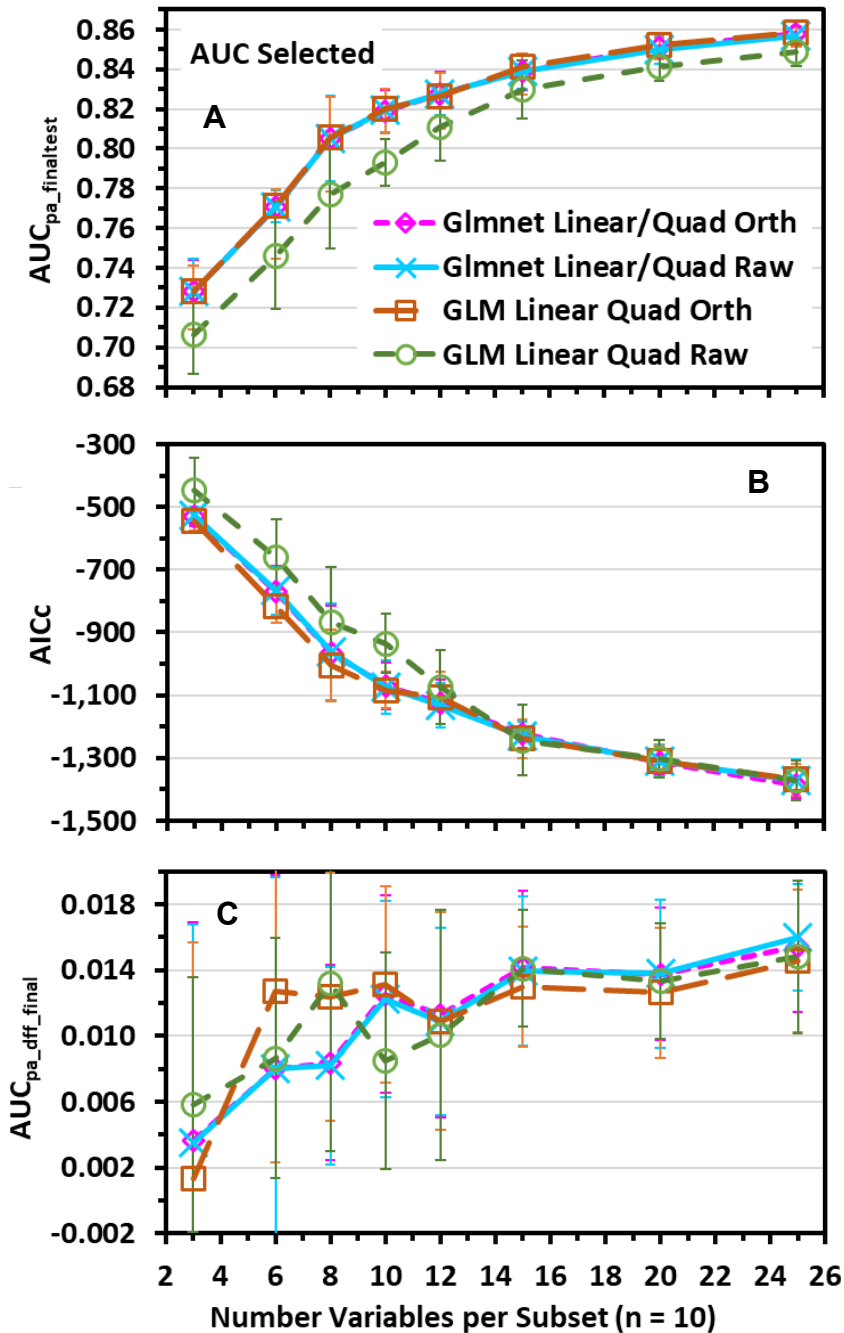
Figure A.3. Low burn severity wildfire activity model evaluation statistics (mean ± SD) for various GLM and Glmnet models with (orthogonal; orth) and without (raw) orthogonalization of linear and quadratic features: (A) $AUC_{pa\_finaltest}$, (B) $AICc_{final}$, (C) $AUC_{pa\_finaltrain}$. Models developed from top ten random subset feature selection algorithm-selected variable subsets ranked by AUC. Variable subsets were selected from 250 randomly generated variable subsets of various sizes derived from 90 variables (Tracy et al., 2018b).
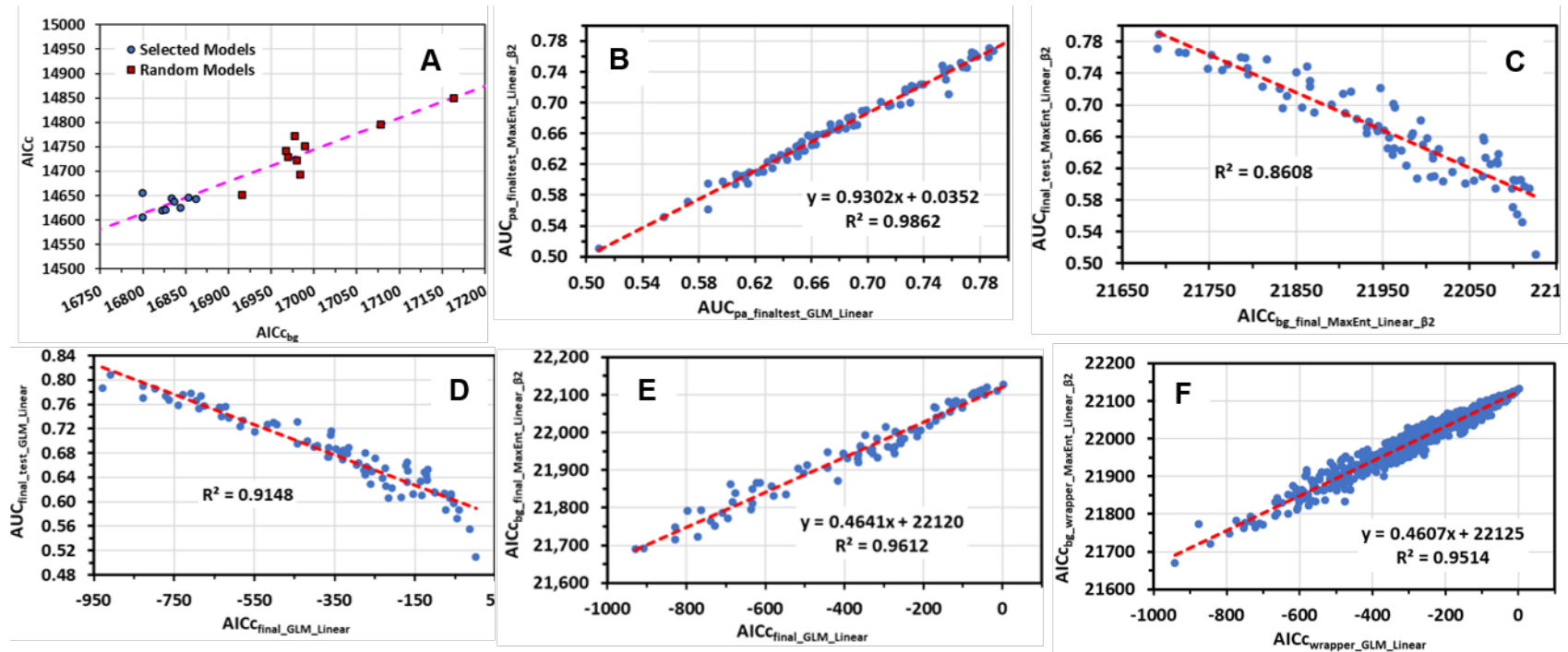
Figure A.4. (A) High burn severity MaxEnt quadratic/hinge β2 wildfire activity model AICc calculated using projected raster models by the ENMeval package versus AICc$_{bg}$ calculated using point model values for ten RSFSA selected models (AUC wrapper) and 10 random models. Models developed for eight-variable subsets out of 10,000 randomly generated subsets for high burn severity with fitted linear regression line (adj. R^2 = 0.90, P < 0.001). (B-E) Relationships between AUC$_{pa\_finaltest}$, AICc (calculated for GLM using fit and null deviance values), and AICc$_{bg}$ for various low burn severity linear MaxEnt β2 and linear GLM wildfire activity niche models (n = 250 for each model method) developed with the same training data and the same random variable subsets ranging from three to 25 variables. (F) Linear relationship between AICc$_{bg\_wrapper}$ for linear MaxEnt and AICc$_{wrapper}$ for linear GLM low burn severity wildfire activity models (n = 624) calculated using the same training data and random variable subsets ranging from three to 20 variables and using the same number of variables; used for predicting AICc$_{bg\_reg}$ for GLM and Glmnet models for comparison with MaxEnt AICc$_{bg}$ (Tracy et al., 2018b).

174
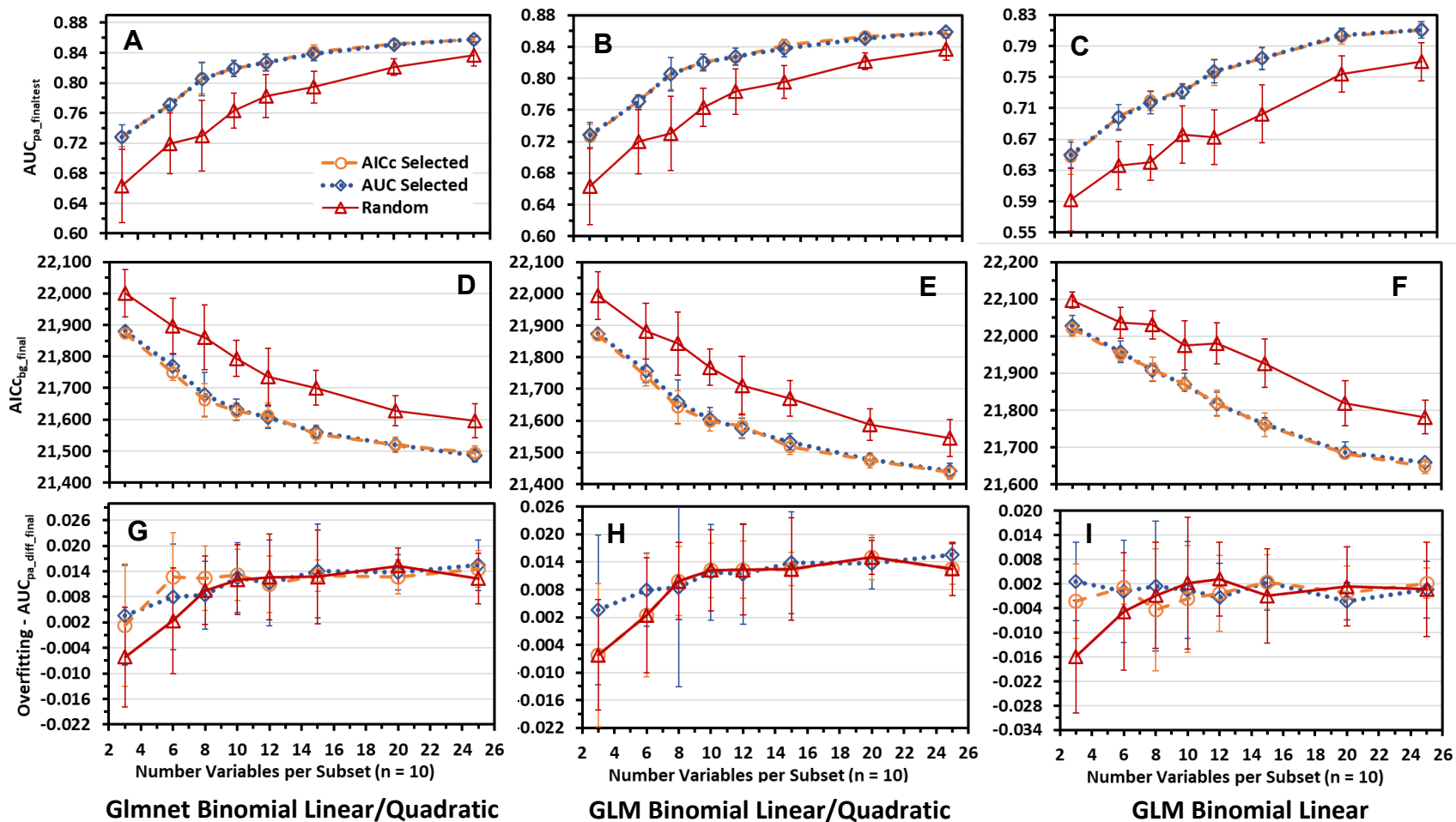
Figure A.5. Low burn severity wildfire activity model evaluation statistics (mean ± SD) for various binomial logistic regression niche modelling methods: (A–C) $AUC_{pa\_finaltest}$, (D-F) $AICc_{bg\_final}$, and (G-I) $AUC_{pa\_diff\_final}$ (overfitting). Models developed from top ten random subset feature selection algorithm-selected variable subsets ranked by AUC or AICc and models developed from ten random subsets. Variable subsets were selected from 250 randomly generated variable subsets of various sizes derived from 90 variables for three modelling methods: Glmnet binomial linear/quadratic (A, D, G); GLM binomial linear/quadratic (B, E, H); and GLM binomial linear (C, F, I) (Tracy et al., 2018b).

175
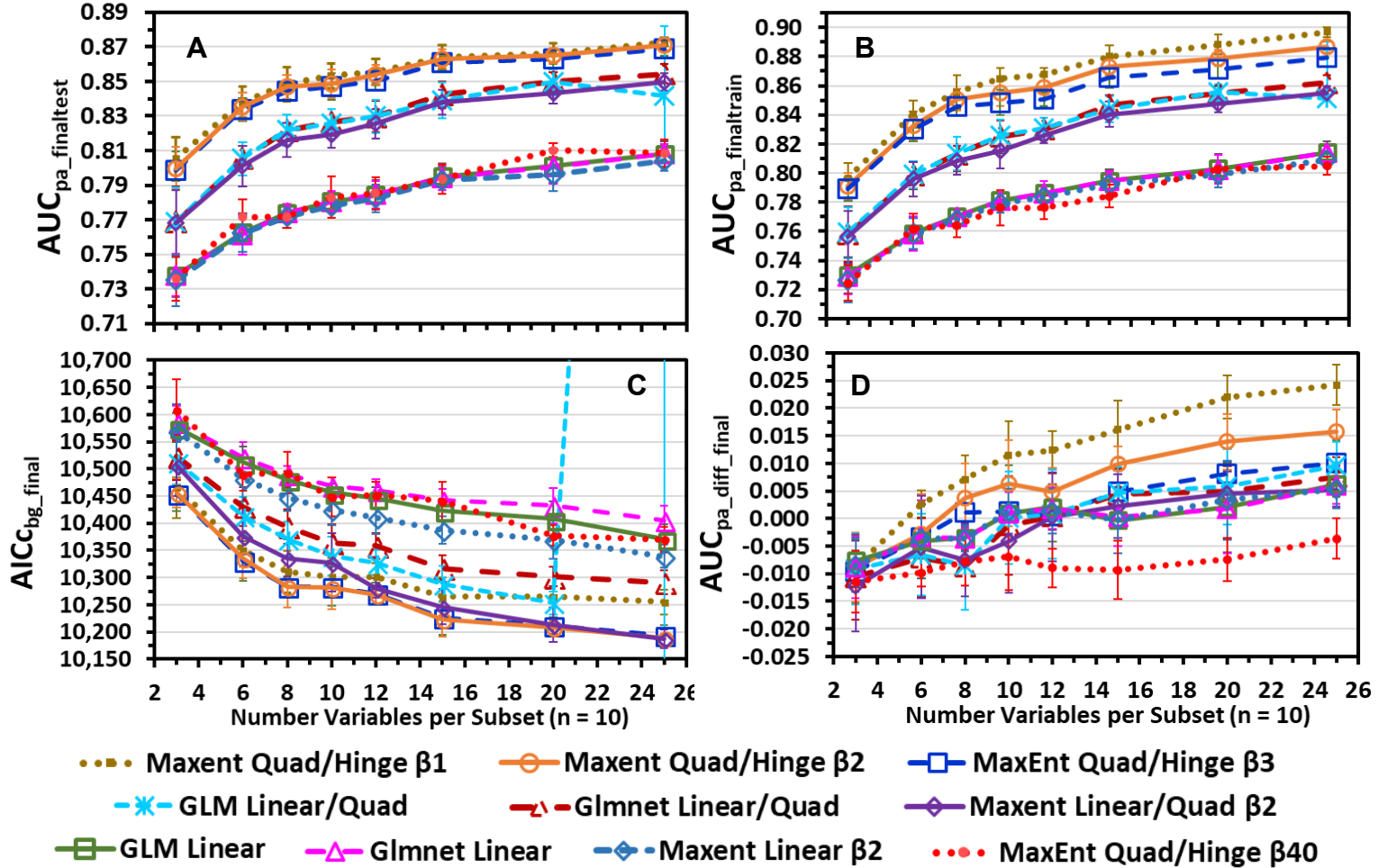
Figure A.6. Moderate burn severity wildfire activity model evaluation statistics (mean ± SD) for various MaxEnt, Glmnet, and GLM models: $AUC_{pa\_finaltest}$ (A), $AUC_{pa\_finaltrain}$ (B), $AICc_{bg\_final}$ (approximated for GLM and Glmnet) (C), and $AUC_{pa\_diff\_final}$ (overfitting; D). Models developed from top ten random subset feature selection algorithm-selected variable subsets ranked by AUC. Variable subsets were selected from 250 randomly generated variable subsets of various sizes derived from 90 variables. Aberrantly high $AICc_{bg}$ values of 13,285 for 25 variables per subset for linear/quadratic GLM model not shown (Tracy et al., 2018b).

176
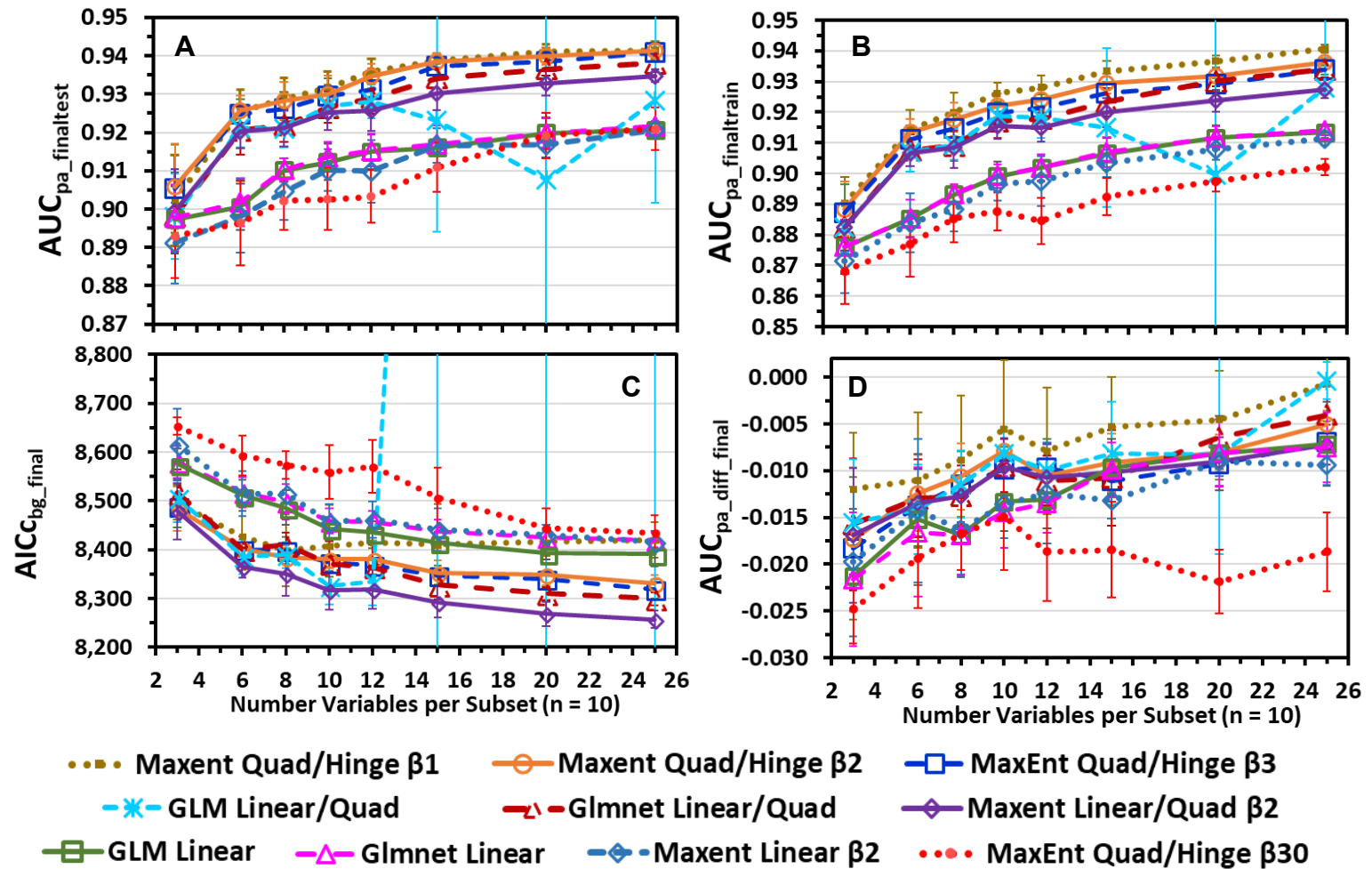
Figure A.7. High burn severity wildfire activity model evaluation statistics (mean ± SD) for various MaxEnt, Glmnet, and GLM models: $AUC_{pa\_finaltest}$ (A), $AUC_{pa\_finaltrain}$ (B), $AICc_{bg\_final}$ (approximated for GLM and Glmnet) (C), and $AUC_{pa\_diff\_final}$ (overfitting; D). Models developed from top ten random subset feature selection algorithm-selected variable subsets ranked by AUC. Variable subsets were selected from 250 randomly generated variable subsets of various sizes derived from 90 variables. Aberrantly high $AICc_{bg}$ values (≈10,000–11,000) above 12 variables per subset for linear/quadratic GLM model not shown (Tracy et al., 2018b).

177
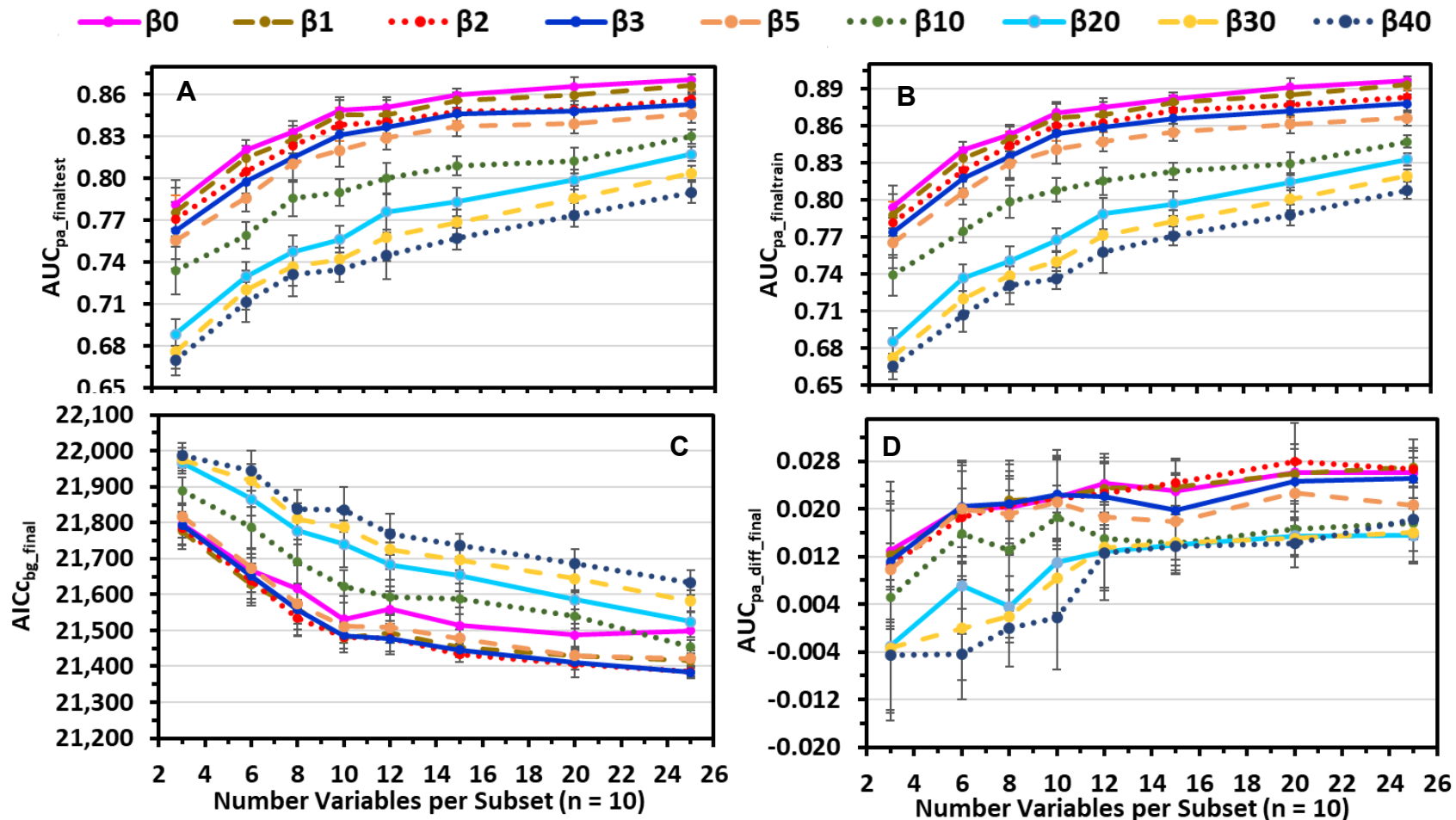
Figure A.8. Low burn severity wildfire activity model evaluation statistics (mean ± SD) for various MaxEnt beta regularization multiplier (β) settings from none (0) to high (40) L1 regularization for quadratic/hinge models: (A) $AUC_{pa\_finaltest}$, (B) $AUC_{pa\_finaltrain}$, (C) $AICc_{bg\_final}$, (D) $AUC_{pa\_diff\_final}$ (overfitting). Models developed from top ten random subset feature selection algorithm-selected variable subsets ranked by AUC. Initial 250 randomly generated variable subsets each for various subset sizes were derived from 90 variables (Tracy et al., 2018b).
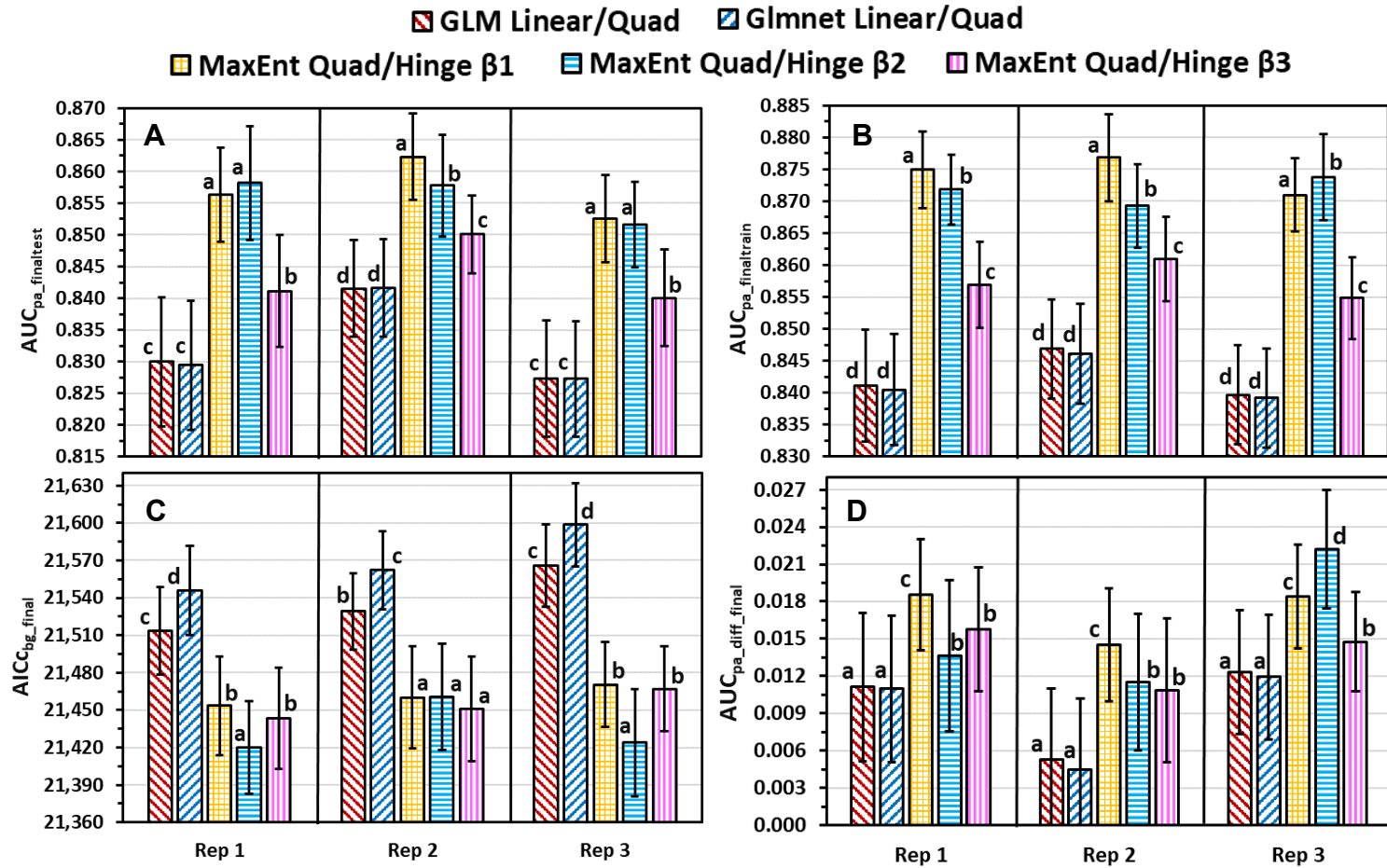
Figure A.9. Low burn severity wildfire activity niche model evaluation statistics (mean ± SD) fo+r various niche modelling methods (see legend) for 15 of 90 variable models: (A) $AUC_{pa\_finaltest}$, (B) $AUC_{pa\_finaltrain}$, (C) $AICc_{bg\_final}$, (D) $AUC_{pa\_diff\_final}$ (overfitting) (optimal higher for $AUC_{pa\_finaltest}$ and $AUC_{pa\_finaltrain}$ and lower for $AICc_{bg\_final}$ and $AUC_{pa\_diff\_final}$). Models developed from three replicates (Rep) of 3,000 variable subsets (total 9,000 subsets per variable subset size) that were narrowed per replicate to 250 (n) subsets filtered by $AUC_{pa\_filtertest}$ with RSFSA (AUC). Means within a replicate with a different letter are significantly different ($P < 0.05$; Welch's one-way ANOVA followed by Games Howell Pairwise Multiple Comparison Test) (Tracy et al., 2018b).

179

Figure A.10. Moderate burn severity wildfire activity niche model evaluation statistics (mean ± SD) for various niche modelling methods (see legend) for 15 of 90 variable models: (A) $AUC_{pa\_finaltest}$, (B) $AUC_{pa\_finaltrain}$, (C) $AICc_{bg\_final}$, (D) $AUC_{pa\_diff\_final}$ (overfitting) (optimal higher for $AUC_{pa\_finaltest}$ and $AUC_{pa\_finaltrain}$ and lower for $AICc_{bg\_final}$ and $AUC_{pa\_diff\_final}$). Models developed from three replicates (Rep) of 3,000 variable subsets (total 9,000 subsets per variable subset size) that were narrowed per replicate to 250 (n) subsets filtered by $AUC_{pa\_filtertest}$ with RSFSA (AUC). Means within a replicate with a different letter are significantly different (P < 0.05; Welch's one-way ANOVA followed by Games Howell Pairwise Multiple Comparison Test) (Tracy et al., 2018b).

180

Figure A.11. High burn severity wildfire activity niche model evaluation statistics (mean ± SD) for various niche modelling methods (see legend) for 15 of 90 variable models: (A) $AUC_{pa\_finaltest}$, (B) $AUC_{pa\_finaltrain}$, (C) $AICc_{bg\_final}$, (D) $AUC_{pa\_diff\_final}$ (overfitting) (optimal higher for $AUC_{pa\_finaltest}$ and $AUC_{pa\_finaltrain}$ and lower for $AICc_{bg\_final}$ and $AUC_{pa\_diff\_final}$). Models developed from three replicates (Rep) of 3,000 variable subsets (total 9,000 subsets per variable subset size) that were narrowed per replicate to 250 (n) subsets filtered by $AUC_{pa\_filtertest}$ with RSFSA (AUC). Means within a replicate with a different letter are significantly different ($P < 0.05$; Welch's one-way ANOVA followed by Games Howell Pairwise Multiple Comparison Test) (Tracy et al., 2018b).

181

Figure A.12. MaxEnt quadratic/hinge (β2) wildfire niche model evaluation statistics (mean ± SD) of $AUC_{pa\_finaltest}$ (A–C), $AICc_{bg\_final}$ (D-F), and $AUC_{pa\_diff\_final}$ (overfitting; G-I). Models developed from three replicates of 3,000 variable subsets of 6 or 15 of 90 variables (total 9,000 subsets per variable subset size) that were narrowed per replicate to 250 (n) subsets filtered by $AUC_{pa\_filtertest}$ with RSFSA (AUC). Means with an asterisk within a replicate are significantly more optimal (higher for $AUC_{pa\_finaltest}$ and lower for $AICc_{bg\_final}$ and $AUC_{pa\_diff\_final}$) ($P < 0.05$; Welch t test) (Tracy et al., 2018b).
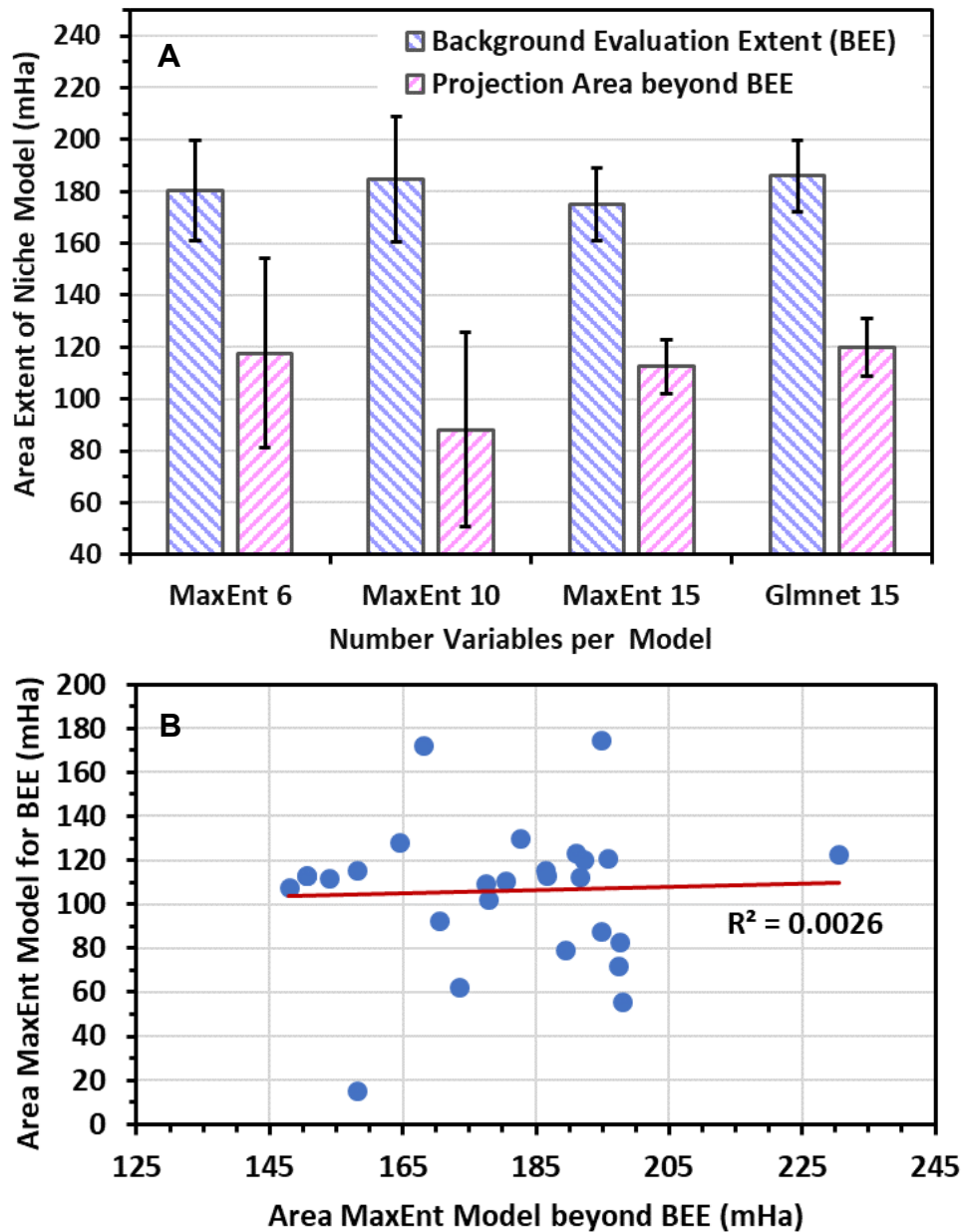
Figure A.13. (A) Area (mHa) of calibrated binary MaxEnt quadratic/hinge (β2) or Glmnet binomial linear/quadratic low burn severity wildfire activity model projections for top nine RSFSA AUC selected models within the background rvaluation extent (BEE) and area beyond the BEE. (B) Area (mHa) of calibrated binary MaxEnt low burn severity wildfire activity model projections within the BEE versus outside of the BEE for 27 MaxEnt models in chart (A) (nine per variable subset sizes 6, 10, and 15) (Tracy et al., 2018b).

models and AICc$_{bg}$ of MaxEnt linear models was fitted and used to approximate AICc$_{bg\_reg}$ for GLM and Glmnet models (Figure A.4F).

Model and Variable Rankings

Using the final selected MaxEnt quadratic/hinge (β2) niche modeling method, thousands of wildfire activity models were ranked in performance by feature selection for each burn severity (see Methods, Random Subset Feature Selection), and the top 10 ranked models from each of three feature selection replications (n = 30), were projected and calibrated to binary presence/absence format.

In order to select the most restrictive models in terms of current projected area burned within the background evaluation extent, the 30 selected models were then subjected to a combined ranking by three regional indices comparing the projected area of presence to the actual area of presence. The three regional indices compared the projected area of presence to the actual area of presence within a projected coordinate system of North American Datum 1983 Equal Area Albers with units of meters: (1) the regional fraction index (RFI), which is the fraction of the actual wildfire presence area overlapped by the projected presence area; (2) the regional excess index (REI), which is the projected wildfire presence area that does not overlap the true presence area (including in Canada and Mexico) divided into the total area of actual presence area (restricted to the US), and (3) the regional bounding index (RBI), which is calculated as 1 – REI/RFI, representing the degree of confinement of the projected wildfire presence area to the actual presence area within the entire projected area (including Canada and Mexico). An RBI value approaching the highest value of 1, indicates that most of the projected presence area is within the actual presence area. An RBI value of zero indicates as much presence area is projected outside the actual presence area as inside the actual presence area. An

184

RBI value of less than zero indicates that more area is projected for presence outside the actual presence area than inside the presence area. A combined ranking of the regional indices with a Multi Multi-Objective Optimization Ratio Algorithm (plus Full Multiplicative Form, MMOORA) of Brauers and Zavadskas (2010) was implemented in the MCDM R package. For the MMOORA combined ranking of the top 30 wildfire models, equal weights were specified for each index, with maximization of RFI, minimization of REI, and maximization of RBI. The top four of 30 selected wildfire models as ranked by MMOORA will be more conservative in terms of projecting a smaller area as suitable for wildfires outside of the presence area (e.g., Figure A.14A–D) in comparison to the other 26 of the 30 selected models (e.g., Figure A.14E–H).

The FSEs for both current and future models were used in statistical comparisons of projected changes in burned areas under current and future climates. The variables used in the top four selected wildfire activity models for each burn severity were jointly ranked using the MCDM R package (Ceballos Martín, 2016) with two criteria: (1) mean variable permutation importance (e.g., Halvorsen, 2013) for the models in which the variable appeared (weighted higher at 0.6); and (2) number of top four models in which variable appears (weighted lower at 0.4).

Contemporary Wildfire Deficit Rating Maps

For each burn severity, a contemporary wildlife deficit or surplus rating map was developed by first using the ArcGIS Combine rasters tool to join the historical wildfire raster for a given burn severity (Figures II.2A-C; presence/absence values of 0 or 1) with the MaxEnt quadratic/hinge $\beta 2$ frequency consensus feature subset ensemble raster for the burn severity (Figures II.7A, 8A, 9A; values of 1-4, from 1 = 1 model projecting fire and 4 = all four models
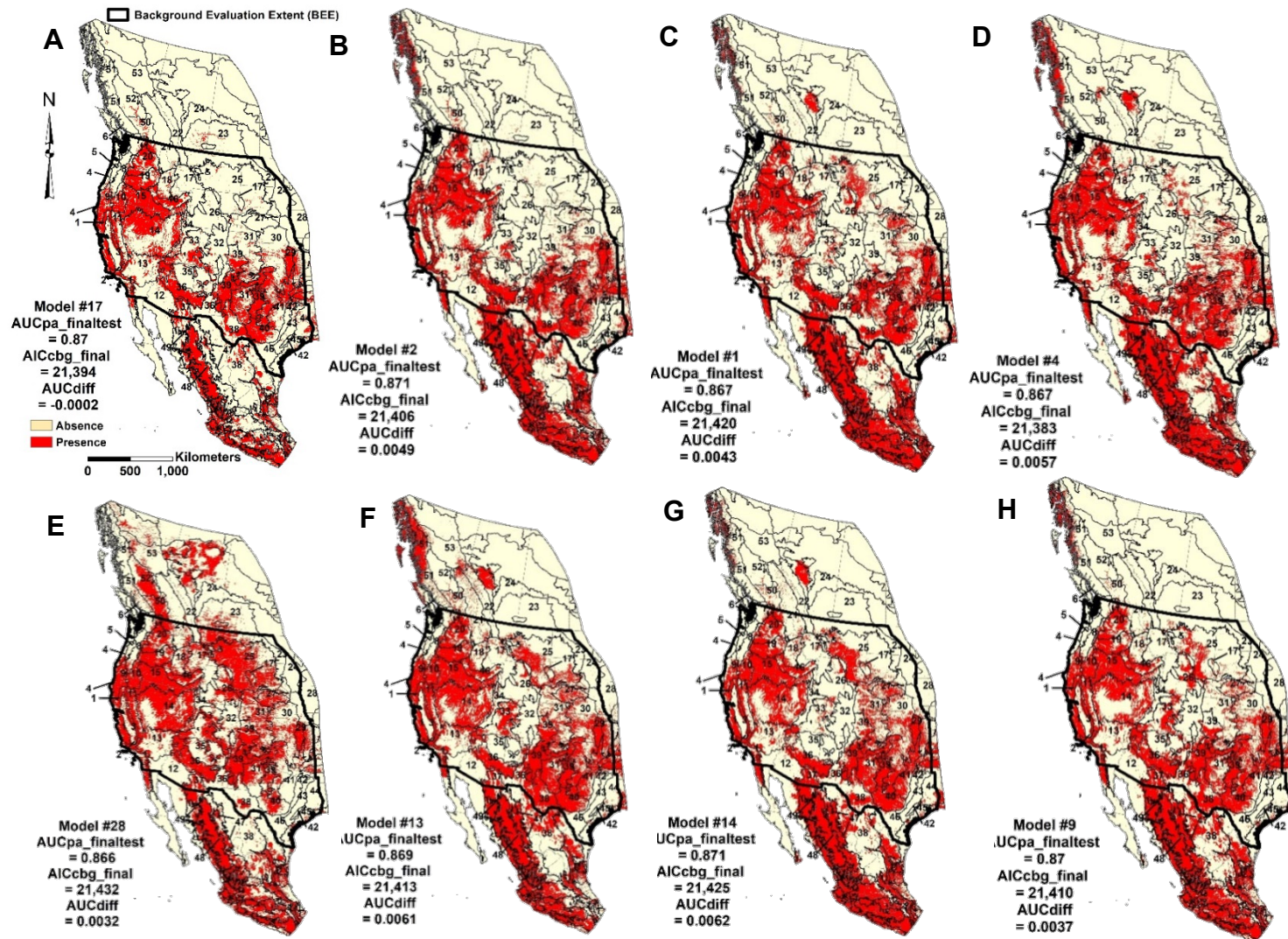
Figure A.14. Low burn severity MaxEnt quadratic/hinge (β2) wildfire activity current climate models of 15 of 90 variables from 30 of 9,000 models selected by AUC$_{pa\_filtertest}$: (A–D) top four of 30 selected by regional indices; (E–H) random four of remaining 16 of 30 (Tracy et al., 2018b).

186
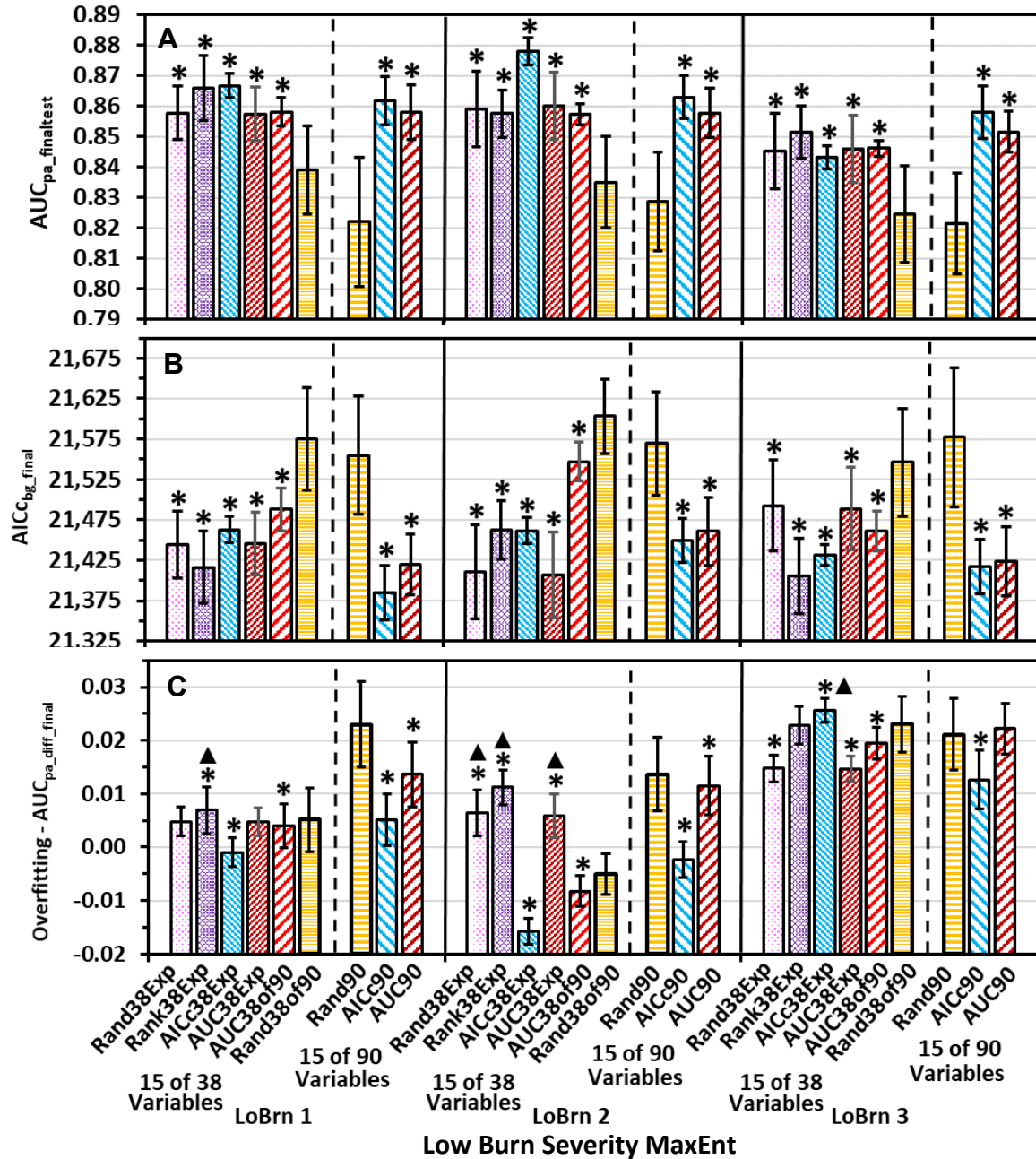
Figure A.15. MaxEnt quadratic/hinge (β2) low burn severity 15-variable wildfire activity model evaluation statistics (mean ± SD) for $AUC_{pa\_finaltest}$ (A), $AICc_{bg\_final}$ (B), and $AUC_{pa\_diff\_final}$ (overfitting; C). Four varieties of random subset feature selection algorithm (RSFSA) models developed from 38 of 90 expert selected variables: (1) random variable subsets (correlation filter only; Rand38Exp); (2) subsets filtered by cumulative expert rank score of variables (see Table A.2; Rank38Exp); (3) subsets ranked by $AICc_{bg\_wrapper}$ (AICc38Exp); and (4) subsets ranked by $AUC_{pa\_wrappertest}$ (AUC38Exp). One variety of RSFSA initiated from three random sets of 38 of 90 variables and ranked by $AUC_{pa\_wrappertest}$ (AUC38of90). Results from models for random, unranked sets of 38 of 90 variables provided for comparison (Rand38of90). Results for models developed from 90 total variables are also presented for comparison (Rand90, AICc90 and AUC90; Figure 6A,D,G). Means for RSFSA selected model statistics within a replicate group with an asterisk are significantly more optimal (higher for $AUC_{pa\_finaltest}$ and lower for $AICc_{bg\_final}$ and $AUC_{pa\_diff\_final}$) from that of random selected models (Rand38of90 or Rand90) (see methods for sample sizes ranging from 250–351 models; $P < 0.05$; Welch t test with Holm correction, preceded by significant Welch ANOVA test, $P < 0.05$; models with asterisk and "▲" are significantly less optimal than random models) (Tracy et al., 2018b).

187

projecting fire). The ArcGIS Reclassification tool was then used to reclassify the combined raster according to the scheme below to indicate a value of contemporary wildfire deficit or surplus.

Values of combined raster pixels were variously assigned as 1-10 and had to be checked against original raster values to determine the correct reclassification scheme. The reclassified raster was then converted to a polygon shapefile and values assigned a wildfire deficit or surplus rating (see Results, Current Climate, below for zipped shapefiles).

Value of Historical 1984-2014 Wildfire Raster (0- absent/1-present; Figures II.2A-C)	Value of MaxEnt Quadratic/Hinge β2 Frequency Consensus Feature Subset Ensemble Raster (Figures II.7A, 8A, 9A)[a]	Numeric Contemporary Wildfire Deficit or Surplus Rating[b]	Description of Contemporary Wildfire Deficit or Surplus Rating
0	4	-4	Very High Deficit
0	3	-3	High Deficit
0	2	-2	Low Deficit
0	1	-1	Very Low Deficit
0	0	No Data	No Data
1	4	0	Balanced
1	3	1	Very Low Surplus
1	2	2	Low Surplus
1	1	3	High Surplus
1	0	4	Very High Surplus

[a]Value represents the number of MaxEnt models agreeing on wildfire projection for 1 km^2 pixel (maximum of four).
[b]Reclassification of combined Historical Wildfire Raster and MaxEnt Quadratic/Hinge β2 Frequency Consensus Feature Subset Ensemble Raster for a given burn severity.

Random Subset Feature Selection Algorithm

Overview

The random subset feature selection algorithm incorporates elements of the random sets feature selection method proposed by Garcia et al. (2006). They utilized a type of randomized search strategy referred to here as *random subset selection* (RSS). Garcia et al. (2006) investigated the ability of RSS to increase efficiency of Support Vector Machines (SVM) classification for binary images of individual plankton. Their random sets feature selection method comprised (1) randomly generating a large number of feature subsets of a given size (e.g., 200 subsets of 10 out of 47 features), (2) using a wrapper criterion of SVM training time to rank the performance of the feature subsets, and (3) combining the features of the higher ranked feature subsets together for developing a final SVM model (e.g., combining top three ranked feature subsets of 10 features). Four substantive modifications were made to their random subset feature selection method in this RSFSA application for niche modeling: (1) employing a correlation filter to maintain maximum absolute correlation of 0.7 among features in randomly generated feature subsets; (2) selecting an approximate optimal feature subset size with the aid of three wrapper criteria, including AUC_{pa} and $AICc_{bg}$, (3) ranking feature subsets of the selected size by a wrapper criteria of either AUC_{pa} or $AICc_{bg}$; and (4) developing an ensemble of top models from top ranked feature subsets rather than combining features from top ranked subsets to develop a single model.

Phases of Feature Selection Criteria

The RSFSA is divided into two phases, each of which are carried out in two stages as described below (Figure II.3).

189

Univariate Filter Phase

In the RSFSA univariate filter phase, the variable filter criterion is an absolute value of Spearman's rank correlation coefficient (r_s) of 0.7 or higher (Dormann et al., 2013), which is an unsupervised univariate correlation filter designed to exclude highly redundant variables. The correlation filter threshold was applied using a sequential forward selection search strategy to build a feature subset of a specified maximum number of variables by randomly adding one variable at a time to the set with the criterion that the absolute correlation between any two variables is less than 0.7. The process was repeated multiple times using a different randomized sequence of variables in order to develop multiple randomly generated variable subsets of the specified size. The multiple iteration of random sequential forward selection is here termed as *multiple randomized sequential forward selection* (MRSFS) (Figure II.3). The MRSFS was implemented quickly in parallel using the filter to generate thousands of variable subsets meeting the correlation criterion. Depending on the size of the initial variable set and the degree of correlation among variables, a percentage of the runs of the univariate filter phase MRSFS searches ended in failure to generate the specified size of variable subset (too many features in the random sequence are discarded for not meeting the correlation criterion with the previously selected features). Duplicate subsets were deleted and the desired number of variable subsets kept for the subset wrapper phase.

Subset Wrapper Phase

The subset wrapper phase of RSFSA required a different search strategy than sequential forward selection. Sequential forward selection with a wrapper criterion would be expensive in terms of the time required to run the classification algorithm for evaluating each individual variable in building each random feature subset. Consequently, for the subset wrapper phase, the

randomized search strategy of *random subset selection* (RSS) was used that was originally developed by Garcia et al. (2006) within the random sets feature selection method (Figure II.3). The random subset selection strategy essentially comprises the parallel calculation of niche model AUC or AICc wrappers from each individual random feature subset generated from the prior univariate filter phase. Point data sampled from environmental rasters, rather than rasters themselves, were used to more rapidly calculate thousands of niche models using samples with data mode for MaxEnt or data matrix fits for GLM and Glmnet. Subset wrapper criteria of either $AUC_{pa\_wrappertest}$ or $AICc_{bg\_wrapper}$ were used in ranking the niche models developed from the random feature subsets.

The availability of final training and testing data withheld from an FSA that can be used in evaluation of FSA-selected models are critical for ensuring that selected models are not fitted to the wrapper phase training and/or testing data, which would produce inflated evaluation statistics (Kohavi and John, 1997; Guyon and Elisseeff, 2003; Kuhn and Johnson, 2013). Consequently, an important step in preparation for the RSFSA subset wrapper phase was the dividing of the presence/absence wildfire occurrence training data available for the niche models in half. One half of the data (50%) was randomly designated for niche model training and testing data within the RSFSA subset wrapper phase (producing wrapper training and testing statistics), and one half (50%) was randomly designated for final niche model training and testing data for final evaluation of the RSFSA-selected models (producing final training and testing statistics) (Figure II.3). The data were divided into 50% RSFSA training and 50% RSFSA validation since both the model training and validation stages require sufficient independent data to provide for 2/3 training and 1/3 testing data. The two halves of wrapper training and testing data and final training and testing data were randomized for each of the three replications (Stracuzzi, 2007) in

order to evaluate the stability of the RSFSA to different sets of training data (Kalousis et al., 2007).

Stages of Feature Selection

Optimal Feature Subset Size Estimation Stage

Stage I of RSFSA involved a subjective estimation of at least two to three potentially optimal feature subset sizes based upon the three model evaluation statistics (Figure II.3). Mean evaluation statistics for ten RSFSA-selected and ten random selected wildfire activity niche models from 250 randomly generated models were plotted and visually compared for each variable subset size between three and 25 of the 90 variables. Preliminary investigations indicated that this range of variable numbers captured most of the range of variability in evaluations statistics for the niche models. The researcher can subjectively weigh the relative importance of higher accuracy and lower underfitting (higher test and train AUC), higher information content (lower $AICc_{bg}$), and lower overfitting (lower AUC_{diff}) in comparing the performance of models developed with various feature subset sizes.

Variable Subset Selection Stage

Once several potentially optimal variable subset sizes were selected, RSFSA Stage II involved selecting the top performing variable subsets (Figure II.3). This stage requires increased replication in order to statistically verify the improvement of RSFSA-selected variable subset models versus random models in the three evaluation statistics. A set of 9,000 random feature subset niche models were generated for each of the selected subset sizes, and these were comprised of three training data set replications of 3,000 variable subset models each. Niche models for the three replications were processed through the RSFSA wrappers to obtain three sets each of 250 RSFSA selected models and 250 random models (correlation filter only).

Statistical comparisons were then made across subset sizes for RSFSA-selected models and between RSFSA selected versus random models for the three replications using different wrapper training and testing data.

Feature Selection Including Expert Variable Screening

The 90 total initial variables was reduced to 38 expert selected variables (Tables II.1, A.2) based on the usefulness of similar variables in previous large-scale modeling efforts for wildfire activity (e.g., Kalabokidis et al., 2002; Parks et al., 2015, 2016). These 38 expert selected variables were input into each of four RSFSA variants using different ranking criteria to select 15-variable subset wildfire activity models. Three replicates were generated of from 1,120 to 1,135 variable subsets of 15 of 38 expert screened variables out of 90 variables (total 3,360 to 3,405 15-variable subsets) that were narrowed per replicate to: (1) 300 (n) subsets randomly selected and filtered by correlation threshold only (Rand38Exp); (2) 351 (n) subsets filtered by expert ranking (Rank38Exp); (3) 250 (n) subsets ranked by $AICc_{bg\_wrapper}$ (AICc38Exp); and (4) 250 (n) subsets ranked by $AUC_{pa\_wrappertest}$ (AUC38Exp). Three replicates were also included of 250 (n) subsets developed from random sets of 38 of 90 variables and ranked using $AUC_{pa\_wrappertest}$ (AUC38of90). Evaluation statistics of models selected by these five RSFSA variants were then compared to those of three replicates of 300 (n) models made from random sets of 38 of 90 variables (Rand38of90; correlation filter only).

Results

Niche Modeling Methods and Feature Selection

With a few exceptions, performance results were generally similar among moderate and high burn severity wildfire activity models for the top performing methods of MaxEnt quadratic/hinge (β1, β2, β3) and GLM and Glmnet linear/quadratic (Figures A10-11). Moderate

burn severity MaxEnt quadratic/hinge models exhibited significantly lower underfitting as indicated by higher training and testing AUC than the three training replicate sets of GLM and Glmnet linear/quadratic models (P < 0.05, Games Howell Pairwise Multiple Comparison Test, preceded by significant Welch's one-way ANOVA test, P < 0.05; Figure A.10A-B). The $\beta1$ and $\beta2$ moderate burn severity MaxEnt quadratic/hinge models had lower underfitting that $\beta3$ models, with $\beta1$ models performing better than $\beta2$ models across most training replicates. The moderate burn severity $\beta2$ and $\beta3$ MaxEnt quadratic/hinge models had significantly lower $AICc_{bg}$ than $\beta1$ MaxEnt quadratic/hinge and GLM and Glmnet linear/quadratic models. Feature selection yielded unstable performance in $AICc_{bg}$ among moderate burn severity GLM linear/quadratic models in training replicate 2. There was much inconsistency in model method performance in overfitting across the training replicates, but GLM and Glmnet linear/quadratic models and $\beta3$ MaxEnt quadratic/hinge models generally performed best (Figure A.10).

In contrast to the above performance results for moderate burn severity modeling methods, high burn severity $\beta1$ MaxEnt quadratic/hinge models consistently outperformed $\beta2$ MaxEnt quadratic/hinge models in terms of underfitting for all training replicates. However, high burn severity $\beta1$ MaxEnt models consistently outperformed $\beta2$ models in regards to overfitting. Unstable results in high burn severity GLM quadrtic/hinge models in performance of both $AUC_{pa\_finaltest}$ and $AICc_{bg}$ were seen in training replicates 2 and 3 (Figures A10-11).

Calculations of both AICc and $AICc_{bg}$ were verified to increase when increasing numbers of model parameters are arbitrarily specified for a given MaxEnt model (Figure A.24). In addition, as the total number of environmental variables increased for MaxEnt models, the number of derived variables increased (Figure A.25A). The MaxEnt algorithm limited the degree of increase in the total number of derived variables as the number of environmental variables
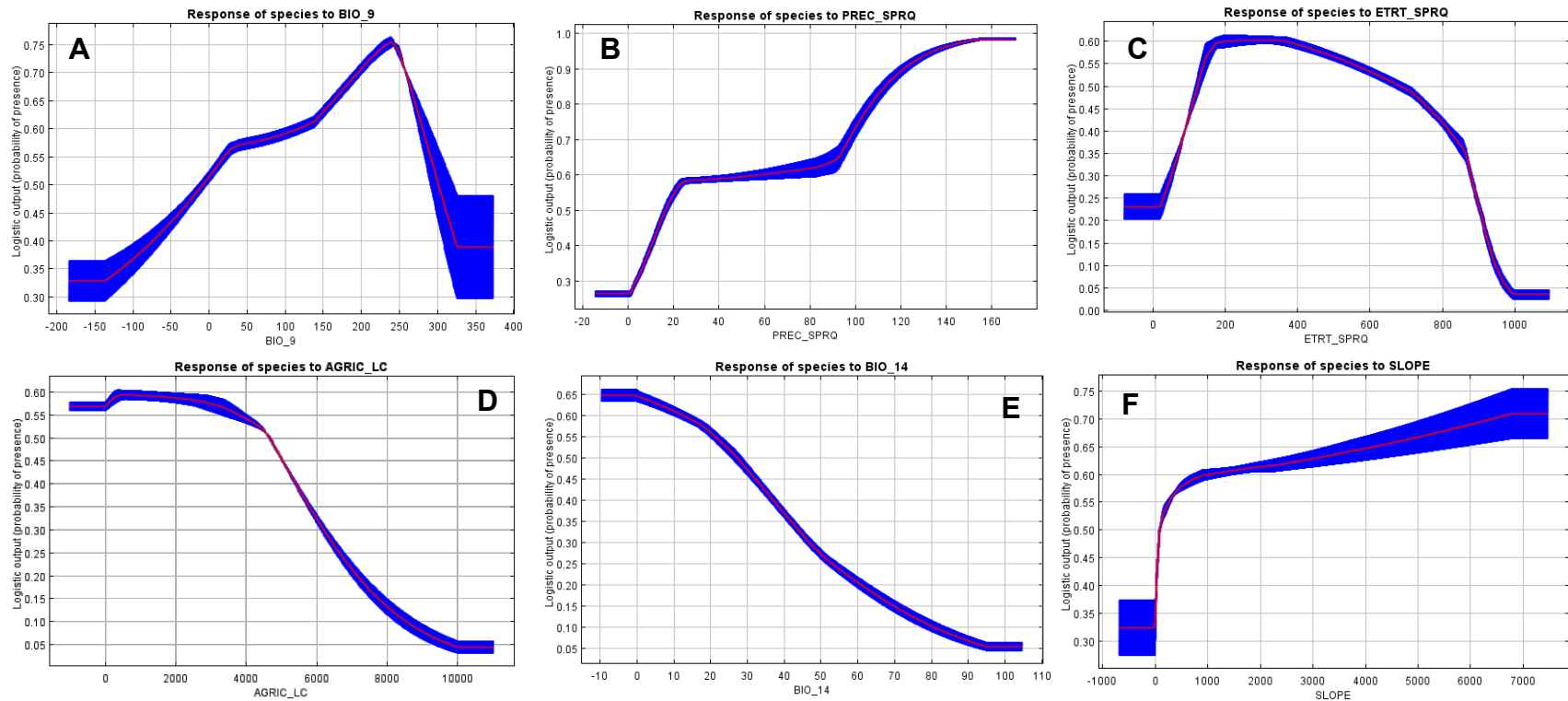
Figure A.16. Low burn severity MaxEnt quadratic/hinge (β2) wildfire activity model variable response curves for top six of 15 variables in permutation importance for top ranked RSFSA selected model (one of four consensus models in Figure 7A): (A) mean temperature of the driest quarter (*bio_9*), (B) precipitation in the spring quarter (*prec_sprq*), (C) AET/PET ratio for the spring quarter (*etrt_sprq*), (D) agricultural land cover (*agric_lc*), (E) precipitation of the driest month (*bio_14*), and (F) slope (*slope*). The curves represent logistic prediction changes as each environmental variable is varied while the other variables are kept at their average sample value (see Table A.4 for permutation importance and other variables) (Tracy et al., 2018b).
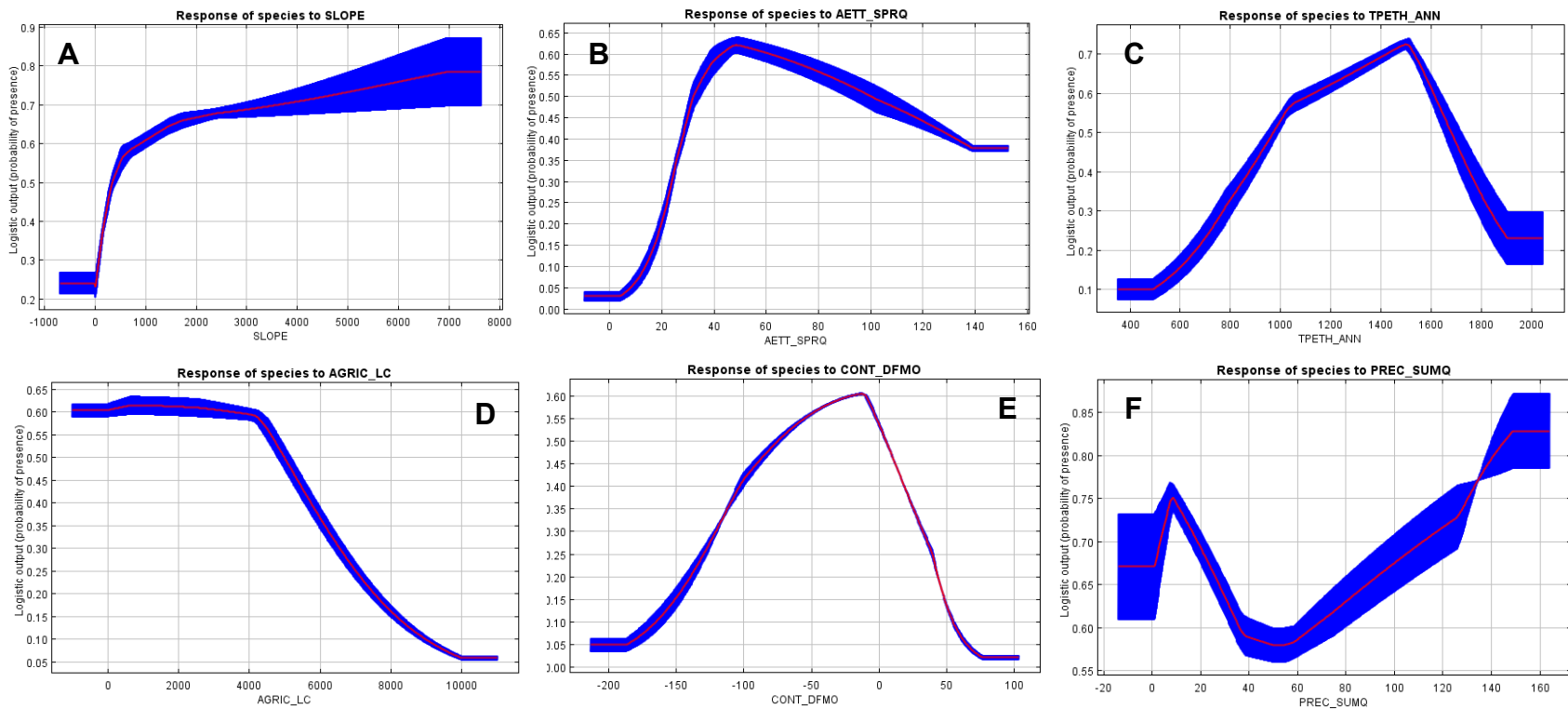
Figure A.17. Moderate burn severity MaxEnt quadratic/hinge (β2) wildfire activity model variable response curves for top six of 15 variables in permutation importance for top ranked RSFSA selected model (one of four consensus models in Figure 7A): (A) slope (*slope*), (B) AET for the spring quarter (*aett_sprq*), (C) total annual PET (*tpeth_ann*), (D) agricultural land cover (*agric_lc*), (E) Driscoll Fong modified continentality index (*cont_dfmo*), and (F) precipitation for the summer quarter (*prec_sumq*). The curves represent logistic prediction changes as each environmental variable is varied while the other variables are kept at their average sample value (see Table A.4 for permutation importance and other variables) (Tracy et al., 2018b).

196
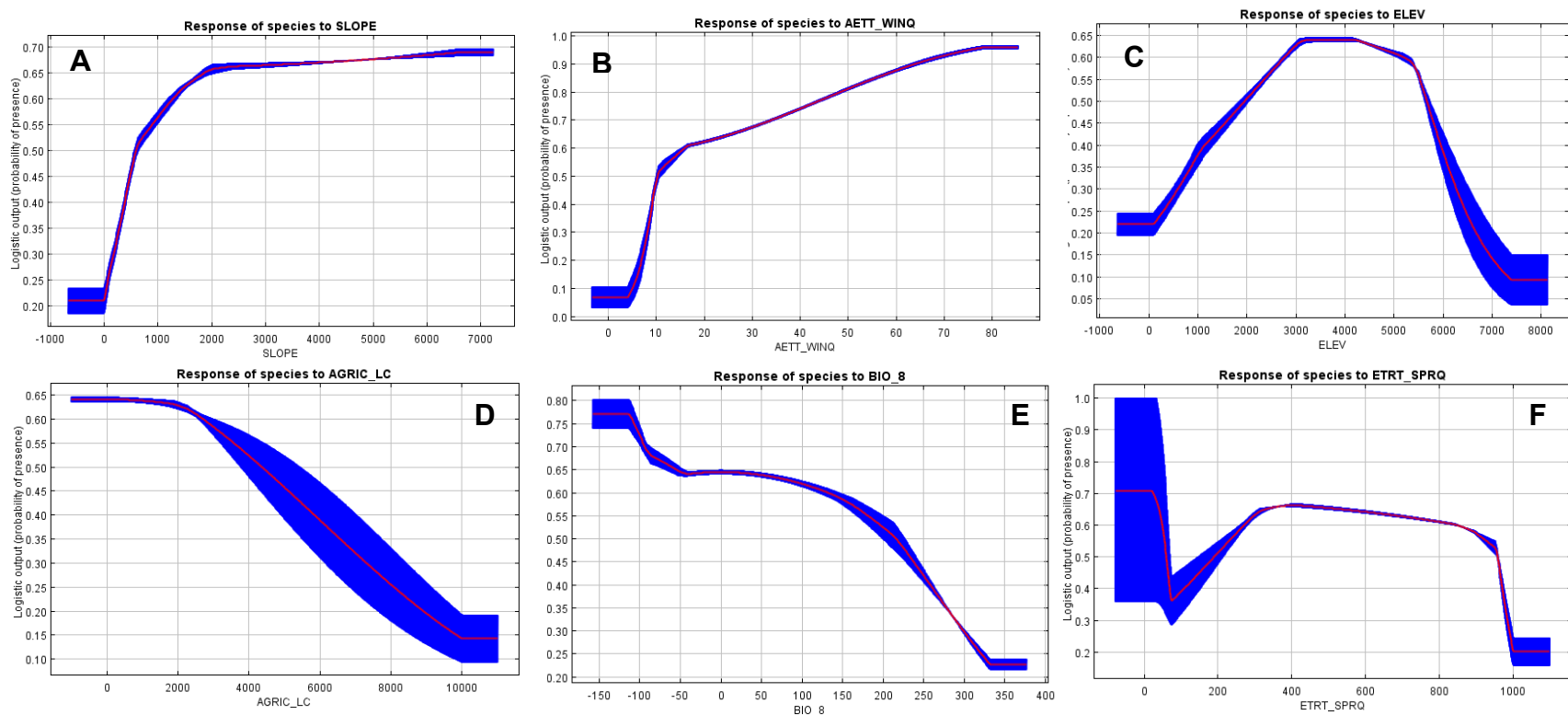
Figure A.18. High burn severity MaxEnt quadratic/hinge (β2) wildfire activity model variable response curves for top six of 15 variables in permutation importance for top ranked RSFSA selected model (one of four consensus models in Figure 7A): (A) slope (*slope*), (B) AET in the spring quarter (*aett_sprq*), (C) elevation (*elev*), (D) agricultural land cover (*agric_lc*), (E) mean temperature of the wettest quarter (*bio_8*), and (F) evapotranspiration ratio of the spring quarter (*etrt_sprq*). The curves represent logistic prediction changes as each environmental variable is varied while the other variables are kept at their average sample value (see Table A.4 for permutation importance and other variables) (Tracy et al., 2018b).
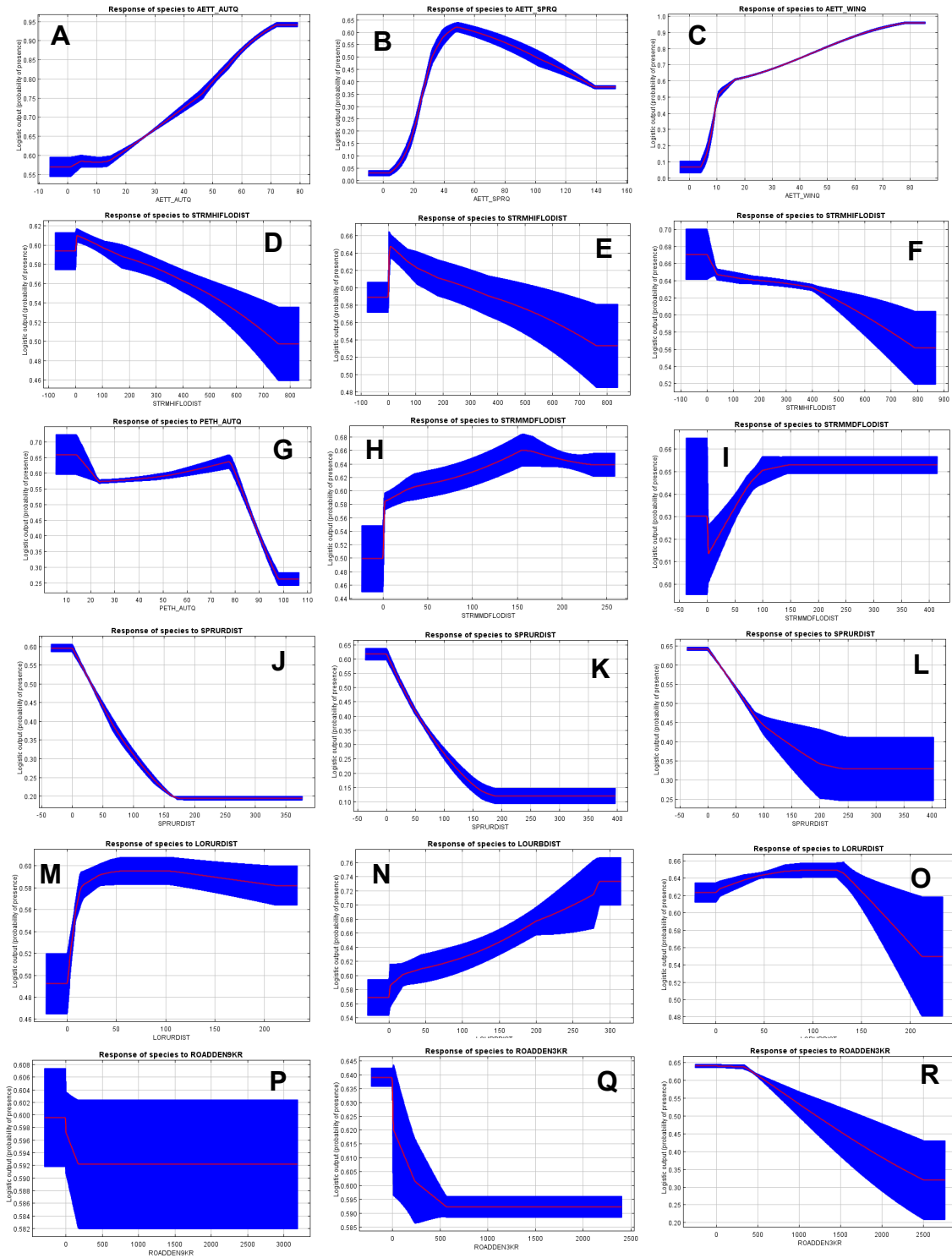
Figure A.19. Variable response curves for low (A,D,G,J,M), moderate (B,E,H,K,N), and high (C,F,I,L,O) burn severity top ranked RSFSA-selected MaxEnt quadratic/hinge (β2) wildfire activity models (one of four consensus models in Figure 7A): (A) *aett_autq*, (B) *aett_sprq*, (C) *aett_winq*, (D–F) *strmhiflodist*, (G) *peth_autq*, (H–I) *strmmdflodist*, (J–L) *sprurdist*, (M,O) *lorurdist*, (N) *lourbdist*, (P) *roadden9kr*, (Q–R) *roadden3kr* (see Table II.1 for abbreviations and Table A.4 for permutation importance) (Tracy et al., 2018b).

198

increased by incorporating lower numbers of derived variables per environmental variable (Figure A.25B).

Selected Features for Wildfire Activity Models

The permutation importance and variable response curves were examined from the MaxEnt output for the individual top random subset feature selection algorithm (RSFSA)-selected 15-variable wildfire model from each of the three burn severities (Table A.5, Figures A.16-19). The top five variables in permutation importance for the top low burn severity wildfire model were (1) mean temperature of the driest quarter (*bio_9*) with an intermediate high value sharply more prone to fire, (2) precipitation in the spring quarter (*prec_sprq*), with a sigmoidal positive association with fire, (3) AET/PET ratio for the spring quarter (*etrt_sprq*), with a graduated intermediate positive association with fire, (4) percent agricultural land cover (*agric_lc*), negatively associated with fire, and (5) precipitation of the driest month (*bio_14*), negatively associated with fire (Figure A.16). Slope (*slope*) was ranked sixth in permutation importance for low burn severity fires with a sigmoid positive association (Figure A.16F).

For the top moderate burn severity wildfire model, the top five variables by permutation importance were (1) *slope*, with a sigmoidal positive association with fire, (2) AET for the spring quarter (*aett_sprq*), with an intermediate value sharply more prone to fire followed by a gradual reduced association with fire at increasing values, (3) total annual PET (*tpeth_ann*), with an intermediate value sharply more associated with fire, (4) percent agricultural land cover (*agric_lc*) with a negative association with fire above a certain intermediate value, and (5) modified Driscoll-Fong continentality index (*cont_dfmo*) with an intermediate value sharply more prone to fire (Figure A.17).

The top five variables by permutation importance for the top high burn severity wildfire model were (1) *slope*, with a sigmoidal positive association with fire, (2) AET for the winter quarter (*aett_winq*), with a partial sigmoid positive response to fire, (3) *elev*, with a broad association with fire for intermediate values, (4) *agric_lc*, with a negative association with fire above a certain early intermediate value and (5) mean temperature of the wettest quarter (*bio_8*), with a negative association with fire above a certain early low value (Figure A.18).

Higher seasonal AET in autumn (*aett_autq*) for low burn severity, spring for moderate burn severity (*aett_sprq*), and winter (*aett_winq*) for high burn severity, were all associated with higher wildfire probability, although there was more of a modal trend for *aett_sprq* (Figures A.19A-C). There was a trend towards higher fire probability with lower distance to high flow accumulation streams (*strmhifldist*) for all three burn severity models (Figure A.19D-E), but these variables were of low permutation importance in the models. In contrast, there was a trend towards lower fire probability with lower distance to medium flow accumulation streams (*strmmdfldist*) for both the moderate and high burn severities (Figure A.19H-I). A lower distance to none to sparse population density areas (*sprurdist*) was positively associated with wildfire probability for all three models of the three burn severities (Figure A.19J-K). At the same time, there was a slight trend towards higher fire probability at higher to low rural density areas (*lorurdist*) for both low and high burn severities (Figure A.19M, O), and higher fire probability at higher distances to low urban density areas (*lourbdist*) for the moderate burn severity (Figure A.19N). There was a trend toward higher wildfire probability with higher densities of roads within a 9 km (*roadden9kr*) and 3 km (*roadden3kr*) radii for low burn severity and moderate and high burn severities, respectively (Figure A.19P-R).

Table A.5. Areas of large low severity fires every 16.5 years or less by ecoregions for actual (1984–2014) and projected current and projected future burn areas (mHa) from MaxEnt wildfire activity models in background evaluation extent and (BEE) and model projection area (see Figures II.2A and 7) (Tracy et al., 2018b).

Ecoregion Map No. - Ecoregion (Area for BEE and Model Projection Area) (*Level I* - Level III; CEC 2005)	Actual Current Area of Burn in BEE (% Ecoreg.)[a]	Model Projected Current Area of Burn (n = 4; or ± SD) BEE (% Ecoregion; % Actual minus % Projected)	Model Projection Area (% Ecoregion)	Model Projected Future Area of Burn (n = 4; ± SD)			
				2050 RCP2.6	2050 RCP8.5	2070 RCP2.6	2070 RCP8.5
Mediterranean California							
1 - California Coastal Sage, Chaparral, and Oak Woodlands (2.09, 4.355)	0.170 (0.081)	1.027 (0.491; -0.283 ± 0.063)	2.373 ± 0.610 (0.545)	1.826 ± 0.788	1.533 ± 0.788	1.856 ± 0.756	1.032 ± 0.598
2 - Southern and Baja California Pine-Oak Mountains (1.784, 1.992)	0.164 (0.092)	1.563 (0.876; -0.784 ± 0.014)‡	1.666 ± 0.062 (0.836)	1.599 ± 0.078	1.566 ± 0.103	1.638 ± 0.065	1.414 ± 0.175
3- Central California Valley (4.593, 4.594)	0.002 (0.0004)	0.793 (0.172; -0.161 ± 0.041)	0.793 ± 0.186 (0.173)	0.478 ± 0.239*	0.311 ± 0.228*	0.484 ± 0.212*	0.135 ± 0.161*
Marine West Coast Forest							
4 - Coast Range (5.159, 5.416)	0.015 (0.003)	0.543 (0.105; -0.102 ± 0.064	0.552 ± 0.337 (0.102)	0.959 ± 0.507	1.136 ± 0.541	0.920 ± 0.510	1.148 ± 0.683
5 - Willamette Valley (1.489, 1.489)	0.0 (0.0)	0.0 (0.0; 0.0)†	0.000 ± 0.000 (0.000)	0.050 ± 0.001	0.094 ± 0.056	0.047 ± 0.083	0.100 ± 0.036
6 - Strait of Georgia/ Puget Lowland (1.583, 3.552)	0.0 (0.0)	0.0 (0.0; 0.0)†	0.004 ± 0.007 (0.001)	0.001 ± 0.001	0.004 ± 0.007	0.000 ± 0.001	0.029 ± 0.057
51 - Pacific and Nass Ranges (--, 10.918)	--	--	1.046 ± 1.096 (0.096)	1.810 ± 1.299	1.630 ± 0.899	1.976 ± 1.401	2.827 ± 0.849
Northwestern Forested Mountains							
7 - North Cascades 3.041, 3.68)	0.010 (0.003)	0.443 (0.146; -0.122 ± 0.014)	0.501 ± 0.063 (0.136)	0.830 ± 0.097*	1.153 ± 0.199*	0.836 ± 0.105*	1.391 ± 0.332*

Ecoregion Map No. - Ecoregion (Area for BEE and Model Projection Area) (*Level I* - Level III; CEC 2005)	Actual Current Area of Burn in BEE (% Ecoreg.)[a]	Model Projected Current Area of Burn (n = 4; or ± SD)		Model Projected Future Area of Burn (n = 4; ± SD)			
		BEE (% Ecoregion; % Actual minus % Projected)	Model Projection Area (% Ecoregion)	2050		2070	
				RCP2.6	RCP8.5	RCP2.6	RCP8.5
8 - Cascades (4.644, 4.644)	0.012 (0.003)	0.437 (0.094; -0.088 ± 0.083)	0.437 ± 0.387 (0.094)	0.957 ± 0.307	1.369 ± 0.253*	1.041 ± 0.307	1.588 ± 0.461*
9 - Klamath Mountains (4.852, 4.852)	0.054 (0.011)	3.395 (0.700; -0.663 ± 0.129)‡	3.395 ± 0.625 (0.700)	4.146 ± 0.286	4.360 ± 0.162	4.113 ± 0.303	4.305 ± 0.168
10 - Eastern Cascades Slopes and Foothills (5.619, 5.619)	0.014 (0.003)	3.802 (0.677; -0.656 ± 0.076)‡	3.802 ± 0.430 (0.677)	4.504 ± 0.192	4.843 ± 0.132	4.536 ± 0.251	4.945 ± 0.015
11 - Sierra Nevada (5.276, 5.276)	0.028 (0.005)	2.571 (0.487; -0.457 ± 0.063)	2.571 ± 0.335 (0.487)	3.159 ± 0.299	3.395 ± 0.312	3.143 ± 0.196	3.455 ± 0.381
17 - Middle Rockies (16.444, 16.444)	0.033 (0.002)	0.735 (0.045; -0.038 ± 0.030)†	0.735 ± 0.487 (0.045)	3.099 ± 0.447*	4.528 ± 0.803*	2.375 ± 0.463*	7.412 ± 2.015*
18 -Idaho Batholith (6.029, 6.029)	0.036 (0.006)	1.460 (0.242; -0.197 ± 0.022)	1.460 ± 0.135 (0.242)	2.895 ± 0.315*	3.963 ± 0.659*	2.376 ± 0.182*	4.524 ± 0.754*
19 - Blue Mountains (7.092, 7.092)	0.044 (0.006)	5.261 (0.742; -0.693 ± 0.072)‡	5.261 ± 0.512 (0.742)	6.284 ± 0.327	6.586 ± 0.158*	6.152 ± 0.395	6.738 ± 0.051*
21 - Columbia Mountains/North Rockies (8.198, 17.932)	0.019 (0.002)	1.440 (0.176; -0.167 ± 0.042)	1.615 ± 0.39 (0.09)	4.623 ± 0.813*	7.056 ± 0.843*	3.671 ± 0.811*	8.785 ± 1.136*
22 - Canadian Rockies (1.888, 10.496)	0.016 (0.009)	0.010 (0.005; 0.009 ± 0.009)†	0.060 ± 0.065 (0.006)	0.440 ± 0.300	1.021 ± 0.316*	0.333 ± 0.278	2.038 ± 0.339*
32 - Southern Rockies (14.572, 14.572)	0.035 (0.002)	0.664 (0.046; -0.04 ± 0.033)†	0.664 ± 0.488 (0.046)	1.813 ± 1.312	2.1 ± 2.232	1.683 ± 1.12	3.486 ± 3.412

Table A.5. Continued.

Ecoregion Map No. - Ecoregion (Area for BEE and Model Projection Area) (*Level I* - Level III; CEC 2005)	Actual Current Area of Burn in BEE (% Ecoreg.)[a]	Model Projected Current Area of Burn (n = 4; or ± SD)		Model Projected Future Area of Burn (n = 4; ± SD)			
		BEE (% Ecoregion; % Actual minus % Projected)	Model Projection Area (% Ecoregion)	2050		2070	
				RCP2.6	RCP8.5	RCP2.6	RCP8.5
33 - Colorado Plateaus (13.493, 13.493)	0.044 (0.003)	3.234 (0.24; -0.234 ± 0.063)	3.234 ± 0.853 (0.24)	5.086 ± 2.534	5.423 ± 2.477	4.726 ± 2.365	5.357 ± 2.844
34 - Wasatch and Uinta Mountains (4.569, 4.569)	0.019 (0.004)	0.556 (0.122; -0.116 ± 0.114)	0.556 ± 0.523 (0.122)	0.982 ± 1.038	1.031 ± 1.047	0.847 ± 0.829	1.302 ± 1.305
52 - Chilcotin Ranges and Fraser Plateau (--, 10.506)	--	--	0.171 ± 0.140 (0.016)	0.749 ± 0.446	2.224 ± 1.298	0.680 ± 0.411	4.403 ± 1.998
53 - Skeena-Omineca-Central Canadian Rocky Mountains (--, 14.006)	--	--	0.087 ± 0.162 (0.006)	0.178 ± 0.22	0.195 ± 0.065	0.214 ± 0.258	0.648 ± 0.299
North American Deserts							
12 - Sonoran Desert (11.697, 21.759)	0.013 (0.001)	1.319 (0.113; -0.101 ± 0.014)	2.777 ± 1.137 (0.128)	2.024 ± 1.088	1.348 ± 0.748	1.272 ± 0.601	0.729 ± 0.426
13 - Mojave Desert (12.960, 12.960)	0.170 (0.013)	3.098 (0.239; -0.212 ± 0.022)	3.098 ± 0.288 (0.239)	3.263 ± 0.560	2.626 ± 0.559	2.508 ± 0.282	1.496 ± 0.448*
14 - Central Basin and Range (30.998, 30.998)	0.624 (0.020)	14.589 (0.471; -0.419 ± 0.025)	14.589 ± 0.790 (0.471)	16.377 ± 2.338	16.409 ± 2.216	15.347 ± 2.397	14.516 ± 1.863
15 - Northern Basin and Range (14.218, 14.218)	0.663 (0.047)	12.669 (0.891; -0.767 ± 0.006)‡	12.699 ± 0.085 (0.891)	13.368 ± 0.154*	13.525 ± 0.218*	13.198 ± 0.196*	13.562 ± 0.126*
16 - Snake River Plain (5.364, 5.364)	0.162 (0.030)	3.432 (0.64; -0.435 ± 0.013)	3.432 ± 0.068 (0.64)	3.676 ± 0.058*	3.670 ± 0.072*	3.603 ± 0.025*	3.519 ± 0.354
20 - Colombia Plateau (8.302, 8.381)	0.085 (0.010)	5.67 (0.683; -0.606 ± 0.004)‡	5.725 ± 0.036 (0.683)	6.032 ± 0.061*	6.007 ± 0.087*	5.997 ± 0.057*	5.729 ± 0.651

203

Table A.5. Continued.

Ecoregion Map No. - Ecoregion (Area for BEE and Model Projection Area) (*Level I* - Level III; CEC 2005)	Actual Current Area of Burn in BEE (% Ecoreg.)[a]	Model Projected Current Area of Burn (n = 4; or ± SD)		Model Projected Future Area of Burn (n = 4; ± SD)			
		BEE (% Ecoregion; % Actual minus % Projected)	Model Projection Area (% Ecoregion)	2050		2070	
				RCP2.6	RCP8.5	RCP2.6	RCP8.5
26 - Wyoming Basin (13.271, 13.271)	0.039 (0.003)	0.619 (0.047; -0.039 ± 0.058)†	0.618 ± 0.764 (0.047)	2.411 ± 0.581*	4.135 ± 0.762*	2.121 ± 0.788	7.527 ± 2.257*
35 - Arizona/New Mexico Plateau (15.010, 15.010)	0.013 (0.001)	2.582 (0.172; -0.165 ± 0.024)	2.582 ± 0.036 (0.172)	3.391 ± 0.607	2.795 ± 0.564	3.134 ± 0.662	2.053 ± 0.578
38 - Chihuahuan Desert (16.215, 50.943)	0.085 (0.005)	6.577 (0.406; -0.369 ± 0.104)	14.664 ± 6.293 (0.288)	6.02 ± 4.101	6.2 ± 4.564	7.05 ± 4.814	7.65 ± 5.143
50 - Thompson-Okanogan Plateau (--, 5.264)	--	--	0.584 ± 0.402 (0.111)	1.952 ± 1.005	2.988 ± 1.189	1.827 ± 1.035	3.735 ± 1.197*
Great Plains							
23 -Northwestern Glaciated Plains (17.496, 40.561)	0.003 (0.0001)	0.429 (0.024; -0.018 ± 0.021)†	0.773 ± 0.277 (0.019)	4.676 ± 1.023*	5.616 ± 1.350*	4.455 ± 0.935*	10.422 ± 2.095*
24 - Aspen Parkland/Northern Glaciated Plains (8.093, 30.764)	0.0 (0.0)	0.0 (0.0; 0.0 ± 0.0)†	0.002 ± 0.003 (0.0)	0.02 ± 0.029	0.027 ± 0.028	0.016 ± 0.021	0.066 ± 0.053
25 - Northwest Great Plains (35.758, 35.758)	0.236 (0.007)	3.141 (0.088; -0.067 82)	3.141 ± 2.927 (0.088)	14.227 ± 3.283*	19.317 ± 1.535*	11.437 ± 2.977*	28.274 ± 1.704*
27 - Nebraska Sandhills (5.912, 5.912)	0.0 (0.0)	1.244 (0.21; -0.191 ± 0.195)	1.244 ± 1.153 (0.21)	1.721 ± 0.998	2.137 ± 0.822	2.036 ± 1.297	3.325 ± 0.264
28 - Western Corn Belt Plains (4.853, 13.889)	0.003 (0.001)	0.324 (0.067; -0.066 ± 0.023)	0.371 ± 0.14 (0.027)	0.367 ± 0.134	0.302 ± 0.111	0.408 ± 0.03	0.298 ± 0.123

Ecoregion Map No. - Ecoregion (Area for BEE and Model Projection Area) (*Level I* - Level III; CEC 2005)	Actual Current Area of Burn in BEE (% Ecoreg.)[a]	Model Projected Current Area of Burn (n = 4; or ± SD)		Model Projected Future Area of Burn (n = 4; ± SD)			
		BEE (% Ecoregion; % Actual minus % Projected)	Model Projection Area (% Ecoregion)	2050		2070	
				RCP2.6	RCP8.5	RCP2.6	RCP8.5
29 - Flint Hills (2.793, 2.793)	0.001 (0.0003)	2.649 (0.949; -0.514 ± 0.015)‡	2.649 ± 0.043 (0.949)	2.672 ± 0.02	2.155 ± 0.4	2.678 ± 0.039	1.93 ± 0.548
30 - Central Great Plains (27.493, 27.493)	0.045 (0.002)	11.522 (0.419; -0.405 ± 0.048)	11.522 ± 1.333 (0.419)	10.741 ± 0.62	6.933 ± 2.702	10.610 ± 0.563	6.652 ± 2.368
31 - High Plains (28.831, 28.831)	0.060 (0.002)	9.32 (0.323; -0.296 ± 0.051)	9.32 ± 1.484 (0.323)	10.719 ± 1.314	10.21 ± 2.218	11.689 ± 0.833	9.8 ± 2.715
39 - Southwest Tablelands (19.886, 19.886)	0.119 (0.006)	14.157 (0.712; -0.66 ± 0.068)‡	14.157 ± 1.349 (0.712)	14.281 ± 2.067	10.858 ± 3.501	15.339 ± 1.432	7.46 ± 4.092
40 - Edwards Plateau (7.497, 7.497)	0.079 (0.011)	5.856 (0.781; -0.745 ± 0.028)‡	5.856 ± 0.212 (0.781)	3.388 ± 1.644	2.321 ± 1.361	1.676 ± 0.511*	4.351 ± 2.845
41 - Cross Timbers (8.821, 8.821)	0.037 (0.004)	5.102 (0.578; -0.520 ± 0.076)‡	5.102 ± 0.67 (0.578)	3.494 ± 0.563*	1.116 ± 0.508*	2.731 ± 0.101*	0.856 ± 0.560*
42 - Texas Blackland Prairies (4.338, 4.338)	0.001 (0.0)	0.162 (0.037; -0.037 ± 0.027)†	0.162 ± 0.118 (0.037)	0.126 ± 0.032	0.003 ± 0.003	0.124 ± 0.242	0.060 ± 0.068
45 - Western Gulf Coastal Plain (5.760, 7.833)	0.118 (0.021)	0.728 (0.126; -0.106 ± 0.019)	1.298 ± 0.174 (0.166)	1.758 ± 0.763	0.755 ± 0.636	1.290 ± 0.506	0.927 ± 0.689
46 - South Texas Plains (5.347, 14.227)	0.008 (0.002)	0.136 (0.025; -0.018 ± 0.012)†	3.399 ± 1.172 (0.239)	4.333 ± 2.269	2.777 ± 1.662	3.346 ± 1.653	5.505 ± 2.949
Temperate Sierras							
36 - Arizona/New Mexico Mountains (10.878, 10.878)	0.158 (0.015)	8.029 (0.738; -0.669 ± 0.038)‡	8.029 ± 0.415 (0.738)	8.261 ± 0.385	7.505 ± 0.532	8.356 ± 0.356	6.661 ± 0.892

Table A.5. Continued.

Ecoregion Map No. - Ecoregion (Area for BEE and Model Projection Area) (*Level I* - Level III; CEC 2005)	Actual Current Area of Burn in BEE (% Ecoreg.)[a]	Model Projected Current Area of Burn (n = 4; or ± SD)		Model Projected Future Area of Burn (n = 4; ± SD)			
		BEE (% Ecoregion; % Actual minus % Projected)	Model Projection Area (% Ecoregion)	2050		2070	
				RCP2.6	RCP8.5	RCP2.6	RCP8.5
48 - Sierra Madre Occidental (--, 15.449)	--	--	14.960 ± 0.913 (0.968)	14.348 ± 2.127	14.185 ± 2.407	14.281 ± 2.234	13.872 ± 2.916
Southern Semiarid Highlands							
37 - Madrean Archipelago (4.3, 7.48)	0.096 (0.022)	3.328 (0.774; -0.694 ± 0.159)‡	5.876 ± 1.628 (0.785)	4.849 ± 2.067	3.78 ± 1.877	4.493 ± 2.016	2.991 ± 1.73
47 - Piedmonts and Plains (--, 13.003)	--	--	8.125 ± 4.8 (0.625)	6.919 ± 4.49	6.177 ± 4.063	6.539 ± 4.238	5.751 ± 3.808
Eastern Temperate Forest							
43 - East Central Texas Plains (5.575, 5.575)	0.004 (0.001)	0.185 (0.033; -0.033 ± 0.019)†	0.185 ± 0.108 (0.033)	0.304 ± 0.234	0.047 ± 0.052	0.158 ± 0.136	0.383 ± 0.43
44 - South Central Plains (7.046, 10.199)	0.08 (0.011)	1.270 (0.180; -0.169 ± 0.04)	2.4 ± 0.279 (0.235)	0.626 ± 0.234*	0.077 ± 0.058*	0.749 ± 0.845	0.007 ± 0.009*
Tropical Dry Forests							
49 - Sinoloa and Sonora Hills and Canyons (--, 8.026)	--	--	6.878 ± 2.095 (0.857)	6.709 ± 2.444	6.614 ± 2.614	6.654 ± 2.517	6.303 ± 3.068

[a]Based on aggregation of 30 m 1984–2014 Monitoring Trends in Burn Severity (MTBS)/LANDFIRE rasters to one km rasters.

† = Projected current burned area less than 5% higher than actual burned area for ecoregion within the BEE. Projected burned areas for other ecoregions are greater than or equal to 5% higher than observed, indicating potential fire deficits.

‡ = Projected current burned area is greater than or equal to 50% higher than actual burned area for ecoregion with the BEE.

* = Projected future burned area significantly different from projected current burned area for ecoregion in projected model area by Welch t test with Holm correction for four comparisons (P < 0.05) if preceded by significant Welch ANOVA test (P < 0.05).

Projections for Wildfire Activity Models

Current Climate

Low Burn Severity

Four of the 12 Level III ecoregions projected to have severe contemporary wildfire deficits in the low burn severity category were in the southern portion of the Great Plains Level I ecoregion (Figure II.7A, Table A.5). Southwestern ecoregions (map numbers in parenthesis) with severe contemporary wildfire deficits include the Madrean Archipelago (37), Arizona/New Mexico Mountains (36), Southern, Baja California Pine Oak Mountains (2), and the Sierra Nevada (11). Northwestern ecoregions with severe contemporary wildfire deficits include three in the Northwestern Forested Mountains Level I ecoregion, and two in the North American Deserts Level I ecoregion (Figure II.7A). Within the area outside of the background evaluation extent in Mexico, high percentages of the Sierra Madre Occidental (48; 97%), Sinoloa and Sonora Hills and Canyons (49; 86%), and Piedmonts and Plains (47; 63%) Level III ecoregions were projected as burned within 16.5 years or less. Very high contemporary wildfire deficits for low burn severity wildfires were widespread from central Texas west to eastern New Mexico, throughout the Arizona/New Mexico Mountains ecoregion, from the northern Great Basin and Range ecoregion north to the Columbia Plateau, and throughout coastal and northern California (Figure A.20; see Tracy et al. [2018b] Appendix A, section 3.3.1 for zipped shapefile).

Moderate Burn Severity

In comparison to the low burn severity wildfire activity model projections, the projected burned areas of 14 Level III ecoregions with severe contemporary wildfire deficits were mostly restricted to the western portion of the study area. An exception was the Edwards Plateau (40) in Texas (Figure II.8A, Table A.6). Seven of these Level III ecoregions are within the Northwestern
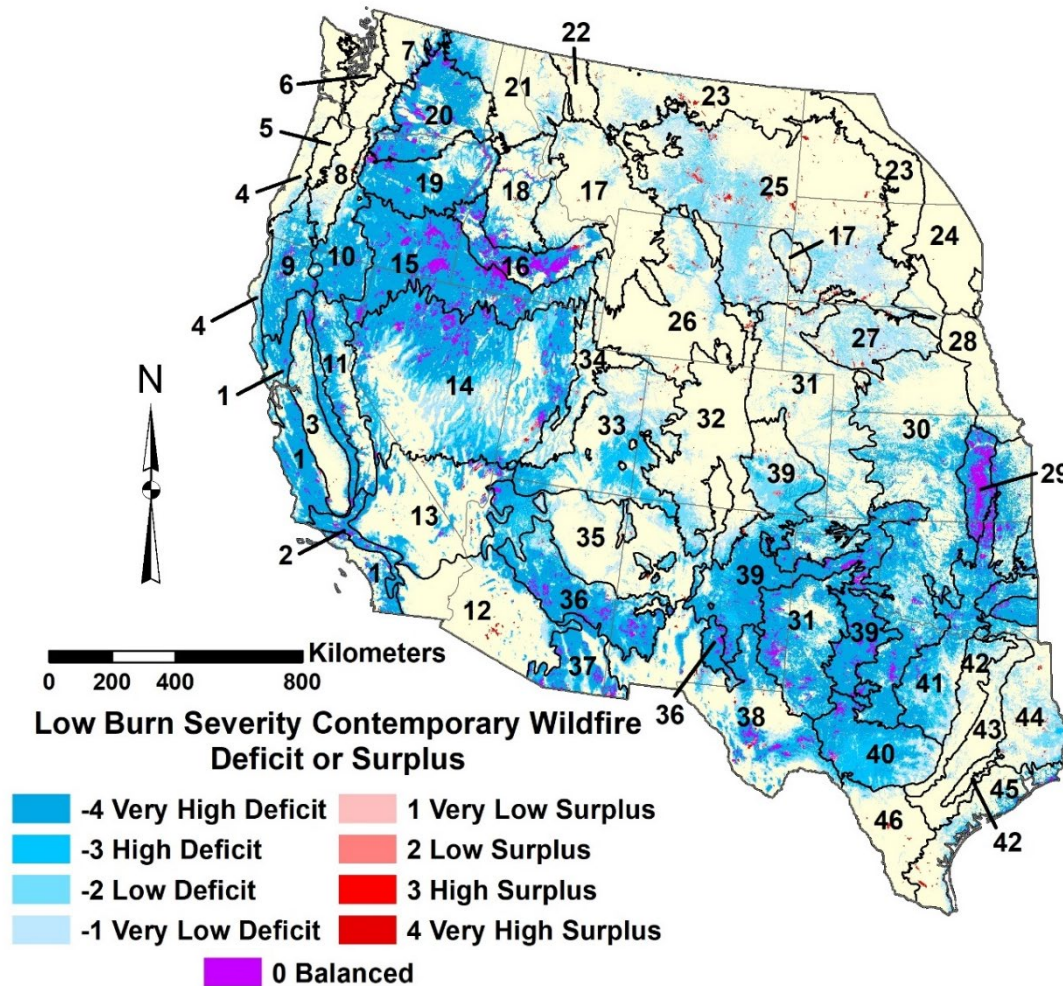
Figure A.20. Low burn severity contemporary wildfire deficit or surplus representing a combination of historical wildfire data (Figure II.2A) and degree of wildfire activity projected by MaxEnt quadratic/hinge (β2) wildfire activity feature subset ensemble models for large wildfires with mean fire interval of ≤ 16.5 yrs per 31 yrs (Figure II.7A) (Tracy et al., 2018b).

Table A.6. Areas of large moderate severity fires every 16.5 years or less by ecoregions for actual (1984–2014) and projected current and projected future burn areas (mHa) from MaxEnt wildfire activity models in background evaluation extent and (BEE) and model projection area (see Figures II.2B and 8) (Tracy et al., 2018b).

Ecoregion Map No. - Ecoregion (Area for BEE and Model Projection Area) (*Level I* - Level III; CEC 2005)	Actual Current Area of Burn in BEE (% Ecoreg.)[a]	Model Projected Current Area of Burn (n = 4; or ± SD)		Model Projected Future Area of Burn (n = 4; ± SD)			
		BEE (% Ecoregion; % Actual minus % Projected)	Model Projection Area (% Ecoregion)	2050		2070	
				RCP2.6	RCP8.5	RCP2.6	RCP8.5
Mediterranean California							
1 - California Coastal Sage, Chaparral, and Oak Woodlands (2.09, 4.355)	0.436 (0.209)	1.215 (0.581; -0.5 ± 0.091)‡	2.838 ± 0.314 (0.651)	2.666 ± 0.181	2.44 ± 0.155	2.53 ± 0.186	1.885 ± 0.212*
2 - Southern and Baja California Pine-Oak Mountains (1.784, 1.992)	0.138 (0.077)	1.724 (0.966; -0.889 ± 0.014)‡	1.892 ± 0.031 (0.95)	1.897 ± 0.025	1.878 ± 0.023	1.892 ± 0.023	1.826 ± 0.014
3- Central California Valley (4.593, 4.594)	0.053 (0.012)	0.61 (0.133; -0.132 ± 0.006)	0.61 ± 0.03 (0.133)	0.481 ± 0.05*	0.287 ± 0.031	0.454 ± 0.051*	0.138 ± 0.034
Marine West Coast Forest							
4 - Coast Range (5.159, 5.416)	0.001 (0.0002)	0.783 (0.152; -0.152 ± 0.222)	0.806 ± 0.191 (0.149)	1.185 ± 1.376	1.416 ± 1.38	1.146 ± 1.399	1.66 ± 1.569
5 - Willamette Valley (1.489, 1.489)	0.0 (0.0)	0.025 (0.017; -0.016 ± 0.02)†	0.025 ± 0.029 (0.017)	0.072 ± 0.082	0.144 ± 0.114	0.084 ± 0.099	0.164 ± 0.135
6 - Strait of Georgia/ Puget Lowland (1.583, 3.552)	0.0 (0.0)	0.02 (0.01; -0.012 ± 0.025)†	0.289 ± 0.577 (0.081)	0.312 ± 0.607	0.373 ± 0.675	0.316 ± 0.622	0.455 ± 0.742
51 - Pacific and Nass Ranges (--, 10.918)	--	--	2.252 ± 4.143 (0.206)	3.371 ± 4.424	4.149 ± 4.214	3.317 ± 4.511	5.312 ± 3.94
Northwestern Forested Mountains							
7 - North Cascades 3.041, 3.68)	0.073 (0.024)	0.971 (0.319; -0.316 ± 0.28)	1.133 ± 1.018 (0.308)	1.868 ± 1.013	2.416 ± 0.802	1.86 ± 1.019	2.739 ± 0.722

209

Table A.6. Continued.

Ecoregion Map No. - Ecoregion (Area for BEE and Model Projection Area) (*Level I* - Level III; CEC 2005)	Actual Current Area of Burn in BEE (% Ecoreg.)[a]	Model Projected Current Area of Burn (n = 4; or ± SD)		Model Projected Future Area of Burn (n = 4; ± SD)			
		BEE (% Ecoregion; % Actual minus % Projected)	Model Projection Area (% Ecoregion)	2050		2070	
				RCP2.6	RCP8.5	RCP2.6	RCP8.5
8 - Cascades (4.644, 4.644)	0.029 (0.006)	0.882 (0.19; -0.187 ± 0.185)	0.882 ± 0.861 (0.19)	1.737 ± 0.796	2.467 ± 0.841	1.797 ± 0.847	3.004 ± 0.971
9 - Klamath Mountains (4.852, 4.852)	0.180 (0.037)	3.439 (0.709; -0.698 ± 0.168)‡	3.439 ± 0.817 (0.709)	4.239 ± 0.217	4.418 ± 0.135	4.197 ± 0.247	4.437 ± 0.18
10 - Eastern Cascades Slopes and Foothills (5.619, 5.619)	0.118 (0.021)	3.495 (0.622; -0.619 ± 0.088)‡	3.495 ± 0.495 (0.622)	4.333 ± 0.191	4.68 ± 0.188*	4.343 ± 0.159	4.828 ± 0.2*
11 - Sierra Nevada (5.276, 5.276)	0.161 (0.03)	3.817 (0.723; -0.718 ± 0.062)‡	3.817 ± 0.326 (0.723)	4.516 ± 0.455	4.704 ± 0.437	4.51 ± 0.416	4.765 ± 0.405
17 - Middle Rockies (16.444, 16.444)	0.105 (0.006)	4.226 (0.257; -0.255 ± 0.034)	4.226 ± 0.553 (0.257)	10.072 ± 0.641*	11.894 ± 0.928*	9.386 ± 0.603*	13.682 ± 0.963*
18 -Idaho Batholith (6.029, 6.029)	0.270 (0.045)	3.193 (0.53; -0.524 ± 0.106)‡	3.193 ± 0.636 (0.53)	5.482 ± 0.202*	5.835 ± 0.126*	5.198 ± 0.268*	5.899 ± 0.083*
19 - Blue Mountains (7.092, 7.092)	0.349 (0.049)	5.675 (0.8; -0.794 ± 0.093)‡	5.675 ± 0.66 (0.8)	6.646 ± 0.085	6.773 ± 0.042	6.613 ± 0.094	6.821 ± 0.039
21 - Columbia Mountains/North Rockies (8.198, 17.932)	0.712 (0.009)	3.524 (0.43; -0.428 ± 0.149)	4.203 ± 1.659 (0.234)	9.625 ± 2.713	11.892 ± 3.102*	8.912 ± 3.027	13.744 ± 2.982*
22 - Canadian Rockies (1.888, 10.496)	0.027 (0.014)	0.236 (0.125; -0.116 ± 0.087)	0.329 ± 0.226 (0.031)	2.155 ± 1.378	3.285 ± 1.448	1.894 ± 1.263	5.108 ± 2.031
32 - Southern Rockies (14.571, 14.571)	0.087 (0.006)	5.621 (0.386; -0.383 ± 0.067)	5.621 ± 0.97 (0.386)	9.252 ± 1.791	10.333 ± 2.015*	8.832 ± 1.751	11.419 ± 2.031*

Table A.6. Continued.

Ecoregion Map No. - Ecoregion (Area for BEE and Model Projection Area) (*Level I* - Level III; CEC 2005)	Actual Current Area of Burn in BEE (% Ecoreg.)[a]	Model Projected Current Area of Burn (n = 4; or ± SD)		Model Projected Future Area of Burn (n = 4; ± SD)			
		BEE (% Ecoregion; % Actual minus % Projected)	Model Projection Area (% Ecoregion)	2050		2070	
				RCP2.6	RCP8.5	RCP2.6	RCP8.5
33 - Colorado Plateaus (13.493, 13.493)	0.05 (0.004)	7.295 (0.541; -0.537 ± 0.039)‡	7.295 ± 0.526 (0.541)	8.421 ± 1.131	8.79 ± 1.229	7.968 ± 1.178	8.006 ± 1.634
34 - Wasatch and Uinta Mountains (4.569, 4.569)	0.025 (0.006)	2.863 (0.627; -0.622 ± 0.103)‡	2.863 ± 0.471 (0.627)	3.614 ± 0.512	3.819 ± 0.473	3.527 ± 0.525	3.96 ± 0.439
52 - Chilcotin Ranges and Fraser Plateau (--, 10.506)	--	--	0.365 ± 0.529 (0.035)	1.638 ± 1.293	3.573 ± 1.763	1.572 ± 1.348	5.525 ± 1.544*
53 - Skeena-Omineca-Central Canadian Rocky Mountains (--, 14.006)	--	--	0.153 ± 0.294 (0.011)	1.244 ± 1.725	2.262 ± 2.604	1.355 ± 1.899	3.49 ± 3.088
North American Deserts							
12 - Sonoran Desert (11.697, 21.759)	0.136 (0.012)	1.068 (0.091; -0.09 ± 0.028)	1.271 ± 0.404 (0.058)	0.834 ± 0.207	0.549 ± 0.153	0.578 ± 0.198	0.237 ± 0.087*
13 - Mojave Desert (12.960, 12.960)	0.354 (0.027)	4.246 (0.328; -0.314 ± 0.038)	4.246 ± 0.497 (0.328)	4.008 ± 0.443	3.219 ± 0.372	3.19 ± 0.422	2.017 ± 0.269*
14 - Central Basin and Range (30.998, 30.998)	1.589 (0.051)	16.462 (0.531; -0.511 ± 0.033)‡	16.462 ± 1.027 (0.531)	18.523 ± 1.658	19.35 ± 2.069	17.403 ± 1.5	18.522 ± 2.815
15 - Northern Basin and Range (14.218, 14.218)	1.766 (0.124)	12.082 (0.85; -0.803 ± 0.029)‡	12.082 ± 0.408 (0.85)	12.77 ± 0.301	12.851 ± 0.28	12.796 ± 0.329	13.046 ± 0.4
16 - Snake River Plain (5.364, 5.364)	1.096 (0.204)	2.668 (0.497; -0.467 ± 0.066)	2.668 ± 0.354 (0.497)	3.006 ± 0.376	3.085 ± 0.4	2.979 ± 0.423	3.22 ± 0.445
20 - Colombia Plateau (8.302, 8.381)	0.636 (0.077)	5.225 (0.629; -0.619 ± 0.045)‡	5.284 ± 0.383 (0.630)	5.771 ± 0.201	5.849 ± 0.205	5.749 ± 0.197	6.014 ± 0.234

Table A.6. Continued.

Ecoregion Map No. - Ecoregion (Area for BEE and Model Projection Area) (*Level I* - Level III; CEC 2005)	Actual Current Area of Burn in BEE (% Ecoreg.)[a]	Model Projected Current Area of Burn (n = 4; or ± SD)		Model Projected Future Area of Burn (n = 4; ± SD)			
		BEE (% Ecoregion; % Actual minus % Projected)	Model Projection Area (% Ecoregion)	2050		2070	
				RCP2.6	RCP8.5	RCP2.6	RCP8.5
26 - Wyoming Basin (13.271, 13.271)	0.099 (0.007)	4.152 (0.313; -0.31 ± 0.042)	4.152 ± 0.558 (0.313)	6.203 ± 1.249	7.119 ± 1.421	6.182 ± 1.145	8.528 ± 1.069*
35 - Arizona/New Mexico Plateau (15.010, 15.010)	0.109 (0.007)	3.079 (0.205; -0.204 ± 0.049)	3.079 ± 0.743 (0.205)	3.656 ± 0.819	3.329 ± 0.921	2.937 ± 0.738	2.357 ± 0.869
38 - Chihuahuan Desert (16.215, 50.943)	0.589 (0.036)	0.9 (0.055; -0.050 ± 0.012)†	3.553 ± 0.905 (0.07)	1.161 ± 0.344*	0.806 ± 0.199*	1.266 ± 0.398*	0.402 ± 0.129*
50 - Thompson-Okanogan Plateau (--, 5.264)	--	--	1.2 ± 1.359 (0.228)	3.156 ± 1.094	4.242 ± 0.74	2.972 ± 1.229	4.74 ± 0.443*
Great Plains							
23 - Northwestern Glaciated Plains (17.496, 40.561)	0.116 (0.007)	0.557 (0.032; -0.032 ± 0.01)†	0.722 ± 0.328 (0.018)	2.244 ± 0.453*	3.217 ± 0.924*	2.221 ± 0.594*	6.093 ± 2.225
24 - Aspen Parkland/Northern Glaciated Plains (8.093, 30.764)	0.0002 (0.0004)	0.0 (0.0; 0.0 ± 0.0)†	0.003 ± 0.004 (0.0)	0.011 ± 0.014	0.021 ± 0.016	0.009 ± 0.012	0.075 ± 0.035
25 - Northwest Great Plains (35.758, 35.758)	0.749 (0.021)	7.642 (0.214; -0.207 ± 0.022)	7.642 ± 0.787 (0.214)	14.116 ± 3.261	17.193 ± 3.681*	13.409 ± 2.234*	23.233 ± 4.031*
27 - Nebraska Sandhills (5.912, 5.912)	0.118 (0.02)	0.255 (0.038; -0.038 ± 0.012)†	0.255 ± 0.07 (0.038)	0.407 ± 0.14	0.521 ± 0.156	0.038 ± 0.057	1.343 ± 0.5
28 - Western Corn Belt Plains (4.853, 13.889)	0.0 (0.0)	0.002 (0.0004;	0.003 ± 0.004 (0.0002)	0.003 ± 0.004	0.003 ± 0.004	0.003 ± 0.004	0.006 ± 0.005

Table A.6. Continued.

Ecoregion Map No. - Ecoregion (Area for BEE and Model Projection Area) (*Level I* - Level III; CEC 2005)	Actual Current Area of Burn in BEE (% Ecoreg.)[a]	Model Projected Current Area of Burn (n = 4; or ± SD)		Model Projected Future Area of Burn (n = 4; ± SD)			
		BEE (% Ecoregion; % Actual minus % Projected)	Model Projection Area (% Ecoregion)	2050		2070	
				RCP2.6	RCP8.5	RCP2.6	RCP8.5
		-0.0004 ± 0.0007)†					
29 - Flint Hills (2.793, 2.793)	1.215 (0.435)	0.033 (0.012; -0.012 ± 0.018)	0.033 ± 0.05 (0.012)	0.063 ± 0.087	0.031 ± 0.036	0.041 ± 0.027	0.025 ± 0.032
30 - Central Great Plains (27.493, 27.493)	0.4 (0.015)	1.825 (0.066; -0.065 ± 0.027)	1.825 ± 0.74 (0.066)	1.392 ± 0.809	0.969 ± 0.504	1.367 ± 0.695	0.942 ± 0.559
31 - High Plains (28.831, 28.831)	0.783 (0.027)	1.209 (0.042; -0.04 ± 005)†	1.209 ± 0.138 (0.04)	2.447 ± 1.106	3.052 ± 1.238	2.335 ± 0.855	4.544 ± 1.844
39 - Southwest Tablelands (19.886, 19.886)	1.036 (0.052)	5.137 (0.258; -0.252 ± 0.047)	5.137 ± 0.935 (0.258)	4.920 ± 1.916	3.744 ± 1.772	5.274 ± 1.865	2.173 ± 1.541
40 - Edwards Plateau (7.497, 7.497)	0.27 (0.036)	4.703 (0.627; -0.617 ± 0.105)‡	4.703 ± 0.791 (0.627)	1.264 ± 0.493*	0.332 ± 0.104*	0.725 ± 0.225*	0.181 ± 0.143*
41 - Cross Timbers (8.821, 8.821)	0.513 (0.058)	1.449 (0.164; -0.160 ± 0.049)	1.449 ± 0.428 (0.164)	0.426 ± 0.375*	0.235 ± 0.371*	0.327 ± 0.283*	0.018 ± 0.031*
42 - Texas Blackland Prairies (4.338, 4.338)	0.0 (0.0)	0.040 (0.009; -0.009 ± 0.007)†	0.040 ± 0.030 (0.009)	0.001 ± 0.002	0.001 ± 0.003	0.0005 ± 0.001	0.0 ± 0.0
45 - Western Gulf Coastal Plain (5.760, 7.833)	0.011 (0.002)	0.017 (0.003; -0.001 ± 0.003)†	0.033 ± 0.033 (0.004)	0.052 ± 0.079	0.021 ± 0.027	0.034 ± 0.054	0.022 ± 0.042
46 - South Texas Plains (5.347, 14.227)	0.038 (0.007)	0.113 (0.021; -0.02 ± 0.013)†	0.996 ± 0.3 (0.07)	0.43 ± 0.21	0.239 ± 0.1*	0.378 ± 0.164	0.280 ± 0.246*
Temperate Sierras							

Table A.6. Continued.

Ecoregion Map No. - Ecoregion (Area for BEE and Model Projection Area) (*Level I* - Level III; CEC 2005)	Actual Current Area of Burn in BEE (% Ecoreg.)[a]	Model Projected Current Area of Burn (n = 4; or ± SD) BEE (% Ecoregion; % Actual minus % Projected)	Model Projection Area (% Ecoregion)	Model Projected Future Area of Burn (n = 4; ± SD) 2050 RCP2.6	2050 RCP8.5	2070 RCP2.6	2070 RCP8.5
36 - Arizona/New Mexico Mountains (10.878, 10.878)	0.756 (0.07)	8.100 (0.745; -0.730 ± 0.059)‡	8.100 ± 0.642 (0.745)	8.06 ± 0.694	7.362 ± 0.927	7.590 ± 0.724	5.838 ± 1.231
48 - Sierra Madre Occidental (--, 15.449)	--	--	13.441 ± 1.322 (0.87)	11.282 ± 2.256	10.141 ± 2.605	11.082 ± 2.277	7.382 ± 2.831
Southern Semiarid Highlands							
37 - Madrean Archipelago (4.3, 7.48)	0.343 (0.08)	2.025 (0.471; -0.449 ± 0.09)	3.633 ± 0.805 (0.485)	2.5 ± 0.836	1.525 ± 0.564*	2.008 ± 0.745	0.621 ± 0.21*
47 - Piedmonts and Plains (--, 13.003)	--	--	1.704 ± 1.113 (0.131)	0.593 ± 0.416	0.359 ± 0.577	0.582 ± 0.149	0.106 ± 1.113
Eastern Temperate Forest							
43 - East Central Texas Plains (5.575, 5.575)	0.003 (0.0005)	0.141 (0.025; -0.025 ± 0.009)†	0.141 ± 0.049 (0.025)	0.004 ± 0.003	0.003 ± 0.006	0.001 ± 0.002	0.0 ± 0.0
44 - South Central Plains (7.046, 10.199)	0.012 (0.002)	0.548 (0.078; -0.076 ± 0.063)	0.882 ± 0.638 (0.086)	0.083 ± 0.117	0.005 ± 0.008	0.023 ± 0.031	0.0 ± 0.0
Tropical Dry Forests							
49 - Sinoloa and Sonora Hills and Canyons (--, 8.026)	--	--	1.747 ± 1.165 (0.218)	0.862 ± 0.895	0.573 ± 0.732	0.734 ± 0.798	0.248 ± 0.358

[a]Based on aggregation of 30 m 1984–2014 Monitoring Trends in Burn Severity (MTBS)/LANDFIRE rasters to one km rasters.

† = Projected current burned area less than 5% higher than actual burned area for ecoregion within the BEE. Projected burned areas for other ecoregions are greater than or equal to 5% higher than observed, indicating potential fire deficits.

‡ = Projected current burned area is greater than or equal to 50% higher than actual burned area for ecoregion with the BEE.

Table A.6. Continued.

Ecoregion Map No. - Ecoregion (Area for BEE and Model Projection Area) (*Level I* - Level III; CEC 2005)	Actual Current Area of Burn in BEE (% Ecoreg.)[a]	Model Projected Current Area of Burn (n = 4; or ± SD)		Model Projected Future Area of Burn (n = 4; ± SD)			
		BEE (% Ecoregion; % Actual minus % Projected)	Model Projection Area (% Ecoregion)	2050		2070	
				RCP2.6	RCP8.5	RCP2.6	RCP8.5

* = Projected future burned area significantly different from projected current burned area for ecoregion in projected model area by Welch t test with Holm correction for four comparisons (P < 0.05) if preceded by significant Welch ANOVA test (P < 0.05).

Forested Mountains Level I ecoregion. Also included are three Level III ecoregions of the North American Deserts, two ecoregions within the Mediterranean California Level I ecoregion, and the Arizona/New Mexico Mountains (36) (Figure II.8A). A high percentage (87%) of the Sierra Madre Occidental (48) in Mexico was projected as burned every 16.5 years or less. Very high contemporary wildfire deficits for moderate burn severity wildfires were similar to that of low burn severity wildfires, with the exception of much reduced deficits projected for parts of west Texas and New Mexico, such as in the High Plains and Southwest Tablelands ecoregions (Figure A.21; see Tracy et al. [2018b] Appendix A, section 3.3.1 for zipped shapefile).

High Burn Severity

Fourteen Level III ecoregions were projected with severe contemporary wildfire deficits (Figure II.9A, Table A.7). These include 12 of the 13 Level III ecoregions in the Northwestern Forested Mountain Level I ecoregion, the only exception being the Colorado Plateau (33). The two other Level III ecoregions include the Southern and Baja California Pine-Oak Mountains (2) and Central Basin and Range (14). Outside the background evaluation extent in western Canada, four Level III ecoregions have fairly high percentages of their area projected as burned every 16.5 years or less, including the Thompson-Okanogan Plateau (50; 69%), Pacific and Nass Ranges (51; 56%), Chilcotin Ranges and Fraser Plateau (52; 45%), and Skeena-Omineca-Central Canadian Rocky Mountains (53; 33%). Outside of the background evaluation extent within Mexico, two Level III ecoregions have high percentages of area projected as burned, the Sierra Madre Occidental (48; 88%) and Sinoloa and Sonora Hills and Canyons (49; 44%).Very high contemporary wildfire deficits for high burn severity wildfires were generally restricted to the western portion of the study area in ecoregions similar to that of moderate burn severity deficits, with notable exceptions such as much higher deficits projected for the Southern Rockies,
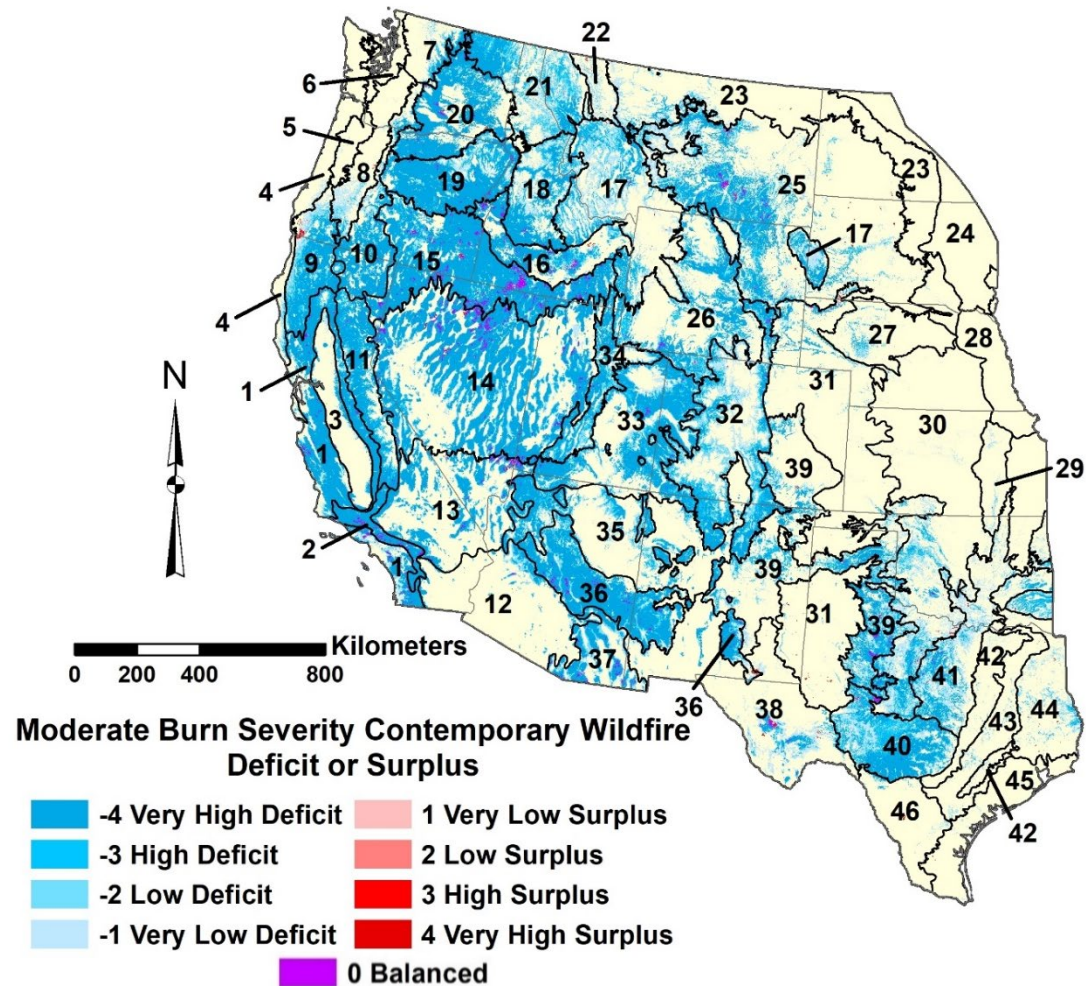
216

Figure A.21. Moderate burn severity contemporary wildfire deficit or surplus representing a combination of historical wildfire data (Figure II.2B) and degree of wildfire activity projected by MaxEnt quadratic/hinge (β2) wildfire activity feature subset ensemble models for large wildfires with mean fire interval of ≤ 16.5 yrs per 31 yrs (Figure II.8A) (Tracy et al., 2018b).

Table A.7. Areas of large high severity fires every 16.5 years or less by ecoregions for actual (1984–2014) and projected current and projected future burn areas (mHa) from MaxEnt wildfire activity model in background evaluation extent and (BEE) and model projection area (see Figures II.2C and 9) (Tracy et al., 2018b).

Ecoregion Map No. - Ecoregion (Area for BEE and Model Projection Area) (*Level I* - Level III; CEC 2005)	Actual Current Area of Burn in BEE (% Ecoreg.)[a]	Model Projected Current Area of Burn (n = 4; or ± SD) BEE (% Ecoregion; % Actual minus % Projected)	Model Projection Area (% Ecoregion)	Model Projected Future Area of Burn (n = 4; ± SD) 2050 RCP2.6	2050 RCP8.5	2070 RCP2.6	2070 RCP8.5
Mediterranean California							
1 - California Coastal Sage, Chaparral, and Oak Woodlands (2.09, 4.355)	0.189 (0.091)	0.83 (0.397; -0.307 ± 0.051)	1.964 ± 0.211 (0.451)	2.408 ± 0.199	2.404 ± 0.248	2.135 ± 0.264	2.169 ± 0.455
2 - Southern and Baja California Pine-Oak Mountains (1.784, 1.992)	0.217 (0.122)	1.665 (0.934; -0.812 ± 0.025)‡	1.797 ± 0.035 (0.902)	1.869 ± 0.026	1.878 ± 0.021	1.834 ± 0.031	1.868 ± 0.038
3- Central California Valley (4.593, 4.594)	0.0005 (0.0001)	0.092 (0.02; -0.02 ± 0.01)†	0.092 ± 0.051 (0.02)	0.186 ± 0.122	0.28 ± 0.246	0.153 ± 0.085	0.392 ± 0.444
Marine West Coast Forest							
4 - Coast Range (5.159, 5.416)	0.0003 (0.00005)	1.136 (0.22; -0.22 ± 0.066)	1.153 ± 0.346 (0.213)	1.663 ± 0.822	1.911 ± 1.026	1.604 ± 0.818	2.079 ± 1.241
5 - Willamette Valley (1.489, 1.489)	0.0 (0.0)	0.071 (0.048; -0.048 ± 0.056)†	0.071 ± 0.084 (0.048)	0.128 ± 0.108	0.169 ± 0.115	0.124 ± 0.102	0.183 ± 0.115
6 - Strait of Georgia/ Puget Lowland (1.583, 3.552)	0.0 (0.0)	0.004 (0.002; -0.002 ± 0.002)†	0.086 ± 0.093 (0.024)	0.268 ± 0.252	0.4 ± 0.325	0.191 ± 0.201	0.542 ± 0.482
51 - Pacific and Nass Ranges (--, 10.918)	--	--	6.059 ± 2.071 (0.555)	6.58 ± 2.312	6.87 ± 1.989	6.654 ± 2.305	7.194 ± 2.02
Northwestern Forested Mountains							
7 - North Cascades 3.041, 3.68)	0.124 (0.04)	1.993 (0.655; -0.615 ± 0.132)‡	2.563 ± 0.436 (0.696)	2.764 ± 0.463	2.937 ± 0.483	2.731 ± 0.428	2.994 ± 0.496

218

Table A.7. Continued.

Ecoregion Map No. - Ecoregion (Area for BEE and Model Projection Area) (*Level I* - Level III; CEC 2005)	Actual Current Area of Burn in BEE (% Ecoreg.)[a]	Model Projected Current Area of Burn (n = 4; or ± SD)		Model Projected Future Area of Burn (n = 4; ± SD)			
		BEE (% Ecoregion; % Actual minus % Projected)	Model Projection Area (% Ecoregion)	2050		2070	
				RCP2.6	RCP8.5	RCP2.6	RCP8.5
8 - Cascades (4.644, 4.644)	0.028 (0.006)	2.664 (0.574; -0.568 ± 0.187)‡	2.664 ± 0.869 (0.574)	3.174 ± 1.061	3.52 ± 1.131	3.164 ± 1.043	3.546 ± 1.07
9 - Klamath Mountains (4.852, 4.852)	0.154 (0.032)	4.284 (0.883; -0.851 ± 0.029)‡	4.284 ± 0.141 (0.883)	4.383 ± 0.121	4.423 ± 0.125	4.392 ± 0.132	4.466 ± 0.074
10 - Eastern Cascades Slopes and Foothills (5.619, 5.619)	0.064 (0.011)	3.655 (0.651; -0.639 ± 0.034)‡	3.655 ± 0.191 (0.651)	3.805 ± 0.149	3.881 ± 0.2	3.857 ± 0.155	3.992 ± 0.342
11 - Sierra Nevada (5.276, 5.276)	0.151 (0.029)	4.805 (0.911; -0.882 ± 0.021)‡	4.805 ± 0.109 (0.911)	4.887 ± 0.083	4.935 ± 0.067	4.885 ± 0.081	4.986 ± 0.057
17 - Middle Rockies (16.444, 16.444)	0.382 (0.023)	10.973 (0.667; -0.644 ± 0.031)‡	10.973 ± 0.516 (0.667)	10.996 ± 0.367	10.803 ± 0.213	11.065 ± 0.358	10.719 ± 0.69
18 -Idaho Batholith (6.029, 6.029)	0.419 (0.069)	5.837 (0.968; -0.899 ± 0.004)‡	5.837 ± 0.027 (0.968)	5.819 ± 0.055	5.788 ± 0.099	5.818 ± 0.05	5.788 ± 0.135
19 - Blue Mountains (7.092, 7.092)	0.058 (0.008)	5.57 (0.785; -0.777 ± 0.045)‡	5.57 ± 0.32 (0.785)	5.734 ± 0.291	5.685 ± 0.445	5.749 ± 0.298	5.817 ± 0.442
21 - Columbia Mountains/North Rockies (8.198, 17.932)	0.033 (0.004)	6.041 (0.737; -0.733 ± 0.067)‡	14.212 ± 1.967 (0.793)	14.547 ± 1.574	14.727 ± 1.475	14.407 ± 1.684	14.797 ± 1.512
22 - Canadian Rockies (1.888, 10.496)	0.122 (0.065)	1.812 (0.96; -0.895 ± 0.008)‡	7.246 ± 2.043 (0.69)	8.006 ± 1.073	8.733 ± 0.56	8.18 ± 0.963	8.844 ± 0.569
32 - Southern Rockies (14.571, 14.571)	0.116 (0.008)	8.394 (0.613; -0.605 ± 0.094)‡	8.934 ± 1.371 (0.613)	8.951 ± 0.884	8.587 ± 1.279	8.982 ± 0.944	8.069 ± 1.579

Table A.7. Continued.

Ecoregion Map No. - Ecoregion (Area for BEE and Model Projection Area) (*Level I* - Level III; CEC 2005)	Actual Current Area of Burn in BEE (% Ecoreg.)[a]	Model Projected Current Area of Burn (n = 4; or ± SD)		Model Projected Future Area of Burn (n = 4; ± SD)			
		BEE (% Ecoregion; % Actual minus % Projected)	Model Projection Area (% Ecoregion)	2050		2070	
				RCP2.6	RCP8.5	RCP2.6	RCP8.5
33 - Colorado Plateaus (13.493, 13.493)	0.04 (0.003)	3.688 (0.273; -0.27 ± 0.038)	3.688 ± 0.519 (0.273)	3.391 ± 1.019	3.641 ± 1.032	3.175 ± 0.928	3.177 ± 1.296
34 - Wasatch and Uinta Mountains (4.569, 4.569)	0.03 (0.007)	3.541 (0.775; -0.768 ± 0.048)‡	3.541 ± 0.218 (0.775)	3.558 ± 0.155	3.597 ± 0.176	3.486 ± 0.174	3.478 ± 0.224
52 - Chilcotin Ranges and Fraser Plateau (--, 10.506)	--	--	4.761 ± 1.129 (0.453)	4.225 ± 1.358	3.994 ± 1.35	4.34 ± 1.356	3.963 ± 1.293
53 - Skeena-Omineca-Central Canadian Rocky Mountains (--, 14.006)	--	--	4.554 ± 3.33 (0.325)	5.324 ± 2.703	5.827 ± 2.334	5.386 ± 2.593	6.23 ± 2.7
North American Deserts							
12 - Sonoran Desert (11.697, 21.759)	0.002 (0.0002)	0.404 (0.035; -0.034 ± 0.011)†	0.68 ± 0.198 (0.031)	1.366 ± 0.335	1.062 ± 0.33	0.665 ± 0.29	0.861 ± 0.745
13 - Mojave Desert (12.960, 12.960)	0.028 (0.002)	1.717 (0.133; -0.130 ± 0.011)	1.717 ± 0.145 (0.133)	2.656 ± 0.123*	2.747 ± 0.196*	1.726 ± 0.331	2.777 ± 0.796
14 - Central Basin and Range (30.998, 30.998)	0.117 (0.004)	9.171 (0.296; -0.292 ± 0.018)	9.171 ± 0.546 (0.2926)	10.076 ± 0.595	10.662 ± 1.134	8.952 ± 0.453	10.158 ± 2.055
15 - Northern Basin and Range (14.218, 14.218)	0.089 (0.006)	6.524 (0.459; -0.453 ± 0.05)	6.524 ± 0.707 (0.459)	7.138 ± 0.813	7.232 ± 1.375	7.36 ± 0.97	7.593 ± 1.836
16 - Snake River Plain (5.364, 5.364)	0.008 (0.001)	0.518 (0.097; -0.095 ± 0.014)	0.518 ± 0.076 (0.097)	0.560 ± 0.124	0.595 ± 0.212	0.558 ± 0.128	0.825 ± 0.61
20 - Colombia Plateau (8.302, 8.381)	0.013 (0.002)	1.161 (0.14; -0.138 ± 0.088)	1.185 ± 0.753 (0.141)	1.439 ± 0.787	1.481 ± 0.825	1.402 ± 0.784	1.824 ± 1.033
26 - Wyoming Basin (13.271, 13.271)	0.008 (0.0006)	1.47 (0.111; -0.11 ± 0.039)	1.47 ± 0.515 (0.112)	1.347 ± 0.160	1.687 ± 0.174	1.449 ± 0.124	1.873 ± 0.482

220

Table A.7. Continued.

Ecoregion Map No. - Ecoregion (Area for BEE and Model Projection Area) (*Level I* - Level III; CEC 2005)	Actual Current Area of Burn in BEE (% Ecoreg.)[a]	Model Projected Current Area of Burn (n = 4; or ± SD)		Model Projected Future Area of Burn (n = 4; ± SD)			
		BEE (% Ecoregion; % Actual minus % Projected)	Model Projection Area (% Ecoregion)	2050		2070	
				RCP2.6	RCP8.5	RCP2.6	RCP8.5
35 - Arizona/New Mexico Plateau (15.010, 15.010)	0.006 (0.0004)	1.009 (0.067; -0.067 ± 0.021)	1.009 ± 0.313 (0.067)	1.456 ± 0.366	1.368 ± 0.506	0.775 ± 0.643	1.11 ± 0.541
38 - Chihuahuan Desert (16.215, 50.943)	0.007 (0.0004)	0.0 (0.0; 0.0 ± 0.0)†	0.0 ± 0.0 (0.0)	0.0 ± 0.0	0.0 ± 0.0	0.0 ± 0.0	0.0 ± 0.0
50 - Thompson-Okanogan Plateau (--, 5.264)	--	--	3.622 ± 0.705 (0.688)	3.634 ± 0.961	3.552 ± 1.099	3.562 ± 0.947	3.667 ± 1.114
Great Plains							
23 -Northwestern Glaciated Plains (17.496, 40.561)	0.0006 (0.00003)	0.098 (0.006; -0.006 ± 0.003)†	0.116 ± 0.067 (0.003)	0.123 ± 0.076	0.101 ± 0.057	0.129 ± 0.083	0.119 ± 0.069
24 - Aspen Parkland/Northern Glaciated Plains (8.093, 30.764)	0.0 (0.0)	0.0 (0.0; 0.0 ± 0.0)†	0.012 ± 0.002 (0.0004)	0.013 ± 0.004	0.013 ± 0.003	0.014 ± 0.003	0.011 ± 0.008
25 - Northwest Great Plains (35.758, 35.758)	0.029 (0.0008)	0.723 (0.020; -0.019 ± 0.009)†	0.723 ± 0.332 (0.02)	0.638 ± 0.144	0.627 ± 0.146	0.649 ± 0.161	0.840 ± 0.370
27 - Nebraska Sandhills (5.912, 5.912)	0.0 (0.0)	0.0 (0.0; -0.0 ± 0.0)†	0.0 ± 0.0 (0.0)	0.0 ± 0.0	0.0001 ± 0.0001	0.0 ± 0.0	0.0004 ± 0.0005
28 - Western Corn Belt Plains (4.853, 13.889)	0.0 (0.0)	0.002 (0.0004; -0.0004 ± 0.0007)†	0.003 ± 0.004 (0.0002)	0.003 ± 0.004	0.003 ± 0.004	0.003 ± 0.004	0.006 ± 0.005
29 - Flint Hills (2.793, 2.793)	0.0 (0.0)	0.0002 (0.0001; -0.0001 ± 0.0001)†	0.0002 ± 0.0004 (0.0001)	0.0002 ± 0.0005	0.0001 ± 0.0005	0.0 ± 0.0	0.0 ± 0.0

221

Table A.7. Continued.

Ecoregion Map No. - Ecoregion (Area for BEE and Model Projection Area) (*Level I* - Level III; CEC 2005)	Actual Current Area of Burn in BEE (% Ecoreg.)[a]	Model Projected Current Area of Burn (n = 4; or ± SD)		Model Projected Future Area of Burn (n = 4; ± SD)			
		BEE (% Ecoregion; % Actual minus % Projected)	Model Projection Area (% Ecoregion)	2050		2070	
				RCP2.6	RCP8.5	RCP2.6	RCP8.5
30 - Central Great Plains (27.493, 27.493)	0.0 (0.0)	0.008 (0.0003; -0.0001 ± 0.001)†	0.008 ± 0.015 (0.0003)	0.002 ± 0.003	0.009 ± 0.014	0.003 ± 0.005	0.0004 ± 0.0006
31 - High Plains (28.831, 28.831)	0.002 (0.00008)	0.027 (0.001; -0.001 ± 0.001)†	0.027 ± 0.031 (0.001)	0.028 ± 0.029	0.047 ± 0.044	0.035 ± 0.036	0.057 ± 0.055
39 - Southwest Tablelands (19.886, 19.886)	0.005 (0.0002)	0.145 (0.007; -0.007 ± 0.004)†	0.145 ± 0.073 (0.007)	0.075 ± 0.019	0.042 ± 0.026	0.109 ± 0.044	0.031 ± 0.036
40 - Edwards Plateau (7.497, 7.497)	0.001 (0.0001)	0.043 (0.006; -0.006 ± 0.008)†	0.043 ± 0.057 (0.006)	0.002 ± 0.002	0.001 ± 0.001	0.007 ± 0.009	0.015 ± 0.021
41 - Cross Timbers (8.821, 8.821)	0.004 (0.0004)	0.012 (0.001; -0.001 ± 0.003)†	0.012 ± 0.023 (0.001)	0.008 ± 0.009	0.086 ± 0.109	0.003 ± 0.003	0.141 ± 0.254
42 - Texas Blackland Prairies (4.338, 4.338)	0.0 (0.0)	0.0 (0.0; 0.0 ± 0.0)†	0.0 ± 0.0 (0.0001)	0.007 ± 0.014	0.12 ± 0.218	0.0 ± 0.0	0.125 ± 0.212
45 - Western Gulf Coastal Plain (5.760, 7.833)	0.002 (0.0003)	0.004 (0.0007; -0.0004 ± 0.001)†	0.005 ± 0.009 (0.0006)	0.011 ± 0.012	0.088 ± 0.121	0.019 ± 0.031	0.013 ± 0.226
46 - South Texas Plains (5.347, 14.227)	0.0 (0.0)	0.0 (0.0; 0.0 ± 0.0)†	0.357 ± 0.162 (0.025)	0.345 ± 0.177	0.146 ± 0.106	0.306 ± 0.165	0.281 ± 0.188
Temperate Sierras							
36 - Arizona/New Mexico Mountains (10.878, 10.878)	0.186 (0.017)	5.663 (0.521; -0.503 ± 0.071)‡	5.663 ± 0.777 (0.521)	5.597 ± 1.111	4.855 ± 1.562	4.838 ± 1.55	3.503 ± 2.305
48 - Sierra Madre Occidental (--, 15.449)	--	--	13.578 ± 1.69 (0.879)	12.623 ± 2.656	12.134 ± 3.387	12.509 ± 2.853	11.09 ± 4.3

222

Table A.7. Continued.

Ecoregion Map No. - Ecoregion (Area for BEE and Model Projection Area) (*Level I* - Level III; CEC 2005)	Actual Current Area of Burn in BEE (% Ecoreg.)[a]	Model Projected Current Area of Burn (n = 4; or ± SD)		Model Projected Future Area of Burn (n = 4; ± SD)			
		BEE (% Ecoregion; % Actual minus % Projected)	Model Projection Area (% Ecoregion)	2050		2070	
				RCP2.6	RCP8.5	RCP2.6	RCP8.5
Southern Semiarid Highlands							
37 - Madrean Archipelago (4.3, 7.48)	0.024 (0.006)	1.061 (0.247; -0.241 ± 0.099)	2.457 ± 1.253 (0.328)	2.107 ± 1.512	1.581 ± 1.315	1.813 ± 1.39	1.157 ± 1.052
47 - Piedmonts and Plains (--, 13.003)	--	--	3.021 ± 3.711 (0.232)	2.366 ± 2.959	2.15 ± 2.569	2.301 ± 2.894	1.981 ± 2.34
Eastern Temperate Forest							
43 - East Central Texas Plains (5.575, 5.575)	0.001 (0.0002)	0.001 (0.0002; 0.0001 ± 0.0004)	0.001 ± 0.002 (0.0002)	0.052 ± 0.065	0.172 ± 0.22	0.006 ± 0.007	0.278 ± 0.325
44 - South Central Plains (7.046, 10.199)	0.012 (0.002)	0.507 (0.072; -0.071 ± 0.074)	1.108 ± 0.896 (0.109)	2.058 ± 1.922	3.121 ± 3.559	1.145 ± 1.54	3.448 ± 3.98
Tropical Dry Forests							
49 - Sinoloa and Sonora Hills and Canyons (--, 8.026)	--	--	3.541 ± 2.638 (0.441)	3.111 ± 2.85	2.874 ± 2.77	2.909 ± 2.678	2.469 ± 2.513

[a]Based on aggregation of 30 m 1984–2014 Monitoring Trends in Burn Severity (MTBS)/LANDFIRE rasters to one km rasters.

† = Projected current burned area less than 5% higher than actual burned area for ecoregion within the BEE. Projected burned areas for other ecoregions are greater than or equal to 5% higher than observed, indicating potential fire deficits.

‡ = Projected current burned area is greater than or equal to 50% higher than actual burned area for ecoregion with the BEE.

* = Projected future burned area significantly different from projected current burned area for ecoregion in projected model area by Welch t test with Holm correction for four comparisons (P < 0.05) if preceded by significant Welch ANOVA test (P < 0.05).
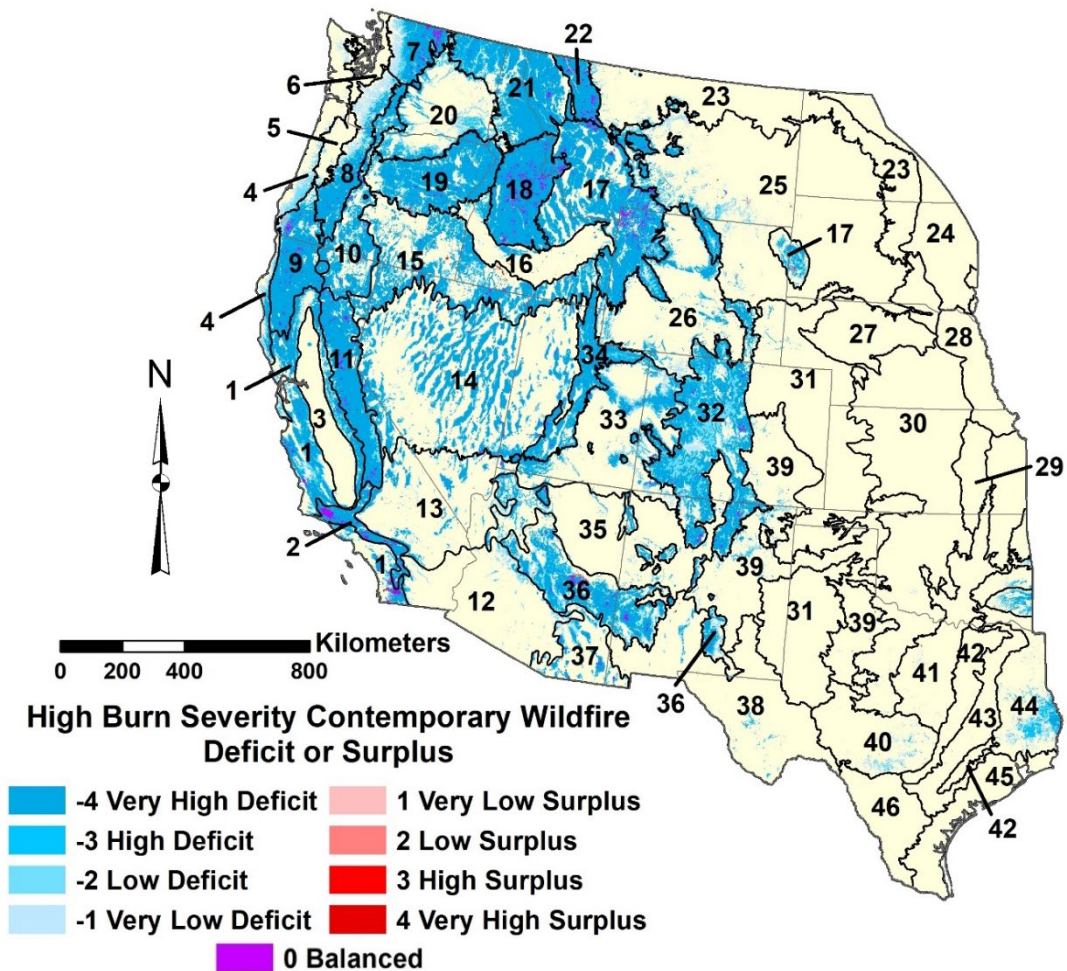
Figure A.22. High burn severity contemporary wildfire deficit or surplus representing a combination of historical wildfire data (Figure II.2C) and degree of wildfire activity projected by MaxEnt quadratic/hinge (β2) wildfire activity feature subset ensemble models for large wildfires with mean fire interval of ≤ 16.5 yrs per 31 yrs (Figure II.9A) (Tracy et al., 2018b).

Northern Basin and Range, and Blue Mountains ecoregions (Figure A.22; see Tracy et al.

[2018b] Appendix A, section 3.3.1 for zipped shapefile).

Future Climate Model Projections

Low Burn Severity

The wildfire activity models for 2050 and 2070 project a significant decrease in area of

low burn severity wildfires in three to four Level III ecoregions, respectively. These ecoregions

are generally south of 40ºN, which is around the southern border of the Wyoming Basin (26)

(Figure II.7B–E, Table A.5). A significant increase in future burned area is projected for the

northern half of western North America in nine to 13 Level III ecoregions for 2050 and 2070,

respectively. Outside of the background evaluation extent, the Thompson-Okanogan Plateau (50)

of western Canada is projected to have a significantly greater burned area in the 2070 RCP8.5

scenario. The important variable of mean temperature of the driest quarter (*bio_9*) is consistently

higher across all latitudes for 2070 RCP 8.5 compared to current climate. Precipitation in the

summer quarter (*prec_sumq*) is generally lower for 2070 RCP 8.5 than current climate in higher

latitudes above 40ºN, but higher in lower latitudes below 27ºN. However, precipitation in the

spring quarter (*prec_sprq*) is generally lower for 2070 RCP 8.5 than current climate in lower

latitudes below 42ºN and higher in the higher latitudes above 47ºN (Figure A.23A-C).

Moderate Burn Severity

Three to five northern Level III ecoregions are projected to have significant decreases in

burned areas for the 2050 and 2070 RCP2.6 scenarios, respectively (Figure II.8B–D; Table A.6).

In addition, seven to nine Level III ecoregions are projected to have significantly reduced burned

areas in in the 2050 and 2070 RCP8.5 scenarios, respectively. None of the seven Level III
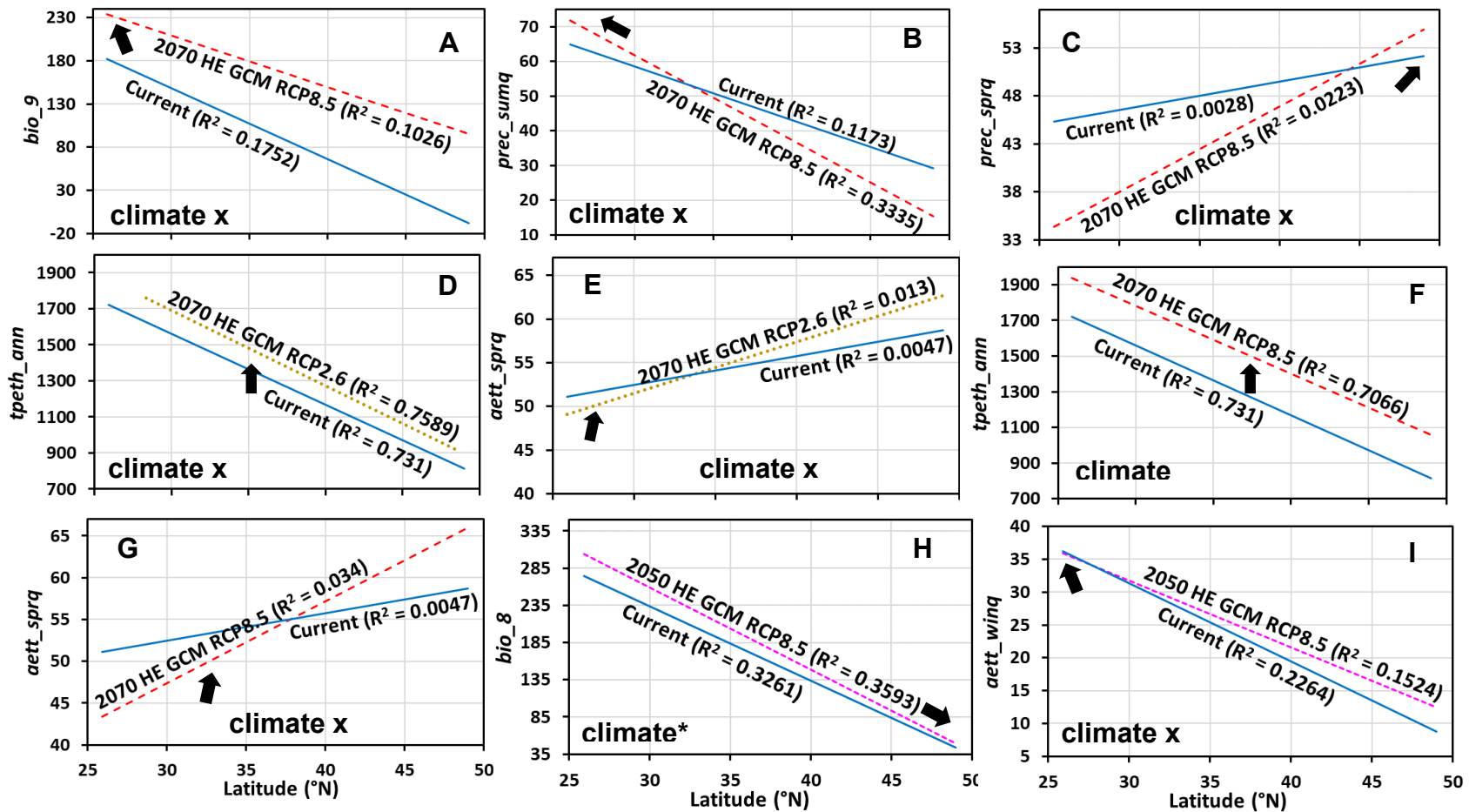
Figure A.23. Linear regressions (with R^2 values) of background point values for top climatic indices for various climate scenarios by permutation importance versus latitude across western North America projection area for top ranking MaxEnt quadratic/hinge (β2) wildfire niche models of (A–C) low burn severity; (D–G) moderate burn severity; and (H–I) high burn severity (climate* = significant difference in climate responses for variable; climate x variable* = significant difference in slopes of variable response to climate; $P < 0.05$ ANOVA) (arrows indicate direction of peak values for wildfire suitability from variable response curves in Figures A.14-17; see Table II.1 for variable abbreviations and Table A.4 for permutation importance) (Tracy et al., 2018b).
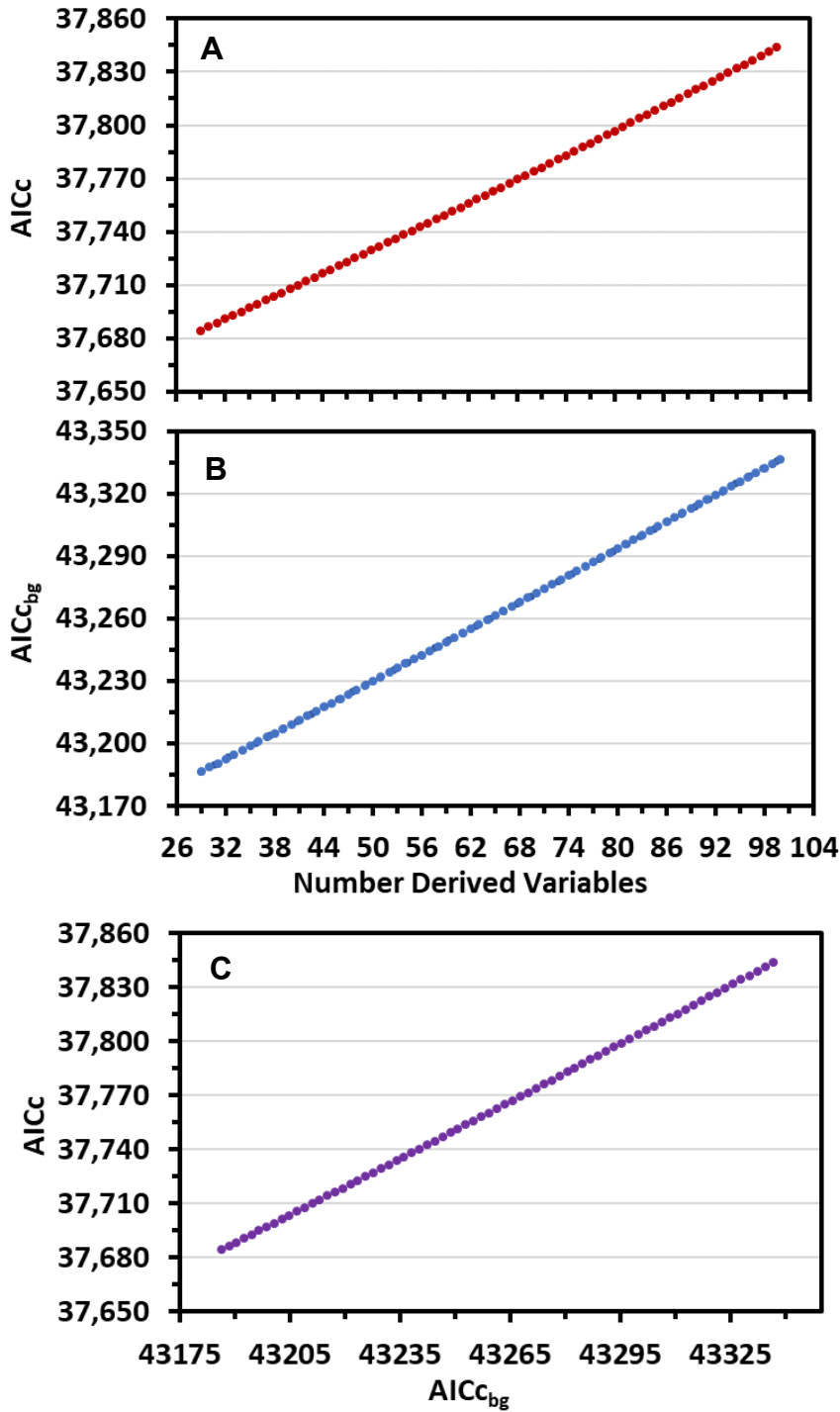
226

Figure A.24. Value of AICc (A) or AICc$_{bg}$ (B) versus number of derived variables (parameters) artificially specified for a MaxEnt quadratic/hinge (β2) wildfire activity model of low burn severity developed from 15 of 90 selected by AUC using RSFSA. (C) AICc versus AICc$_{bg}$ for various numbers of parameters specified for same model (Tracy et al., 2018b).
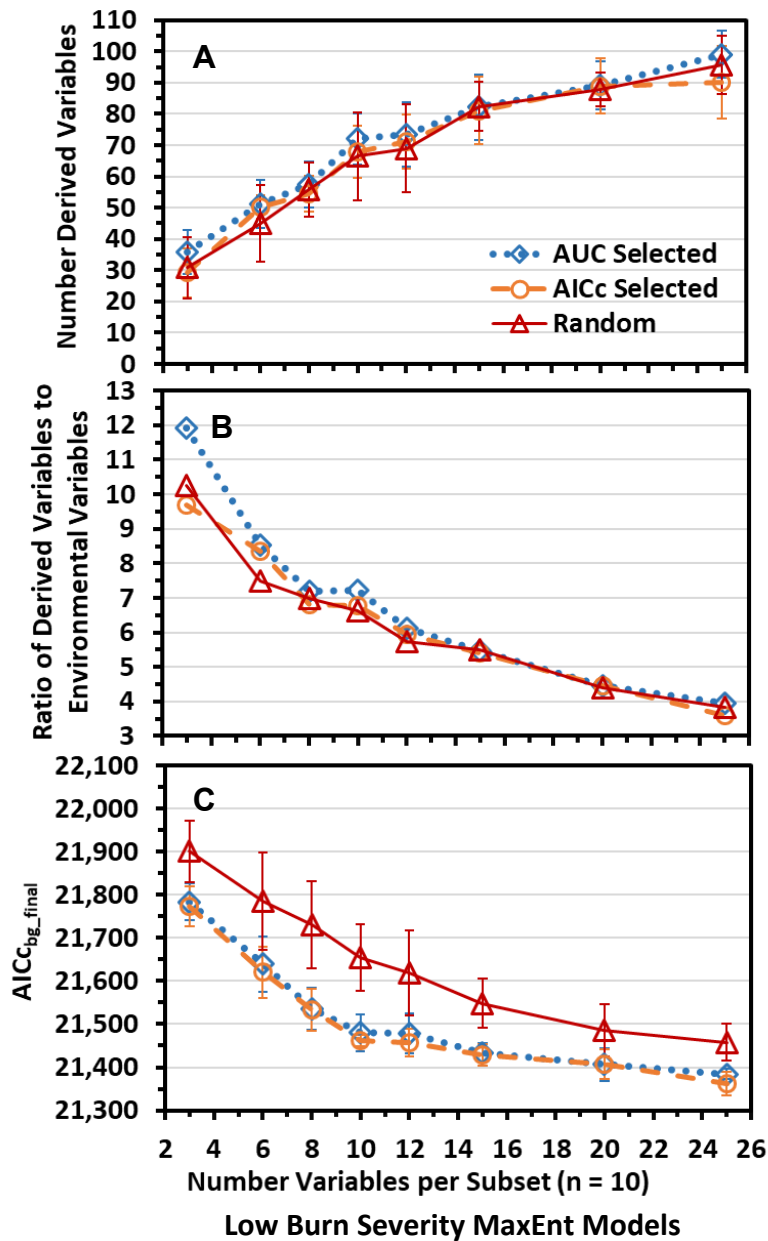
Figure A.25. MaxEnt quadratic/hinge (β2) low burn severity wildfire activity model characteristics for (A) the number of MaxEnt derived variables (mean ± SD), (B) the ratio of MaxEnt derived variables to environmental variables, and (C) $AICc_{bg\_final}$ (mean ± SD; from Figure 5D). Models developed from top ten variable subsets selected by AUC or AICc using RSFSA and ten random subsets out of 250 randomly generated variable subsets of various sizes derived from 90 variables (Tracy et al., 2018b).

ecoregions outside of the background evaluation extent were projected to have significant differences in burned area for large moderate burn severity wildfires. The important variable of annual total potential evapotranspiration (*tpeth_ann*) is generally higher across all latitudes for 2070 for both RCP values compared to current climate. However, actual evapotranspiration for the spring quarter (*aett_sprq*) for 2070 is only higher than current climate at latitudes above around 35ºN for both RCP values (Figure A.23D-G).

High Burn Severity

Only a single ecoregion, the Mojave Desert (13), was projected to significantly change in the area of high burn severity wildfires in a future climate scenario wildfire activity model. The burned area for the Mojave Desert was projected to increase in both of the 2050 scenarios for RCP2.6 and RCP8.5 (Figure II.9B–D; Table A.7). For example, the Panamint Mountains (sky island habitat) of Death Valley were projected to have high burn severity wildfires in both the current and future climate scenario wildfire models, but some future scenario models include additional burned areas southeast of the Panamint Mountains, such as the lower elevations of Galena Canyon and Warm Springs Canyon. There is little difference between important variables of mean temperature of the wettest quarter (*bio_8*) and actual evapotranspiration in the winter quarter (*aett_winq*) between 2050 RCP8.5 and current climate across all latitudes (Figure A.23H-I).

Discussion

Projections for Wildfire Activity Models

Future Climate

More northern ecoregions were projected with larger areas of moderate burn severity wildfires in future RCP8.5 compared to RCP2.6 scenarios. This difference may be related to

229

greater changes for RCP8.5 in two important variables: (1) higher AET in the spring quarter (*aett_sprq*) in the north, but not the south, and (2) higher total annual evapotranspiration (*tpeth_ann*) (Tables A.3-4, Figure A.23D–G). Higher spring AET may be related to increased primary productivity, and higher total annual evapotranspiration may be related to increased annual vegetation water stress, both of which may favor moderate severity wildfires in northern ecoregions. Future projections for decreased areas of moderate burn severity wildfires in southern ecoregions, may be associated with reduced AET in the spring quarter (*aett_sprq*) for the south leading to potentially lower primary productivity, which is again stronger for RCP8.5 than RCP2.6 (Figure A.21E,G).

The general lack in projected changes in burned areas for high burn severity wildfires may be related to the relatively small future departures from current values for the identified important variables, such as mean temperature of the wettest quarter (*bio_8*) and actual evapotranspiration in the winter quarter (*aett_winq*) (Tables A.3-4, Figure A.23H-I).

References (not appearing in main References section)

Abatzoglou JT, Kolden CA (2013) Relationships between climate and macroscale area burned in the western United States. International Journal of Wildland Fire 22:1003-1020.

Balice RG, Miller JD, Oswald BP, Edminster C, Yool SR (2000) Forest Surveys and Wildfire Assessment in the Los Alamos Region; 1998-1999. Publication No. LA-13714-MS, Los Alamos National Lab, Los Alamos, New Mexico, NM, 86 pp.

Brauers WK, Zavadskas EK (2010) Project management by MULTIMOORA as an instrument for transition economies. Technological and Economic Development of Economy 1:5-24.

Ceballos Martín, BA (2016) Package 'MCDM'. 9 pp. Available from https://cran.r-project.org/web/packages/MCDM/MCDM.pdf (6 February 2016)

Chiu CA, Lin PH, Hsu CK, Shen ZH (2012) A novel thermal index improves prediction of vegetation zones: associating temperature sum with thermal seasonality. Ecological Indicators 23:668-674.

Dijkstra L, Poelman H (2014) A Harmonized Definition of Cities and Rural Areas: The New Degree of Urbanization. Regional Working Paper 01/2014, European Commission Directorate-General for Regional and Urban Policy, Brussels, Belgium, 24 pp, Available from

http://ec.europa.eu/regional_policy/sources/docgener/work/2014_01_new_urban.pdf (15 December 2016)

Evans IS (1972) General geomorphometry, derivatives of altitude, and descriptive statistics. In: Chorley RJ (eds) Spatial Analysis in Geomorphology, Harper and Row, New York, pp. 17-90.

Guisan A, Weiss SB, Weiss AD (1999) GLM versus CCA spatial modeling of plant species distribution. Plant Ecology 143:107-122.

Hamilton DA, Hann W (2015) Mapping landscape fire frequency for fire regime condition class. In: Keane RE, Jolly M, Parsons R, Riley K (eds) Proceedings of the Large Wildland Fires Conference, 9–23 May, 2014, Missoula, Montana, USDA Forest Service Proceedings RMRS-P-73, USDA Forest Service, Rocky Mountain Research Station, Fort Collins, Colorado, pp. 111-119. Available from

http://www.fs.fed.us/rm/pubs/rmrs_p073/rmrs_p073_111_119.pdf (20 December 2016)

Iverson LR, Dale ME, Scott CT, Prasad A (1997) A GIS-derived integrated moisture index to predict forest composition and productivity of Ohio forests (USA). Landscape Ecology 12:331-348.

Kuhn, M (2008). Building predictive models in R using the caret package. Journal of Statistical Software 28, 26 pp.

Kuhn M, Johnson K (2013) An introduction to feature selection. In: Kuhn, M, Kjell, J (eds.), Applied Predictive Modeling, Springer, New York, pp. 487-519.

Langford S, Stevenson S, Noone D (2014) Analysis of low-frequency precipitation variability in CMIP5 historical simulations for southwestern North America. Journal of Climate 27:2735-2756.

Littell JS, Gwozdz RB (2011) Climatic water balance in regional fire years in the Pacific Northwest, USA: linking regional climate and fire and at landscape scales. In: McKenzie, DM (ed), The Landscape Ecology of Fire, Springer, Netherlands, Vol. 213, pp. 177-139.

McCune B, Keon D (2002) Equations for potential annual direct incident radiation and heat load. Journal of Vegetation Science 13:603-606.

Moore ID, Lewis A, Gallant JC (1993) Terrain attributes: estimation methods and scale effects. In: Jakeman AJ, Beck MB, McAleer M (eds), Modeling Change in Environmental Systems, John Wiley and Sons Inc., New York, pp. 189-214.

National Wildfire Coordinate Group (NWCG) (2016) Glossary; Size Class of Fire. Available from http://www.nwcg.gov/term/glossary/size-class-of-fire (21 December 2016)

Pike RJ, Wilson SE (1971) Elevation relief ratio, hypsometric integral and geomorphic area altitude analysis. Bulletin of the Geological Society of America 82:1079-1084.

Rivas-Martinez S, Sanchez-Mata D, Costa M (1999) North American boreal and Western temperate forest vegetation. Itinera Geobotanica 12:5–316. Available from http://www.globalbioclimatics.org/book/namerica2/namerica.htm (31 December 2017)

Rollins MG (2009) LANDFIRE: a nationally consistent vegetation, wildland fire, and fuel assessment. International Journal of Wildland Fire 18:235-249.

Schwind B (2008) Monitoring trends in burn severity: report on the Pacific Northwest and Pacific Southwest fires—1984 to 2005. Available from http://www.mtbs.gov/files/MTBS_pnw-psw_final.pdf (9 January 2017)

Sheffield J, Barrett AP, Colle B, Nelun Fernando D, Fu R, Geil KL, Hu Q, Kinter J, Kumar S, Langenbrunner B, Lombardo K (2013) North American climate in CMIP5 experiments. Part I: evaluation of historical simulations of continental and regional climatology. Journal of Climate 26:9209-9245.

Stage AR (1976) Notes: An expression for the effect of aspect, slope, and habitat type on tree growth. Forest Science 22:457-460.

Stephenson N (1998) Actual evapotranspiration and deficit: biologically meaningful correlates of vegetation distribution across spatial scales. Journal of Biogeography 25:855-870.

Thornthwaite CW (1948) An approach toward a rational classification of climate. Geographical Review 38:55-94.

Willmott CJ, Feddema JJ (1992) A more rational climatic moisture index. The Professional Geographer 44:84-88.

APPENDIX B

(CHAPTER II)[*]

Parameters for Selected 15-Variable MaxEnt Wildfire Activity Models

For each of the four top MaxEnt quadratic/hinge β2 models of each burn severity selected by the random feature subset selection algorithm, lists of the 15 environmental variables and embedded pdf files of the MaxEnt lambda files detailing the derived features and model parameters are provided (Tables B.1-3). The lambda text files are provided as output by MaxEnt version 3.3.3 software as a text file, such as "species.lambdas". Four types of features are listed in each MaxEnt wildfire activity model lambda file (based on MaxEnt settings restricted to hinge and quadratic features): (1) raw or linear features are indicated with no prefix or suffix around the variable name (linear features have coefficient of zero since not used in models when hinge features are used); (2) quadratic (2nd power) features are indicated with a suffix of "^2" after the variable name; (3) forward hinge features are signified by a prefix of " ' " before the variable name; and (4) reverse hinge features are identified with a prefix of " ` " before the variable name. There can be several derived forward and reverse hinge features for a single environmental variable. See Wilson (2009) for further explanation of the numeric parameters of feature types and other details of MaxEnt version 3.3.3 lambdas files. Elith et al. (2011) and Halvorson (2013) provide further explanation of model parameters of derived feature types. Halvorsen (2013) emphasized the importance of detailed information on MaxEnt model parameters and noted that it is very rarely provided in publications. (See main References section for References).

234

Table B.1. Low burn severity MaxEnt quadratic/hinge β2 wildfire activity model environmental variables and associated derived features (Tracy et al., 2018b).

Model Number (No. Derived Features) with 15 Environmental Variables and Lambdas Text File of Derived Features[a]			
Model 1 (103)	Model 2 (101)	Model 4 (94)	Model 17 (96)
agric_lc	agric_lc	agric_lc	aett_autq
bio_19	bio_9	bio_2	agric_lc
bio_3	cont_index	bio_8	bio_14
cont_dfmo	diss3kr	bio_9	bio_9
elev	elev	cti	cont_index
etrt_ann	ew_indx	diss3kr	err3kr
ew_indx	medrurdist	elev	etrt_sprq
hirurdist	prec_sumq	lorurdist	lorurdist
imi	prec_winq	medurbdist	peth_autq
mnpopden3r	roadden9kr	prec_sumq	prec_sprq
prec_sumq	slope	roadden19kr	roadden9kr
scai	sprurdist	roadden13kr	scai
slope	strmloflodist	taett_tann	slope
tpi19kr	taett_tann	tmax_autq	sprurdist
urban_lc	tpeth_m_taett	tpi19kr	strmhiflodist
LoBrn15VarModel1_lambdas.pdf	LoBrn15VarModel2_lambdas.pdf	LoBrn15VarModel4_lambdas.pdf	LoBrn15VarModel17_lambdas.pdf

[a]For abbreviations, see Table II.1.

235

Table B.2. Moderate burn severity MaxEnt quadratic/hinge β2 wildfire activity model environmental variables and associated derived features (Tracy et al., 2018b).

Model Number (No. Derived Features) with 15 Environmental Variables and Lambdas Text File of Derived Features[a]			
Model 6 (89)	Model 10 (90)	Model 16 (85)	Model 20 (81)
aett_autq	*aett_sprq*	*aett_sprq*	*agric_lc*
agric_lc	*aett_winq*	*agric_lc*	*bio_1*
bio_17	*agric_lc*	*bio_2*	*bio_7*
bio_7	*bio_1*	*bio_3*	*bio_9*
bio_8	*bio_17*	*cont_dfmo*	*cont_dfmo*
elev	*bio_9*	*lourbdist*	*etrt_sprq*
hiurbdist	*diss3kr*	*prec_sumq*	*medrurdist*
lourbdist	*hli*	*roadden3kr*	*medurbdist*
mnpopden3r	*lorurdist*	*sei*	*mnpopden9r*
prec_sumq	*popden*	*slope*	*roaddist*
slope	*prec_sumq*	*sprurdist*	*sei* (not used)
strmhiflodist	*roadden3kr*	*strmhiflodist*	*slope*
strmmdflodist	*sei*	*strmmdflodist*	*strmmdflodist*
tpeth_ann	*slope*	*tpeth_ann*	*tpi3kr*
tpi19kr	*strmdist*	*tpi9kr*	*tpi9kr*
ModBrn15VarModel6 _lambdas.pdf	ModBrn15VarModel1 0_lambdas.pdf	ModBrn15VarModel1 6_lambdas.pdf	ModBrn15VarModel2 0_lambdas.pdf

[a]For abbreviations, see Table II.1.

Table B.3. High burn severity MaxEnt quadratic/hinge β2 wildfire activity model environmental variables and associated derived features (Tracy et al., 2018b).

Model Number (No. Derived Features) with 15 Environmental Variables and Lambdas Text File of Derived Features[a]			
Model 2 (95)	Model 5 (103)	Model 18 (89)	Model 21 (89)
agric_lc	*aett_winq*	*aett_sprq*	*aett_sprq*
bio_15	*agric_lc*	*agric_lc*	*agric_lc*
bio_2	*bio_4*	*bio_14*	*bio_15*
bio_8	*bio_8*	*bio_15*	*bio_3*
bio_9	*elev*	*bio_7*	*diss3kr*
cont_index	*etrt_sprq*	*bio_8*	*elev*
elev	*lorurdist*	*imi*	*etrt_sumq*
hli	*peth_sumq* (not used)	*mnpopden3r*	*hli*
peth_autq	*roadden3kr*	*peth_winq*	*lorurdist*
popden (not used)	*slope*	*peth_sumq*	*prec_winq*
prec_autq	*sprurdist*	*roadden19kr*	*roadden9kr*
prec_sumq	*strmhiflodist*	*sei*	*scai*
roadden9kr	*strmmdflodist*	*slope*	*slope*
slope	*tmin_autq*	*strmmdflodist*	*strmhiflodist*
strmhiflodist	*tpi3kr*	*urban_lc*	*tpeths_tpetha*
HiBrn15VarModel2_lambdas.pdf	HiBrn15VarModel5_lambdas.pdf	HiBrn15VarModel18_lambdas.pdf	HiBrn15VarModel21_lambdas.pdf

[a]For abbreviations, see Table II.1.

APPENDIX C

(CHAPTER III)

Methods

MaxEnt Migration Pathways

The random subset feature selection algorithm (RSFSA; Tracy et al. 2018b) was utilized to identify six out of 80 variable subsets as optimal for maximizing accuracy (AUC_{psa}), minimizing complexity (AICc), and minimizing overfitting (AUC_{psa_diff}) in MaxEnt migration models (Figure C.1A-C). The top 250 of 3,000 six-variable MaxEnt models selected by AUC_{psa} exhibited significantly higher AUC_{psa} and lower AICc than 300 random MaxEnt models for all three training data set replications (Figure C.1 D,E). Significantly lower overfitting (AUC_{psa_diff}) was only evident for AUC_{psa} selected MaxEnt models in one replication (Figure C.1F). Out of 9,000 randomly generated six-variable MaxEnt models the top 12 as ranked by AUC_{psa} were selected for inclusion in a feature subset ensemble model (Figure III.2A). Joint ranking of environmental variables employed in the top 12 selected models using weighted criteria (0.6 for mean variable permutation importance; 0.4 for frequency of variable appearance in top 12 models) was performed with a Multi Multi-Objective Optimization Ratio Algorithm (plus Full Multiplicative Form, MMOORA) of Brauers and Zavadskas (2010), which is implemented in the MCDM R package (Ceballos Martín, 2016).

Kernel Density Estimation Model Migration Pathways

To calculate the monarch roost human population density index, the raw roost data was first converted to a 10 km resolution raster with values of one for roost presence and "no data". This process produced one roost record per 10 km grid cell. The 5 km resolution human

Table C.1. Eastern monarch fall overnight roost records from 2002-2016 (Journey North 2017).

Year	Observations	Earliest Day of Year	Latest Day of Year	Duration (Days)
2002	25	239	309	70
2003	103	215	321	106
2004	70	214	314	100
2005	189	227	305	78
2006	173	223	360	137
2007	269	217	360	143
2008	136	222	312	90
2009	160	228	311	83
2010	336	223	315	92
2011	185	314	314	91
2012	138	312	312	76
2013	109	242	317	75
2014	245	236	340	104
2015	422	227	339	115
2016	243	234	335	121
Total	2803			
Mean ± SD per Year	186.9 ± 103.4	238.2 ± 31.5	324.3 ± 18.1	98.7 ± 22.4

Table C.2. Eighty environmental predictor indices (10 km resolution) used in developing 12 selected MaxEnt monarch overnight roost niche models with six of 80 variables.

Variable Index (Source)	Grid Name Abbreviation	Variable Frequency in 12 Selected Models (% of 72)[a]
57 Climatic Indices (for 1960–1990 derived from WorldClim [2014] of Hijmans et al. [2005])		
19 Bioclim Indices (WorldClim 2014)		
Annual mean temperature	bio_1	0 (0.0)
Mean diurnal range (mean of monthly TMAX – TMIN)	bio_2	0 (0.0)
Isothermality (bio_2/bio_7) (× 100)	bio_3	0 (0.0)
Temperature seasonality (standard deviation × 100)	bio_4	0 (0.0)
Maximum temperature of warmest month	bio_5	0 (0.0)
Minimum temperature of coldest month	bio_6	0 (0.0)
Temperature annual range (bio_5 – bio_6)	bio_7	0 (0.0)
Mean temperature of wettest quarter	bio_8	0 (0.0)
Mean temperature of driest quarter	bio_9	0 (0.0)
Mean temperature of warmest quarter	bio_10	2 (2.8)
Mean temperature of coldest quarter	bio_11	0 (0.0)
Annual precipitation	bio_12	0 (0.0)
Precipitation of wettest month	bio_13	0 (0.0)
Precipitation of driest month	bio_14	0 (0.0)
Precipitation seasonality (coefficient of variation)	bio_15	6 (8.3)
Precipitation of wettest quarter	bio_16	1 (1.4)
Precipitation of driest quarter	bio_17	1 (1.4)
Precipitation of warmest quarter	bio_18	0 (0.0)
Precipitation of coldest quarter	bio_19	1 (1.4)
Subtotal		11 (15.3)
19 Supplementary Climatic (SuppClim) Indices[b,c]		
Annual mean minimum temp. of coldest month (TMIN)	tmin_ann	0 (0.0)
	tmin_winq,	0 (0.0)
	tmin_sprq,	4 (5.6)
	tmin_sumq,	0 (0.0)
Quarterly mean monthly minimum temperature (4)	tmin_autq	2 (2.8)
Annual mean maximum temp. of warmest month (TMAX)	tmax_ann	0 (0.0)

Table C.2. Continued.

Variable Index (Source)	Grid Name Abbreviation	Variable Frequency in 12 Selected Models (% of 72)[a]
Annual mean monthly rainfall (P) (mm)	*prec_ann*	0 (0.0)
	prec_winq,	0 (0.0)
	prec_sprq,	4 (5.6)
	prec_sumq,	1 (1.4)
Quarterly mean monthly rainfall (50%) (4)	*prec_autq*	0 (0.0)
Effective Warmth Index (from mean monthly temperatures × 10 above 5ºC)	*ew_indx*	1 (1.4)
Rivas-Martinez (RM) ombrothermic index (from monthly MTMP and P)	*ombro_index*	1 (1.4)
RM continentality index (TMAX – TMIN) × 10 (CONT)	*cont_index*	0 (0.0)
RM thermicity index (MTMP + TMX_COLD + TMN_COLD) × 10	*therm_index*	0 (0.0)
Subtotal		15 (20.8)

19 Actual and Potential Evapotranspiration (AET-PET) Indices (PET; Zomer et al. 2007; 2008; AET; Trabucco and Zomer 2010)[c]

Total annual reference evapotranspiration from Hargreaves model (PETH) (mm)	*tpeth_ann*	0 (0.0)
	peth_winq,	0 (0.0)
	peth_sprq,	1 (1.4)
	peth_sumq,	1 (1.4)
Quarterly mean monthly PETH (4)	*peth_autq*	0 (0.0)
Thornwaite summer concentration thermal efficiency (summer PETH/annual PETH) × 1000	*tpeths_tpetha*	0 (0.0)
Willmott and Feddema climate moisture index (from total annual PETH and PREC) × 1000	*im_index*	0 (0.0)
Total annual actual evapotranspiration from Thornwaite-Mather water balance model (TMWBM) (AETT) (mm)	*taett_tann*	4 (5.6)
	aett_winq,	1 (1.4)
	aett_sprq,	2 (2.8)
	aett_sumq,	0 (0.0)
Quarterly mean monthly AETT (4)	*aett_autq*	4 (5.6)
Total annual evapotranspiration ratio (AETT/PETH) × 10	*etrt_ann*	1 (1.4)

241

Table C.2. Continued.

Variable Index (Source)	Grid Name Abbreviation	Variable Frequency in 12 Selected Models (% of 72)[a]
	etrt_winq,	0 (0.0)
	etrt_sprq,	1 (1.4)
	etrt_sumq,	0 (0.0)
Quarterly mean monthly AETT/PETH (4) × 1000	*etrt_autq*	0 (0.0)
Modified Driscoll-Yee Fong Continentality index[d]	*cont_dfmo*	4 (5.6)
Climate water deficit (*tpeth_ann – taett_tann*)	*cwd_ann*	2 (2.8)
Subtotal		21 (29.2)

12 Topographic Indices

Eight Geomorphologic Indices (derived from 15 arc second resolution HydroSHEDs grids of Lehner et al. 2008; last six indices calculated using Geomorphometry and Gradient Metrics Toolbox for ArcGIS [Evans et al. 2014])[c]

Elevation	*elev*	0 (0.0)
Slope	*slope*	1 (1.4)
Topographic Position Index (TPI), 19 km circular radius	*tpi19kr*	1 (1.4)
Compound Topographic Index (CTI)	*cti*	1 (1.4)
Heat Load Index (HLI)	*hli*	0 (0.0)
Integrated Moisture Index (IMI)	*imi*	3 (4.2)
Site Exposure Index (SEI)	*sei*	1 (1.4)
Slope Cosine Aspect Index (SCAI)	*scai*	1 (1.4)

Four Hydrogeomorphologic Indices (derived from 15 arc second resolution HydroSHEDs polyline river network shapefile of Lehner et al. 2008)

Distance to Streams (STRMDIST)	*strmdist*	0 (0.0)
Distance to Low Flow Accumulation Areas (< 5,000 cells; STRMLOFLODIST)	*strmloflodist*	3 (4.2)
Distance to Medium Flow Accumulation Areas (5,000–60,000 cells; STRMMDFLODIST)	*strmmdflodist*	1 (1.4)
Distance to High Flow Accumulation Areas (>60,000 cells; STRMHIFLODIST)	*strmhiflodist*	3 (4.2)
Subtotal		15 (20.8)

11 Land Cover Indices (percent cover per 1 km[2] for 2001 to 2005 from Tuanmu and Jetz [2014] and EarthEnv [2016])

Cultivated and Managed Vegetation	*agric_lc*	1 (1.4)

Table C.2. Continued.

Variable Index (Source)	Grid Name Abbreviation	Variable Frequency in 12 Selected Models (% of 72)[a]
Barren	*barren_lc*	1 (1.4)
Deciduous Broadleaf Trees	*decbrdtree_lc*	1 (1.4)
Evergreen Broadleaf Trees	*evgbrdtree_lc*	1 (1.4)
Regularly Flooded Vegetation	*floodveg_lc*	1 (1.4)
Herbaceous Vegetation	*herb_lc*	1 (1.4)
Mixed/Other Trees	*mixothtree_lc*	1 (1.4)
Evergreen/Deciduous Needleleaf Trees	*needletree_lc*	1 (1.4)
Shrubs	*shrub_lc*	0 (0.0)
Urban/Built-up	*urban_lc*	1 (1.4)
Open Water	*water_lc*	1 (1.4)
Subtotal		10 (13.9)

[a]Frequency out of six variables times 12 models = 72 instances.
[b]Quarters: winter – Jan, Feb, Mar; spring – Apr, May, Jun; summer – Jul, Aug, Sep; autumn – Oct, Nov, Dec. PREC = precipitation; TMAX = mean temperature of warmest month; TMIN = mean temperature of coldest month; TMAX_COLD = mean maximum temperature of coldest month; TMN_COLD = mean minimum temperature of coldest month.
[c]For additional sources of indices and details see Tracy et al. (2018).
[d]Incorporates moisture correction factor of AET/PET × 10.

Table C.3. MaxEnt model variable permutation importance for 42 of 80 variables used in top 12 six-variable monarch overnight roost models selected by random subset feature selection algorithm.

Variable[a]	MaxEnt Model Permutation Importance, Mean ± SD (number of top 12 models)	Multi Multi-Objective Optimization Ranking by Mean Permutation Importance (0.6 weight) and Number Appearances in Top 12 Models (0.4 weight)[b]
tmin_sprq	54.8 ± 4.2 (4)	1
aett_autq	36.3 ± 3.2 (4)	2
taett_tann	25.3 ± 1.3 (4)	3
prec_sprq	16.0 ± 1.5 (4)	4
tmin_autq	47.6 ± 9.1 (2)	5
bio_15	9.5 ± 7.2 (6)	6
bio_10	36.9 ± 6.2 (2)	7
cont_dfmo	10.0 ± 8.5 (4)	8
aett_sprq	25.0 ± 4 (2)	9
cwd_ann	14.8 ± 3.8 (2)	10
ew_indx	54.0 ± 0 (1)	11
aett_winq	35.8 ± 0 (1)	12
ombro_index	31.7 ± 0 (1)	13
tmax_sumq	31.0 ± 0 (1)	14
etrt_ann	24.6 ± 0 (1)	15
etrt_sprq	23.4 ± 0 (1)	16
strmhiflodist	0.2 ± 0.1 (3)	17
strmloflodist	0.2 ± 0.1 (3)	18
imi	0.1 ± 0 (3)	19
bio_19	19.0 ± 0 (1)	20
bio_17	17.8 ± 0 (1)	21
peth_sprq	15.6 ± 0 (1)	22
tmax_sprq	14.3 ± 0 (1)	23
bio_16	12.3 ± 0 (1)	24
peth_sumq	12.1 ± 0 (1)	25
prec_sumq	11.4 ± 0 (1)	26
decbrdtree_lc	11.3 ± 0 (1)	27
mixothtree_lc	4.3 ± 0 (1)	28
needletree_lc	1.4 ± 0 (1)	29
urban_lc	1.2 ± 0 (1)	30
slope	1.1 ± 0 (1)	31
agric_lc	0.7 ± 0 (1)	32
scai	0.3 ± 0 (1)	33
cti	0.1 ± 0 (1)	34
evgbrdtree_lc	0.1 ± 0 (1)	35

Table C.3. Continued.

Variable[a]	MaxEnt Model Permutation Importance, Mean ± SD (number of top 12 models)	Multi Multi-Objective Optimization Ranking by Mean Permutation Importance (0.6 weight) and Number Appearances in Top 12 Models (0.4 weight)[b]
barren_lc	0.1 ± 0 (1)	36
herb_lc	0.1 ± 0 (1)	37
water_lc	0.0 ± 0 (1)	38
sei	0.0 ± 0 (1)	39
strmmdflodist	0.0 ± 0 (1)	40
floodveg_lc	0.0 ± 0 (1)	41
tpi19kr	0.0 ± 0 (1)	42

[a]See Table C.2 for variable abbreviations and sources of variables.
[b]Variables ranked using weighted joint criteria with MCDM R package.

Table C.4. Shapefiles of geographic information system (GIS) layers developed in eastern monarch butterfly fall migration study (see Chapter III, Methods for additional details and sources).

GIS Layers (Source)	Shapefile[a]
Monarch Flyways (This Study)	
Monarch Eastern Flyway (Fig. 6)	MonarchEasternFlywayShapefile.zip
Monarch Central Flyway (Fig. 6)	MonarchCentralFlywayShapefile.zip
MaxEnt and Kernel Density Estimation Model (KDEM) Migration Pathways from Monarch Roosts (Journey North 2017, This Study)	
Monarch Roost 2002-2016 MaxEnt Feature Subset Ensemble 100% Consensus Boundary (Fig. 2A)	MonarchRoost2002_2016CombinedMaxEntConsensusShapefile.zip
Monarch Roost 2002-2016 KDEM Training Set Ensemble 100% Consensus Boundary (Figs. 2B, 3B)	MonarchRoost2002_2016CombinedKDEMConsensusShapefile.zip
Monarch Roost 2002-2016 KDEM Training Set Ensemble Binary Minimum Consensus Boundary (Figs. 5A,6)	MonarchRoost2002_2016CombinedBinaryMinimumConsensusShapefile.zip
Monarch Roost 2005-2016 KDEM Annual Ensemble 100% Consensus Boundary (Figs. 3C, 7B)	MonarchRoost2005_2016AnnualKDEMConsensusShapefile.zip
Monarch Southern Core Migration Pathways (This Study)	
Monarch Central Funnel (Figs. 3C, 7)	MonarchCentralFunnelShapefile.zip
Monarch Coastal Funnel (Figs. 3C, 7)	MonarchCoastalFunnelShapefile.zip
Spatially Identified Potential Migratory Hazards (This Study)	
Monarch Roadkill Hotspots (Fig. 7A)	MonarcRoadkillHotspotsShapefile.zip
High Cultivated Land Cover (Areas with ≥ 90% Anthropogenic Cultivated or Urban Land Cover per 1 km, with at Least 70% Cultivated Land Cover (Fig. 7B)	HighCultivatedLandCoverShapefile.zip
2014 Neonicotinoid Use in US Counties (imidacloprid, clothianidin, and thiamethoxam) (Fig. 7B)	NeonicotinoidUse2014USCountiesShapefile.zipi

Table C.4. Continued.

GIS Layers (Source)	Shapefile[a]
Texas and Louisiana Counties with Mosquito Control Districts (Fig. 7C)	MosquitoControlDistrictsinTX_LACountiesShapefile.zip
Southeastern US Counties with Ultra-Low Volume (ULV) Mosquito Control Treatments (Fig. 7C)	MosquitoULVcontroinSE_USCountiesShapefile.zip
Latest Fall ULV Spraying in Southeastern US Cities (Fig. 7C)	MosquitoULVSprayCitiesLateFallDatesShapefile.zip

[a] Zipped shapefiles are available upon request from author and are to be made available in appendix of Kantola et al. (2018).
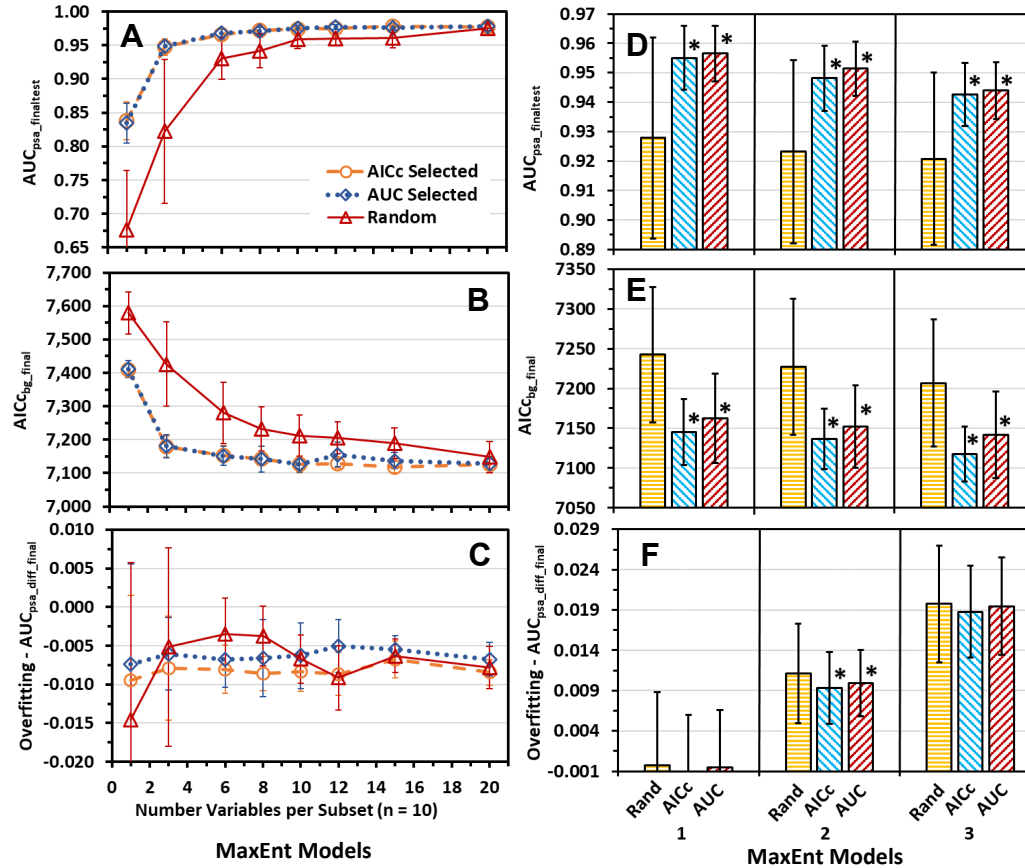
Figure C.1. MaxEnt migration model evaluation statistics (mean ± SD) of $AUC_{psa\_finaltest}$ (A,D), $AICc_{bg\_final}$ (B,E), and $AUC_{psa\_diff\_final}$ (overfitting; C,F) for models developed from (A-C) top ten variable subsets selected by AUC_{psa} or AICc using random subset feature selection (RSFSA) and ten random subsets out of 250 randomly generated six-variable subsets of various sizes derived from 80 variables; and (D-F) top 250 variable subsets out of 3,000 subsets per three training set replicates selected by AUC_{psa} or AICc using RSFSA and top 300 random generated six-variable subsets out of 3,000 subsets derived from 80 variables. Means for AUC_{psa} selected or AICc selected model statistics within a replicate with an asterisk are significantly more optimal (higher for $AUC_{psa\_finaltest}$ and lower for $AICc_{bg\_final}$ and $AUC_{psa\_diff\_final}$) from that of random selected models ($P < 0.05$; Welch t test with Holm correction, preceded by significant Welch ANOVA test, $P < 0.05$)

248

population density grid (CIESIN, 2005) was aggregated to 10 km resolution to match the resolution of the occurrence data. A focal mean of population density was then calculated within 30 by 30 km windows. The roost presence raster (values of one where present) was divided by the population density raster to yield a raw monarch roost by human population density index, with smaller numbers indicating higher populations. Values of the raw human population density index that were below one were changed to one, and values above ten were limited to ten, yielding a monarch roost human population density index raster. The raster was converted to a point shapefile with values ranging continuously from one in densely populated areas (most points) to 10 in sparsely populated areas. The KDE surface was then calculated based on this shapefile, with the index limits of one to ten constraining the maximum influence of human population density to a factor of 10.

Anthropogenic Fall Migration Hazards

Monarch roadkill hotspot points in Texas and Mexico were identified through citizen science reports from Journey North (2017), Correo Real (2015), and Rogelio Carrerra (Universidad Autonoma de Nuevo Leon, Nuevo Leon, Mexico, personal communication). Potentially reduced nectar plant habitat availability was identified for polygon areas with $\geq 90\%$ anthropogenic (cultivated or urban) land cover per 1 km, having at least 70% cultivated land cover (Tuanmu and Jetz, 2014; EarthEnv, 2016). Polygon layers for counties in the US with the potentially highest contamination of flower nectar food resources near field crops were identified from the top one third and middle third of counties in terms of total use of major neonicotinoids (imidacloprid, clothianidin, thiamethoxam) for the year 2014 (EPest-high method; US Geological Survey [USGS] 2018). Polygon layers were created of counties in Texas and Louisiana with organized mosquito control districts that potentially apply adulticides using ultra-

low volume (ULV) truck sprays in October to November (Texas Mosquito Control Association, 2018; Louisiana Mosquito Control Association, 2018). Polygon layers were also created for counties (including only cities within counties) with mosquito abatement programs potentially utilizing ULV adulticides in October to November within coastal states from Texas to Georgia from a variety of sources (Georgia Mosquito Control Association, 2018; Mississippi State Department of Health, 2018; Florida Medical Entomology Laboratory, 2018), including examination of the most current mosquito control information that could be located for various city, county, and parish websites found through internet searches. Mosquito control websites were used to obtain the latest fall months for ULV spray mosquito treatments, including October in the Central Flyway (City of Dallas, 2017; City of Del Rio, 2018), November along the Texas Coast in the Eastern Flyway (League City, 2016), and December in Cameron Parish, Louisiana (Louisiana Mosquito Control Association, 2016).

Results

Annual Kernel Density Estimation Model Migration Pathways

The average width of the kernel density estimation model (KDEM) migration pathway in the northern portion of the Central Flyway (37-50°N latitude, from northern Oklahoma border northwards) varied by 662 km, ranging from 694 km in 2013 to 1,356 km in 2007 (Figure C.2A). The average width of the KDEM migration pathway in the southern portion of the Central Flyway (27-37°N) varied by 392 km, ranging from 519 km in 2013 to 910 km in 2011 (Figure C.2D). The annual north to south shift from average for the northern portion of the KDEM migration pathway in the Central Flyway varied by 143 km, ranging from 73 km to the south in 2015 to 70 km to the north in 2012 (Figure C.2B). The annual north to south shift from average for the southern portion of the KDEM migration pathway in the Central Flyway varied by 131

Figure C.2. Monarch migration pathway characteristics for the Central Flyway from training set ensembles of kernel density estimation models (KDEMs) (n = 3) for 2002–2016 and annually from 2005 to 2016 for (A-C) northern area from 37 to 50°N and (D-F) southern area from 27 to 37°N. Includes (A,D) the average KDEM width and the shift of the KDEM centroid north or south (B,E) or east to west (C,F) compared to the 2002–2016 minimum frequency consensus KDEM.

251

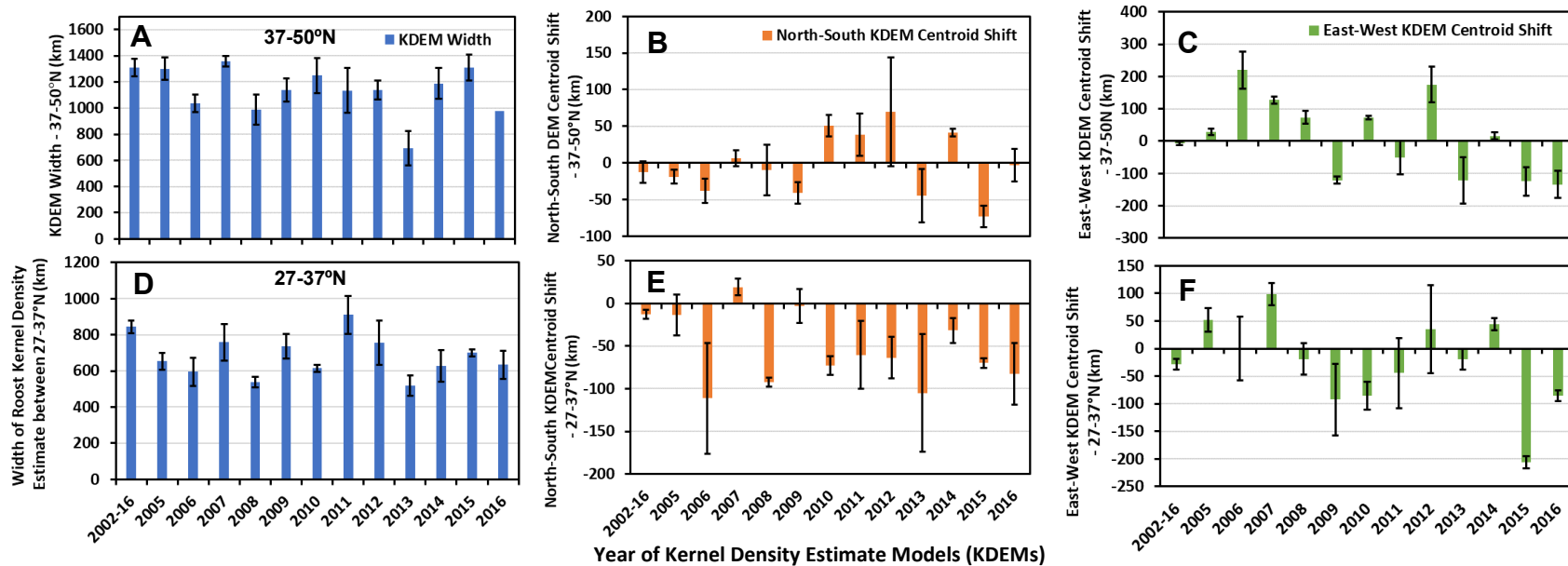Figure C.3. Spearman rank correlation (r_s) between annual 2005 to 2016 monarch overwintering population areas in Mexico and monarch migration pathway characteristics in the Central Flyway from training set ensembles of kernel density estimation models (KDEMs) (n = 3): (A-C) northern area from 37 to 50°N and (D-F) southern area from 27 to 37°N. Includes (A,D) the average KDEM width and the shift of KDEM centroid north or south (B,E) or east to west (C,F) compared to 2002–2016 minimum frequency consensus KDEM (see Figure C.2 for original dimensional characteristics).
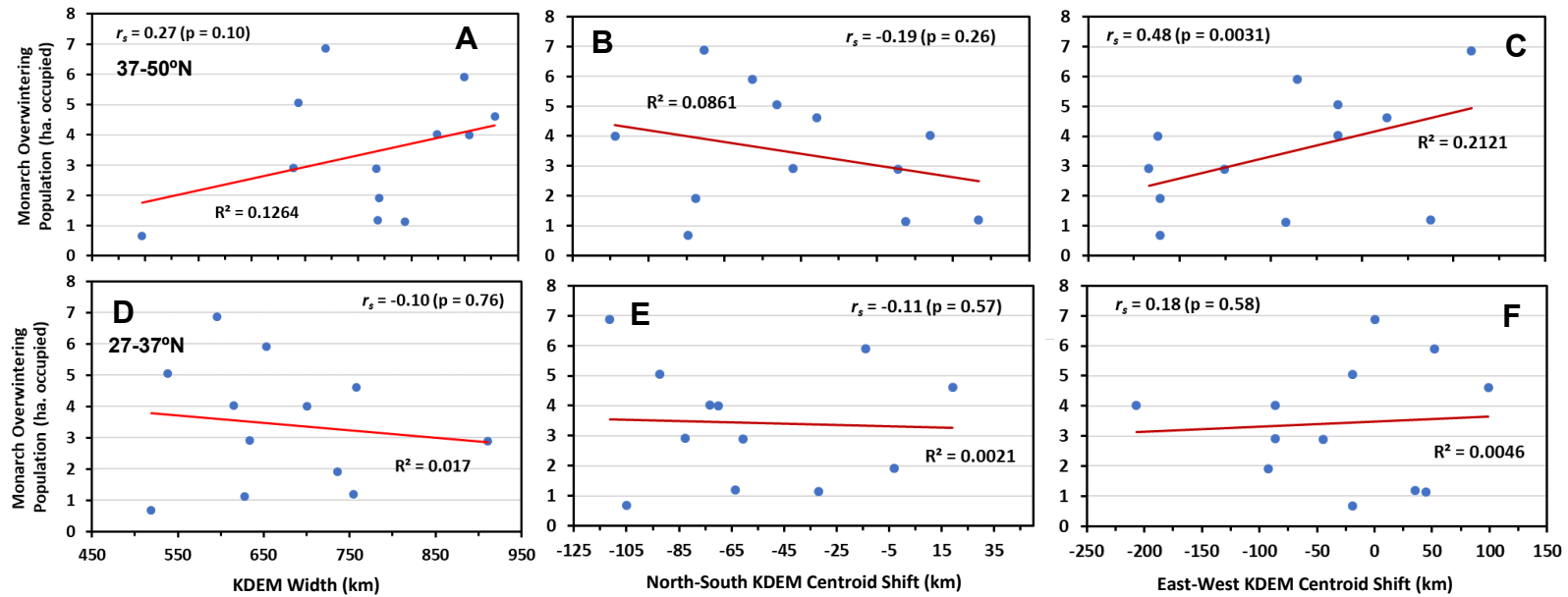
km, ranging from 111 km to the south in 2006 to 19 km to the north in 2007 (Figure C.2E). The annual east to west shift from average for the northern portion of the KDEM migration pathway in the Central Flyway varied by 353 km, ranging from 134 km to the west in 2016 to 220 km to the east in 2006 (Figure C.2C). The annual east to west shift from average for the southern portion of the KDEM migration pathway in the Central Flyway varied by 306 km, ranging from 207 km to the west in 2015 to 99 km to the east in 2007 (Figure C.2F).

References (not appearing in main References section)

Brauers WK, Zavadskas EK (2010) Project management by MULTIMOORA as an instrument for transition economies. Technological and Economic Development of Economy 1:5-24.

Ceballos Martín BA (2016) Package 'MCDM'. 9 pp. Available from https://cran.r-project.org/web/packages/MCDM/MCDM.pdf   (6 February 2016)

City of Dallas (2017) Fight the bite: Mosquito prevention in Dallas 2017. Available from http://www.dallascitynews.net/2017sprayalerts (23 June 2018)

City of Del Rio (2018) Vector control: Vector spray pattern map. Available from https://www.cityofdelrio.com/737/Vector-Control (10 June 2018)

EarthEnv (2016) EarthEnv: Global, Remote-sensing Supported Environmental Layers for Assessing Status and Trends in Biodiversity, Ecosystems, and Climate; Global 1-km Consensus Land Cover. Available from http://www.earthenv.org/landcover (16 January 2017)

Florida Medical Entomology Laboratory (2018) Florida mosquito control programs. Available from http://mosquito.ifas.ufl.edu/florida_mosquito_control_districts.htm (10 June 2018)

Georgia Mosquito Control Association (2018) Georgia mosquito control program contacts. Available from

http://www.gamosquito.org/resources/GA_Mosquito_Control_Programs2017.pdf (10 June 2018)

Kantola T, Tracy JL, Baum KA, Quinn MA, Coulson RN (2018) Spatial risk assessment of eastern monarch butterfly road mortality during fall migration within the southern corridor. Manuscript submitted for publication.

League City (2016) Fight the bite: Update on mosquito spraying for League City. 26 April, 2016. Available from https://www.leaguecity.com/CivicAlerts.aspx?AID=1753 (10 June 2018)

Louisiana Mosquito Control Association (2016) District news: Cameron Parish. LeMaringouin Newsletter, April 2016. Available from http://www.lmca.us/newsletter.htm (6 September 2018)

Louisiana Mosquito Control Association (2018) Mosquito districts. Available from http://www.lmca.us/districts.htm (8 June 2018)

Mississippi State Department of Health (2018) Mosquito control grants awarded to local communities. 8 May 2018. Available from https://msdh.ms.gov/msdhsite/_static/23,19820,341.html (10 June 2018)

Texas Mosquito Control Association (2018) Organized mosquito control districts in Texas. Available from http://www.texasmosquito.org/Districts.html (8 June 2018)

Tuanmu MN, Jetz W (2014) A global 1-km consensus land-cover product for biodiversity and ecosystem modelling. Global Ecology and Biogeography 23:1031-1045.

US Geological Survey (2018) National Water Quality Assessment Project: Pesticide National Synthesis Project; 2014. Available from https://water.usgs.gov/nawqa/pnsp/usage/maps/countylevel/ (8 June 2018)

APPENDIX D

(CHAPTER IV)

Spring 2017 Texas Monarch Roadkill Survey

Methods

Monarch roadkill surveys were conducted from 12 April to 21 May, 2017 over much of

the central-eastern portion of Texas approximately bounded by US highway 59 to the east, about

29ºN to the south, about 101ºW to the west and US highway 287 to the north (Figure A.1).

Surveys were conducted over four one-week periods progressing from south to north. Monarch

roadkill counts were collected from one by 100 m transects along the edge of one side of the

road following the described procedures for the fall 2016–2017 roadkill surveys.

Results

Monarch roadkill was detected within only two of the 54 transects, and both detections

were single males (Figure A.1). One monarch roadkill was along Texas highway 7 east of Marlin

on 28 April, and another was along US highway 380 west of Runaway Bay on 10 May.

Texas Monarch Roadkill Survey Data

Fall 2016–2017 Monarch Roadkill Survey Raw Data – Unthinned (Geographic; WGS84)

Fall2016_2017Monarc
hRoadkillData.pdf

Fall 2016–2017 monarch roadkill survey raw data – thinned to 2 km and shifted to roadway

(North America Albers Equal Area Conic, NAD83)

Fall2016_2017Monarc
hRoadkillThinned.pdf

Spring 2017 monarch roadkill survey raw data – unthinned (geographic; WGS84)

Spring2017MonarchR
oadkillData.pdf

Texas and Mexico Monarch Roadkill Data from Other Sources

MonarchRoadkillOthe
rData.pdf

Texas Monarch Roadkill Survey Data and MaxEnt Roadkill Extrapolations

Fall2016_2017Monarc
hRoadkillDataExtrapo

MaxEnt Roadkill Consensus Model

A zipped shapefile represents the MaxEnt frequency consensus of the feature subset

ensemble of ten monarch roadkill models developed from random subsets of ten of 20 variables

(Figure IV.4; MonarchCentralFunnelRoadkillMaxEnt10ModeFSEConsensusSumShapefile.zip;

available from author and to be made available in appendix of published verions).

Environmental Variables

All environmental rasters were converted to and processed within the North American

Albers Equal Area Conic projection (North American 1983 datum) to best preserve spatial

relationships. The void-filled SRTM DEM was hydrologically processed before identifying

streams with different levels of flow accumulation and calculating various topographic moisture

indices. The percent cover of various Globeland30 land cover types (Chen et al., 2015) within a

500 m circular radius window size was calculated in ArcGIS (ESRI, Redlands, CA, USA). Road layers of the three major road types from 2017 were downloaded from Geofabrik (http://download.geofabrik.de/) and converted to rasters aligned with the DEM. Euclidean distances to urban areas, various road types, and stream layer flow accumulation categories were calculated in ArcGIS.

Correo Real Roadkill Report

The Correo Real (2015) Fall bulletin No. 15 from 8 November, 2015 is not available at the Correo Real (Royal Mail) Mexican monarch citizen science website, which only has publications since 2016 (http://correoreal.org.mx/noticias/). The original Spanish translation and a version with October 2015 Mexico roadkill reports roughly translated into English (in red) are embedded below.

CorreoReal2015_MexicoRoadkillSpanish.pd

CorreoReal2015_MexicoRoadkillEnglishPart

Monarch Population Decline Curve

The initial and final modeled number of hectares in the modeled standard geometric power curve (Fig. 5) was used in a standard geometric population growth equation $P_t = P_o(1 + r/n)^{nt}$, where P_t is the final hectares (2.11), P_o is the initial hectares (11.79), t is the number of years (23), n is the number of sub-periods (1), and r is the population growth (or declination) rate. Solving for r yields an average -7.21% population decline per year over the last 23 years,

Table D.1. Thirty environmental predictor indices (30.8 m resolution) evaluated for developing monarch roadkill models.

Variable Index	Abbreviation[a]	Source
Six Road Indices (based on three major road types of highways, primary roads, and secondary roads)		
Road density, km road per 500 m circular radius	*roadden500mr**	Derived from OpenStreetMap (Geofabrik, 2017)
Road density, km road per 3 km circular radius	*roadden3kr**	"
Distance to highways (motorways and trunks)	*hwydist**	"
Distance to primary roads	*primrddist**	"
Distance to secondary roads	*secrddist**	"
Traffic volume for 2015	*traffic_vol*	OpenStreetMap (Geofabrik, 2017) and Federal Highway Administration (2017)
Three Human Population Density Indices		
Human population density per km in 3 km circular radius	*popden3kr**	Derived from CIESIN (2016)
Human population density per km in 9 km circular radius	*popden9kr**	"
Distance to urban areas ≥ 300 humans per km	*urbdist**	"
Nine Topographic Indices		
Elevation	*elev**	NASA JPL (2013)
Topographic Position Index (TPI), 500 m circular radius[b]	*tpi500mr*	Derived from 1 arc second resolution SRTM elevation (NASA JPL, 2013)
TPI, 3 km circular radius[b]	*tpi3kr**	"
Compound Topographic Index (CTI)[b]	*cti*	"
Distance to Streams (STRMDIST)	*strmdist*	"
Distance to Low Flow Accumulation Areas (100–5,000 cells; STRMLOFLODIST)	*strmloflodist*	"
Distance to Medium Flow Accumulation Areas (5,000–60,000 cells; STRMMDFLODIST)	*strmmdflodist*	"

Table D.1. Continued.

Variable Index	Abbreviation[a]	Source
Latitude	*latitude**	Derived using ArcGIS
Eight Land Cover Indices (percent cover in 500 m radius window)		
Artificial surfaces	*artsur_500mr**	Globeland30 (Chen et al., 2015)
Barren lands	*bare_500mr*	"
Cultivated land	*cult_500mr**	"
Forests	*forest_500mr*	"
Grasslands	*grslnd_500mr**	"
Shrublands	*shrub_500mr**	"
Water bodies	*water_500mr*	"
Wetland	*wetlnd_500mr*	"
Four Climatic Indices[c]		
Autumn quarterly mean monthly maximum temperature	*tmax_autq**	for 1960–1990 derived from WorldClim (2017) of Hijmans et al. (2005)
Annual mean monthly rainfall (P) (mm)	*prec_ann**	"
Autumn quarterly mean monthly Actual Evapotranspiration/Potential Evapotranspiration × 1000	*etrt_autq**	"
Autumn mean quarterly wind speed (m/second)	*wndsp_autq**	for 1970–2000 derived from WorldClim2 (2017) of Fick and Hijmans (2017)

[a]Asterisks indicate 20 of 30 variables selected for developing final MaxEnt monarch roadkill niche models.

[b]Calculated using Geomorphometry and Gradient Metrics Toolbox for ArcGIS (Evans et al., 2014).

[c]Autumn quarter includes October, November, and December.

Table D.2. Monarch butterfly roadkill estimates for separate 2016 and 2017 data over the Sonora-Sheffield roadkill hotspot, background evaluation extent (BEE) and the Central Funnel extrapolated from each 2016-2017 data MaxEnt roadkill model according to estimated roadkill per km for the length of predicted roadkill presence of each road type.[a]

| | Hotspot Data Separated | | | | | | | |
| | 2016 | | | | 2017 | | | |
MaxEnt Model Number	Sonora-Sheffield Hotspot	BEE	Funnel	BEE as % Funnel	Sonora-Sheffield Hotspot	BEE	Funnel	BEE as % Funnel
1	63,117	544,753	1,551,614	35%	4,644	511,192	1,836,491	28%
2	62,489	921,991	1,643,275	56%	4,644	1,035,782	1,931,566	54%
3	63,100	995,924	1,723,338	58%	4,641	1,050,918	1,972,208	53%
4	62,694	920,454	1,603,772	57%	4,644	1,048,271	1,902,672	55%
5	62,962	362,150	795,855	46%	4,644	380,488	923,739	41%
6	61,770	574,432	1,078,945	53%	4,650	637,490	1,277,795	50%
7	63,052	1,001,916	1,557,014	64%	4,638	1,146,775	1,854,326	62%
8	63,046	790,029	1,241,274	64%	4,644	912,455	1,459,983	62%
9	63,053	625,162	1,218,973	51%	4,638	696,543	1,438,663	48%
10	62,580	393,397	855,252	46%	4,638	412,760	991,107	42%
Mean	62,786	713,021	1,326,931	53.04%	4,643	783,267	1,558,855	49.5%
SD	424	244,184	337,027	8.96%	4	289,973	397,394	10.5%
% Over-wintering Population[b]	0.09%	0.86%	1.56%		0.01%	1.26%	2.48%	
% of Funnel Mortality	5.96%	54.33%			0.30%	50.25%		

[a] Based upon multiplying length of road type by roadkill density per km (presence only) for road type in each MaxEnt model. See section 4 for estimations of roadkill rates for each road type and the km of road type per MaxEnt model.

[b] Based on 84.61 and 61.4 million monarchs overwintering in 2016 and 2017, respectively (Monarch Watch, 2018b). Overwintering estimates were averaged for the combined 2016-2017 data. The figure of 21.1 million monarchs per hectares overwintering was used in estimations (Thogmartin et al., 2017).

260

Table D.3. Monarch butterfly roadkill estimates for combined 2016 and 2017 data over the Sonora-Sheffield roadkill hotspot, background evaluation extent (BEE) and the Central Funnel extrapolated from each 2016-2017 data MaxEnt roadkill model according to estimated roadkill per km for the length of predicted roadkill presence of each road type.[a]

MaxEnt Model Number	Hotspot Data Separated 2016-2017					Hotspot Data Merged 2016-2017		
	Sonora-Sheffield Hotspot	BEE	Funnel	BEE as % Funnel		BEE	Funnel	BEE as % Funnel
1	72,331	546,899	1,417,915	39%		2,381,698	5,790,868	41%
2	71,703	979,939	1,484,293	66%		5,490,391	5,791,553	95%
3	72,309	1,022,358	1,499,601	68%		5,510,246	5,266,688	105%
4	71,908	985,509	1,468,816	67%		5,533,646	5,918,898	93%
5	72,176	396,537	753,275	53%		2,079,664	3,062,060	68%
6	70,997	621,348	1,012,343	61%		3,451,465	4,259,790	81%
7	72,255	1,072,235	1,440,533	74%		6,011,376	5,697,998	105%
8	72,260	858,286	1,152,658	74%		4,678,765	4,255,994	110%
9	72,256	674,753	1,129,339	60%		3,752,613	4,644,830	81%
10	71,782	426,792	799,592	53%		2,244,533	3,249,800	69%
Mean	71,997.63	758,465	1,215,836	61.6%		4,113,440	4,793,848	84.8%
SD	419.59	256,087	288,294	11.1%		1,526,878	1,068,548	21.3%
% Over-wintering Population[b]	0.10%	1.03%	1.64%			5.33%	6.16%	
% of Funnel Mortality	5.92%	62.38%				85.81%		

[a] Based upon multiplying length of road type by roadkill density per km (presence only) for road type in each MaxEnt model. See section 4 for estimations of roadkill rates for each road type and the km of road type per MaxEnt model.

[b] Based on average of 73 million monarchs overwintering from both 2016 (84.61 million) and 2017 (61.4 million) (Monarch Watch, 2018b). Overwintering estimates were averaged for the combined 2016-2017 data. The figure of 21.1 million monarchs per hectares overwintering was used in estimations (Thogmartin et al., 2017).
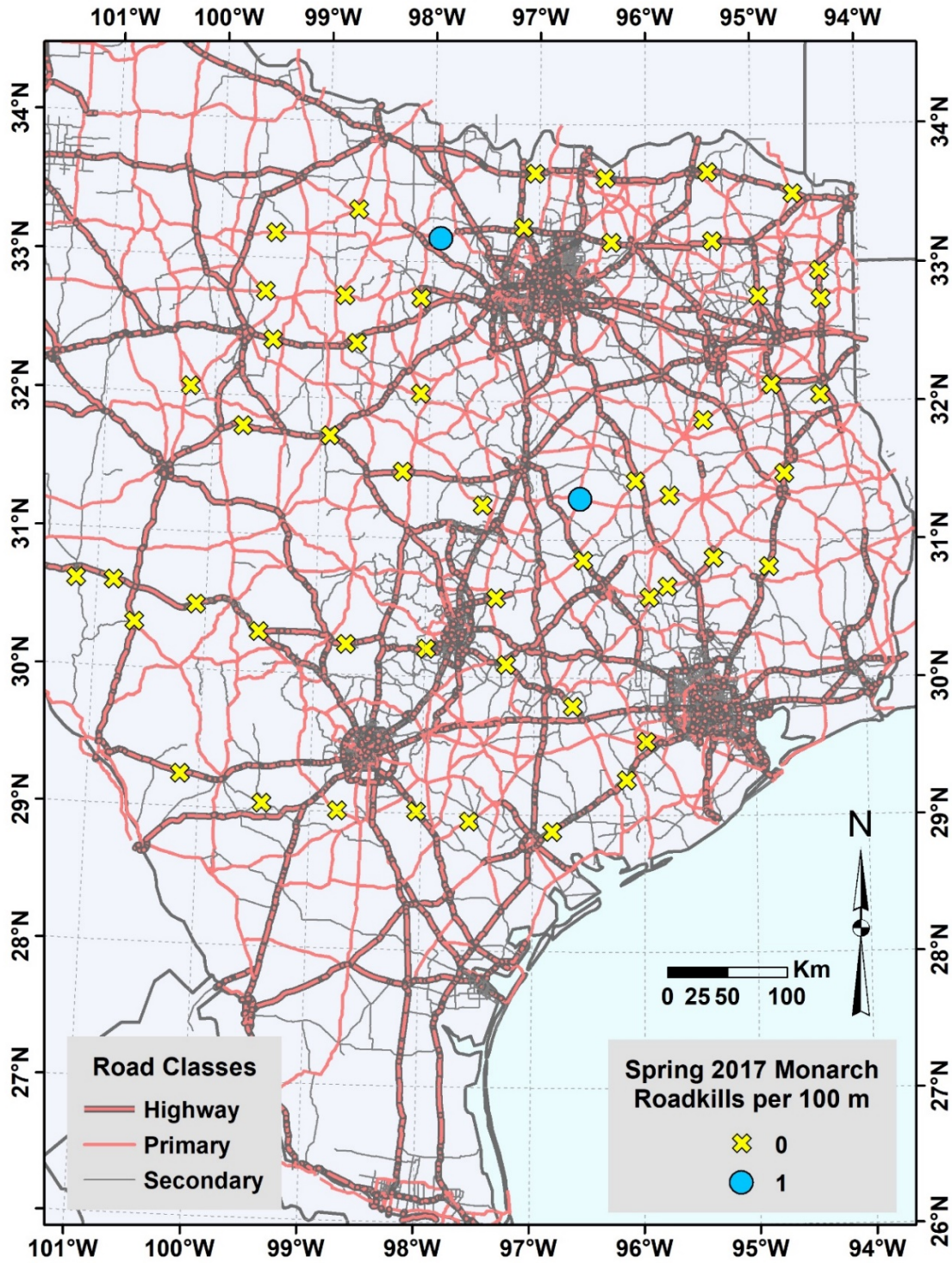
Figure D.1. Monarch roadkill spring 2017 survey results for 100 m transects along major road classes within Texas.
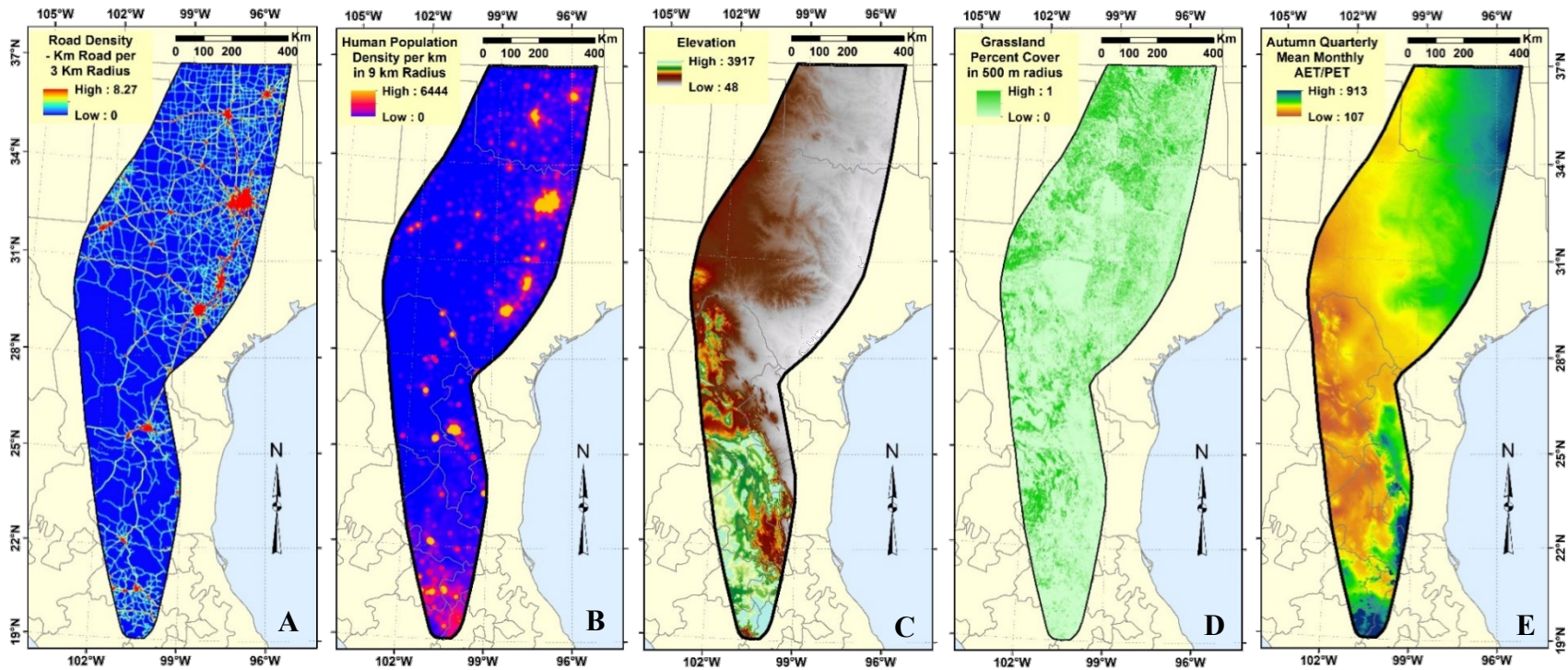
Figure D.2. Representative important environmental variables (30 m resolution) for five types of indices in MaxEnt niche models of monarch fall migratory roadkill within the Central Funnel: (A) road index of kilometers of road per three km radius (*roadden3kr*); (A) human population index of population density within a 9 km radius (*popden9kr*); (C) topographic index of elevation (*elev*); (D) land cover index of percent cover of grasslands in a 500 m radius (*grslnd_500mr*); and (E) climatic index of autumn quarterly mean monthly actual evapotranspiration (AET)/potential evapotranspiration (PET) × 100 (see Table IV.2 for variable importance).
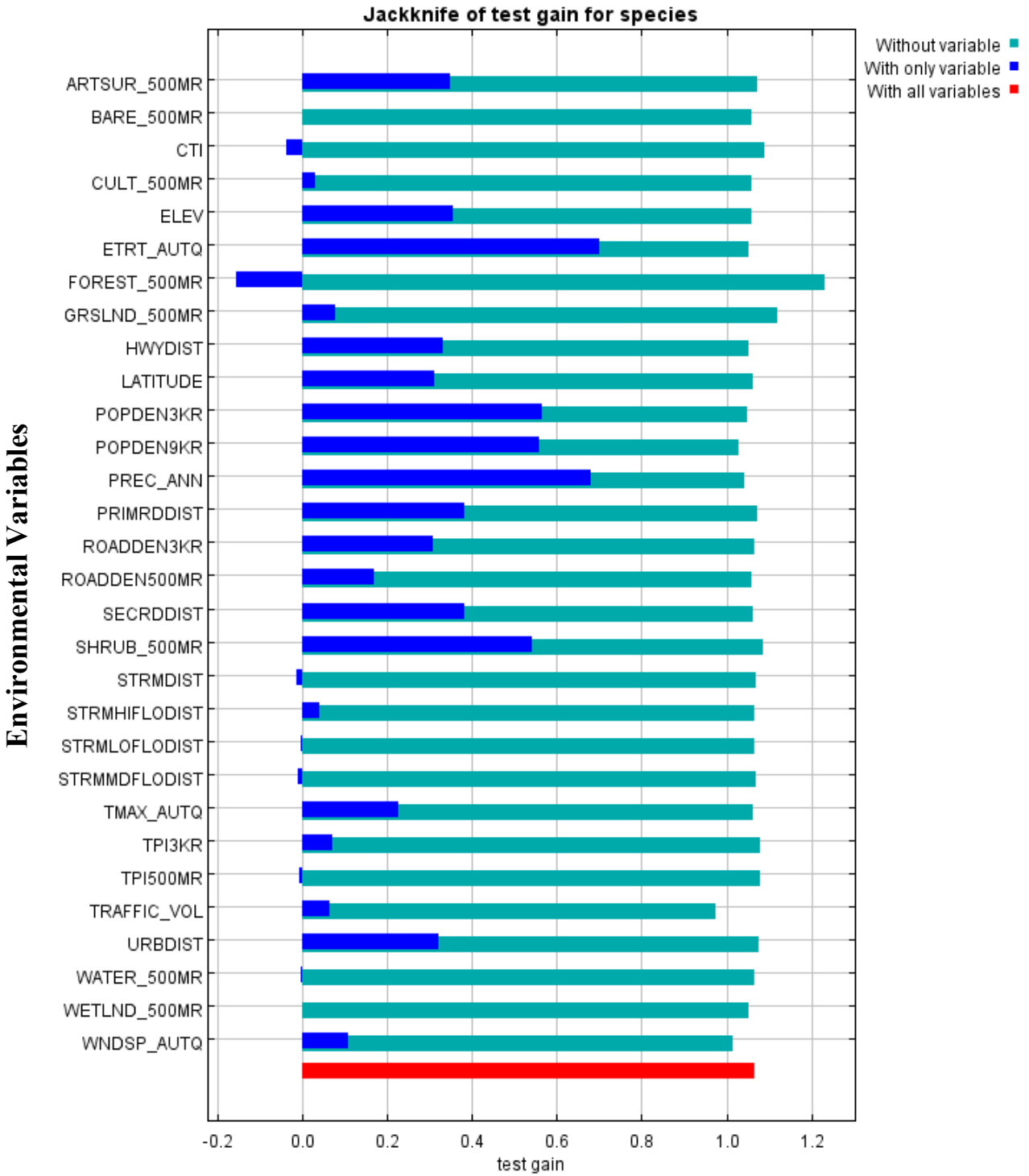
Figure D.3. MaxEnt variable importance in jackknife analysis of test gain for 30 total environmental variables in monarch roadkill model (see Table D.1 for variable abbreviations).
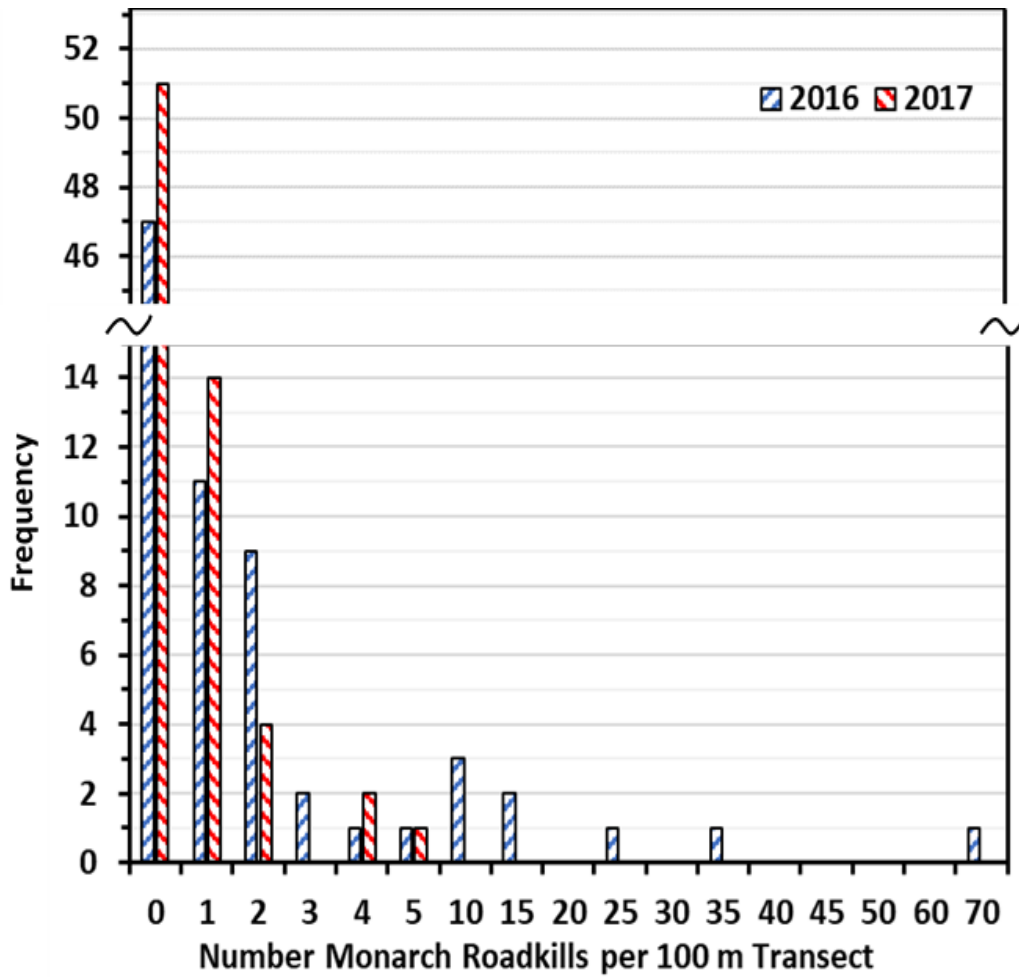
Figure D.4. Frequency distribution of monarch roadkill counts (spatially thinned to 2 km) for 100 m transects for fall 2016 and 2017 along major road classes within the background evaluation extent of the monarch Central Funnel in Texas (Figures IV.1-2).

References (not appearing in main References section)

Chen J, Chen J, Liao A, Cao X, Chen L, Chen X, He C, Han G, Peng S, Lu M, Zhang W (2015) Global land cover mapping at 30 m resolution: A POK-based operational approach. ISPRS Journal of Photogrammetry and Remote Sensing 103:7-27.

Federal Highway Administration (2017) Office of Highway Policy Information: Highway Performance Monitoring System public release of geospatial data in shapefile format; 2015 Texas and Oklahoma polyline shapefiles with average annual daily traffic (AADT). Available from https://www.fhwa.dot.gov/policyinformation/hpms/shapefiles.cfm (6 March 2018)

Fick SE, Hijmans RJ (2017) WorldClim 2: new 1-km spatial resolution climate surfaces for global land areas. International Journal of Climatology 37:4302-4315.

Geofabrik (2017) OpenStreetMap Data Extracts. Available from http://download.geofabrik.de/ (6 March, 2018)

NASA Jet Propulsion Laboratory (JPL) (2013) NASA Shuttle Radar Topography Mission [SRTM] United States 1 arc second. Version 3. 6oS, 69oW. NASA EOSDIS Land Processes DAAC, USGS Earth Resources Observation and Science (EROS) Center, Sioux Falls, South Dakota (https://lpdaac.usgs.gov). Available from http://dx.doi.org/10.5067/MEaSUREs/SRTM/SRTMUS1.003 (1 January 2015)

WorldClim2 (2017) WorldClim Version 2. Available from http://www.worldclim.org/version1 (6 March 2018)